

**MECHANISMS OF DEADLY AND INFECTIOUS VIRUSES:
*LEARNING HOW LIPID ENVELOPED VIRUSES ASSEMBLE***

by
Monica Leigh Husby

A Dissertation

*Submitted to the Faculty of Purdue University
In Partial Fulfillment of the Requirements for the degree of*

Doctor of Philosophy



Medicinal Chemistry & Molecular Pharmacology
West Lafayette, Indiana
May 2020

THE PURDUE UNIVERSITY GRADUATE SCHOOL
STATEMENT OF COMMITTEE APPROVAL

Dr. Robert Stahelin, Chair

Department of Medicinal Chemistry & Molecular Pharmacology

Dr. Richard Kuhn

Department of Biological Sciences

Dr. Douglas LaCount

Department of Medicinal Chemistry & Molecular Pharmacology

Dr. Angeline Lyon

Department of Chemistry

Approved by:

Dr. Andy Hudmon

Dedicated to my parents, my family, and all the friends who became family.

ACKNOWLEDGMENTS

The doctoral research presented in this thesis is the result of collaboration across numerous individuals, facilities, and universities. The teachers, research faculty and staff at Albion College and Midwestern University were formative in my desire to pursue a doctoral degree in biomedical research. It was at the time of finishing my Master's degree at Midwestern University that I became aware of the work of Dr. Paul Farmer, which inspired me to get involved in infectious disease research. Upon starting my Ph.D. at the University of Notre Dame in 2015, I was introduced to my future advisor, Dr. Rob Stahelin, who was investigating Malaria and hemorrhagic fever viruses in his laboratory. After joining his lab, Dr. Stahelin asked about my interests and I explained my desire to contribute to pre-clinical work investigating therapeutics to target infectious diseases, and over the last five years Dr. Stahelin has helped mold the projects presented in this document. I have endlessly grateful to the technical support, numerous conversations, mentorship, leadership and guidance Dr. Stahelin has provided. He encouraged me to apply for an internal NIH-funded fellowship at the University of Notre Dame called the Chemistry, Biology, and Biochemistry Interface (CBBI) Program, which I was awarded and provided funding to our research for the subsequent year. I would like to thank the CBBI committee, as well as the faculty members on my thesis committee, Dr. Bradley Smith and Dr. Sharon Stack. Two years into my doctoral work, Dr. Stahelin asked me to join him in transitioning our lab to Purdue University, which I accepted. Although I only spent two years at the University of Notre Dame, I am eternally grateful for the research facilities, faculty, fellow students and staff for their contribution to my education and research.

Moving to Purdue University in 2017 was instrumental to my successes throughout my doctoral training. The staff and research facilities that became available at Purdue University were a critical aspect, including the Medicinal Chemistry & Molecular Pharmacology support staff (Barb Mullenberg and Roz Batta) that assisted me during transferring universities, and the electron microscopy facilities, Bindley imaging facilities who helped train me. Additionally, the faculty members that agreed to serve on my thesis committee on short notice without previous knowledge of my research or myself, I owe gratitude towards. Dr. Angeline Lyon, Dr. Richard Kuhn, and Dr Doug LaCount, thank you for the time you have taken for serving on my committee and helping advance my research projects. On countless occasions each of you has contributed to the

development of my research, either through individual meetings, group lab meetings, committee meetings, you or members of your lab collaborating with me, and of course participating in my dissertation process.

I would also like to thank Dr. Rob Stahelin for helping me advance collaborative projects across numerous universities. Importantly, the paramyxovirus project that I have worked on with Dr. Michael Norris and Dr. Erica Sapphire at the La Jolla Institute for Immunology has been an extremely rewarding experience and I would like to express my gratitude to everyone involved in this project. Furthermore, I would like to thank every previous and current lab member that I have worked alongside throughout my training. Each one has provided technical support and guidance in their own unique ways and I deeply value the friendships that have developed as a result. Specifically, Kaveesha Wijesinghe, Carolyn LaBonia and Caroline Plescia thank you for making our research feel like a team effort and creating a friendly and productive workplace. Additionally, the Stahelin Lab manager, Dr. Nathan Dissinger, thank you for your endless technical support and for providing excellent mentorship- you have been a true delight to work for.

Thank you to many friends who have helped me in good times and bad times, and all the in-betweens. We have celebrated so many life experiences together, and I am grateful to you all. Sometimes, friends become family and many of you have become mine. And of course, to my best friend- Patrick Rothstein- thank you for your support over the last five years. Your friendship and love have been paramount to my life within the doctoral program and outside of it. I was lucky to meet you along this journey, and owe much of my success to your patience, wisdom, and kindness.

Lastly, to my family. My parents, Marge & Terry, Mike & Judy, you have all supported me in ways that transcend any words. You have always believed in my potential and done everything in your capacity to help. I have and always will strive to make you proud and will always be here for you as you each have for me. My siblings, Marie, Matt, Mason, Ashley and Lindsay (and their spouses!), thank you for being role models, beacons of love, and always there for sharing fun adventures and memories with. To my grandparents who are no longer here in person, your spirits have stayed with me along every step of the journey. And to my grandmother Barb and grandfather Roger, I am so grateful to have been able to share this journey with you. Grandma Barb, you have and always will be one of the most admirable people I know. Your strength, intelligence, beauty, kindness, humor, creativity and hope is an example to all on how to lead a fulfilling and giving life.

TABLE OF CONTENTS

LIST OF FIGURES	12
LIST OF ABBREVIATIONS.....	23
ABSTRACT.....	27
CHAPTER 1. DEADLY AND INFECTIOUS VIRUSES: AN INTRODUCTION TO MONONEGAVIRALES	28
1.1 Mononegavirales: Who are they?	28
1.1.1 Filovirus history.....	29
1.1.1.1 Marburg virus.....	30
1.1.1.2 Ebola virus	31
1.1.2 Paramyxovirus history	32
1.1.2.1 Measles virus.....	32
1.1.2.2 Nipah virus.....	33
1.2 Viral Structure.....	34
1.3 Viral Life Cycles.....	36
1.3.1 Entry	36
1.3.1.1 pH dependent entry: Filoviruses	37
1.3.1.2 pH independent entry: Paramyxoviruses	37
1.3.2 Replication.....	38
1.3.3 Viral assembly and budding	39
1.4 Vaccines and therapeutics.....	41
1.4.1.1 Vaccine development.....	42
1.4.1.2 Anti-viral development	44
1.5 References.....	46
CHAPTER 2. HIJACKING THE PLASMA MEMBRANE: MECHANISMS OF VIRAL BUDDING	50
2.1 A roadmap of the plasma membrane	50
2.1.1 Viruses and the plasma membrane	52
2.2 Anionic Lipids: Key players in membrane function & viral infection	53
2.2.1 Phosphatidylserine.....	53

2.2.2	Phosphatidylinositols	54
2.2.3	Phosphatidic acid	57
2.3	Lipid transport & implications for viral infection.....	57
2.3.1	Lipid transport proteins.....	58
2.3.2	ATP-dependent lipid transport	58
2.3.2.1	Lipid scramblases.....	58
2.3.2.2	Scramblases in viral infection: Apoptotic mimicry	60
2.4	Viral budding at the plasma membrane	60
2.5	Structural basis of matrix protein function	61
2.5.1	Filovirus matrix proteins.....	62
2.5.1.1	Structural overview of eVP40	62
2.5.1.2	Structural overview of mVP40	63
2.5.2	Paramyxovirus matrix proteins.....	64
2.5.2.1	Structural overview of HeV-M	64
2.5.2.2	Structural overview of NDV-M	65
2.6	Protein – lipid interactions	66
2.6.1	Types of protein-lipid interactions.....	66
2.6.2	Tools to study protein-lipid interactions.....	67
2.7	Matrix protein – membrane interactions.....	68
2.7.1	Matrix protein lipid specificity	69
2.7.2	Membrane penetration by matrix proteins.....	70
2.7.3	Lipid induced matrix protein assembly	71
2.7.4	Matrix protein induced membrane remodeling	71
2.8	Membrane domains: A revolving door for viral entry and exit?	73
2.8.1	Lipid rafts.....	73
2.8.1.1	Viral exploitation of lipid rafts.....	74
2.8.2	Caveolae	77
2.8.2.1	Viruses & Caveolae	77
2.9	Matrix proteins & host proteins	79
2.9.1	The ESCRT machinery.....	79
2.9.1.1	ESCRT in viral budding.....	79

2.9.2 The actin network	81
2.10 References	83
CHAPTER 3. MOLECULAR DETAILS OF PARAMYXOVIRUS MATRIX PROTEIN & PLASMA MEMBRANE ASSOCIATION	94
3.1 Introduction.....	94
3.2 Materials and Methods.....	95
3.2.1 Plasmids.....	95
3.2.2 Reagents.....	95
3.2.3 Cell Culture & Transfections.....	95
3.2.4 Lipids	96
3.2.5 Pharmacological Treatments	97
3.2.6 Liposome (LUVs) Preparation	98
3.2.7 Liposome Sedimentation Assays.....	98
3.2.8 Scanning Electron Microscopy.....	99
3.2.9 Cellular Confocal Microscopy.....	99
3.3 Results.....	99
3.3.1 MeV-M and NiV-M generate spherical and filamentous cell surface extensions.....	99
3.3.2 Determining MeV-M and NiV-M lipid affinity	102
3.3.2.1 MeV-M and NiV-M associate with phosphatidylserine enriched membranes	102
3.3.2.2 MeV-M and NiV-M differentially associate with phosphatidylinositol membranes	103
3.3.3 Additive and synergistic binding	104
3.3.4 MeV-M and NiV-M interact with anionic lipids through electrostatic and stereospecific interactions.....	106
3.3.4.1 Electrostatics govern binding to phosphatidylserine	107
3.3.4.2 MeV-M and NiV-M interact with phosphatidylinositol lipids through stereospecific interactions.....	107
3.3.5 Live cell imaging depicts differential mechanisms of membrane association	109
3.3.5.1 Investigating charge sensing mechanisms	109
3.3.5.2 MycVPtase and PI(4,5)P ₂ depletion.....	110
3.3.5.3 Apilimod treatment to explore role of PI(3,5)P ₂	115

3.3.5.4 Wortmannin	117
3.3.6 PI Kinase inhibitors: potential anti-viral strategies	119
3.3.7 MeV-M and NiV-M localize to regions of plasma membrane enriched in PI(4.5)P ₂	122
3.4 Discussion	123
3.5 References	128
CHAPTER 4. CHARACTERIZING MARBURG VP40 ASSEMBLY	132
4.1 Introduction	132
4.2 Materials and Methods	134
4.2.1 Reagents & plasmids	134
4.2.2 Cells & transfections	135
4.2.3 Protein Purification	135
4.2.4 Functional budding assays and western blotting	136
4.2.5 Liposome Sedimentation Assays	137
4.2.6 Number & Brightness (N&B) analysis on mammalian cells	137
4.3 Results	138
4.3.1 mVP40 mutants form dimers in solution	138
4.3.2 Mutation of putative oligomerization interfaces does not alter anionic lipid binding	140
4.3.3 Aberrant oligomerization is observed in mVP40 mutants	141
4.3.3.1 Mutating residues with the NTD-oligomerization interface significantly interferes with mVP40 oligomerization	142
4.3.3.2 Mutating residues in the CTD-oligomerization interface alters high ordered mVP40 oligomerization	144
4.3.4 Oligomerization deficient mutants fail to produce VLPs	146
4.4 Discussion	148
4.5 References	150
CHAPTER 5. THE EBOLA VIRUS MATIX PROTEIN CLUSTERS PHOSPHATIDYLSERINE, A CRITICAL STEP IN VIRAL BUDDING WHICH CAN BE REDUCED WITH AN FDA APPROVED DRUG TO INHIBIT VIRAL SPREAD	152
5.1 Introduction	152

5.2	Materials and Methods.....	154
5.2.1	Reagents & solutions	154
5.2.2	Plasmids	154
5.2.3	Lipids and LUV preparation	155
5.2.4	Cell culture, transfections, pharmacological treatments	155
5.2.5	Immunoblotting	155
5.2.6	Protein purification	156
5.2.7	Plasma membrane localization confocal microscopy	156
5.2.8	Cellular Top Fluor TMR-PS clustering confocal microscopy	156
5.2.9	Number & Brightness	157
5.2.10	Chemical crosslinking	157
5.2.11	Surface plasmon resonance	158
5.2.12	Lipidomics	158
5.2.13	BSL-4 immunofluorescence assay	159
5.2.14	VLP collections & functional budding assays	160
5.2.15	Scanning electron microscopy	160
5.2.16	Transmission electron microscopy imaging	161
5.2.17	DiI entry assay	161
5.2.18	Toxicity analysis	162
5.2.19	Mathematical model of in vitro experiments	162
5.2.20	Statistical testing	164
5.3	Results	164
5.3.1	EBOV VP40 localizes to PS enriched regions in membranes	164
5.3.2	EBOV-VP40 enhances clustering of PS in living cells	165
5.3.3	eVP40 membrane binding and oligomerization are dependent on phosphatidylserine content in lipid membranes	168
5.3.4	Total cellular and plasma membrane levels of phosphatidylserine are reduced by fendiline treatment	170
5.3.5	Fendiline reduces PS clustering	172
5.3.6	Fendiline significantly inhibits authentic EBOV and MARV replication	176

5.3.7	Fendiline reduced EBOV-VP40 but not MARV-VP40 localization to the plasma membrane*	180
5.3.8	VP40 oligomerization is significantly reduced by fendiline treatment	183
5.3.9	Fendiline reduced VLP production at the plasma membrane	184
5.3.10	VLP morphology is altered by fendiline treatment	187
5.3.11	Fendiline blocks EBOV eVLP entry	187
5.3.12	Mathematical model of in vitro experiments*	191
5.4	Discussion	194
5.5	References	196
APPENDIX		200

*Indicates experiment performed by collaborators

LIST OF FIGURES

Figure 1.1. Phylogenetic tree of 4 viral families within the Mononegavirales order of RNA viruses. *Bornaviridae*, *Filoviridae*, *Paramyxoviridae*, and *Rhabdoviridae* families are shown. Abbreviations: avian parainfluenza virus type 6 (ApaV6), BDV (Borna disease virus), BEFV (bovine ephemeral fever virus), CDV (canine distemper virus), HeV (Hendra virus), HMPV (human metapneumovirus), HRSV (human respiratory syncytial virus), MARV (Marburg virus), MeV (measles virus), MuV (mumps virus), NDV (Newcastle disease virus), NiV (Nipah virus), PIV3 (parainfluenza virus type 3), PVM (pneumonia virus of mice), RABV (rabies virus), SeV (Sendai virus), PIV5 (parainfluenza virus 5), TRTV (turkey rhinotracheitis virus), VSV (vesicular stomatitis Indiana virus), ZEBOV (Zaire Ebola virus). Source: Fauquet CM, Mayo MA, Maniloff J, et al., eds. *Virus Taxonomy*. Eighth Report of the International Committee on the Taxonomy of Viruses. London: Elsevier/Academic Press; 2005..... 29

Figure 1.2. An electron micrograph of MARV from the 1967 outbreak in Germany. Source: Werner Slenczka, Hans Dieter Klenk, Forty Years of Marburg Virus, *The Journal of Infectious Diseases*, Volume 196, Issue Supplement_2, November 2007, Pages S131–S135 31

Figure 1.3. RNA genome of EBOV and MeV/NiV. EBOV, MARV, NiV, and MeV are (-) sense RNA viruses with a genome that encodes 6-7 structural proteins. **(a)** RNA genome of EBOV. NP: nucleoprotein, VP35: viral protein 35, VP40: viral protein 40, sGP: glycoprotein, GP1 and GP2: cleaved products of glycoprotein, VP30: viral protein 30, VP24: viral protein 24, L: polymerase. **(b)** RNA genome of MeV/NiV. N: nucleoprotein, P: phosphoprotein, M: matrix protein, F: fusion protein, G/H: attachment protein, L: polymerase. The attachment protein is H in MeV and G in NiV..... 34

Figure 1.4. Structure of filoviruses and paramyxoviruses. **(a)** Cartoon of filovirus structure, which is filamentous in shape, is surrounded by a lipid envelope (brown) studded with glycoproteins (red). Underneath the lipid envelope is the viral matrix (green), and at the core is the nucleocapsid containing proteins and the genome (dark blue). **(b)** Transmission electron micrograph of a viral like particle produced from mammalian cells expressing VP40 highlighting the filamentous shape of filoviruses. **(c)** Cartoon of paramyxovirus structure, which is predominately spherical in shape, is surrounded by a lipid envelope (brown) studded with attachment (orange) and fusion proteins (red). Underneath the lipid envelope is the viral matrix (green), and at the core is the nucleocapsid containing proteins and the genome (dark blue). **(d)** Transmission electron micrograph of a MeV highlighting the spherical shape of paramyxoviruses. Micrograph of MeV courtesy of the CDC and Cynthia S. Goldsmith & William Bellini, PhD .. 35

Figure 1.5. Schematic of the life cycle of filoviruses and paramyxoviruses. **(a)** *Filoviruses* enter cells through a micropinocytosis process while *paramyxoviruses* enter through direct fusion of the viral lipid envelope and plasma membrane. **(b)** Structural rearrangements occur within the glycoproteins of these viruses which allow the release of viral components into the cytoplasm. **(c)** Transcription of the (-) sense RNA genome commences and is followed by replication, both of which occur within the cytosol. **(d)** Following transcription and replication, mRNA is translated into new viral proteins which travel through the cell and assemble into new virions at the plasma

membrane. This process is mediated by VP40. (e) Following the assembly of new virions at the plasma membrane, membrane scission occurs releasing the virion into the extracellular space. 41

Figure 2.1. A roadmap to the plasma membrane and the lipids that comprise it. (a) Cartoon of the plasma membrane, which serves as a physical barrier protecting the intracellular space from the extracellular space and is composed of a lipid bilayer with a hydrophobic core and interfacial hydrophilic region. (b) The general structure of a phospholipid, which contains a hydrophilic headgroup and hydrophobic acyl chains esterified to a glycerol backbone. (c) The main phospholipids that comprise the outer leaflet of the plasma membrane include phosphatidylcholine, ceramide and sphingomyelin. (d) The main phospholipids that comprise the inner leaflet of the plasma membrane include phosphatidylethanolamine and the anionic phospholipids: phosphatidic acid, phosphatidylserine, and phosphatidylinositols..... 51

Figure 2.2. Overview of different phosphatidylinositol species. (a) General structure of phosphatidylinositol structure with a inositol ring and phosphate conjugated to the acyl chains via the glycerol backbone. The phosphatidylinositols can be phosphorylated at the D3, D4, or D5 positions generating seven unique species. (b) The three mono-phosphorylated phosphatidylinositols. (c) The three di-phosphorylated phosphatidylinositols. (d) The one tri-phosphorylated phosphatidylinositol. PIP: phosphatidylinositol phosphate. 55

Figure 2.3. Ribbon diagrams of *filovirus* matrix proteins. (a) eVP40 dimeric structure and (b) mVP40 dimeric structure with red arrows indicating dimeric interface and black arrows indicating membrane binding interface. eVP40 PDB: 4LDB and mVP40 PDB: 5B0V. 62

Figure 2.4. Ribbon diagrams of *paramyxovirus* matrix proteins. (a) HeV-M dimeric structure and (b) NDV-M dimeric structure. HeV-M PDB: 6BK6 and NDV-M PDB: 4G1G. 65

Figure 2.5. Membrane curvature at the plasma membrane and during viral budding. (a) Positive and (b) Negative curvature are seen throughout cellular organelles and within the plasma membrane during endocytosis and exocytosis-type events. (c-d) Steps of viral budding where negative curvature is generated during (c) early stages of membrane deformation, (d) growth of the progeny virion and (e) scission of new virion into extracellular space. 72

Figure 3.1. Morphology of NiV-M and MeV-M viral budding using SEM. COS-7 and HEK293 cells were transfected with either NiV-M, MeV-M or eVP40. After 24 hours of transfection, cells were fixed using 2.5% glutaraldehyde and processed for SEM imaging. (a) Representative micrographs of HEK293 cells expressing the indicated protein (or mock transfected) showing spherical budding particles emanating from the cell surface. Mock (*top panel*), MeV-M (*middle panel*), NiV-M (*bottom panel*) (b) Representative micrographs of COS-7 cells (*top two panels*) and HEK293 cells (*bottom two panels*) expressing the indicated protein (or mock transfected) showing filamentous budding particles emanating from the cell surface. Mock (*left panel*), NiV-M (*middle-left panel*), MeV-M (*middle-right panel*), eVP40 (*right panel*). SEM: scanning electron microscopy..... 101

Figure 3.2. Lipid binding properties of MeV-M and NiV-M. Liposome sedimentation assays and western blotting were performed on LUVs with varying anionic lipids and MeV-M or NiV-M. Supernatant (unbound protein) and pellet (protein bound to LUVs) were separated and analyzed through western blotting using a HRP-conjugated antibodies. (a-c) Phospholipid binding properties of MeV-M and NiV-M. Representative western blot showing MeV-M (a) and NiV-M

(b) bind to LUVs containing 30% PS but not control vesicles (PC:PE) or PA. (c) Densitometry analysis was performed on supernatant and pellet fraction bands to determine % MeV-M bound. % protein bound was calculated using the following equation= pellet density/total band density; where total band density=supernatant+ pellet band density. (d-f) Phosphatidylinositol binding properties of MeV-M and NiV-M. (d) Representative western blot showing MeV-M binds to LUVs containing PI(3.5)P2 and PI(4.5)P2. (e) Representative western blot showing NiV-M binds to LUVs containing PI(4.5)P2 and PI(3.4.5)P3. (f) Densitometry analysis was performed on supernatant and pellet fraction bands to determine % NiV-M bound, which was calculated the same as (c). Black and gray dashed line indicates extent of MeV-M and NiV-M binding to control vesicles, respectively. Values are reported as mean \pm s.d. N=5-6 n=3. A one-way ANOVA with multiple comparisons was performed. ****p<0.0001, ***p<0.0005 **p<0.003 *p<0.05. PC: phosphatidylcholine; PE: phosphatidylethanolamine; PA: phosphatidic acid; PS: phosphatidylserine; PIP: phosphatidylinositol- phosphate; S: supernatant fraction; P: pellet fraction; LUVs: large unilamellar vesicles; 104

Figure 3.3. Effect of multiple lipids on MeV-M and NiV-M affinity to liposomes. Liposome sedimentation assays and western blotting were performed on LUVs with varying anionic lipids and MeV-M or NiV-M. Supernatant (unbound protein) and pellet (protein bound to LUVs) were separated and analyzed through western blotting using a HRP-conjugated antibodies. (a-b) MeV-M liposome sedimentation assays using LUVs with 30% PS +/- PIP shows MeV-M binding saturates ~60%. (a) Representative western blot showing MeV-M binds to each anionic lipid composition (b) Densitometry analysis was performed on supernatant and pellet fraction bands to determine % MeV-M. % protein bound was calculated using the following equation= pellet density/total band density; where total band density=supernatant+ pellet band density. (c-d) MeV-M liposome sedimentation assays using LUVs with 15% PS +/- PIP shows MeV-M binds in an additive fashion (PS+PI(3.5)P2) and synergistic mechanism (PS+PI(4.5)P2). (d) Densitometry analysis was performed on supernatant and pellet fraction bands to determine % MeV-M bound. (e-f) NiV-M liposome sedimentation assays using LUVs with 30% PS +/- PIP shows synergistic binding with LUVs containing both PS and PI(4.5)P2 (e) Representative western blot showing NiV-M binding to LUVs containing 30%PS, 1% PI(4.5)P2) and PS+PI(4.5)P2 (f) Densitometry analysis was performed on supernatant and pellet fraction bands to determine % NiV-M bound, which was calculated the same as in (b&d). Values are reported as mean \pm s.d. N=5-6 n=3. PC:PE were used in each LUV composition and mol% PC was modified to account for changes in anionic lipid mol%. PC: phosphatidylcholine; PE: phosphatidylethanolamine; PA: phosphatidic acid; PS: phosphatidylserine; PIP: phosphatidylinositol- phosphate; S: supernatant fraction; P: pellet fraction; LUVs: large unilamellar vesicles; 106

Figure 3.4. Evaluation of changing NaCl on MeV-M and NiV-M interaction with lipids. Liposome sedimentation assays and western blotting were performed on LUVs with varying anionic lipids and MeV-M or NiV-M under different NaCl conditions (150 mM, 300 mM, 500 mM). Supernatant (unbound protein) and pellet (protein bound to LUVs) were separated and analyzed through western blotting using HRP-conjugated antibodies. (a-b) Representative western blots of MeV-M (a) and NiV-M (b) showing the effect of increasing NaCl on their affinity to LUVs with varying lipid compositions. (c-d) Densitometry analysis was performed on supernatant and pellet fraction bands to determine % MeV-M bound (c) and % NiV-M bound (d) for each lipid composition in each NaCl condition. % protein bound was calculated using the following equation= pellet density/total band density; where total band density=supernatant+ pellet band

density. Control vesicles are PC:PE. Additionally, PC:PE were used in each LUV composition and mol% PC was modified to account for changes in anionic lipid mol%. Values are reported as mean \pm s.d. N=5-6 n=3. A one-way ANOVA with multiple comparisons was performed. ****p<0.0001, ***p<0.0005 **p<0.003 *p<0.05. 108

Figure 3.5. Effect of membrane charge neutralization on peripheral protein plasma membrane localization. COS-7 cells expressing the indicated GFP/mRFP-fused proteins for 24 hours were treated with the membrane permeable base, 37.5 μ M sphingosine (or ethanol vehicle; 1:2000 vol:vol), for 1 hour at 37°C prior to staining with WGA AlexaFluor™647 (plasma membrane stain) and Hoescht (DNA stain) and subsequent imaging on a fluorescence confocal microscope. Cells with or without GFP fluorescence signal localized to the PM were counted to calculate the % of cells with PM localization. **(a,c,d,e)** Representative confocal images of COS-7 cells expressing each indicated protein: **(a)** Polycationic fluorescent probe KR ϕ -mRFP +/- sphingosine treatment **(c)** filovirus matrix protein EGFP-eVP40 +/- sphingosine treatment **(d)** GFP-NiV-M +/- sphingosine treatment **(e)** GFP-MeV-M +/- sphingosine treatment. **(b)** % cells with PM localization was determined by counting the number of cells with high GFP fluorescence signal intensity at the PM and the number of cells without GFP fluorescence signal intensity at the PM. In each replicate, a minimum of 45 cells were counted. Scale bar= 5 μ m. Values are reported as mean \pm s.d. N \geq 135 n=3. A one-way ANOVA with multiple comparisons was performed (compared to the vehicle treatment group for that protein). ****p<0.0001. WGA: wheat germ agglutinin; PM: plasma membrane 110

Figure 3.6. Effect of enzymatic depletion of PI(4,5)P2 on peripheral protein plasma membrane localization. COS-7 cells expressing the indicated GFP-fused proteins for 24 hours were expressed alone, with MycVPtase-WT or with MycVPtase- Δ 1. Immediately prior to imaging cells were stained with WGA AlexaFluor™647 (plasma membrane stain) and Hoescht (DNA stain) and subsequently imaged on a fluorescence confocal microscope. Cells were counted and binned into whether they displayed high fluorescence signal localization at the PM. **(a-c)** Representative confocal images of COS-7 cells expressing each indicated protein alone (*left panels*) or with MycVPtase-WT (*middle panels*) or MycVPtase- Δ 1 (*right panels*): **(a)** the PI(4,5)P2 sensor, PLC δ -PH **(b)** the filoviral matrix protein **(c)** the PS sensor, GFP-LactC2. **(d)** % cells with PM localization was determined by counting the number of cells with high fluorescence signal at the M and the number of cells without high fluorescence signal at the PM. In each replicate, a minimum of 45 cells were counted. **(e-f)** Representative confocal images of COS-7 cells expressing either GFP-NiV-M **(e)** or GFP-MeV-M **(f)** alone (*left panels*) or with MycVPtase-WT (*middle panels*) or MycVPtase- Δ 1 (*right panels*). Scale bar= 5 μ m. Values are reported as mean \pm s.d. N \geq 135 n=3. A one-way ANOVA with multiple comparisons was performed (compared to the protein expressed alone group for that protein). ****p<0.0001. WGA: wheat germ agglutinin; PM: plasma membrane..... 113

Figure 3.7. Effect on PIKfyve inhibition with Apilimod treatment on peripheral protein membrane localization and vesicle size. COS-7 cells expressing the indicated GFP/mCherry-fused proteins for 24 hours were treated with 200 nM Apilimod (or ethanol vehicle 1:2000 vol:vol) for 1 hour at 37°C. Following treatment, cells were stained with WGA AlexaFluor™647 (plasma membrane stain) and Hoescht (DNA stain) and subsequently imaged on a fluorescence confocal microscope. Cells were counted and binned into either displaying high fluorescence localization at the plasma membrane or not. **(a)** Representative confocal images of COS-7 cells expressing EGFP-eVP40 +/- Apilimod treatment **(b)** Quantification of plasma membrane localization for

panels (a,c,d): % cells with PM localization was determined by counting the number of cells with high fluorescence signal at the PM and the number of cells without high fluorescence signal at the PM. In each replicate, a minimum of 45 cells were counted (c) Representative confocal images of COS-7 cells expressing PLC δ -PH-GFP +/- Apilimod treatment. (d) Representative confocal images of COS-7 cells expressing GFP-MeV-M +/- Apilimod treatment. Scale bar= 5 μ m. Values are reported as mean \pm s.d. N \geq 135 n=3. A one-way ANOVA with multiple comparisons was performed (compared to the vehicle treated group for each protein). **p=0.0041. (e-f) Analysis of Apilimod treatment on intracellular vesicle size using COS-7 cells expressing LAMP-1. (e) Representative confocal images of COS-7 cells expressing LAMP-1-mCherry +/- Apilimod treatment. (f) Quantification of vesicle size from panel (e): intracellular vesicles were measured using imageJ and plotted. n=1. Scale bar= 5 μ m. Individual measurements are reported. A two-tailed t-test was performed ****p<0.0001. PIKfyve: phosphatidylinositol-3-phosphate 5-kinase; LAMP1: lysosomal associated membrane protein-1. 116

Figure 3.8. Effect of PI3K inhibition with wortmannin on peripheral protein plasma membrane localization. COS-7 cells expressing the indicated GFP/mRFP-fused proteins for 24 hours were treated with 100 nM wortmannin or ethanol vehicle (1:2000 vol:vol) for 1 hour at 37°C, stained with WGA AlexaFluor™647 (plasma membrane stain) and Hoescht (DNA stain) and subsequently imaged on a fluorescence confocal microscope. Cells were counted and binned into either displaying high fluorescence localization at the plasma membrane or not. (a-d) Representative confocal images of COS-7 cells expressing each indicated protein treated with vehicle (left panels) or wortmannin (right panels) (a) Cells expressing PI(3,4,5)P3 sensor AKT-PH-mRFP (b) Cells expressing filovirus matrix protein EGFP-eVP40 (c) Cells expressing GFP-NiV-M (d) Cells expressing GFP-MeV-M (e) % cells with PM localization was determined by counting the number of cells with high fluorescence at the PM and the number of cells without high fluorescence at the PM. In each replicate, a minimum of 45 cells were counted. Scale bar= 5 μ m. Values are reported as mean \pm s.d. N \geq 135 n=3. A one-way ANOVA with multiple comparisons was performed (compared to the vehicle treated group for that protein). ****p<0.0001. PI3K: phosphatidylinositol 3-kinase..... 118

Figure 3.9. Effect of PIK inhibitors on paramyxovirus matrix protein plasma membrane localization. COS-7 cells expressing the GFP-NiV-M or GFP-MeV-M were treated with the indicated compounds after 8 hours of protein expression. Cells were treated with vehicle (DMSO, 1:1000 vol:vol) or compound for 24 hours, stained with WGA AlexaFluor™647 (plasma membrane stain) and Hoescht (DNA stain), fixed in 4% PFA and subsequently imaged on a fluorescence confocal microscope. Cells were counted and binned into either displaying high fluorescence localization at the plasma membrane or not. (a-b) Representative confocal images of COS-7 cells expressing GFP-MeV-M (a) or GFP-NiV-M (b) and treated with vehicle (left panel) or compound (right panels). (c) % cells with PM localization was determined by counting the number of cells with high fluorescence at the PM and the number of cells without high fluorescence at the PM. In each replicate, a minimum of 45 cells were counted. Scale bar= 5 μ m. Values are reported as mean \pm s.d. N \geq 135 n=3. A one-way ANOVA with multiple comparisons was performed (compared to the vehicle treated group for that protein). ****p<0.0001. PIK: phosphatidylinositol kinase; PFA: paraformaldehyde; 121

Figure 3.10. Correlation of PI(4,5)P2 and paramyxovirus matrix proteins at the plasma membrane in cells. COS-7 cells were transfected with either GFP-MeV-M (a-b) or GFP-NiV-M (c-d). At 24 hours post transfection, cells were washed, and media supplemented with TF-TMR-

PI(4.5)P₂ was added to cells for 30 min. Following incubation, cells were washed thoroughly, stained with WGA-AlexaFluor™ 647 (plasma membrane), fixed with 4% PFA and imaged on a fluorescence confocal microscope. **(a)** Representative confocal images of COS-7 cells expressing GFP-MeV-M supplemented with TF-TMR-PI(4.5)P₂. **(b)** Plot profile analysis of fluorescence signals correlation between GFP-MeV-M (solid green line) and TF-TMR-PI(4.5)P₂ (red dotted line). White line indicates where plot profile analysis was performed. **(c)** Representative confocal images of COS-7 cells expressing GFP-NiV-M supplemented with TF-TMR-PI(4.5)P₂. **(d)** Plot profile analysis of fluorescence signals correlation between GFP-NiV-M (solid green line) and TF-TMR-PI(4.5)P₂ (red dotted line). White line indicates where plot profile analysis was performed. scale bar= 5µm. TF-TMR-PI(4.5)P₂: TopFluor TMR-PI(4.5)P₂. 123

Figure 4.1. Model of mVP40 assembly based on two oligomerization interfaces within the NTD and CTD regions. **(a)** top and side views of filamentous mVP40 (higher order structure) composed of two hexamers assembled in an end-end fashion; each hexamer is formed through a NTD-NTD interaction while the end-end connection between two hexamers is facilitated by a CTD-CTD interaction. **(b)** Zoomed view of the mVP40 structure at the NTD oligomer interface (*upper panel*) highlighting W83 and N148 residues (pink) involved in the oligomerization overlaid with the Ebola virus VP40 (eVP40) structure with corresponding residues W95 and E160 (purple). The CTD interface (*bottom panel*) highlighting the proposed residues L226 and S229 involved in hexamer-hexamer interaction. Both were modeled using PyMOL based on mVP40 dimer structure (PDB ID: 5B0V) and eVP40 (PDB ID: 4LDB). (prepared for manuscript by Kaveesha Wijesinghe). mVP40: Marburg VP40; NTD: N-terminal domain; CTD: C-terminal domain..... 133

Figure 4.2. Mutation of the predicted oligomerization interfaces of mVP40 did not alter dimer formation. Size exclusion chromatography of 6xHis- mVP40 constructs purified from *Escherichia coli* was performed to assess the ability of mVP40 to dimerize. **(a)** mVP40 WT chromatogram indicated the presence of dimeric mVP40. **(b)** mVP40 T105R chromatograph indicated the T105R point mutation resulted in loss of dimeric mVP40, as previously reported¹¹. **(c)** mVP40 W83R/N148A chromatogram indicated the W83R/N148A protein is still able to form a dimer. **(d)** W83R/N148A/L226R chromatogram indicated the W83R/N148A/L226R protein did not disrupt dimer formation. **(e)** L226R chromatogram indicated the L226R point mutation did not disrupt dimer formation. 139

Figure 4.3. *In vitro* lipid binding profile of mVP40 mutants revealed no change in anionic lipid binding compared to mVP40-WT. Liposome sedimentation assays were performed using the indicated mVP40 construct and either control membranes (no anionic lipids) and anionic membranes (30% PS and 2.5% PI(4,5)P₂). 6xHis-mVP40 WT, 6xHis-mVP40 T105R, 6xHis-mVP40 L226R, 6xHis-mVP40 W83R/N148A, and 6xHis-mVP40 W83R/N148A/L226R purified from *Escherichia coli* Rosetta pLysS cells and further purified using SEC. **(a)** Representative western blot from liposome sedimentation assays with the supernatant fraction (top panel) and pellet fraction (bottom panel). 6xHis-mVP40 was probed with a Mouse α-His primary antibody and HRP-Sheep α-Mouse secondary antibody, and detected using ECL. BioRad Kaleidoscope protein ladder was used for a reference to protein size. **(b)** Quantification of liposome sedimentation assays. To determine % mVP40 bound, the mVP40 supernatant density and mVP40 pellet density was measured using densitometry analysis (performed in ImageJ). The ratio of mVP40 pellet density vs. total mVP40 density (pellet + supernatant) was calculated and the average was plotted (N=6, n=3). Values are reported as mean ± standard deviation, and a two-way ANOVA was performed (*p<0.05 and ****p<0.0001) 141

Figure 4.4. Cellular oligomerization profile of mVP40 mutants analyzed through Number & Brightness. HEK293 cells transiently expressing GFP-fused mVP40 constructs were imaged at 24 hours post transfection and Number & Brightness analysis was performed using SimFCS software. **(a)** Representative images of the workflow in SimFCS for Number & Brightness analysis of GFP-mVP40 WT, GFP-mVP40 W83R, GFP-mVP40 W83R/N148A, GFP-mVP40 W83R/N148A/L226R, The original composite of the time-lapse images (left panel), the number of pixels vs. intensity plot (middle panel) and brightness selection plot of the cell (right panel) are shown for each construct. **(b)** The percent pixels with a brightness value of xx-xx (monomer) are shown in red, xx-xx (hexamer-12mer) are shown in green, xx-xx (12mer-24mer) are shown in blue and xx-xx (>24mer) are shown in pink. The percent pixels with each corresponding brightness value were calculated per cell and the average value for each construct was plotted. Values are reported as mean \pm standard deviation. A two-way ANOVA with multiple comparisons was performed, where * $p < 0.05$, ** $p < 0.005$ and **** $p < 0.0001$. N=15, n=3 **(c)** Representative images of the workflow in SimFCS for Number & Brightness analysis of GFP-mVP40 T105R, GFP-mVP40 L226R, GFP-mVP40 L226R/S229R. The original composite of the time-lapse images (left panel), the number of pixels vs. intensity plot (middle panel) and brightness selection plot of the cell (right panel) are shown for each construct. 145

Figure 4.5. Perturbation of mVP40 oligomerization reduces VLP production. Functional budding assays were performed to assess the capacity of mVP40 WT and mutants to produce VLPs. Cell lysate and VLP samples were collected from HEK293 cells after 24 hours of transient expression of the indicated GFP-mVP40 protein in the presence and absence of mGP. **(A)** Representative western blot of functional budding assays. Cell lysate samples were probed for mVP40 using either the antibody information (top panel) and for the loading control GAPDH using antibody information (bottom panel). **(B)** Representative western blot of VLP samples from functional budding assays. VLP samples were probed for mVP40 using either the antibody information. In both **(A)** and **(B)** protein bands were detected using ECL reagent and the BioRad Kaleidoscope protein ladder was used as a reference for protein size. **(C)** Quantification of the budding index for each mVP40 protein was determined by densitometry analysis (performed in ImageJ). The budding index (normalized to mVP40 WT) was quantified by measuring the ratio of mVP40 band density in the VLP fraction compared to total mVP40 band density (cell lysate density + VLP density). In each western, mVP40 cell lysate density was normalized to the GAPDH loading control band density. Values are reported as the mean \pm standard deviation. n=3-4 and a one-way ANOVA with multiple comparisons was performed (**** $p < 0.0001$). 147

Figure 5.1. Fluorescence profiles of PS and GFP-WT-eVP40 in HEK 293 cells through confocal microscopy. **(a)** Representative confocal images from live cell imaging of HEK293 expressing various GFP-fused proteins (GFP; green) following supplementation with TopFluor® TMR-PS (red). Solid white lines indicate where plot profile analysis was performed; scale bar= 10 μ m. **(b-c)** Validation of ability to detect exogenously added fluorescently labelled PS within the inner leaflet of the plasma membrane of cells **(b)** Plot profile analysis of HEK293 cells expressing cytosolic GFP. **(c)** Plot profile analysis of HEK293 cells expressing the PS sensor GFP-LactC2 **(d-e)** Investigation of functionally distinct eVP40 proteins ability to bind to fluorescently labelled PS within the inner leaflet of the plasma membrane in living cells. **(d)** Plot profile analysis of HEK293 cells expressing GFP-WT-eVP40. **(e)** Plot profile analysis of HEK293 cells expressing GFP-K224A-eVP40 (PS-binding residue mutant). **(f)** Plot profile analysis of HEK293 cells expressing GFP-WE/A-eVP40 (oligomerization deficient mutant). TopFluor TMR-PS

fluorescence signal intensity (red dotted line) and GFP fluorescence signal intensity (green solid line). 166

Figure 5.2. Clustering of PS by eVP40 in HEK 293 cells. (a) Representative confocal images of HEK293 cells expressing various GFP-fused proteins (green) and supplemented with TopFluor® TMR-PS (red); Yellow arrows: high intensity PS fluorescence regions (b) %PM with PS clusters = area of high intensity fluorescent PS clusters / total plasma membrane area. Black bars: control proteins and blue bars: eVP40 proteins. Values are reported as mean \pm s.d.; N>18, n=3; A one-way ANOVA was performed with multiple comparisons compared to the control GFP %PS clustering (***p=0.0007, **p=0.004). PS: phosphatidylserine; PM: plasma membrane. (c) Representative images of the step-wise image analysis workflow of quantifying PS clustering in living HEK293 cells expressing GFP-fused proteins using a custom ImageJ macro. (d) Representative images from live cell imaging experiments of HEK293 cells expressing control GFP-fused proteins specific for the plasma membrane (GPI), and specific lipids, PS (LactC2) and PI(4,5)P₂ (PLC δ -PH). scale bar= 10 μ m. 169

Figure 5.3 Effect of PS concentration on eVP40 binding affinity to and oligomerization on membranes. (a-c) SPR demonstrates that eVP40 affinity to LUVs increases in relation to PS concentration. (a) Representative normalized sensorgram of His6-eVP40 binding to LUVs containing 1% PS indicating an apparent affinity of 2.5 μ M. (b) Representative normalized sensorgram of His6-eVP40 binding to LUVs containing 11% PS indicating an apparent affinity of 0.65 μ M. (c) Representative normalized sensorgram of His6-eVP40 binding to LUVs containing 22% PS indicating an apparent affinity of 0.18 μ M. (d-e) PS concentration in LUVs enhances the ability of His6-eVP40 to oligomerize on membranes. (d) Representative western blot of chemical crosslinking performed on His6-WT-eVP40 following incubation with LUVs of varying PS content (detected by Mouse α -His antibody & HRP-Sheep α -Mouse). (e) Oligomerization capacity was determined from the western blot band density ratio of oligomers/(monomer + dimer) from chemical crosslinking experiments. A one-way ANOVA was performed with multiple comparisons compared to the control 0% PS LUVs control (30% PS *p= 0.021; 60% PS *p=0.017). n=3. Values are reported as mean \pm s.d.; SPR: surface plasmon resonance; LUVs: large unilamellar vesicles; PS: phosphatidylserine; HRP: horseradish peroxidase. 171

Figure 5.4. Toxicity and Lipidomic analysis of Fendiline treated cells. (a). CellTiter-Glo® viability results of HEK293 cells. HEK293 cells were treated with fendiline for 24 hours (black line) and 48 hours (blue line) and viability was assessed as a % viability of control. (b-d) Lipidomic analysis (LC/MS/MS) of total lipids extracted from HEK293 cells treated with the indicated concentration of fendiline (48 hours). (b) PS level analysis from lipidomic analysis (LC/MS/MS) of total lipids extracted from HEK293 cells treated with indicated concentration of fendiline. (c) PS saturation analysis from lipidomic analysis (LC/MS/MS) of total lipids extracted from HEK293 cells treated with the indicated concentration of fendiline. (d) PA level analysis from lipidomic analysis (LC/MS/MS) of total lipids extracted from HEK293 cells treated with 5 μ M. Values are normalized to DMSO control and are reported as mean \pm s.d.; n=3; A one-way ANOVA was performed with multiple comparisons compared to the control DMSO. (*p=0.0120, ***p=0.0003). 173

Figure 5.5. Confocal microscopy of cells expressing PS sensor, GFP-LactC2 and treated with Fendiline. Analysis of PS plasma membrane localization in response to 24 hour fendiline treatment (a-b) and 48 hour fendiline treatment (c-d). Representative confocal images from live

cell imaging of HEK293 cells expressing GFP-LactC2 and treated with fendiline for 24 hours (a) and 48 hours (c). Effect of fendiline on PS plasma membrane localization at 24 hours (b) and 48 hours (d) was calculated by the ratio of GFP fluorescence at the (plasma membrane intensity/intracellular intensity). Values are normalized to DMSO control and are reported as mean \pm s.d.; N>15, n=3; A one-way ANOVA was performed with multiple comparisons compared to the DMSO control. (b): **p=0.0045; ***p=0.0003 (d) (**p=0.0031). scale bars= 10 μ m. 174

Figure 5.6. Number & Brightness analysis of LactC2 to identify PS clustering in HEK293 cells. (a) N&B analysis of HEK293 cells expressing the control GFP. Analysis was performed at 48 hours post treatment (DMSO) to align with N&B analysis performed on experiments with HEK293 cells expressing GFP-LactC2 or GFP-eVP40 and treated with the control or fendiline. *Left panel:* Representative images from time-lapse (30 frames) of HEK293 expressing EGFP and treated with fendiline for 48 hours. *Middle panel:* Brightness and Intensity plots for representative image. *Right panel:* Selection map correlating each pixel in the representative image to an oligomerization state (b value) (red: monomer). (b-c) Analysis of PS clustering in HEK293 cells in response to fendiline treatment through N&B analysis. (b) *Left panel:* Representative images from time-lapse (30 frames) imaging of HEK293 expressing GFP-LactC2 and treated with fendiline for 48 hours. *Middle panel:* Brightness and Intensity plots for each representative image. *Right panel:* Selection map correlating each pixel in the representative image to an oligomerization state (b value) (red: monomer-5mer, green: 5mer-10mer, blue: >10mer). (c) Average % pixels quantification from panel (b)= Percentage of GFP-LactC2 with brightness values corresponding to monomer-5mer (~1.-1.5), 5mer-10mer (~1.5-1.9) and >10mer (>1.9) over the total pixels within each image. Values are reported as mean \pm s.d.; N \geq 9, n=3; A two-way ANOVA was performed with Dunnett's multiple comparisons compared to the control DMSO % average pixels (****p<0.0001, **p=0.0043). GFP-LactC2: phosphatidylserine sensor; N&B: Number & Brightness analysis. scale bar= 5 μ m. 175

Figure 5.7. Viability assay of Vero cells following Fendiline treatment. (a) CellTiter-Glo® viability results of Vero cells. Cells were treated with control or fendiline for 48 hours according to the BSL-4 infection model; d-1/0 (black line), e.d. (blue line) and e.o.d (gray line) and viability was assessed as a % viability of control. 176

Figure 5.8. Evaluation of fendiline efficacy in the inhibition of authentic EBOV and MARV spread. a-d Effect of fendiline on EBOV infection. (a) Representative confocal images of Vero E6 cells infected with EBOV (Kikwit) at the indicated MOI and treated with the indicated concentration of fendiline. Cells were pretreated 24 hours prior to infection with the indicated concentration of fendiline. Post infection, cells were treated 1 hour later (d -1/0), treated every day (e.d), or treated every other day (e.o.d) and fixed at either 48 hours, 72 hours or 96 hours post infection. (green=EBOV; blue= nuclei). White numbering in top right corner indicates %infection (b-d) Quantification of % inhibition of EBOV by fendiline. (b) 48 hours (MOI 1.0) (c) 72 hours (MOI 0.1) (d) 96 hours (MOI 0.1). Values are reported as mean \pm s.d. A one-way ANOVA was performed with multiple comparisons was performed. n=3. (e-h) Effect of fendiline on MARV infection. (e) Representative confocal images of Vero E6 cells infected with MARV (Ci67) at the indicated MOI and treated with the indicated concentration of fendiline. Cells were pretreated 24 hours prior to infection with the indicated concentration of fendiline. Post infection, cells were treated 1 hour later (d -1/0), treated every day (e.d), or treated every other day (e.o.d) and fixed at either 48 hours, 72 hours or 96 hours post infection. (green=MARV; blue= nuclei). White numbering in top right corner indicates %infection. (f-h) Quantification of % inhibition of MARV

by fendiline. (f) 48 hours (MOI 1.0) (g) 72 hours (MOI 0.1) (h) 96 hours (MOI 0.1). Values are reported as mean \pm s.d. A one-way ANOVA was performed with multiple comparisons was performed. n=3. EBOV: Ebola virus; MOI: multiplicity of infection; MARV: Marburg virus; d. - 1/0: treatment 1 hour after infection; e.d.: treatment every day; e.o.d.: treatment every other day. 178

Figure 5.9. Analysis of eVP40/mVP40 cellular localization and oligomerization following fendiline treatment. (a-c) Effect of fendiline on eVP40 and mVP40 PM localization in HEK293 cells after 48 hours of treatment. (a) Representative confocal images from live cell imaging experiments of HEK293 cells expressing EGFP-WT-eVP40 (top panel) and EGFP-WT-mVP40 (bottom panel) after 48 hours of fendiline treatment. scale bars= 10 μ m. Effect of fendiline on eVP40 (b) and mVP40 (c) PM localization was quantified by the ratio of EGFP fluorescence intensity at the PM / total EGFP fluorescence intensity (and normalized to DMSO control). N>15, n=3. Values are reported as mean \pm s.d. A one-way ANOVA with multiple comparisons was performed compared to the DMSO control. (d-e) Analysis of eVP40 oligomerization in HEK293 cells in response to 48 hour fendiline treatment using N&B analysis. (d) *Left panel:* Representative images from time-lapse (30 frames) of HEK293 expressing EGFP-WT-eVP40 and treated with fendiline for 48 hours. scale bar = 5 μ m. *Middle panel:* Brightness and Intensity plots for each representative image. *Right panel:* Selection map correlating each pixel in the representative image to an oligomerization state (b value) (red: monomer-hexamer, green: hexamer-12mer, blue: 12mer-24mer, pink: >24mer). (e) Average % pixel quantification from panel (d)= % of GFP-WT-eVP40 with brightness values corresponding to monomer-hexamer (~1.-1.6), hexamer-12mer (~1.6-2.0), 12mer-24mer (2.0-3.2) and >24mer (>3.2) over the total pixels within each image. Values are reported as mean \pm s.d.; N \geq 9, n=3; A two-way ANOVA was performed with Dunnett's multiple comparisons compared to the control DMSO % average pixels (**p=0.0035). 181

Figure 5.10. VLP production and morphology in HEK293 cells in the presence of fendiline. (a-d) Functional budding assays assessed at 24 hours (a-b) and 48 hours (c-d) post treatment. (a) Representative western blot of budding assays performed at 24 hours. VLP samples (top panel) and cell lysate samples (bottom panel) collected from HEK293 cells and immunoblotted for eVP40 expression; GAPDH served as a loading control. eVP40 detected by (Rabbit α -eVP40 and HRP-Goat α -Rabbit); GAPDH detected by mouse α -GAPDH and HRP-Sheep α -Mouse) (b) Quantification of relative budding index at 24 hours post fendiline treatment. Relative budding index was determined by the western blot band density of eVP40 in the VLP fraction/(total eVP40 cell lysate + eVP40 VLP band density) and was normalized to the DMSO control. Cell lysate eVP40 band density was normalized to GAPDH band density prior to use in budding index quantification. n=3. Values are reported as mean \pm s.d. A one-way ANOVA was performed with multiple comparisons compared to the DMSO control. (c) Representative western blot of budding assays performed at 48 hours. VLP samples (top panel) and cell lysate samples (bottom panel) collected from HEK293 cells and immunoblotted for eVP40 expression; GAPDH served as a loading control. eVP40 detected by (Rabbit α -eVP40 and HRP-Goat α -Rabbit); GAPDH detected by (Mouse α -GAPDH and HRP-Sheep α -Mouse) (d) Quantification of relative budding index at 48 hours post fendiline treatment. Relative budding index was determined by the western blot band density of eVP40 in the VLP fraction/(total eVP40 cell lysate + eVP40 VLP band density) and was normalized to the DMSO control. Cell lysate eVP40 band density was normalized to GAPDH band density prior to use in budding index quantification. n=3. Values are reported as mean \pm s.d. A one-way ANOVA was performed with multiple comparisons compared to the DMSO control.

(*p=0.0260) (e-f) SEM micrographs of HEK93 cells. (e) Representative micrographs of mock transfected HEK293 cells harvested after 48 hours of no treatment or DMSO treatment. (f) Representative micrographs of HEK293 cells expressing FLAG-eVP40 and harvested after 48 hours of no treatment, DMSO treatment, or the indicated concentration of fendiline. VLPs: virus like particles; SEM: scanning electron microscopy; GAPDH: glyceraldehyde 3-phosphate dehydrogenase; HRP: horseradish peroxidase. 186

Figure 5.11. Effect of fendiline on eVLP morphology and TIM-1 dependent eVLP entry. (a-c) TEM analysis of eVLP morphology. (a) Representative transmission electron micrographs of eVLPs purified from HEK293 cells expressing FLAG-eVP40 and eGP following 48 hours of DMSO (left panel) or 5 μ M fendiline treatment (right panel). (b) Quantification of eVLP length (μ m) of DMSO-derived eVLPs (black) and fendiline-derived eVLPs (blue). N>50, n=3. A two-tailed t-test was performed (**p=0.0139). (c) Quantification of eVLP diameter (nm) of DMSO-derived eVLPs (black) and fendiline-derived eVLPs (blue). N>50, n=3. A two-tailed t-test was performed (*p=0.0430). (d-e) Fluorescence based DiI TIM-1 dependent entry assay. (d) Representative confocal images from the DiI-entry assay comparing entry of eVLPs produced from DMSO (top panel) and fendiline-treated HEK293 cells (bottom panel) into target cells (HEK293 cells transiently expressing increasing amounts of TIM-1; 0.0 μ g, 0.5 μ g, 1.0 μ g). A stack of 10 frames was acquired for each image. DiI (initially red) was recolored to yellow for easier observation in print; blue (Hoechst 3342 stain); scale bar = 10 μ m. (e) Quantification of eVLP entry was performed by calculating the total number of DiI punctate / the total number of DiI-positive cells. Three images from each z-stack was quantified. N=9, n=3. A one-way ANOVA was performed with multiple comparisons against the 0.0 μ g TIM-1 condition for both DMSO- and fendiline derived eVLPs.(****p<0.0001; **p=0.0093). Values are reported as mean \pm s.d. eVLP: entry-competent viral like particles; TEM: transmission electron microscopy; TIM-1: t-cell immunoglobulin receptor-1; eVLPs: entry-competent VLPs; eGP: Ebola glycoprotein; DiI: 1,1'-Diocetadecyl-3,3,3',3'-Tetramethylindocarbocyanine Perchlorate. 189

Figure 5.12. Calibrated mathematical model reproduces key observations in multiple experimental datasets. Percentage infected cells is shown for various fendiline concentrations given prior to infection (d-1/0, a-c) or daily (e.d., d-f). (a,d) MOI 1; (b,c,e,f) MOI 0.1. (g-h) Model predicted cell and viral dynamics for MOI 0.1. (i) Model predicted dose response curves for fendiline effects on viral budding and entry in the BSL4 experiments. 192

Figure 5.13. Calibration results from the first and second phase of model development. (a-c) First phase calibration results between experimental (black bars) and simulation (gray) data from budding (a-b) and entry (c) assays. (d-e) Second phase calibration results showing comparison between experimental and simulation data from cell viability assays. The mathematical model was calibrated to this data and the data in Figure 5.12 simultaneously. 193

LIST OF ABBREVIATIONS

Acid sphingomyelinase	ASM
Atomic force microscopy	AFM
Bicinchoninic acid assay	BCA
Biosafety level 2	BSL-2
Biosafety level 4	BSL-4
Center for Disease Control	CDC
Chinese hamster ovary cells	CHO
Cryo-electron tomography	Cryo-ET
C-terminal domain	CTD
Democratic Republic of Congo	DRC
Detergent resistant membranes	DRM
Diacylglycerol	DAG
Dulbecco's modified eagle medium	DMEM
Ebola virus	EBOV
Ebola virus glycoprotein	eGP
Ebola virus matrix protein 40	eVP40
Electron microscopy	EM
Endoplasmic reticulum	ER
Endosomal sorting complex required for- transport	ESCRT
Entry-competent viral like particles	eVLPs
Fluorescence correlation spectroscopy	FCS
Fusion protein	F
Giant unilamellar vesicles	GUV
Glycoprotein	GP
Heat shock protein 90	Hsp90
Hendra virus	HeV
Hendra virus matrix protein	HeV-M
Hepatitis C Virus	HCV

HIV-1 gag matrix protein	HIV-1 gag
Human immunodeficiency virus	HIV
Hydrogen-deuterium exchange mass spectroscopy	HDXMS
Influenza A virus matrix protein	M1
Inositol triphosphate	IP3
Isopropyl β -d-1-thiogalactopyranoside	IPTG
Japanese encephalitis virus	JE
Large unilamellar vesicles	LUV
Late domains	L-domains
Lipid binding domain	LBD
Lipid transport protein	LTP
Marburg virus	MARV
Marburg virus matrix protein 40	mVP40
Matrix protein	M
Measles attachment protein	H
Measles virus	MeV
Measles virus matrix protein	MeV-M
Membrane contact sites	MCS
Methyl- β -cyclodextrin	M β CD
Minimum Essential Medium	MEM
Multiplicity of Infection	MOI
Neural precursor cell expressed developmentally down-regulated protein 4	NEDD4
Newcastle disease virus	NDV
Newcastle disease virus matrix protein	NDV-M
Niemann-Pick C1 protein	NPC1
Nipah virus	NiV
Nipah virus attachment protein	G
Nipah virus matrix protein	NiV-M
Non-essential amino acids	NEAA

N-terminal domain	NTD
Nuclear export sequence	NES
Nucleoprotein	NP
Number & Brightness	N&B
Oxysterol-related binding protein 5	ORP5
Oxysterol-related binding protein 8	ORP8
Parainfluenza virus	PIV
Penicillin/Streptomycin	P/S
Pharmacodynamics	PD
Phenylmethylsulfonyl fluoride	PMSF
Phosphate buffered saline	PBS
Phosphatidic acid	PA
Phosphatidylcholine	PC
Phosphatidylethanolamine	PE
Phosphatidylinositol 3-kinase	P3K
Phosphatidylinositol 4-kinase alpha	PI4K α
Phosphatidylinositol 4-kinase beta	PI4K β
Phosphatidylinositol 5-kinase	PI5K
Phosphatidylinositol triphosphate	PIP3
Phosphatidylinositols	PIPs
Phosphatidylserine	PS
Phosphatidylserine synthase 1	PSS1
Phosphatidylserine synthase 2	PSS2
Phospholipase C	PLC
Phospholipase D	PLD
Phosphoprotein	P
Pleckstrin homology	PH
Protein kinase C	PKC
Raster image correlation spectroscopy	RICS
Respiratory syncytial virus	RSV
Ribonucleoprotein complex	RNP

RNA-dependent RNA polymerase	RdRP
Scanning electron microscopy	SEM
Sendai virus	SeV
Sendai virus matrix protein	SeV-M
Signaling lymphocytic activation molecule 1	SLAM
Size exclusion chromatography	SEC
Supported lipid bilayers	SLB
Surface plasmon resonance	SPR
T-cell immunoglobulin and mucin domain protein 1	TIM-1
TopFluor tetramethylrhodamine-phosphatidylserine	TMR-PS
Total internal reflection microscopy	TIRF
Transmembrane protein 16 F	TMEM16F
Transmission electron microscopy	TEM
United States Army Medical Research Institute of Infectious Diseases	USAMRIID
Vesicular stomatitis virus	VSV
Vesicular stomatitis virus matrix protein	VSV-M
Viral like particles	VLPs
Viral protein 35	VP35
Viral protein 40	VP40
World Health Organization	WHO
XK family protein 8	XKr8

ABSTRACT

Viruses are pathogenic agents which affect all varieties of organisms, including plants, animals and humans. These microscopic particles are genetically simple organisms which encode a limited number of proteins that undertake a wide range of functions. While structurally distinct, viruses often share common characteristics that have evolved to aid in their infectious life cycles. A commonly underappreciated characteristic of many deadly viruses is a lipid envelope coat that surrounds them. Lipid enveloped viruses comprise a diverse range of pathogenic viruses, known to cause disease in both animals and human which often leads to high fatality rates, many of which lack effective and approved therapeutics. This report focuses on learning how a multifunctional protein within lipid enveloped viruses, the matrix protein, interacts with the plasma membrane of cells to enter and exit cells. Specifically, four viruses are investigated, Measles virus and Nipah virus (within the *Paramyxoviridae* family) and Ebola virus and Marburg virus (within the *Filoviridae* family). Through numerous *in vitro* experiments, functional cellular assays, a myriad of microscopy techniques, and experiments in high containment bio-safety level 4 settings, this report identifies specific lipids at play during the viral assembly process for each virus. Moreover, mechanistic insight is presented as to how each matrix protein interacts with the plasma membrane to facilitate: membrane association, viral matrix protein oligomerization and assembly, the rearrangement of lipids within the plasma membrane, and viral production. Lastly, numerous small molecule inhibitors targeting specific lipids, (e.g. phosphatidylserine and phosphatidylinositol 4,5 biphosphate) within the cell were investigated for their efficacy in inhibiting matrix protein-dependent viral like particle production and viral spread in cells. As a whole, these projects lend credence to the significant role that lipids and the plasma membrane play throughout lipid enveloped viral life cycles, and provide compelling evidence for the merit of future drug-development research geared at targeting the matrix protein-plasma membrane interaction.

CHAPTER 1. DEADLY AND INFECTIOUS VIRUSES: AN INTRODUCTION TO MONONEGAVIRALES

1.1 Mononegavirales: Who are they?

RNA viruses comprise a diverse group of obligate intracellular parasites which require a living host (human, animal, plant) to survive. Respected as masterminds of cellular mimicry, viruses survive by diverting and manipulating cellular machinery and systems. The ability of RNA viruses to commandeer complex cellular processes is remarkable, intentional, and necessary as they have limited genomic capacity only encoding a handful of proteins. Moreover, high replication rates and encoding errors renders RNA viruses prone to genetic mutations more frequently than any other known organism, a major obstacle in vaccine and anti-viral development.

Mononegavirales is a diverse order of RNA viruses established in 1991, initially comprised of three viral families grouped by their structure and morphology. As of 2018, the Mononegavirales expanded to eight families encompassing some of the most infectious and fatal viruses known to cause disease in humans and animals¹. Mononegavirales include both established and emerging viruses, such as the dangerous *Rhabdoviridae* (includes rabies virus which can lead to 95% fatality in untreated cases), *Pneumoviridae* (includes respiratory syncytial virus (RSV), one of the most common human viral infections), and the highly infectious and lethal *Filoviridae* (Ebola virus (EBOV) and Marburg virus (MARV)) and *Paramyxoviridae* (measles *morbillivirus* (MeV), mumps, and *Henipaviridae* Hendra virus (HeV) and Nipah virus (NiV)) (**Figure 1.1**)¹⁻⁵.

Members of the Mononegavirales order are lipid enveloped viruses constructed from a 10-20 kb long single stranded non-segmented RNA genome⁵ which encodes 5-10 proteins⁶. These proteins subvert host processes during infection, leading to a wide range of diseases. For example, the *Filoviridae* family comprises three genera of viruses, including EBOV and MARV which are known to cause life-threatening hemorrhagic fever^{4,5}. Meanwhile, the *Paramyxoviridae* family comprises four genera, including *morbillivirus* and *henipavirus* which cause a range of respiratory and neurological disorders^{1,7}.

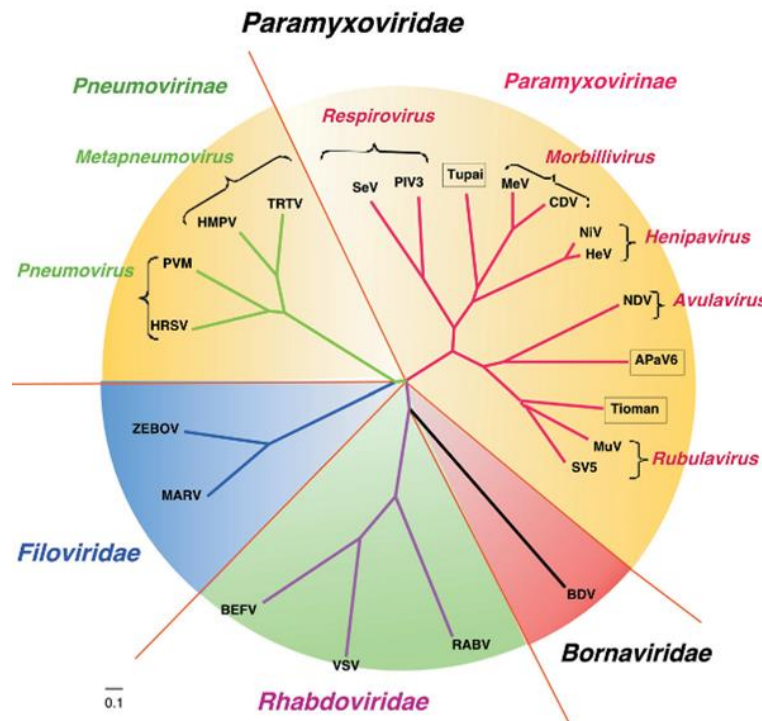


Figure 1.1. Phylogenetic tree of 4 viral families within the Mononegavirales order of RNA viruses. *Bornaviridae*, *Filoviridae*, *Paramyxoviridae*, and *Rhabdoviridae* families are shown. Abbreviations: avian parainfluenza virus type 6 (APaV6), BDV (Borna disease virus), BEFV (bovine ephemeral fever virus), CDV (canine distemper virus), HeV (Hendra virus), HMPV (human metapneumovirus), HRSV (human respiratory syncytial virus), MARV (Marburg virus), MeV (measles virus), MuV (mumps virus), NDV (Newcastle disease virus), NiV (Nipah virus), PIV3 (parainfluenza virus type 3), PVM (pneumonia virus of mice), RABV (rabies virus), SeV (Sendai virus), PIV5 (parainfluenza virus 5), TRTV (turkey rhinotracheitis virus), VSV (vesicular stomatitis Indiana virus), ZEBV (Zaire Ebola virus). Source: Fauquet CM, Mayo MA, Maniloff J, et al., eds. *Virus Taxonomy*. Eighth Report of the International Committee on the Taxonomy of Viruses. London: Elsevier/Academic Press; 2005.

MeV is one of the most infectious viruses known to humans. However, poor vaccination rates in underdeveloped countries conflated with a decline in vaccination in the United States, measles disease has persisted as a global health burden⁸. In 2018, The World Health Organization (WHO) updated their blueprint of priority pathogens, intended to spotlight diseases of the highest risk to humans due to their epidemic risk and lack of countermeasures. Of this list of priority pathogens, three of those belong to the Mononegavirales order, EBOV, NiV, and MARV. EBOV and MARV both cause life-threatening hemorrhagic fever, while NiV leads to severe neurological deficits. EBOV, NiV, and MARV display fatality rates of up to 90% and are known to spread through human-human contact. Each of these viruses poses a substantial threat to global health and public safety as there are no licensed vaccines or drugs to target these deadly viruses. Their placement on this list, and the tens of thousands of lives that have been lost underscore the imminent need to prioritize research and drug discovery efforts for these deadly pathogens^{7,9}.

1.1.1 Filovirus history

EBOV and MARV cause viral hemorrhagic fever disease, a severe multisystem syndrome. Initial discovery of both EBOV and MARV was challenging, as disease onset is slow and shares similar symptoms as typhoid fever which was common in the affected regions. Viral hemorrhagic

fever presents as a severe acute disease, manifesting with headache, fever, myalgia, and upon systemic infection leads to multi-organ failure^{4,5}. Although EBOV and MARV were both discovered in the late 1900s, evolutionary history analysis suggests they diverged from their ancestors more than one thousand years ago. Moreover, the rate of EBOV and MARV genetic variation is increasing^{10,11}, which may be a factor to explain why disease was not identified in humans until the 1900s.

Filoviruses spread through human-human contact. Initial infection transmission to humans occurs from contact with infected animals, or bites from infected animals. The animal reservoir for MARV has been identified as Egyptian fruit bats, and it is suspected that fruit bats are also the reservoir for EBOV. As of 2018 only 1 MARV has been identified with 2 variants, Marburg Marburg and Ravn Marburg⁴. Unlike MARV, five EBOV genera have been identified and all but one cause disease in humans^{1,4}.

1.1.1.1 Marburg virus

Marburg virus, named for a village in Germany, was the first member of the *Filoviridae* family to be discovered when cases of hemorrhagic fever were being investigated in 1967 by German bacteriologists Walter Mannheim and Rudolf Siegart¹².

During the onset of the outbreak in 1967, patients initially presented with mild symptoms which did not seem dangerous and patients were therefore treated within their homes. As the illness progressed, clinicians suspected typhoid fever and admitted patients to a nearby hospital. Initially researchers were unable to identify the pathogen through light and electron microscopy (EM) techniques. Mannheim and Siegart began challenging guinea pigs with blood from infected patients and reported that from passage to passage pathogenicity was increasing. They ultimately identified intracytoplasmic inclusions of liver cells from the infected animals, and sent blood samples from the guinea pigs on to a EM facility located in Harburg Germany. This facility was where MARV was finally identified using a novel EM technique¹² and a micrograph of an isolate from the outbreak is shown in **Figure 1.2**. Throughout the outbreak, 31 laboratory workers and medical personnel became ill, and seven people succumbed to the virus^{4,13}. The source of MARV was eventually identified as African green monkeys imported from Uganda, which were being

used for kidney cell cultures and vaccine production. Subsequent outbreaks throughout the 1970s and 1980s exhibited moderate fatality rates ranging from 25-33%. However, in 1998 a MARV outbreak struck the Democratic Republic of Congo (DRC) and killed 77% of those infected, a fatality rate similar to that of its relative EBOV^{4,12}.

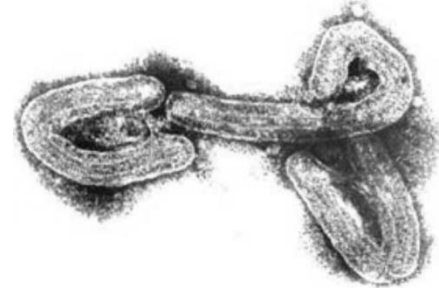


Figure 1.2. An electron micrograph of MARV from the 1967 outbreak in Germany. Source: Werner Slenczka, Hans Dieter Klenk, Forty Years of Marburg Virus, *The Journal of Infectious Diseases*, Volume 196, Issue Supplement_2, November 2007, Pages S131–S135

1.1.1.2 Ebola virus

Ebola virus (EBOV) emerged nine years after the MARV outbreak of 1967, in two simultaneous outbreaks within Sudan and the DRC (formally known as Zaire). Named after a nearby river in Zaire, EBOV was initially identified by a Belgium scientist Dr. Peter Piot and his colleagues⁴. Between August and September of 1976, dozens of patients reported to hospitals in the DRC with a “mystery” illness of severe hemorrhagic fever. Nearly 73% of those infected were dying, and again practitioners suspected typhoid fever. By late September, blood specimens from patients who had died reached a laboratory in Belgium, directed by Stefaan Pattyn. EM of collected specimens revealed a Marburg-like virus, and WHO immediately instructed all specimens to be sent to high containment facilities, such as the Centers for Disease Control (CDC) in Atlanta, Georgia. At this time, a similar mystery illness was surfaced in Sudan. Shortly thereafter it was determined the two outbreaks were from serologically distinct versions of a new virus, EBOV. The DRC outbreak resulted in a 88% case fatality rate and the Sudan outbreak had a 53% case fatality rate¹⁴.

Nearly 40 years after the initial discovery of *filoviruses* an EBOV outbreak emerged in the West African country Guinea. Unprecedented in size, the 2013 EBOV outbreak lasted more than three years and infected more people than all 29 previous outbreaks combined. By 2015 the outbreak had reached seven countries across three continents. Geography, infrastructure, cultural beliefs, economic factors, and failure to respond created the perfect storm for a catastrophic epidemic, which resulted in more than 11,000 people dying from the disease^{4,15,16}.

Despite pressures to develop *filovirus* vaccines and therapies, as of September 2019 we are amidst the second longest EBOV outbreak, which has claimed 3,000 lives. The duration and breadth of each of the last two EBOV outbreaks, as well as the high case fatality rates for both

EBOV and MARV underline that the development of effective and licensable countermeasures are indispensable to global public health safety.

1.1.2 Paramyxovirus history

Paramyxoviruses constitute an important family of pathogenic viruses known to cause disease in humans, and are leading causes of respiratory disease in children⁵. Each member of the *Paramyxoviridae* family is highly contagious, which spread through the respiratory route causing mild to severe upper and lower respiratory infections^{5,17}.

MeV is one of two members of the genus *morbillivirus*, originating from the Latin word *morbus*, meaning plague. Although MeV is an established virus whose history dates back centuries, no known animal reservoir has been identified. Regardless of an available and safe vaccine, MeV remains a leading cause of death among children^{8,18}.

NiV is also one of two members in its genus *henipavirus*, named for the region where it was discovered, a Nipah River Village within Malaysia. NiV is an emerging virus, only identified ~20 years ago. Several species of bats within the genus *Pteropus* are the suspected natural reservoir of NiV, a reservoir shared between NiV and *filoviruses*. Moreover, evolutionary history suggests NiV diverged from its most common ancestor very recently, having only occurred in 1947. With evolutionary and fatality rates similar to *filoviruses*, NiV, EBOV, and MARV are highly variable and dangerous viruses classified as a Biosafety Level-4 pathogens^{5,19,20}.

1.1.2.1 Measles virus

The earliest evidence of MeV came from the tenth century AD in Arab writings and has circulated in human populations for centuries^{7,18}. In 1757, MeV was identified by a Scottish physician to be an infectious agent within the blood and by the early 1900s was a recognized disease with more than 6,000-related deaths in the first year of reporting²¹. During the mid-1900s, an estimated 4 million people within the United States were infected annually, nearly every child would become infected by the time they were 15, and widespread outbreaks occurred every 2-3 years^{21,22}.

MeV is one of the most infectious viruses known to infect humans, with the potential of an infected individual infecting up to 15 people⁸. Transmitted by coughing, sneezing, or close contact,

MeV can remain active and contagious in the air or on surfaces for two hours. Long regarded as an unavoidable hurdle of childhood development, MeV symptoms present as a high fever, cough, and a maculopapular rash. Furthermore, immunosuppressive properties of MeV can lead to life threatening secondary infections in the respiratory and/or neurological systems^{8,17}.

Successful vaccination arrived in the 1960s, and by the early 2000s infection rates dropped to roughly 800,000 children annually. By 2017, that number had dropped even further to just over 100,000 annual infections, with the vaccine preventing more than 20 million deaths over the previous 15 years^{8,22}. Although the MeV vaccine has been around for more than 50 years, poor vaccination rates persist in developing countries and has resurfaced in the United States, presenting a major health burden. Although the CDC has put pressure on eradicating the highly infectious disease, there are currently no countries with total MeV elimination⁸.

1.1.2.2 Nipah virus

Henipaviruses, such as NiV and HeV are highly virulent and lethal emerging viruses, discovered merely a few decades ago⁷. In September of 1998 a pig farming town in the western state of Ipoh, Malaysia was struck with cases of an atypical disease. Additional outbreaks began in nearby towns, and clinicians believed a mosquito borne virus, Japanese encephalitis (JE) was responsible. Immediate measures were taken to fog mosquitoes and increase JE virus immunizations, however atypical features of the illness suggested JE was not responsible for the illnesses²³.

By March of 1999, virologists at the University of Malaysia successfully isolated the virus and identified it as a new *paramyxovirus* similar to HeV²³. It became apparent that pigs were associated with outbreak, which resulted in the culling of more than one million pigs across the region. The 1998 NiV outbreak persisted for nearly six months and killed 105 people⁷. Soon after, fruit bats were identified as the natural reservoir and the outbreak had been traced back to fruit trees planted near pig farms, which brought infected bats and pigs in close proximity.

Just two years later in 2001 simultaneous outbreaks occurred in Bangladesh and India. Like the initial MARV and EBOV outbreaks, the infectious agent could not be immediately identified. Unlike in Malaysia, pig farming is not common in these Bangladesh and India. Subsequently, the origin of these outbreaks were linked to people drinking date palm sap that had been infected by fruit bats.

Since 2001, annual NiV outbreaks have occurred. With case fatality rates as high as 90% and clear evidence of human-human transmission, NiV poses a significant threat to public health⁷. Moreover, NiV possesses a high potential to transfer host species as it can also infect a wide range of animal hosts ranging from fish to vertebrates⁷. Furthermore, NiV has been isolated on several continents, and with no available treatments there is an urgent need to research mechanisms of this emerging and lethal virus²⁴.

1.2 Viral Structure

The structure and morphology of viruses arise from a complex network of stable protein-protein, protein-RNA, and protein-lipid interactions. These interactions are stringently dependent on multimeric complexes of thousands of viral proteins. All members of the Mononegavirales order of viruses carry along a core set of proteins, encoded by their RNA genome (**Figure 1.3**).

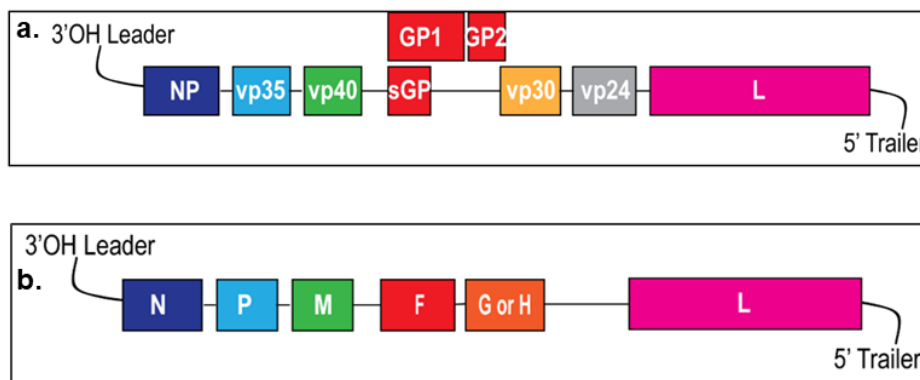


Figure 1.3. RNA genome of EBOV and MeV/NiV. EBOV, MARV, NiV, and MeV are (-) sense RNA viruses with a genome that encodes 6-7 structural proteins. **(a)** RNA genome of EBOV. NP: nucleoprotein, VP35: viral protein 35, VP40: viral protein 40, sGP: glycoprotein, GP1 and GP2: cleaved products of glycoprotein, VP30: viral protein 30, VP24: viral protein 24, L: polymerase. **(b)** RNA genome of MeV/NiV. N: nucleoprotein, P: phosphoprotein, M: matrix protein, F: fusion protein, G/H: attachment protein, L: polymerase. The attachment protein is H in MeV and G in NiV.

There are four principal units of Mononegavirales viral structure: a linear (-) sense genome, helical nucleocapsid structure, extensive matrix layer, and the lipid envelope

studded with surface glycoproteins. The genome is protected by a nucleocapsid complex, comprised of the nucleoprotein (NP) and accessory proteins. The genome-nucleocapsid structure is encapsulated by an extensive grid-like scaffold comprised by the self-assembly of the matrix protein. Lastly, the virus is bound by a lipid envelope derived from the host plasma membrane, which is studded with glycoproteins to aid in attachment and fusion⁶.

Filoviruses and *paramyxoviruses* contain several proteins with conserved structure and function (**Figure 1.4**). Within the nucleocapsid lies the NP, considered the main structural component of the nucleocapsid complex, which interacts with both the RNA genome and other

viral proteins. Additionally, *filoviruses* and *paramyxoviruses* encode an RNA-dependent polymerase (RdRP), coined the L protein. The L protein of *filoviruses* and *paramyxoviruses* is quite large (>2,000 amino acids) and is the only known viral protein known to possess enzymatic activity. An essential polymerase cofactor can be found in both *filoviruses* (viral protein 35, VP35) and *paramyxoviruses* (phosphoprotein, P). The most abundant protein in *filoviruses* and *paramyxoviruses* is the singular matrix protein, viral protein 40 (VP40) and matrix protein (M), respectively. The matrix protein homo-oligomerizes into an extensive matrix interlaced between the nucleocapsid complex and lipid envelope. The matrix layer is paramount to the structural morphology and integrity observed

in both viral families. Moreover, the matrix protein is so abundant it is estimated that more than 8,000 VP40 proteins populate one EBOV particle³⁰. Lastly, critical to viral attachment and fusion are the glycoproteins. Glycoproteins, embedded in the lipid envelope, are the most well characterized viral protein⁴. EBOV and MARV contain one glycoprotein (GP)⁴, while two are found within MeV (fusion protein, F, and attachment protein, H) and NiV (fusion protein, F, and attachment protein, G)⁷.

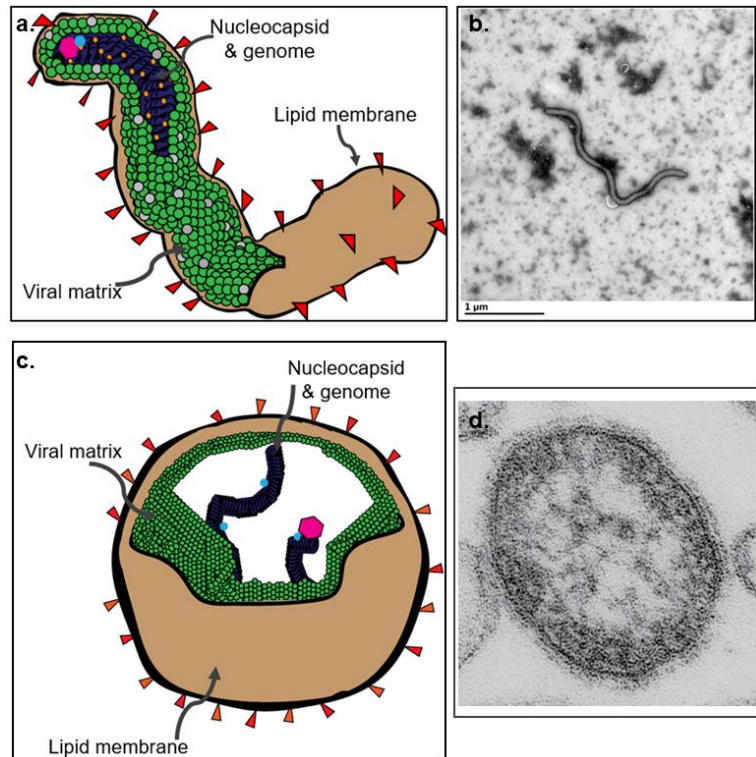


Figure 1.4. Structure of *filoviruses* and *paramyxoviruses*. (a) Cartoon of filovirus structure, which is filamentous in shape, is surrounded by a lipid envelope (brown) studded with glycoproteins (red). Underneath the lipid envelope is the viral matrix (green), and at the core is the nucleocapsid containing proteins and the genome (dark blue). (b) Transmission electron micrograph of a viral like particle produced from mammalian cells expressing VP40 highlighting the filamentous shape of filoviruses. (c) Cartoon of paramyxovirus structure, which is predominately spherical in shape, is surrounded by a lipid envelope (brown) studded with attachment (orange) and fusion proteins (red). Underneath the lipid envelope is the viral matrix (green), and at the core is the nucleocapsid containing proteins and the genome (dark blue). (d) Transmission electron micrograph of a MeV highlighting the spherical shape of paramyxoviruses. Micrograph of MeV courtesy of the CDC and Cynthia S. Goldsmith & William Bellini, PhD

Whether spherical or filamentous, lipid enveloped viruses are typically small in size. Derived from the Latin word *filum* meaning thread, *filoviruses* are filamentous and elongated rod-shaped structures, characteristically 80 nm in diameter. These filamentous structures display tremendous plasticity and can bend and loop back on itself⁴. Conversely, *paramyxoviruses* such as MeV and NiV can be spherical or filamentous and therefore a wide range of diameters (40-1900 nm) are observed^{25,26}.

1.3 Viral Life Cycles

Filoviruses and *paramyxoviruses* are lipid enveloped viruses, who contain not only similar proteins, but share several key events of their respective life cycle (**Figure 1.5**). Upon infection, these viruses enter cells through interactions with their surface glycoprotein and protein receptors on host cells. After either direct fusion with either the plasma membrane or fusion of the viral with an endocytic compartment membrane, each virus is unpackaged as its contents are released into the cytosol for protein and RNA synthesis to begin. Although these viruses traverse through different pathways within the cell, their matrix proteins coalesce at the plasma membrane, directing other viral components to follow. Assembly and budding of progeny virions ensues, and the viral life cycle continues.

1.3.1 Entry

The initial step of the viral life cycle, viral entry, is the first account of cellular mimickery utilized by RNA viruses (**Figure 1.5 a**). EBOV, MARV, MeV, and NiV manipulate protein-protein and protein-lipid interactions to gain access into the cellular cytoplasm. Each of these viruses achieve entry through recognition of their glycoprotein and lipid envelope with characteristic host protein receptors on the cell surface. Different organisms, tissues and cell types express varying identities and levels of surface receptors, which accounts for variable host species, disease manifestation and pathophysiology observed amongst these viruses^{4,5,7}. Lastly, apoptotic mimickery is a mechanism numerous viruses employ to enhance viral entry, however, this mechanism will be discussed in detail in a later section.

1.3.1.1 pH dependent entry: Filoviruses

Initial association between EBOV/MARV and host cells occurs via a dual-attachment mechanism by the host cell surface protein receptor, T-cell immunoglobulin and mucin domain protein1 (TIM-1). TIM-1 directly binds to GP as well as a specific lipid within the lipid envelope, phosphatidylserine (PS)²⁷. It is important to note that this process is mediated by lectin receptors in different cell types such as dendritic cells²⁸.

Upon entry into cells, EBOV/MARV enter the acidic environment of endocytic compartments. Cleavage of GP by endosomal proteases is triggered by the low pH and exposes a previously buried fusion loop, permitting GP's interaction with an additional host protein receptor, NPC1²⁹. The GP-NPC1 interaction triggers a conformational change in the fusion loop of GP, which initiates fusion of the viral and endosomal membranes allowing viral components to empty in to the cytosol for the next stage of the viral life cycle⁴ (**Figure 1.5 b**).

1.3.1.2 pH independent entry: Paramyxoviruses

Although MeV and NiV both cause respiratory illnesses, differences in the host proteins receptors they hijack for entry is reflected by their distinctive hosts and pathogenesis.

MeV entry is initiated by interaction of the H protein with the host cell surface receptor signaling lymphocyte activation molecule family member 1 (SLAM/CD150). SLAM receptors are found within the respiratory epithelium and vasculature, the initial site of MeV infection. However, SLAM receptors are not widely expressed across mammals, explaining the limited host transfer potential of MeV. Following entry, MeV is disseminated into the lymph nodes where it can then traverse to B and T cells, the site of MeV replication^{7,8,30}. NiV entry is mediated between the interaction of the G protein and the host cell surface receptor, Ephrin-B2. Ephrin-B2 is expressed on microvascular endothelial cells in the respiratory epithelium and in neurons. Notably, Ephrin-B2 is highly conserved across mammals, which accounts for the wide range of animals susceptible to NiV infection⁷.

Following initial viral-host association between the attachment proteins and their respective receptors, the viral membrane is directly fused with the plasma membrane. Similar to *filovirus* entry, this process is mediated by structural changes in the glycoprotein, however proceeds in a pH independent manner. Both attachment proteins, G and H, possess a globular head

domain which undergoes conformational rearrangement upon interaction with the host protein receptor. This interaction triggers a conformational rearrangement of a stalk region with the attachment proteins. Upon this rearrangement, the stalk of the attachment proteins triggers a rearrangement of the fusion protein, which initiates the cascade for fusion of the viral and cell membranes and release of viral components into the intracellular space^{7,8} (**Figure 1.5 b**).

1.3.2 Replication

Filoviruses and *paramyxoviruses* have a ~19 kb non-segmented genome with conserved gene order, encoding seven and six structural proteins, respectively^{5,7}. Additionally, these viral families utilize a RdRP for viral transcription and replication. Due to the “stop-start” model of gene transcription by the RdRP on the non-segmented RNA genome, a gradient of gene products is observed with genes at the 3’ end of the genome transcribed more abundantly than those at the 5’ end. Although some viruses within the Mononegavirales order replicate in the nucleus (influenza virus), *filoviruses* and *paramyxoviruses* transcription and replication takes place within the cytosol in cytosolic inclusion bodies as sites of viral replication and transcription^{4,7} (**Figure 1.5 c**).

Following uncoating within the cytosol, the nucleocapsid complex proteins commence coordinating transcription of the (-) sense RNA genome. Transcription of the negative sense genome must occur prior to replication, to produce the (+) sense RNA gene products required for protein translation and production of new (-) sense genomes. Extensive work in cellular minigenome systems has assisted in identifying the viral components necessary and sufficient for viral replication.

Three viral proteins have emerged as required components for replication: NP, P or VP35, and L^{4,31,32}. NP is an RNA binding protein that multimerizes into a helical assembly wrapped around the genome. Upon independent expression in mammalian cells, NP forms cytoplasmic inclusion bodies, where it has been shown to interact with host RNA^{4,33}. L is a multi-domain enzymatic component of the system, responsible for transcription, replication, genome capping and polyadenylation⁶. Contrasting to the expression of NP, independent expression of L results in a diffuse cytoplasmic localization. Lastly, P/VP35 serve as a cofactor by linking the L and NP proteins. Moreover, it has been proposed that P/VP35 carry out chaperone functions by obstructing the self-association of NP and non-productive associations between NP and RNA, allowing

replication to complete before NP begins its helical assembly around the viral genome⁶. When expressed together, NP, P/VP35, and L colocalize in the cell and fulfill each requirement for productive viral transcription and replication.

1.3.3 Viral assembly and budding

Cellular trafficking can be simplified into two canonical modes of transport, vesicular (endosomal trafficking) and non-vesicular (actin and microtubules). These transportation modalities are maintained in virus trafficking. Although *filoviruses* and *paramyxoviruses* embark on different journeys throughout cellular compartments, each viral protein unites at the plasma membrane where viral budding and release occurs (**Figure 1.5 d**).

While replication occurs in inclusion bodies within the cytosol for both families of viruses, the matrix proteins direct the trafficking of viral components to the plasma membrane. Consequently, proper trafficking of the matrix proteins to the plasma membrane is a crucial prerequisite for efficient viral assembly and budding. Early in infection, matrix proteins are cytosolically localized, and in the case of MARV, highly associated with intracellular membranes³⁴. Interestingly, each matrix protein is observed to transiently translocate into the nucleus, however the function of nuclear localization is not well understood³⁵. In the case of M proteins, ubiquitination and nuclear-cytoplasmic transport is required for efficient viral production^{36–38}. Additionally, there is significant evidence of filoviral VP40 ubiquitination, suggested by pronounced interactions between VP40 and ubiquitin ligases such as neural precursor cell expressed developmentally down-regulated protein 4 (NEDD4)^{39–42}.

Matrix protein mediated viral assembly requires the spatial and temporal alignment of each viral component. Following viral replication, the ribonucleoprotein (RNP) complexes in filoviruses and paramyxoviruses traverse to the matrix protein enriched regions of the plasma membrane via the actin network^{43,44}. In-depth live cell imaging experiments have highlighted that once at the cell periphery, filovirus RNPs are directed within filopodia by VP40 in an actin-dependent manner^{44–46}. The role of actin in MeV and NiV transport is not as clearly defined. Pharmacological inhibition of actin polymerization perturbs the assembly and release of MeV particles⁴⁷ and a recent proteomics analysis of NiV infected cells suggested a role for actin in NiV trafficking and release⁴⁸. Furthermore, the endocytic pathway and specifically Rab-11 positive recycling endosomes have also been implicated in MeV and NiV RNP transport^{48,49}.

In addition to the RNPs, the glycoproteins must convene with the matrix proteins at sites of viral assembly. During viral infection, GP travel independently of other viral proteins to the plasma membrane where they are randomly distributed. Filovirus GP hijacks the secretory pathway to arrive at the plasma membrane, however detailed reports of this observation are lacking^{50,51}. In the case of *paramyxoviruses*, the glycoproteins (F, G, H) travel to the basolateral membrane when expressed independently in polarized cells. However, upon co-expression with the M protein, the glycoproteins are redistributed to the apical side of the cell where budding occurs^{52,53}. This phenomenon is also observed in MARV budding within polarized cells; however, in the opposite direction. In MARV budding, GP will localize to the apical membrane, and upon co-expression with mVP40 will redistribute to the basolateral membrane where budding will occur⁵⁴. Investigations into the polarity of EBOV budding have not been performed.

A direct interaction between matrix proteins and glycoproteins has been established for HIV-1⁵⁵, influenza⁵⁶, as well as the paramyxoviruses. Biochemical and cryo-electron tomography (cryo-ET) studies have shown MeV and NiV M proteins directly interact with the cytoplasmic tails of F and H proteins, respectively^{8,57-59}. However, the function of this interaction is not well understood. Specifically, recent cryo-ET and super-resolution techniques of MeV and NiV proteins has provided conflicting evidence as to whether M redistributes the glycoproteins within the apical membrane to sites of viral assembly or if glycoprotein localization is stochastic^{58,60}. Unlike paramyxoviruses, a direct filovirus matrix protein VP40 and GP interaction has not been established. However, a VP40-GP relationship is suggested by the finding that viral budding is enhanced when both proteins are expressed compared to VP40 alone⁶¹. Whether through a direct or indirect interaction, glycoproteins play an imperative role in successful viral budding.

Viral assembly is the penultimate step of the viral life cycle, followed by membrane scission and release (**Figure 1.5 e**). Upon congregation of the glycoproteins, matrix proteins, and RNPs within the plasma membrane, progeny virions must be released to propagate the viral life cycle. A required step for viral assembly and scission is the generation of significant membrane deformation, or negative curvature^{62,63}. Membrane curvature is ubiquitous throughout the cell and is regulated by the combined effort of membrane lipids and proteins. Negative curvature observed within viral budding is akin to the membrane pushing out away from the cytosol and is believed to be mediated by accumulation of viral components at the plasma membrane, rearrangement of the actin network, and host machinery such as the ESCRT proteins^{63,64}. Irrespective of viral

morphology, *filovirus* and *paramyxovirus* virions pinch off from the plasma membrane, ready to disseminate throughout the host. While significant advancements in viral life cycles has identified key shared pathways, viral budding is the least well characterized. Furthermore, the intimate role between plasma membrane lipids and RNA viral components has not been elucidated. This interface of viral assembly remains an underexplored platform for drug development and as a commonly overlooked feature of lipid-enveloped viruses, an in-depth understanding of assembly processes between the plasma membrane and matrix proteins may provide the framework for a pan viral therapy.

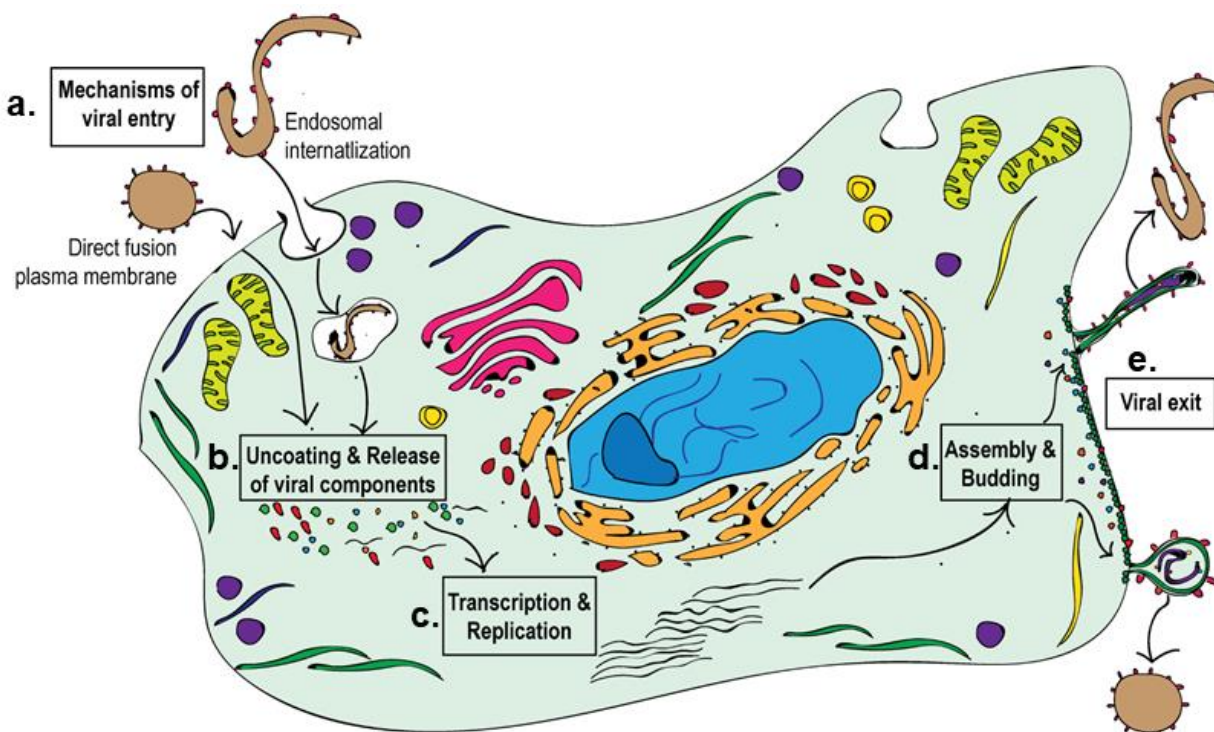


Figure 1.5. Schematic of the life cycle of *filoviruses* and *paramyxoviruses*. (a) *Filoviruses* enter cells through a micropinocytosis process while *paramyxoviruses* enter through direct fusion of the viral lipid envelope and plasma membrane. (b) Structural rearrangements occur within the glycoproteins of these viruses which allow the release of viral components into the cytoplasm. (c) Transcription of the (-) sense RNA genome commences and is followed by replication, both of which occur within the cytosol. (d) Following transcription and replication, mRNA is translated into new viral proteins which travel through the cell and assemble into new virions at the plasma membrane. This process is mediated by VP40. (e) Following the assembly of new virions at the plasma membrane, membrane scission occurs releasing the virion into the extracellular space.

1.4 Vaccines and therapeutics

There are two classical approaches to developing effective anti-virals: therapeutics targeting the viral components directly or targeting the virus indirectly through inhibiting host

processes required for the viral life cycle. Although there are FDA approved drugs to inhibit several (-) sense RNA viruses (such as rabies, RSV and influenza)⁶⁵, anti-viral therapies for *filoviruses* and *Henipaviridae* are lacking. Prior to the licensing of a novel vaccine in December of 2019 for EBOV⁶⁶, the only available treatment for these fatal viruses was supportive care for nutrition, electrolyte management, fluid intake and necessary antibiotics required to treat secondary infections. Furthermore, although a MeV vaccine is available, for those who either chose to not vaccinate or do not have access to the vaccine, supportive care and antibiotics are also the only available treatment. On account of increasing pressure to develop effective vaccines and anti-virals, significant advances have been made to understand the fundamental structural biology and biochemistry of viral lifecycles. Unfortunately, many aspects of late stages in the viral lifecycle, such as assembly and budding, remain largely unclear and an effective and licensed therapeutic against EBOV, MARV, MeV, and NiV remain unavailable.

1.4.1.1 Vaccine development

The advent of vaccination began more than 50 years ago with the smallpox vaccine, and since vaccine development has been heralded as one of the most significant advances to medicine in human history. Vaccination has helped either eliminate or eradicate infectious viruses such as polio, small pox, varicella, mumps, rubella and until 2019, MeV. To this end, developing a safe, inexpensive, and effective vaccine is a significant step to eliminating disease, however considerable hurdles remain in vaccine development. Foremost, vaccine development can span 10-20 years to complete each of the early, clinical and late development stages required to be brought to market. Secondly from inception to implementation, billions of dollars must be spent to investigate the efficacy and safety of vaccines as well as manufacture, distribute and stockpile the vaccine for use.

The inception of EBOV vaccine development began in the 1980s. However, a lack of market demand left many of these stalled in the early phases of clinical development. The EBOV outbreak of 2013 increased the pressure to bring a vaccine to market, and since then numerous experimental vaccines have been tested in subsequent outbreaks. Successes with *filovirus* vaccine development can be attributed to groundbreaking advances into structural biology of the glycoprotein (GP), a surface exposed viral protein responsible for viral entry.

One of the first experimental vaccines tested during the 2013 EBOV outbreak was the rVSV-EBOV vaccine. rVSV-EBOV is a recombinant vesicular stomatitis virus (VSV) expressing GP of EBOV. Throughout the 2013 and subsequent outbreaks rVSV-EBOV has demonstrated strong protective efficacy through ring vaccination, however it remains unclear if it can be used as a post-exposure prophylaxis⁶⁵. In December 2019, rVSV-ZEBOV became the first FDA licensed vaccine against EBOV (under the name Ervebo)⁶⁶. Prior to licensing the vaccine was being tested in the Kivu outbreak and has shown high levels of protection in individuals possibly exposed to the virus. However, the vaccine is only efficacious against one EBOV genera (Zaire) and also does not protect against MARV. Lastly, the vaccine is only being used in patients over the age of 18, leaving many younger generations at risk⁶⁶. ZMapp, also designed against GP, is a viral fusion inhibitor antibody cocktail that has been investigated against EBOV infections. Initial studies found ZMapp to be safe and protective against EBOV infections, however it later became evident that its efficacy was no more than the standard treatment of care and has since stopped being administered⁶⁷.

Two of the more promising experimental vaccines being investigated are mAB114 and REGN-EB3. REGN-EB3 is an antibody cocktail that possesses neutralizing and non-neutralizing properties targeting GP and immune function. Similar to REGN-EB3, mAB114 has neutralizing and non-neutralizing properties. mAB114 binds GP to inhibit entry and also blocks a later step during entry between GP and the host cell receptor, Niemann-Pick C1 (NPC1). Both REGN-EB3 and mAB114 have demonstrated promise in clinical trials, however their efficacy is still being evaluated^{65,67}. It is important to note that each of these candidate vaccines target GP, a viral protein with the highest mutation rates and escape mutations within the GP have already been observed⁶⁵. Not unlike candidate vaccines for filoviral infections, experimental vaccines for NiV infections have focused on neutralizing surface exposed proteins, the fusion (F) and attachment (G) protein. Investigational vaccines have shown promise *in vitro*⁶⁸ and in animal models⁶⁹; however, no data is available on their efficacy in humans. Equivac®, a licensed vaccine against HeV for horses available in Australia, has shown potential for immunization efficacy against NiV in ferrets and African green monkeys, however failed to protect pigs. As NiV poses a significant threat to agriculture and pig farming, a vaccine for pigs may also help contain NiV infections. The efficacy of three vaccine candidates are currently being tested in pigs, each targeted against F and G⁶⁹. Lastly, although fatality rates are severely high for NiV infections, the sporadic nature of their

outbreaks has suggested a limited market for vaccine development, ultimately stalling immediate pressure on their development.

Unlike filoviral and NiV infections, a safe, effective, and inexpensive vaccine is available to treat MeV⁸. Vaccines have the unique property of protecting against an infectious agent at both the individual and population level, a concept known as herd immunity. In order to maintain protection within a population, 95% of the population must be vaccinated. The goal of any vaccine is to eliminate viral infections (no infection for 12 months) and ultimately completely remove the infection, or eradicate it, as in the case with polio virus. The discovery of the MeV vaccine was a landmark success in combating MeV infections around the world.

Strong vaccination campaigns pioneered successful reduction of MeV cases within the United States. In 2017 there were only 120 cases reported within the United States. Alarming, in 2019, there were over 1,000 cases of MeV within the United States, directly related to a decline in vaccination rates and not vaccine failure⁷⁰. Moreover, with a decline in vaccination within the United States, underdeveloped and economically strained countries such as the DRC have continuously struggled to contain MeV. Approximately 100,000 people died from MeV in 2017. Although it costs approximately \$1 USD to immunize a child against MeV, the current decline in MeV vaccination has put the likelihood of MeV elimination severely at risk²².

1.4.1.2 Anti-viral development

Although vaccine development has garnered noteworthy attention, in the event of a widespread epidemic in developing countries, a global epidemic, or the use of an infectious agent as a biological weapon, there is an imperative need to develop post-exposure therapeutics. Developing an efficacious anti-viral is contingent on a complex understanding of viral life cycle stages. Research in these fields has led to licensed anti-virals against nearly every stage of a viral life cycle, such as early stage inhibitors targeting attachment and fusion (for human immunodeficiency virus (HIV), rabies, and RSV), uncoating inhibitors (influenza virus), viral assembly (variola virus) and viral release (influenza virus)⁶⁵.

The most abundant class of anti-virals being explored for *filoviruses* and *Henipaviridae* target replication or are inhibitors of nucleic acid synthesis^{65,71}. Remdesivir, a nucleoside analogue, has been tested against both filoviral and NiV infections and have exhibited anti-viral effects in cell culture and nonhuman primates for EBOV⁷² and anti-viral effects in primates for NiV⁷³.

Remdesivir works by inhibiting RNA transcription and replication. Moreover, by an unknown mechanism Remdesivir displays selectivity for viral RNA polymerases over host polymerase⁷². Ribavirin was tested in the initial NiV outbreak, however it remains unclear if it was protective in humans⁷³.

An alternative and attractive avenue for therapeutic development is FDA drug repurposing. This technique significantly reduces not only cost but also time for drug development by repurposing drugs currently approved by the FDA for a new disease. Although targeting host protein-viral protein interactions is challenging, FDA-repurposing these interactions has been a focus for both *filovirus* and *paramyxovirus* drug development. In the case of NiV infections, repurposing proteasome inhibitors has shown promise³⁷. Additionally, targeting heat shock protein 90 (HSP90) has been successful in certain cancers and has shown promise in *filovirus* and *paramyxovirus* infections⁶. Targeting late stages of the viral life cycle, such as assembly and budding has often focused on viral interactions with host proteins within the endosomal sorting complex required for transport (ESCRT) family. *In vitro* and cellular studies highlighted that targeting viral-ESCRT interactions have shown therapeutic efficacy in blocking viral assembly and budding.

Viruses within the Mononegavirales are genetically, structurally, and functionally related; therefore, investigations into their assembly process could be fruitful in unearthing a landmark pan-viral therapeutic. More information is needed regarding late stages of viral budding in order to identify innovative drug anti-viral drug targets.

1.5 References

1. Amarasinghe, G. K. *et al.* Taxonomy of the order Mononegavirales: update 2018. *Arch. Virol.* **163**, 2283–2294 (2018).
2. Stallcup, K. C., Raine, C. S. & Fields, B. N. Cytochalasin B inhibits the maturation of measles virus. *Virology* **124**, 59–74 (1983).
3. Cox, R. M. & Plemper, R. K. Structure and organization of paramyxovirus particles. *Curr. Opin. Virol.* **24**, 105–114 (2017).
4. Emanuel, J., Marzi, A. & Feldmann, H. Filoviruses: Ecology, Molecular Biology, and Evolution. in *Advances in Virus Research* vol. 100 189–221 (Academic Press Inc., 2018).
5. Liu, L. Fields Virology, 6th Edition. *Clin. Infect. Dis.* **59**, 613–613 (2014).
6. Latorre, V., Mattenberger, F. & Geller, R. Chaperoning the mononegavirales: Current knowledge and future directions. *Viruses* vol. 10 (2018).
7. Thibault, P. A., Watkinson, R. E., Moreira-Soto, A., Drexler, J. F. & Lee, B. Zoonotic Potential of Emerging Paramyxoviruses: Knowns and Unknowns. in *Advances in Virus Research* vol. 98 1–55 (Academic Press Inc., 2017).
8. Rima, B. K. & Duprex, W. P. Morbilliviruses and human disease. *J. Pathol.* **208**, 199–214 (2006).
9. WHO | List of Blueprint priority diseases. *WHO* (2018).
10. Suzuki, Y. & Gojobori, T. The origin and evolution of Ebola and Marburg viruses. *Mol. Biol. Evol.* **14**, 800–806 (1997).
11. Carroll, S. A. *et al.* Molecular Evolution of Viruses of the Family Filoviridae Based on 97 Whole-Genome Sequences. *J. Virol.* **87**, 2608–2616 (2013).
12. Slenczka, W. & Klenk, H. D. Forty Years of Marburg Virus. *J. Infect. Dis.* **196**, S131–S135 (2007).
13. Siebert, R., Shu, H. & ... W. S. On the etiology of an unknown human infectious disease caused by monkeys. *DMW-German ...* (1967).
14. Breman, J. G. *et al.* Discovery and Description of Ebola Zaire Virus in 1976 and Relevance to the West African Epidemic during 2013–2016. *J. Infect. Dis.* **214**, S93–S101 (2016).
15. 2014–2016 Ebola Outbreak in West Africa | History | Ebola (Ebola Virus Disease) | CDC. <https://www.cdc.gov/vhf/ebola/history/2014-2016-outbreak/index.html>.
16. Coltart, C. E. M., Lindsey, B., Ghinai, I., Johnson, A. M. & Heymann, D. L. The Ebola outbreak, 2013–2016: Old lessons for new epidemics. *Philosophical Transactions of the Royal Society B: Biological Sciences* vol. 372 (2017).
17. Lamb, R. A. & Parks, G. D. Paramyxoviridae: the viruses and their replication. 1449–1496 (2007).
18. Furuse, Y., Suzuki, A. & Oshitani, H. Origin of measles virus: divergence from rinderpest virus between the 11th and 12th centuries. *Virol. J.* **7**, 52 (2010).
19. Tong, Y. G. *et al.* Genetic diversity and evolutionary dynamics of Ebola virus in Sierra Leone. *Nature* **524**, 93–96 (2015).
20. Baize, S. *et al.* Emergence of Zaire Ebola Virus Disease in Guinea - Preliminary Report. *Nature* **524**, 1–8 (2015).
21. Measles | History of Measles | CDC. <https://www.cdc.gov/measles/about/history.html>.
22. Organization, W. H. Measles. <https://www.who.int/news-room/fact-sheets/detail/measles> (2019).
23. Ang, B. S. P., Lim, T. C. C. & Wang, L. Nipah Virus Infection. (2018)

doi:10.1128/JCM.01875-17.

24. Nor, M. N. M., Gan, C. H. & Ong, B. L. *Nipah virus infection of pigs in peninsular Malaysia. Rev. sci. tech. Off. int. Epiz.* vol. 19 (2000).
25. Hyatt, A. D., Zaki, S. R., Goldsmith, C. S., Wise, T. G. & Hengstberger, S. G. Ultrastructure of Hendra virus and Nipah virus within cultured cells and host animals. *Microbes and Infection* vol. 3 297–306 (2001).
26. Liu, Y. C., Grusovin, J. & Adams, T. E. Electrostatic Interactions between Hendra Virus Matrix Proteins Are Required for Efficient Virus-Like-Particle Assembly. *J. Virol.* **92**, (2018).
27. Kuroda, M. *et al.* Interaction Between TIM-1 and NPC1 Is Important for Cellular Entry of Ebola Virus. *J. Virol.* **89**, 6481–93 (2015).
28. Alvarez, C. P. *et al.* C-type lectins DC-SIGN and L-SIGN mediate cellular entry by Ebola virus in cis and in trans. *J. Virol.* **76**, 6841–4 (2002).
29. Chandran, K., Sullivan, N. J., Felbor, U., Whelan, S. P. & Cunningham, J. M. Endosomal proteolysis of the Ebola virus glycoprotein is necessary for infection. *Science* **308**, 1643–5 (2005).
30. Delpeut, S., Sisson, G., Black, K. M. & Richardson, C. D. Measles Virus Enters Breast and Colon Cancer Cell Lines through a PVRL4-Mediated Macropinocytosis Pathway. *J. Virol.* **91**, (2017).
31. Conzelmann, K. K. Reverse genetics of Mononegavirales. *Current Topics in Microbiology and Immunology* vol. 283 1–41 (2004).
32. Whelan, S. P. J., Barr, J. N. & Wertz, G. W. Transcription and replication of nonsegmented negative-strand RNA viruses. *Current Topics in Microbiology and Immunology* vol. 283 61–119 (2004).
33. Noda, T., Hagiwara, K., Sagara, H. & Kawaoka, Y. Characterization of the Ebola virus nucleoprotein-RNA complex. *J. Gen. Virol.* **91**, 1478–1483 (2010).
34. Kolesnikova, L., Bamberg, S., Berghofer, B. & Becker, S. The Matrix Protein of Marburg Virus Is Transported to the Plasma Membrane along Cellular Membranes: Exploiting the Retrograde Late Endosomal Pathway. *J. Virol.* **78**, 2382–2393 (2004).
35. Harrison, M. S., Sakaguchi, T. & Schmitt, A. P. Paramyxovirus assembly and budding: Building particles that transmit infections. *International Journal of Biochemistry and Cell Biology* vol. 42 1416–1429 (2010).
36. Pohl, C., Duprex, W. P., Krohne, G., Rima, B. K. & Schneider-Schaulies, S. Measles virus M and F proteins associate with detergent-resistant membrane fractions and promote formation of virus-like particles. *J. Gen. Virol.* **88**, 1243–50 (2007).
37. Wang, Y. E. *et al.* Ubiquitin-regulated nuclear-cytoplasmic trafficking of the Nipah virus matrix protein is important for viral budding. *PLoS Pathog.* **6**, e1001186 (2010).
38. Wang, Y. E., Pernet, O. & Lee, B. Regulation of the nucleocytoplasmic trafficking of viral and cellular proteins by ubiquitin and small ubiquitin-related modifiers. *Biology of the Cell* vol. 104 121–138 (2012).
39. Han, Z. *et al.* ITCH E3 Ubiquitin Ligase Interacts with Ebola Virus VP40 To Regulate Budding. *J. Virol.* **90**, 9163–71 (2016).
40. Han, Z. *et al.* Ubiquitin Ligase WWP1 Interacts with Ebola Virus VP40 To Regulate Egress. *J. Virol.* **91**, (2017).
41. Harty, R. N., Brown, M. E., Wang, G., Huibregtse, J. & Hayes, F. P. A PPxY motif within the VP40 protein of Ebola virus interacts physically and functionally with a ubiquitin ligase:

- Implications for filovirus budding. *Proc. Natl. Acad. Sci. U. S. A.* **97**, 13871–13876 (2000).
42. Urata, S. & Yasuda, J. Regulation of Marburg virus (MARV) budding by Nedd4.1: A different WW domain of Nedd4.1 is critical for binding to MARV and Ebola virus VP40. *J. Gen. Virol.* **91**, 228–234 (2010).
 43. Schudt, G. *et al.* Transport of Ebolavirus Nucleocapsids Is Dependent on Actin Polymerization: Live-Cell Imaging Analysis of Ebolavirus-Infected Cells. *J. Infect. Dis.* **212 Suppl 2**, S160-6 (2015).
 44. Schudt, G., Kolesnikova, L., Dolnik, O., Sodeik, B. & Becker, S. Live-cell imaging of Marburg virus-infected cells uncovers actin-dependent transport of nucleocapsids over long distances. *Proc. Natl. Acad. Sci. U. S. A.* **110**, 14402–14407 (2013).
 45. Takamatsu, Y., Kolesnikova, L. & Becker, S. Ebola virus proteins NP, VP35, and VP24 are essential and sufficient to mediate nucleocapsid transport. *Proc. Natl. Acad. Sci. U. S. A.* **115**, 1075–1080 (2018).
 46. Adu-Gyamfi, E., Digman, M. A., Gratton, E. & Stahelin, R. V. Single-particle tracking demonstrates that actin coordinates the movement of the Ebola virus matrix protein. *Biophys. J.* **103**, L41-3 (2012).
 47. Dietzel, E., Kolesnikova, L. & Maisner, A. Actin filaments disruption and stabilization affect measles virus maturation by different mechanisms. *Viol. J.* **10**, (2013).
 48. Johnston, G. P. *et al.* Nipah Virus-Like Particle Egress Is Modulated by Cytoskeletal and Vesicular Trafficking Pathways: a Validated Particle Proteomics Analysis. *mSystems* **4**, (2019).
 49. Nakatsu, Y. *et al.* Intracellular Transport of the Measles Virus Ribonucleoprotein Complex Is Mediated by Rab11A-Positive Recycling Endosomes and Drives Virus Release from the Apical Membrane of Polarized Epithelial Cells. *J. Virol.* **87**, 4683–4693 (2013).
 50. Bavari, S. *et al.* Lipid raft microdomains: A gateway for compartmentalized trafficking of Ebola and Marburg viruses. *J. Exp. Med.* **195**, 593–602 (2002).
 51. Becker, S., Klenk, H. D. & Mühlberger, E. Intracellular transport and processing of the Marburg virus surface protein in vertebrate and insect cells. *Virology* **225**, 145–55 (1996).
 52. Lamp, B. *et al.* Nipah Virus Entry and Egress from Polarized Epithelial Cells. *J. Virol.* **87**, 3143–3154 (2013).
 53. Maisner, A., Klenk, H. & Herrler, G. Polarized budding of measles virus is not determined by viral surface glycoproteins. *J. Virol.* **72**, 5276–8 (1998).
 54. Kolesnikova, L., Ryabchikova, E., Shestopalov, A. & Becker, S. Basolateral Budding of Marburg Virus: VP40 Retargets Viral Glycoprotein GP to the Basolateral Surface. *J. Infect. Dis.* **196**, S232–S236 (2007).
 55. Cosson, P. Direct interaction between the envelope and matrix proteins of HIV-1. *EMBO J.* **15**, 5783–5788 (1996).
 56. Jin, H., Leser, G. P., Zhang, J. & Lamb, R. A. Influenza virus hemagglutinin and neuraminidase cytoplasmic tails control particle shape. *EMBO J.* **16**, 1236–1247 (1997).
 57. Johnston, G. P. *et al.* Cytoplasmic Motifs in the Nipah Virus Fusion Protein Modulate Virus Particle Assembly and Egress. *J. Virol.* **91**, (2017).
 58. Ke, Z. *et al.* Promotion of virus assembly and organization by the measles virus matrix protein. *Nat. Commun.* **9**, (2018).
 59. Tahara, M., Takeda, M. & Yanagi, Y. Altered Interaction of the Matrix Protein with the Cytoplasmic Tail of Hemagglutinin Modulates Measles Virus Growth by Affecting Virus Assembly and Cell-Cell Fusion. *J. Virol.* **81**, 6827–6836 (2007).

60. Liu, Q., Chen, L., Aguilar, H. C. & Chou, K. C. A stochastic assembly model for Nipah virus revealed by super-resolution microscopy. *Nat. Commun.* **9**, (2018).
61. Licata, J. M., Johnson, R. F., Han, Z. & Harty, R. N. Contribution of Ebola Virus Glycoprotein, Nucleoprotein, and VP24 to Budding of VP40 Virus-Like Particles. *J. Virol.* **78**, 7344–7351 (2004).
62. Soni, S. P. & Stahelin, R. V. The Ebola virus matrix protein VP40 selectively induces vesiculation from phosphatidylserine-enriched membranes. *J. Biol. Chem.* **289**, 33590–7 (2014).
63. Rossman, J. S. & Lamb, R. A. Viral Membrane Scission OVERVIEW OF MEMBRANE SCISSION. *Annu Rev Cell Dev Biol* **29**, 551–569 (2013).
64. Lee, I.-H., Kai, H., Carlson, L.-A., Groves, J. T. & Hurley, J. H. Negative membrane curvature catalyzes nucleation of endosomal sorting complex required for transport (ESCRT)-III assembly. **112**, (2015).
65. Hoenen, T., Groseth, A. & Feldmann, H. Therapeutic strategies to target the Ebola virus life cycle. *Nat. Rev. Microbiol.* doi:10.1038/s41579-019-0233-2.
66. FDA. First FDA-approved vaccine for the prevention of Ebola virus disease, marking a critical milestone in public health preparedness and response | FDA. <https://www.fda.gov/news-events/press-announcements/first-fda-approved-vaccine-prevention-ebola-virus-disease-marking-critical-milestone-public-health> (2019).
67. Kupferschmidt, K. Finally, some good news about Ebola: Two new treatments dramatically lower the death rate in a trial. *Science* (80-.). (2019) doi:10.1126/science.aaz1032.
68. Dang, H. V *et al.* An antibody against the F glycoprotein inhibits Nipah and Hendra virus infections. *Nat. Struct. Mol. Biol.* (2019) doi:10.1038/s41594-019-0308-9.
69. McLean, R. K. & Graham, S. P. Vaccine development for Nipah virus infection in pigs. *Frontiers in Veterinary Science* vol. 6 (2019).
70. Center for Disease Control. Measles Cases and Outbreaks | CDC. <https://www.cdc.gov/measles/cases-outbreaks.html> (2019).
71. Thakur, N. & Bailey, D. Advances in diagnostics, vaccines and therapeutics for Nipah virus. *Microbes and Infection* (2019) doi:10.1016/j.micinf.2019.02.002.
72. Tchesnokov, E. P., Feng, J. Y., Porter, D. P. & Götte, M. Mechanism of inhibition of ebola virus RNA-dependent RNA polymerase by remdesivir. *Viruses* **11**, (2019).
73. Lo, M. K. *et al.* Remdesivir (GS-5734) protects African green monkeys from Nipah virus challenge. *Sci. Transl. Med.* **11**, (2019).

CHAPTER 2. HIJACKING THE PLASMA MEMBRANE: MECHANISMS OF VIRAL BUDDING

2.1 A roadmap of the plasma membrane

The plasma membrane is a highly regulated and dynamic component of the cell indispensable to life. Formed by energetically favorable interactions between diverse classes of macromolecules such as proteins and lipids, the plasma membrane acts as a physical barrier guarding cells from the extracellular environment. Lipids, the bulk constituent of all cellular membranes, are a diverse and complex class of macromolecules. Nearly every cellular process during normal cell function, cell stress, cell death, and pathogenic infection are influenced by lipid biology.

The canonical bilayer structure of the plasma membrane stems from the self-assembly of amphiphilic phospholipids, an entropically driven process. The plasma membrane spans ~10 nm, and consists of an internal hydrophobic core flanked by an interfacial hydrophilic region¹ (**Figure 2.1 a**). Phospholipids consist of one or two hydrophobic acyl chains esterified to the sn-1 and sn-2 positions on the glycerol backbone. These acyl chains, typically 16 or 18 carbons with zero, one or two double bonds, point inwards when constituted into membranes. Esterified to the sn-3 position are characteristic hydrophilic headgroups, oriented towards the cytosolic milieu^{2,3} (**Figure 2.1 b**). The molecular architecture and biochemical properties of the acyl chain length, saturation, and headgroups gives rise to distinguishable properties dictating how each lipid behaves within membranes and how they interact with proteins.

A distinguishing feature of the plasma membrane is the asymmetric composition of the inner and outer leaflets (**Figure 2.1 c-d**). Phosphatidylcholine (PC) is the bulk constituent of the outer leaflet of the plasma membrane. PC contains a choline headgroup, which is neutral at a physiological pH. The outer leaflet is also enriched in sphingolipids, including sphingomyelin and ceramide. Phosphatidylethanolamine (PE) is the major lipid found within the inner leaflet of the plasma membrane. PE is a zwitterionic lipid containing an ethanolamine headgroup. Differences in the headgroup size and shape of PC and PE results in the self-assembly of these lipids into the curved bilayer configuration of the plasma membrane.

Lastly, while the bulk density of the plasma membrane is comprised of zwitterionic and neutral lipids, significant negative charge density is a distinguishing feature of the plasma membrane inner leaflet. The preferential partitioning of anionic within the inner leaflet provides a

negatively charged surface where anionic lipids serve as specialized recruitment factors for peripheral protein binding, protein activation and signaling cascades (**Figure 2.1 d**). These defining properties of the plasma membrane are fundamental to not only to cellular processes, but also disease states.

Due to advancements in mass spectrometry techniques, or lipidomics, more than 10,000 lipid species have been identified^{3,4}. The wide range of lipid molecules gives rise to differential compositions and concentrations in varying tissues, cells, and organelles with innumerable functional consequences. Although an expansive supply of lipids exists within eukaryotic cells, they can be categorized into three major classes: glycerophospholipids, sphingolipids, and sterols. The focus of this thesis will be phospholipids (and to a lesser extent cholesterol), and how their biochemistry and function is hijacked during infection and assembly of RNA viruses.

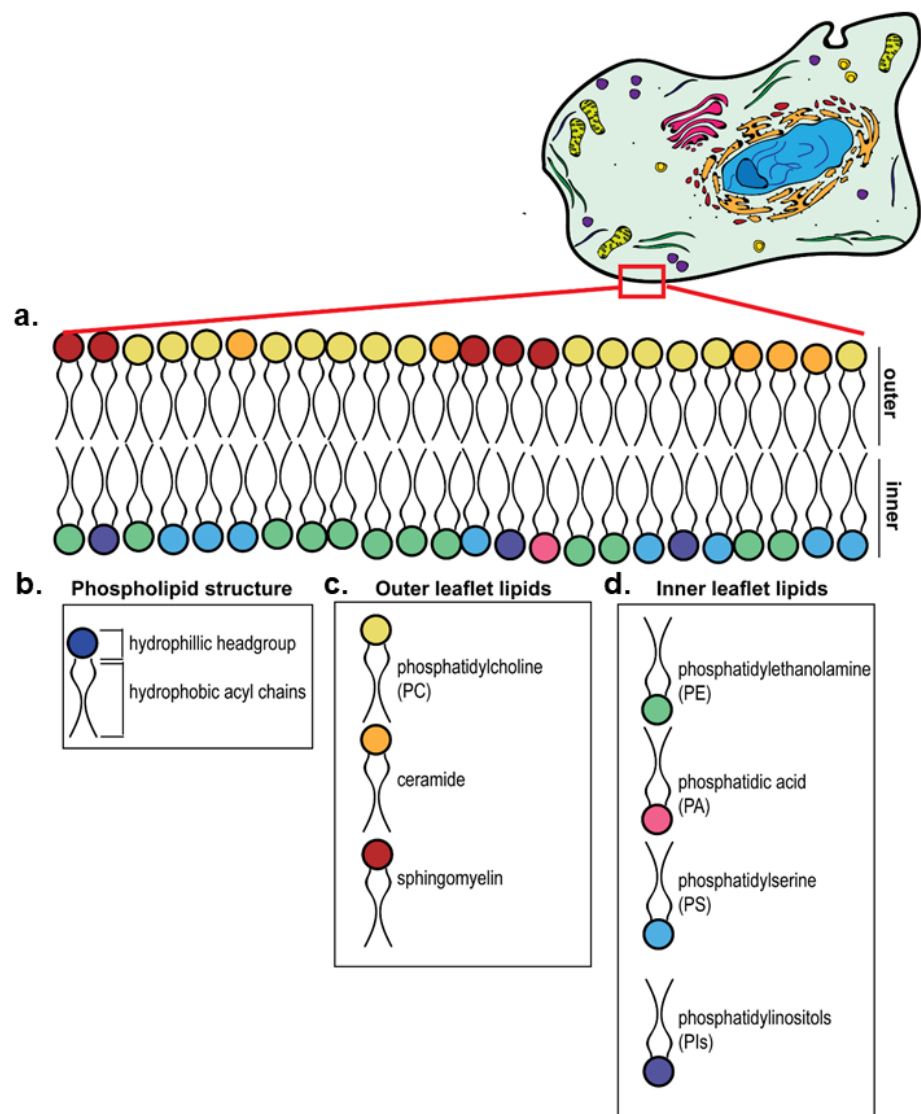


Figure 2.1. A roadmap to the plasma membrane and the lipids that comprise it. (a) Cartoon of the plasma membrane, which serves as a physical barrier protecting the intracellular space from the extracellular space and is composed of a lipid bilayer with a hydrophobic core and interfacial hydrophilic region. (b) The general structure of a phospholipid, which contains a hydrophilic headgroup and hydrophobic acyl chains esterified to a glycerol backbone. (c) The main phospholipids that comprise the outer leaflet of the plasma membrane include phosphatidylcholine, ceramide and sphingomyelin. (d) The main phospholipids that comprise the inner leaflet of the plasma membrane include phosphatidylethanolamine and the anionic phospholipids: phosphatidic acid, phosphatidylserine, and phosphatidylinositols.

2.1.1 Viruses and the plasma membrane

Whether enveloped or non-enveloped, viruses are obligate intracellular parasites that utilize lipids and membranes for every aspect of their life cycle. Although a bona fide role for lipids and lipid signaling in various diseases has gained momentum, information regarding their mechanistic roles in (-) sense RNA viruses is scarce. Lipid biology has been examined in cancer biology (reviewed in⁵), (+) sense RNA viruses such as *flaviviruses* (reviewed in⁶⁻⁸), and the retrovirus HIV⁹. Within the scope of (+) sense RNA viruses, most of the focus resides in viral replication compartments, lipoproteins and lipid droplets, membrane contact sites, lipid transfer proteins, and the upregulation of phospholipid synthesis.

Positive sense RNA viruses are known to divert host lipids to construct unique viral replication compartments, which are deformations of the plasma membrane associated with viral replication⁷. These membrane-associated replication complexes are not observed in (-) sense RNA viruses, which replicate in perinuclear inclusions within the cytoplasm or within the nucleus itself. Furthermore, lipidomic analysis of (+) sense RNA viruses have highlighted that certain lipids are upregulated during lipid infection (reviewed in¹⁰); however, a detailed investigation into the lipidome of (-) sense RNA viruses or their effect of lipid metabolism is lacking.

Mononegavirales are (-) sense RNA viruses, encapsulated by a lipid envelope they acquire during budding¹¹. This chapter aims at illuminating the current understanding of (-) sense RNA virus budding processes, with a detailed focus on interactions between Mononegavirales matrix proteins with plasma membrane lipids. Furthermore, this chapter will specifically focus on critical viral genera such as *morbillivirus* (MeV), *henipavirus* (NiV), and *filoviruses* (EBOV and MARV).

EBOV, MARV, NiV and MeV bud from the plasma membrane where their respective matrix proteins assemble and direct the formation of the budding viral particle. Remarkably, when independently expressed in mammalian cells, MeV-M, NiV-M, eVP40, and mVP40 all lead to the production of viral like particles (VLPs), nearly identical to infectious virions. While this phenomenon has been rigorously documented, a detailed understanding of the process is lacking. Currently, there are no FDA approved therapeutics to target these *filoviruses* or *paramyxovirus*. Although a largely underexplored avenue, a therapeutic to inhibit viral budding may be a platform for slowing down viral spread and allowing the immune system to mount a measurable response. A comprehensive overview of their assembly mechanisms will provide detailed analysis of how these viruses assemble and identify shared aspects across viral families. Unearthing common virus-

lipid mechanisms across viral families is a compelling new strategy for the development of pan-viral therapeutics.

2.2 Anionic Lipids: Key players in membrane function & viral infection

The inner leaflet of the plasma membrane contains a high concentration of anionic lipids, which contribute to a significantly negatively charged surface at the interface of the plasma membrane and intracellular space. Predictably, a wide range of functions, including membrane protein regulation, signal transduction, membrane remodeling events, and protein oligomerization are influenced by the interplay of lipids and proteins at the inner leaflet-cytosol interface^{3,12}.

There are three major anionic lipids found within the inner leaflet, phosphatidylserine (PS), phosphatidylinositols (PIPs), and phosphatidic acid (PA). Importantly, each of these lipids regulate not only cellular processes but have been implicated in nearly every stage of the viral life cycle.

2.2.1 Phosphatidylserine

PS is the most abundant anionic lipid within the inner leaflet, constituting up to 30 mol %⁴. With a phosphoserine headgroup esterified to the glycerol backbone, PS contains a net negative charge (-1) at physiological pH. Mediated by non-specific electrostatics and/or the C2 lipid binding domain (LBD), PS is a central lipid in not only peripheral protein membrane recruitment, but also activation of peripheral proteins such as protein kinase c (PKC)¹³⁻¹⁵. Synthesized in the endoplasmic reticulum (ER), PS is transported to the plasma membrane through two main pathways: through the golgi apparatus or transported to the mitochondria where it is either metabolized to PE or transported to the plasma membrane^{3,14}. Two enzymes are responsible for PS production in mammalian cells from PC or PE, phosphatidylserine synthase-1 (PSS1) and phosphatidylserine synthase-2 (PSS2), respectively.

Although PS is a major contributor to cell biology and viral infection, there is a dearth of knowledge available to the transcriptional regulation of PS synthesis. Information regarding PS regulation has largely been limited to yeast and bacterial systems, and regulation in mammalian cells and viral infection remains yet to be established¹⁶⁻¹⁸.

An advancement to investigations of PS biochemistry came with the construction of genetically modified Chinese hamster ovary cells (CHO) line, PSA-3 cells. A mutation in the PSS1

gene renders PSA-3 cells incapable of synthesizing PS from PE. This genetic mutation results in up to a 50% reduction in PS concentration^{14,19}. Although PSA-3 cells are a promising tool to study viral infection in the context of PS levels, research has been limited to a small number of RNA viruses^{20,21} and future exploration is needed.

Lastly, an intimate relationship between PS and cholesterol has been reported. Cholesterol is the most abundant cellular lipid and a major contributor to membrane fluidity, which can be found at differing concentrations within the inner and outer leaflet of the plasma membrane²². Like PS, cholesterol is concentrated within the inner leaflet of the plasma membrane where in unison the two lipids affect a wide range of structural and biochemical processes central to cell and viral biology⁴. Together, PS and cholesterol have been implicated in caveolae assembly (membrane invaginations)²³, regulation of signaling cascades²⁴, and providing platforms for virion assembly²⁵. While cholesterol is found in both the outer and inner leaflet, a recent report revealed that inner leaflet PS concentration is critical to maintaining cholesterol localization within the inner leaflet²⁶. Upon extraction of membrane cholesterol with methyl- β -cyclodextrin (MBCD) the PS biosensor LactC2 was displaced from the plasma membrane and redistributed to internal membranes^{23,27}, which indicates that upon cholesterol removal from the plasma membrane, PS levels within the plasma membrane are concomitantly reduced.

Advances in super-resolution microscopy, RNA interference, and lipidomics provide the framework for unraveling the molecular details between PS and viral life cycles. As PS is the most abundant anionic lipid within the plasma membrane and is utilized by diverse viruses, resolving its role in viral life cycle is an important step to understanding how to slow down viral replication and spread. Moreover, the interconnected relationship between PS and other membrane lipids and membrane structures suggest targeting PS levels may be a multifaceted anti-viral approach.

2.2.2 Phosphatidylinositols

PIPs are a class of lipids that comprise a small fraction of total lipids ($\sim 2\text{-}9\%$)³ but have wide-reaching cellular functions. Within the context of normal cell function, PIPs are essential signaling molecules responsible for the activation of GTPases for cytoskeletal remodeling and vesicular transport, ultimately impacting a myriad of cellular processes²⁸. Esterified to the sn-3 position of the glycerol backbone is an inositol headgroup. Regulated by 19 kinases and 28 phosphatases (reviewed in^{3,29}) the six carbon inositol headgroup can be phosphorylated at the D3,

D4, and D5 positions (**Figure 2.2 a**). Consequently, seven unique species of either mono, di, or tri phosphorylated PIPs exist with a negative charge of -2 to -4. While there are seven unique PIP species, this review will focus on those relevant to (-) sense RNA viruses (**Figure 2.2 b-d**).

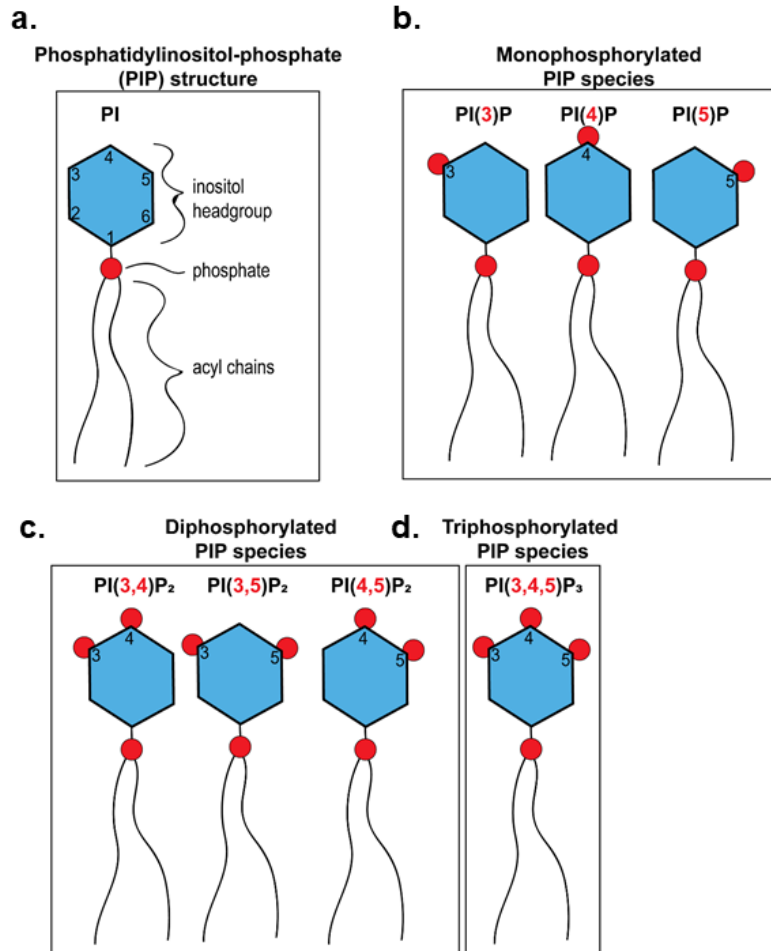


Figure 2.2. Overview of different phosphatidylinositol species. (a) General structure of phosphatidylinositol structure with a inositol ring and phosphate conjugated to the acyl chains via the glycerol backbone. The phosphatidylinositols can be phosphorylated at the D3, D4, or D5 positions generating seven unique species. (b) The three mono-phosphorylated phosphatidylinositols. (c) The three di-phosphorylated phosphatidylinositols. (d) The one tri-phosphorylated phosphatidylinositol. PIP: phosphatidylinositol phosphate.

Each unique PIP is differentially located throughout the cell, contributing to organelle identity. PI(3)P, PI(3,5)P₂, PI(4)P, PI(4,5)P₂ are enriched within the early endosomes, late endosomes, ER/Golgi and plasma membrane, respectively²⁸. A signature role for PI(5)P and its cellular footprint is still under debate and consequently its role in (-) sense RNA viruses has not been probed.

PI(3)P, concentrated within the endocytic pathway, is an important lipid component which actively participates in dynamic membrane events and intracellular trafficking. Although numerous DNA viruses (African swine fever virus) and (+) sense RNA viruses (e.g. tombusviruses³⁰ and herpesviruses³¹) are reported to utilize PI(3)P within their replication organelles and

throughout their life cycle, a role for PI(3)P has not been established in (-) sense RNA viruses.

PI(4)P is primarily concentrated within the ER and golgi apparatus with an additional PI(4)P pool residing within the plasma membrane serving as the precursor for PI(4,5)P₂ generation³². PI(4)P is synthesized from PI by the enzyme PI(4)-kinase- α (PI4K α) and PI(4)-

kinase- β (PI4K β). Considerable evidence is available stipulating a role for PI4K α and PI(4)P in (+) sense RNA viruses (e.g. picornaviruses³³ and hepatitis C virus). Currently, a direct role for PI(4)P in (-) sense RNA viruses has not been elucidated.

PI(3,5)P₂ is found abundantly within the late endocytic compartments where it has distinctive roles in actin regulated vesicular transport³⁴. Importantly, PI(3,5)P₂ has been implicated in EBOV entry, where it is purported to be required for efficient delivery of the glycoprotein (GP) to Niemann pick-C1 (NPC-1) within early endosomes³⁵.

The only tri-phosphorylated PIP species is PI(3,4,5)P₃ (PIP₃), which is primarily found at low levels within the plasma membrane. Although PIP₃ levels in quiescent cells are generally low, enrichment of membranes with PIP₃ has substantial implications within the cell. Numerous peripheral proteins are recruited to PIP₃ through pleckstrin homology domains (PH), stimulating diverse signaling pathways (including actin polymerization)³⁶. The activation of PI3-kinase (PI3K) to make PIP₃ has been connected to influenza A virus replication. Moreover the non-structural protein 1 of influenza virus A has been reported to directly bind to the regulatory subunit of PI3K³⁷.

Although several lipids have been implicated in entry, transport, and replication of viruses, the major player in viral budding is PI(4,5)P₂. PI(4,5)P₂ is the signature and most abundant PIP within the plasma membrane. One of the most established signaling cascades relevant to PI(4,5)P₂ metabolism is the inositol triphosphate (IP₃) and diacylglycerol (DAG) cascade. The membrane associated lipid enzyme phospholipase C (PLC) hydrolyzes PI(4,5)P₂ to generate IP₃ and DAG. The polar properties of IP₃ permit its translocation to the ER where it stimulates an increase in cytosolic Ca²⁺. Conversely, the nonpolar nature of DAG keeps it retained within the plasma membrane where it propagates the cascade by activating PKC³.

While signaling properties are one facet of the cellular implications of PI(4,5)P₂, PI(4,5)P₂ is also a key participant in a myriad of aspects central to viral budding. PI(4,5)P₂ has been identified as a key factor required for HIV-1 assembly, as well as EBOV and MARV assembly by directly associating with viral proteins as well as regulating cellular proteins and pathways active during viral budding. PI(4,5)P₂ has also been implicated in clathrin-mediated endocytosis for viral entry^{38,39}. Investigations using an inducible system and expression of a catalytically inactive PI5-kinase (PI5K) for cellular PI(4,5)P₂ depletion showed that PI(4,5)P₂ and dynamin (a PI(4,5)P₂ effector protein involved in clathrin-mediated endocytosis) were significant components to vesicular stomatitis virus (VSV) cellular entry⁴⁰.

2.2.3 Phosphatidic acid

Lastly, PA represents the smallest fraction of anionic lipids within the inner leaflet, constituting ~1 mol% of total lipids. Structurally, PA is the smallest and simplest of all phospholipids. The phosphoric acid headgroup of PA carries a -1 to -2 net charge at physiological pH⁴¹ and is important in recruiting cytosolic proteins^{3,42}, such as Dishevelled, a downstream component of the Wnt signaling pathway⁴³. Protein interactions with PA are thought to be mediated primarily by electrostatics as a canonical LBD targeted to PA has not been identified.

The small phosphoric headgroup gives PA its distinctive conical shape. The inverted conical shape favors the generation of negative curvature (equivalent to a virus budding out of the cell), posturing PA as a central lipid component of membrane fission and fusion events. Beyond membrane curvature, PA has astonishing implications in membrane biology, regulation of protein activity, and direct signaling roles. The extensive biological functions of PA dictate its tight regulation and maintenance of low concentrations by cellular phosphatases⁴¹.

PA is transiently produced by the hydrolysis of PC by phospholipase D (PLD)^{3,44,45}. Interestingly in the context of viral assembly, PI(4,5)P₂ is a cofactor for PLD membrane recruitment and enzymatic activity. Furthermore, PA and PLD have been implicated in the replication of a plant virus⁴⁶, the entry of influenza virus⁴⁷, a multitude of (+) sense RNA viruses (reviewed in⁸), and retroviruses (reviewed in⁴⁸), however investigations into their role in (-) sense RNA viruses has been limited to influenza virus. Through the development of chemical inhibitors of PLD enzymes and RNAi, influenza viral entry⁴⁷, transport and replication⁴⁹ have all been linked to an increase in PLD activity⁵⁰.

2.3 Lipid transport & implications for viral infection

The final stages in most lipid (e.g. PC, PE, PS, PIPs, cholesterol) biosynthesis pathways occurs at the ER; however, different organelles have varying lipid compositions and membrane properties. Generally, lipids are not water soluble and therefore cannot simply diffuse throughout the cytosol to reach their organelle destinations. Taken together, one can envision that lipid transport within the cell is a complicated process. Currently, lipid transport within the cell is broken down into three routes: utilization of soluble transport proteins, vesicular transport, and close membrane contact sites (MCS)⁴.

2.3.1 Lipid transport proteins

Lipid transport proteins (LTP) primarily function to move lipids between adjacent membranes at MCS. The best characterized MCS exist between the ER and PM and postulate the two membranes are separated by $<15\text{ nm}^3$. LTPs predominantly adopt a conserved β -barrel protein fold structure with a hydrophobic pocket capable of transporting one lipid molecule at a time. Several LTPs have been identified for the transport and counter transport of PS, PIPs, and cholesterol, including oxysterol-binding protein-related proteins 5 and 8 (ORP5 and ORP8) and transmembrane protein 24^{3,51,52}.

MCS and LTPs have been widely investigated in several RNA viruses. Specifically, the construction of membranous replication organelles at the plasma membrane and mitochondrial fragmentation are mechanisms where (+) sense RNA viruses (e.g. *picornaviruses*⁵³ and HCV⁵⁴) pilfer LTP functions. However, it is currently not known how (-) sense RNA viruses interact with LTPs or how viral infection alters LTP localization, activity, or expression.

2.3.2 ATP-dependent lipid transport

Not only is lipid transport throughout the cell restricted, lipid movement within membranes is as well. Within membranes, lipids can diffuse and rotate laterally. However, the steep energetic cost of their polar headgroup traversing the hydrophobic core prohibits their ability to freely switch bilayer leaflets^{3,55–57}. This observation is supported by the estimation that lipids can diffuse 10^9 faster laterally than they can switch leaflets of the bilayer^{3,57,58}. Limitations on lipid transport is overcome by the presence of ATP-dependent enzymes known as lipid translocases (i.e. flippases and floppases). There are 14 known flippases, responsible for flipping lipids to the inner leaflet, as well as floppases responsible for flopping lipids to the outer leaflet³, yet no direct relationship between lipid translocases and (-) sense RNA viruses has been established.

2.3.2.1 Lipid scramblases

Lipid scramblases are another type of ATP-dependent lipid transport enzymes found in membranous organelles, such as the ER and plasma membrane. Through either a Ca^{2+} dependent or independent manner, scramblases execute bi-directional lipid transport which is indispensable

to maintaining both the membrane symmetry and asymmetry found within the ER and plasma membrane, respectively^{3,59}.

Scramblase activity has not been reported for every lipid; however, some of the most well-defined scramblases are plasma membrane PS scramblases. Under normal conditions plasma membrane scramblases work to maintain PS within the inner leaflet. The maintenance of this PS asymmetry is crucial to sustaining normal cell function. However, certain cellular processes require the exposure of PS to the outer leaflet such as the blood coagulation pathway^{3,60,61} and apoptosis^{3,62,63}.

During the coagulation cascade the exposure of PS to the outer leaflet of platelets is mediated by the inhibition of a cellular translocase and the Ca^{2+} -dependent activation of the PS scramblase, transmembrane protein 16F (TMEM16F)^{3,64-66}. PS exposure propagates the cascade by promoting the assembly of various proteins central to the coagulation pathway. In fact, failure to expose PS on platelets due to mutations in TMEM16F lead to a mild bleeding condition, Scott syndrome^{3,67}.

Apoptosis, present in all multicellular organisms, is a rapid and efficient cellular response intended to remove dead or harmful cells and ensure healthy development and function. The apoptotic process is fundamental to organism homeostasis, and aberrant clearing of harmful cells can lead to inflammatory and autoimmune disorders.

Following recognition of a surface-exposed “eat-me” signals, phagocytes will engulf target cells in an actin-dependent manner and traffic the material throughout the cell for degradation, a process similar to macropinocytosis. The most well-known “eat-me” signal is the externalization of PS to the outer leaflet of the plasma membrane where it is recognized by surface receptors on phagocytes as well as several other cell types.

The externalization of PS occurs during early stages of apoptosis and is accompanied by a more than 2-fold increase in PS synthesis^{68,69}. In the apoptotic state the Ca^{2+} independent PS scramblase, XK family protein 8 (Xkr8) is activated by cleaved caspases and signals the host immune system and macrophages to clear the dying cell^{3,70}. The role of Xkr8 in clearing apoptotic cells was substantiated by the finding that Xkr8 knockdown in mammalian cells resulted in inefficient clearing of apoptotic cells^{3,70}.

2.3.2.2 Scramblases in viral infection: Apoptotic mimicry

Extensive experimental evidence has confirmed that viral pathogens mimic apoptotic “eat-me” signals as a clever mechanism to enhance cellular entry in a process known as apoptotic mimicry. The exploitation of apoptosis has been experimentally substantiated for a diverse set of non-enveloped and lipid enveloped viruses, including (+) sense RNA enveloped viruses (*alphaviridae*, *flaviviridae*) and (-) sense RNA enveloped viruses (*arenaviruses*, and the Mononegavirales *Filoviridae* and *rabdoviridae*). There are currently no reports of apoptotic mimicry strategies employed by members of the *Paramyxoviridae* family; however, it is important to note that during entry of *paramyxoviruses* the viral envelope directly fuses with the host cell therefore no engulfment mechanism occurs.

Filoviruses are one family of Mononegavirales known to exploit apoptotic mimicry to gain entry into host cells. During EBOV entry, host cell T-cell immunoglobulin and mucin domain protein 1 (TIM-1) receptors recognize viral GP residing in the outer viral envelope. However, in a dual-factor recognition process, TIM-1 will also recognize PS within the viral envelope as a means to enhance entry⁷¹. During infection, eVP40 is the main viral component postulated to initiate exposure of PS to the outer leaflet during budding²¹. However, recent evidence reports that GP and eVP40 accomplish this mechanism through activation of Xkr8 activation⁷². Future investigations will need to be performed to distill a thorough understanding of the process.

2.4 Viral budding at the plasma membrane

Viral budding by lipid enveloped viruses is an exemplary illustration of how viruses hijack their host to support their own life. This arduous task is predominately facilitated by the multifunctional properties of their matrix proteins. Moreover, the pleomorphic structure of lipid enveloped viruses highlights the high conformational plasticity and multifunctionality of matrix proteins.

Matrix proteins transform into different higher ordered structures to execute necessary tasks. As the central organizer of viral budding, matrix proteins assemble into an extensive scaffold underneath the plasma membrane. This scaffold serves as a bridge between the viral envelope (derived from the plasma membrane) and the internal nucleocapsid containing genome. Moreover, matrix proteins are responsible for actively recruiting viral components to viral budding sites^{73–76}.

2.5 Structural basis of matrix protein function

Matrix proteins across viral families share significant structural and functional properties, even in the absence of sequence homology. Therefore, understanding the structural and functional roles of matrix proteins is a compelling strategy to developing a pan-viral therapeutic. The first step in understanding this process is a comprehensive understanding of the matrix protein structures and the lipids they interact with during viral assembly.

In particular, the VP40 matrix protein of *filoviruses* and the M matrix protein of *paramyxoviruses* share numerous conserved structural features. Currently, crystal structures are available for eVP40, mVP40, Hendra virus matrix protein (HeV-M), Newcastle disease virus (NDV-M). Each of these matrix proteins is comprised of two distinct N-terminal and C-terminal domains connected by a 6-16 amino acid linker region^{77,78}. Additionally, eVP40, mVP40, HeV-M and NDV-M exist as dimers in solution, a process mediated by hydrophobic interactions between α -helices within the N-terminal domain. Membrane targeting is facilitated by highly conserved basic patches located within the C-terminal domain⁷⁷⁻⁸¹. This highly basic region has been identified in VSV matrix protein (VSV-M)⁸², Hendra virus matrix protein (HeV-M)⁸¹, Newcastle disease virus matrix protein (NDV-M)⁷⁹, eVP40^{77,80}, mVP40⁷⁸, MeV-M, and NiV-M (manuscript in preparation).

Oligomerization of the matrix proteins is an additional conserved structural and functional property of matrix proteins, required to form the viral matrix which underlies the viral envelope. Matrix proteins can self-assemble into extensive higher-order structures *in vitro*. Moreover, incubation with lipids is known to promote this structural re-organization. Differences in oligomerization mechanisms have been reported, where *filovirus* matrix proteins oligomerize through a tail-tail mechanism while *paramyxovirus* matrix proteins assemble through a head-tail fashion.

A nexus between the structural heterogeneity of EBOV, MARV, NiV, and MeV viral structure lies in the capacity of their respective matrix proteins to differentially associate with membranes and assemble into unique yet similar viral scaffolds. Appreciation of the structural and biochemical differences in each of these matrix proteins affords a clearer interpretation of how each protein independently imposes viral stability and structure by driving viral budding.

2.5.1 Filovirus matrix proteins

eVP40 and mVP40 are the sole two *filovirus* matrix proteins which share striking similarity in both sequence, structure, and function (**Figure 2.3 a-b**). Overall the two proteins are 39% identical in sequence and form a butterfly shaped dimeric protomer which associates with the cellular membranes to drive viral budding^{78,80}. Their N-terminal domains are 42% identical in sequence with similar structural folds. The N-terminal domains of each protein drive oligomerization, and while numerous oligomeric states have been identified for eVP40^{83–88}, far less is known regarding mVP40 oligomerization^{84,89}. Moreover, greater diversity is present in their

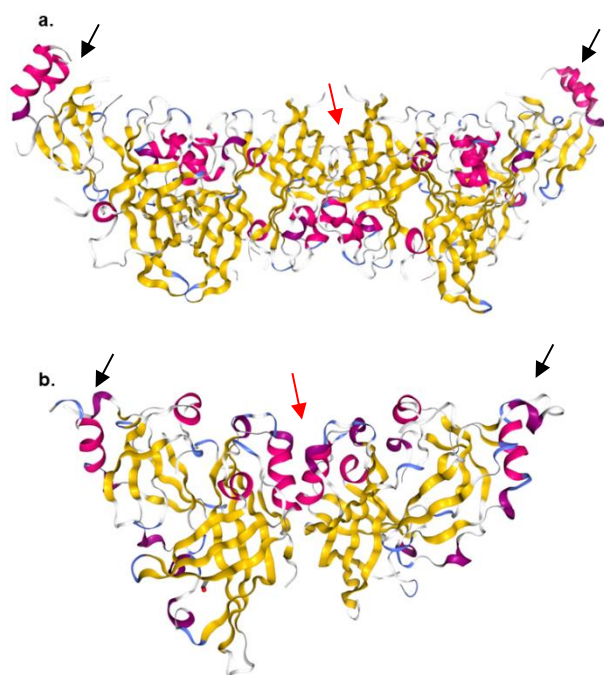


Figure 2.3. Ribbon diagrams of *filovirus* matrix proteins. (a) eVP40 dimeric structure and (b) mVP40 dimeric structure with red arrows indicating dimeric interface and black arrows indicating membrane binding interface. eVP40 PDB: 4LDB and mVP40 PDB: 5B0V.

distinct EBOV species^{80,84,88,92}.

Connected to the N-terminal domain by a six amino acid linker is the C-terminal domain⁸⁰. The C-terminal domain consists of two β -sheets connected to two α -helices by a disordered loop. Within the C-terminal domain is a surface exposed highly conserved basic patch consisting of six lysine residues, two of which (K224 and K225) reside within a flexible ten residue loop that

C-terminal domains which share only 16% identity. As the C-terminal domains are the putative membrane binding domains, differences have arose as to how each protein interacts with lipids throughout the cell and at the plasma membrane^{21,90,91}.

2.5.1.1 Structural overview of eVP40

Long believed to exist as a monomer⁷⁷, in 2015 structural and biochemical advancements led to the discovery of the dimeric eVP40 crystal structure⁸⁰ (**Figure 2.3 a**). The ~74 kDa eVP40 dimer crystal structure (3.1 Å) revealed an N-terminal domain containing a β -barrel sandwich and 4 small α -helices. The N-terminal includes two α -helices responsible for the hydrophobic dimer interface, conserved across antigenically

projects away from the C-terminal domain⁸⁰. The positive surface charge within the C-terminal domain is required for eVP40 membrane localization, as C-terminal truncations diminished binding to cellular membranes and abrogated budding⁹³.

In addition to the landmark discovery of the dimeric eVP40 structure, Bornholdt et al. (2015) discovered a hexameric eVP40 crystal structure postulated to be the building block of matrix assembly. Rearrangement of dimeric VP40 to the hexameric structure occurs via tail-tail interactions of C-terminal domains⁸⁰. This rearrangement requires the N-terminal to disengage from the C-terminal domain, a process postulated to be directed by salt-bridge interactions^{83,86,94}.

Significant mutational analyses have been performed since the discovery of the eVP40 crystal structure, identifying numerous key residues in dimerization (L117, T112), RNA binding (R134), oligomerization (M241, W95), and membrane binding (K224, K225, K274, K275)^{80,95,96}.

2.5.1.2 Structural overview of mVP40

mVP40 is a 303 amino acid protein composed of a distinct N-terminal domain connected to the C-terminal domain by a nine-residue linker. In 2016, the crystal structure of mVP40 (2.8 Å) was elucidated and characterized by size exclusion chromatography-multi angle light scattering to be a 63 kDa protomer (**Figure 2.3 b**). With comparable folds to the eVP40 dimer, the N-terminal domain of mVP40 consists of seven β -strands, two α -helices, three 3_{10} helices. Two α -helices within the N-terminal domain comprise a dimeric interface fortified by hydrophobic interactions between 13 amino acids⁷⁸, which resembles the eVP40 dimer interface. Dimerization of mVP40⁷⁸ and eVP40⁸⁰ is critical for association and/or trafficking to the plasma membrane, as point mutants of both proteins blocking dimerization fail to associate to the plasma membrane.

Attached to the N-terminal domain by a nine-residue linker are the six β -strands and six α -helices of the C-terminal domain. Similar to eVP40, the C-terminal domain contains a high density of surface exposed positively charged amino acids within two basic loops that extend away from the center of the protein. While both eVP40 and mVP40 have similar C-terminal basic patches, the architecture of these membrane targeting domains is quite different. The architecture of mVP40 basic patch differs from that of eVP40 in that it is flatter, more extended and more loosely folded⁷⁸. These differences may account, at least partially, for the observed lipid specificity and membrane targeting mechanisms employed by the two related proteins.

Although robust oligomerization of mVP40 is required for virion assembly and this process is readily observed *in vitro* and in cells⁸⁴, no distinct higher ordered oligomeric state of mVP40 has been resolved as of 2019 (aside from an octameric ring⁸⁴). Consequently, models of mVP40 oligomerization have been inferred from eVP40 assembly oligomerization. Two residues critical to eVP40 oligomerization are conserved in mVP40, W95 and E160 in eVP40⁸⁰ and W83 and N148 in mVP40⁷⁸. Disengagement of the N-terminal domain from the C-terminal domain during rearrangement exposes these two residues in eVP40. In fact, point mutations at W83 and N148 in mVP40 abrogates mVP40 plasma membrane binding and VLP egress^{78,89}. Although the dimer crystal structure opened the door to numerous structure-function investigations of mVP40, continued efforts investigating mVP40 assembly mechanisms are needed.

2.5.2 Paramyxovirus matrix proteins

While the *paramyxovirus* glycoproteins display significant structural diversity, a high degree of similarity is observed within the matrix protein structure⁹⁷. The structural conservation across *paramyxovirus* matrix proteins permit investigations into their membrane binding in the absence of available crystal structures of matrix proteins from each virus. Prior to the groundbreaking discovery of the MeV-M and NiV-M crystal structures by the Sapphire group in 2019, studies on the membrane binding properties of MeV-M and NiV-M were inferred from related crystal structures, such as HeV-M (**Figure 2.4 a**) and NDV-M (**Figure 2.4 b**).

2.5.2.1 Structural overview of HeV-M

HeV-M and NiV-M are emerging enveloped (-) sense RNA viruses, belonging to the *henipavirus* genus. The crystal structure of HeV-M was recently elucidated (2.5 Å), and shares 90% sequence identity with NiV-M. Like many matrix proteins, HeV-M exists as a dimer in solution with two structurally similar domains aligning perpendicular to each other and stabilized through hydrophobic interactions (**Figure 2.4 a**). The resulting 7 nm diameter diamond shape dimer consists of an N-terminal domain connected to the C-terminus by a disordered 11-amino acid linker⁸¹.

Like eVP40 and mVP40, oligomerization of HeV-M is facilitated through the N-terminal domains⁸¹ and independent expression of HeV-M results in VLP production⁹⁸. Within HeV-M,

oligomerization is proposed to occur via a head-tail assembly model facilitated by electrostatic interactions between $\alpha 1$ helix and $\alpha 2$ helix (both within N-terminal domain). Moreover, an arginine (Arg 57) and glutamate (Glu 108) are the postulated residues involved in this process. Importantly, these residues are conserved across *paramyxovirus* matrix proteins. Lastly, as previously discussed (in Chapter 1.3.3), cytoplasmic-nuclear transport of paramyxoviruses is required for efficient viral release. Two putative nuclear export sequences have been identified within the $\alpha 2$ helix of HeV-M, which are buried within the dimeric unit⁸¹.

2.5.2.2 Structural overview of NDV-M

Belonging to the *avulavirus* genus, Newcastle disease virus is an avian paramyxovirus known to cause significant disease in birds^{79,99}. Analogous to other members of the *paramyxoviruses* family, transient NDV-M translocation into the nucleus is required for viral budding^{79,100,101}. The absence of a MeV-M crystal structure has required inferences regarding MeV-M function to be based on the NDV-M crystal structure (2.2Å resolution), which shares 20% sequence identity with MeV-M¹⁰².

NDV-M is a 364 amino acid protein that forms a dimer in solution (**Figure 2.4 b**). Within each monomer is a primarily α -helical N-terminal domain which facilitates dimerization through hydrophobic interactions between two opposing α -helices. The N-terminal domain is connected to the C-terminal domain by a 16 amino acid linker. A hydropathy plot of the NDV-M amino acid sequence indicates the protein is largely hydrophobic⁷⁹, an additional commonality of matrix proteins. Moreover, the surface of NDV-M has a significant number of exposed positive residues creating an extremely positive surface¹⁰².

The putative membrane binding interface of NDV-M is highly positively charged, determined from superimposing the crystal structure to the subunit density of the matrix layer within EM tomograms¹⁰². Within the

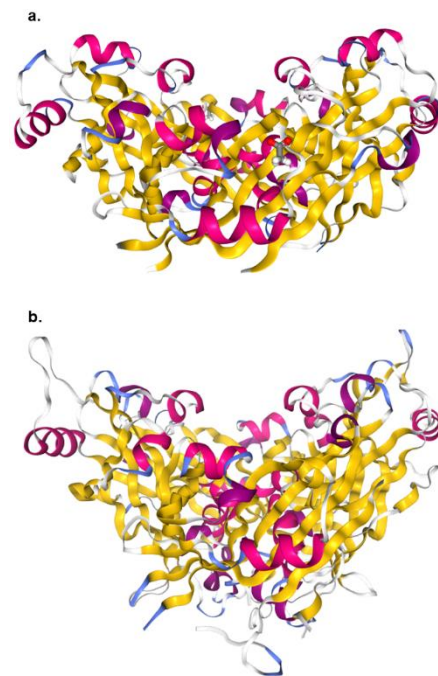


Figure 2.4. Ribbon diagrams of paramyxovirus matrix proteins. (a) HeV-M dimeric structure and (b) NDV-M dimeric structure. HeV-M PDB: 6BK6 and NDV-M PDB: 4G1G.

superimposition of the dimer to the tomogram matrix layer, two α -helical oligomerization contact sites were identified. Through analytical ultracentrifugation of NDV-M at pH 4 and pH 7, electrostatics were identified as the driving force for the self-assembly of NDV-M⁷⁹. Lastly, the NDV-M dimer array surface is highly curved, hypothesized to promote the necessary curvature for membrane bending during viral budding¹⁰².

2.6 Protein – lipid interactions

Within membranes lipids interact with a diverse range of integral and peripheral proteins. Designed to execute specialized functions at the plasma membrane and throughout the cell, protein-lipid interactions are highly dynamic processes under strict spatial and temporal regulation. These interactions are critical to regulate lipid concentration, membrane dynamics and cell structure with astonishing implications on cytoskeleton remodeling, signaling and cellular trafficking. Different modes of protein-lipid interactions are present within the cell, and the molecular basis of these interactions have direct implications on the biology they carry out^{22,29,33}.

The molecular architecture of lipids dictates how they interact with proteins in the formation of small and supramolecular complexes within the membrane and at the membrane-cytosol interface. Although there are generally two primary modes underlying protein-lipid interactions (electrostatics and hydrophobics), protein-lipid interactions are often multimodal as a strategy to strengthen the interaction¹⁰³. Moreover, the identification and characterization of specific LBDs in proteins play an essential role in protein trafficking to and interacting with cellular membranes¹⁰⁴.

2.6.1 Types of protein-lipid interactions

Electrostatic interactions based on charge complementarity between proteins and lipids drive the majority of peripheral protein-lipid interactions. The extent of exposed cationic amino acids within proteins are the primary determinant for the strength and duration of electrostatic interactions. These interactions can occur at a long range, where an intracellular cationic protein is attracted to the negative charge density within the inner leaflet of the plasma membrane. If the protein is not extensively positively charged, the resulting electrostatic interactions tend to be weak and transient. Alternatively, oligomerization of a slightly positively charged protein significantly

increases the positive charge density on the protein surface resulting an increase in electrostatic contacts between the protein and the membrane.

Hydrophobic interactions are ubiquitous between proteins and lipids. These interactions are mediated by structural elements like amphipathic helices, hydrocarbon modifications (e.g. prenyl, farnesyl), fatty acyl modification (e.g. myristate, palmitate) or unstructured hydrophobic regions of the peripheral protein that can partition into the membrane hydrocarbon core as a mechanism to anchor the protein to the membrane. Additionally, the insertion into the membrane is an alternative mechanisms by which cytosolic proteins increase their residence time at the plasma membrane¹⁰⁵. When both electrostatics and hydrophobic interactions are used in series with one another, the strength and duration of the interaction is greatly increased. For example, electrostatic interactions can guide the initial association of a protein with the lipid posturing the seamless positioning for a more stable hydrophobic interaction to occur¹⁰³.

Additionally, soluble peripheral proteins are actively recruited to the inner leaflet through the presence of LBDs¹⁰³. As cellular membranes contain > 1,000 different lipids species, LBDs are an effective tool utilized by proteins to accomplish the required specificity in tightly regulated protein-lipid processes¹⁰⁴. While nearly a dozen LBDs are known, the most well understood and pertinent to the field of viral budding are C1 (binds DAG), C2 (binds PS), and PH (binds PIP₃ and PI(4,5)P₂)^{103,104}.

Viral proteins are an elegant example of how viruses mimic cellular protein-lipid interactions to sustain disease. Moreover, like cellular proteins, viral matrix proteins have evolved to utilize numerous modes of protein-lipid interactions to assemble and bud from cells. Several tools are available to delineate the membrane binding properties of viral matrix proteins. Although a wealth of techniques are available, there is a paucity of information regarding viral matrix protein-lipid binding.

2.6.2 Tools to study protein-lipid interactions

Protein-lipid interactions are assessed through a myriad of cellular, biochemical, biophysical, and microscopy techniques. *In vitro* techniques are available to probe the affinity of protein-lipid interactions (liposome sedimentation assays)¹⁰⁶, the kinetics of binding interactions (surface plasmon resonance, SPR)¹⁰⁷, and direct visualization of dynamic lipid-protein interactions (fluorescence imaging of giant unilamellar vesicles (GUVs))¹⁰⁸. Fluorescence microscopy, raster

image correlation spectroscopy (RICS), and atomic force microscopy (AFM) are commonly used visualization techniques utilized to address the effects of protein-lipid binding on lipid domain formation and protein oligomerization. Additionally, structural insight into protein-lipid interactions has been made possible with x-ray crystallography and hydrogen-deuterium exchange mass spectroscopy (HDXMS)¹⁰⁹. Several cellular protein crystal structures in complex with a lipid partner have been resolved, such as TIM-1 and PS¹¹⁰, yet there are no available crystal structures of viral matrix proteins with lipids.

Biomimetic membranes are valuable tools to elucidate *in vitro* protein-lipid interactions and protein-protein interaction at the interface of the cytosol and plasma membrane. To study membrane remodeling events like vesiculation and tubulation, large biomimetic membranes (GUVs) are most commonly used. GUVs are large (10-100 μm) affording them significant curvature and plasticity.

2.7 Matrix protein – membrane interactions

Discovery of the lipid binding properties and lipid requirements for HIV-1 and influenza matrix protein assembly helped pave the way for efforts investigating how other dangerous viruses interact with the plasma membrane during viral exit. Both matrix proteins of HIV-1 (HIV-1 gag)^{98,111,112} and influenza (M1)^{113–115} have positively charged domains that interact differentially with the plasma membrane, with PI(4,5)P₂ and PS, respectively.

Positively charged membrane targeting surfaces are also present in *filovirus* and *paramyxovirus* matrix proteins. The interaction of *paramyxovirus* matrix proteins¹¹⁶, eVP40⁹³, and mVP40¹¹⁷ with membranes are extremely stable, indicated by the retention of each protein on membranes in high salt conditions. However, detailed analysis of these interactions are still not clear.

Concurrently with the discovery of the eVP40 and mVP40 crystal structure, research was underway to delineate their membrane targeting properties. Earlier studies identified that the C-terminal domain was required for targeting eVP40 and mVP40 to the membrane, and that the interaction was mediated by electrostatic^{78,88} and hydrophobic⁹³ interactions. However, a clear cognate lipid binding partner for membrane targeting or matrix self-assembly had not been identified.

Conversely, evidence describing the membrane binding properties of *paramyxoviruses* is extremely limited. Research on *paramyxovirus* matrix protein membrane interactions has focused on lipid rafts and the effect of protein structure on membrane binding and matrix assembly rather than direct protein-lipid interactions. Mutational analysis of HeV-M and NDV-M revealed a preponderance of positive surface charge and it is therefore hypothesized that electrostatics play a role in plasma membrane localization; however, no specific lipids have been identified.

2.7.1 Matrix protein lipid specificity

PS has a multifunctional role in EBOV budding, postured as a critical lipid for eVP40 membrane targeting, eVP40 assembly and VLP production. When monitored in the PSA-3 cells (PS deficient), eVP40 plasma membrane localization, oligomerization and VLP formation was nearly undetectable compared to the parental cell line. Moreover, PS feedback experiments restored eVP40 plasma membrane localization and VLP formation to near normal levels²¹. This was the first line of evidence that suggested PS was important for not only eVP40 plasma membrane but also the eVP40 assembly and production of VLPs. This interaction was corroborated by *in vitro* studies which reported an apparent affinity of eVP40 to PS containing vesicles similar to that of the high affinity PS probe, Lact-C2²¹. Lastly, PS has also been implicated in M1 membrane binding, oligomerization and budding¹¹³.

PI(4,5)P₂ is also central to eVP40 viral production. Liposome sedimentation assays highlight that eVP40 binds to large unilamellar vesicles (LUVs), and that eVP40 binding to membranes is strongest when PS and PI(4,5)P₂ are both present. Functionally, PI(4,5)P₂ purportedly plays a role in extensive oligomerization and egress of VLPs. Using a RICS method (Number & Brightness, N&B) on cells enzymatically depleted of PI(4,5)P₂, extensive oligomerization of EGFP-eVP40 was inhibited at the plasma membrane⁹¹. Moreover, scanning electron microscopy (SEM) of cells expressing eVP40 showed minimal VLP production in cells enzymatically depleted of PI(4,5)P₂ (compared to healthy cells⁹¹).

mVP40 also interacts with plasma membrane through electrostatic interactions between its highly basic C-terminal domain and anionic lipids. However, mVP40 does not appear to display lipid specificity and is hypothesized to interact with the membrane through a charge sensing mechanism⁹⁰. Charge sensing is a common mechanism used by peripheral proteins where the protein interacts non-specifically with the membrane solely based on electrostatics. Upon

neutralization of membrane charge with sphingosine¹⁵, mVP40 was significantly displaced from the plasma membrane of cells⁹⁰. Similar studies were performed with eVP40, however neutralization of membrane charge failed to displace eVP40 from the plasma membrane⁹¹, further corroborating the finding that eVP40 interacts with the membrane through stereospecific interactions with PS and PI(4,5)P₂ lipids.

2.7.2 Membrane penetration by matrix proteins

HIV-1 gag and eVP40 are two matrix proteins purported to partition within the membrane as a mechanism to enhance their association with the plasma membrane. HIV-1 gag inserts into the membrane via a myristolated glycine residue. SPR analysis of a myristolated gag and unmyristolated gag revealed that myristylation of HIV-1 gag increased the affinity of gag to acidic membranes by a factor of 10¹¹⁸.

Currently, there is no evidence that eVP40 or mVP40 are lipidated. However, evidence suggests these two related matrix proteins have differing capabilities to penetrate the plasma membrane. Though monolayer membrane penetration experiments, no membrane insertion was detected when mVP40 was incubated with an anionic plasma membrane monolayer⁹⁰. Analogous investigations showed significant membrane penetration by eVP40^{119,120}. A hydrophobic loop within the C-terminal domain of eVP40 was shown to mediate membrane penetration, and mutation of key residues within this loop abrogated eVP40 oligomerization and VLP egress in cells. A follow-up study utilized fluorescence quenching with a membrane comprised of brominated lipids and revealed eVP40 penetrates 8.1 Å into lipid bilayers¹¹⁹. Importantly, a plasma membrane like composition was required for eVP40 membrane penetration indicating this mechanism is limited to eVP40 interactions with the plasma membrane and not internal membranes¹²⁰. Taken together, these findings support the hypothesis that eVP40 membrane penetration within the plasma membrane is imperative to eVP40 budding¹²⁰.

Information on the insertion of other matrix proteins within the Mononegavirales order is scarce. X-ray crystallographic studies presented preliminary evidence that M1 of influenza A may insert into the membrane¹²¹. Investigators postulated M1 membrane insertion is mediated through amphipathic helices within its N-terminal domain¹²². Furthermore, the adsorption of M1 onto uncharged lipid monolayers¹²³ suggest it's interaction with the plasma membrane extends beyond charge specific interactions with anionic lipids, like PS. However, to date there is no direct

evidence supporting membrane penetration of any *paramyxovirus* matrix protein. It should be noted that detailed investigations into membrane penetration of *paramyxovirus* matrix proteins have yet to be performed.

2.7.3 Lipid induced matrix protein assembly

The structural plasticity of matrix proteins was first documented in 1982 when it was observed that the matrix protein of Sendai virus (SeV-M) self-assembled into ordered tubes and sheets *in vitro*¹²⁴. EM, AFM, and RICS has shed light on the structural plasticity of matrix proteins.

The *in vitro* self-assembly of matrix proteins upon association with lipids has also been widely reported across the Mononegavirales order. In the presence of PC, the *Pneumoviridae* human metapneumovirus calcium binding matrix protein assembles into flexible tubes¹²⁵. AFM was employed to investigate the assembly of the *paramyxovirus* NDV-M. Upon incubation with a negatively charged mica surface (representative of the negative charge of the plasma membrane inner leaflet), NDV-M assembled into an extensive scaffold⁷⁹.

Similar observations have been reported outside of the Mononegavirales order using confocal microscopy and RICS analysis. The interaction of M1 of influenza virus with anionic lipids has been long established⁷⁶. Recent investigations have aimed to delineate which lipids M1 interacts with and which M1 processes are influenced by lipid binding^{113,126}. Fluorescence scanning microscopy experiments were performed utilizing fluorescently-labelled M1 proteins and supported lipid bilayers (SLBs) containing PS, which confirmed that M1-membrane binding is mediated by PS¹²⁶. To understand the molecular implications of this interaction, RICS analysis was used to assess the oligomerization of M1 in the presence of PS containing SLBs. RICS analysis revealed that M1 multimerized extensively upon incubation with SLBs containing 40% PS¹²⁶, which is analogous to the observed self-assembly of other matrix proteins from EM and AFM experiments.

2.7.4 Matrix protein induced membrane remodeling

During membrane remodeling membrane shape and curvature are altered as the membrane yields new shapes, such as tubes and vesicles (**Figure 2.5 a-b**). This is observed throughout viral budding, as negative curvature (**Figure 2.5 b**) occurs upon bending of the membrane as a new

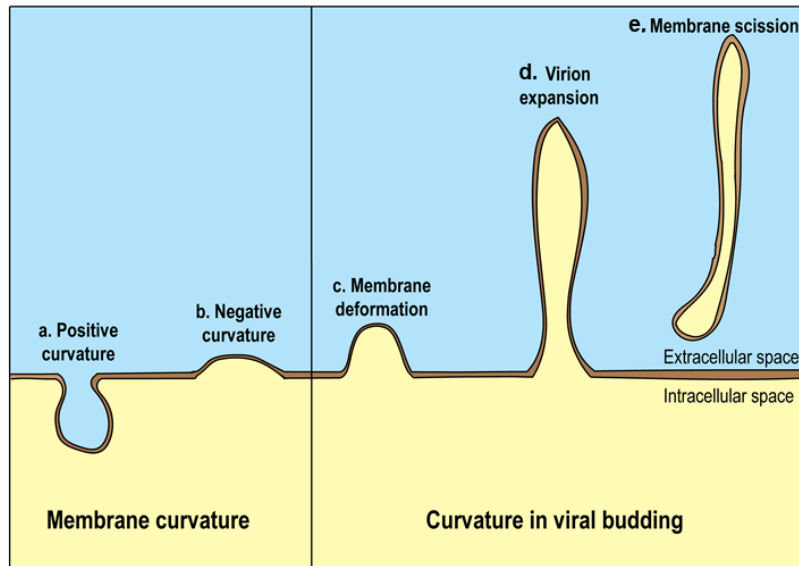


Figure 2.5. Membrane curvature at the plasma membrane and during viral budding. (a) Positive and (b) Negative curvature are seen throughout cellular organelles and within the plasma membrane during endocytosis and exocytosis-type events. (c-d) Steps of viral budding where negative curvature is generated during (c) early stages of membrane deformation, (d) growth of the progeny virion and (e) scission of new virion into extracellular space.

virion is pushed out from the plasma membrane into the extracellular space during viral growth and eventually membrane scission occurs to release the new virion (**Figure 2.5 c-e**). Compelling evidence to support a role for matrix proteins facilitating membrane remodeling during viral budding is the inherent capacity of matrix proteins to deform membranes in the absence of other viral components, *in vitro* and in cells^{127–130}.

Early evidence of membrane deformation induced by a matrix protein was from VSV-M, a member of the *Rhabdoviridae* family of Mononegavirales. VSV-M associates with membranes through basic patches on its N-terminal domain^{11,71,127}. Upon incubation of fluorescently labelled GUVs with VSV-M, confocal microscopy revealed VSV-M induced significant membrane deformation when PS was incorporated into the GUVs. Moreover, VSV-M was shown to coalesce with fluorescently-labelled PS on the surface of membranes which resulted in invaginations of the membrane in PS-VSV-M enriched regions¹²⁷.

Membrane deformations (e.g. vesiculation, and tubulation) on GUVs has been observed for numerous matrix proteins of (-) sense RNA viruses. Unsurprisingly, *filovirus* and *paramyxovirus* matrix proteins have demonstrated capacity to remodel membranes. When incubated with fluorescently labeled GUVs, NDV-M transformed regions of the spherical GUVs into budding-like filamentous structures. Notably, this observation was found using GUVs consisting of PC and PE¹³¹, therefore no conclusions could be drawn on how an anionic lipid such as PS may contribute to NDV-M mediated membrane deformation. Conversely, when incubated with fluorescently labelled GUVs, eVP40 selectively induced vesiculation from PS containing

membranes¹³⁰, which was corroborated by ultrastructural transmission electron microscopy (TEM) studies¹¹⁹. Furthermore, eVP40 capacity to remodel membranes is abrogated when point mutations are made in the membrane penetrating hydrophobic loops, suggesting membrane penetration is required for eVP40 membrane remodeling¹¹⁹.

Membrane deformation is also observed in (-) sense RNA viruses outside of the Mononegavirales order. The ability of M1 of influenza virus A to deform membranes was investigated using GUVs and confocal microscopy, cryo-TEM, and fluorescence correlation spectroscopy (FCS). GUV studies highlighted that M1 binding to and deformation of GUVs was PS dependent. Moreover, FCS was used to show that M1 binding was insufficient to induce deformation, but that multimerization of M1 was responsible for deforming the membrane¹²⁸. A similar relationship between M1 and PS has also been shown through similar techniques for influenza C virus¹²⁹.

2.8 Membrane domains: A revolving door for viral entry and exit?

The asymmetric distribution of lipids within the plasma membrane in conjunction with the innate structural and biophysical properties of lipids gives rise to the construction of dynamic protein-lipid supramolecular complexes. Two of the most well studied membrane structures are caveolae and lipid rafts. These structures are utilized during normal cellular processes such as endocytosis, signaling cascades, and cell division. Central to membrane biology, it is no surprise that these structures are commonly hijacked during the entry and budding steps of DNA viruses, RNA viruses and retroviruses.

2.8.1 Lipid rafts

Although lipid raft membrane domains were first studied in the 1970s¹³², it wasn't until 1997 that a modern understanding of lipid rafts was outlined¹³³. Although inadequate isolation techniques rendered the existence of lipid rafts controversial, advances in microscopy techniques and the advent of super-resolution microscopy has aided a more comprehensive and convincing characterization of their properties and their consequences¹¹⁵.

The current accepted model of lipid rafts defines them as highly dynamic microdomains enriched in cholesterol, sphingolipids and other saturated lipids with limited ability to diffuse

freely. Lipid rafts are typically <50 nm in size and contain approximately 10,000 lipid molecules¹¹⁵. The importance of lipid rafts to membrane and cell biology is supported by their occurrence in various cellular locations (e.g. plasma membrane, golgi apparatus, and endocytic pathway).

The formation of lipid rafts is largely attributed to the biochemical properties of cholesterol. Cholesterol has a rigid ringed backbone, and it's small headgroup is too small to adequately shield water from the hydrophobic core of the lipid bilayer. As a result, cholesterol tightly associates with saturated lipids to properly protect the hydrophobic acyl chains from the cytosolic milieu.

Cholesterol and sphingolipids are generally regarded as the bulk constituent within lipid rafts; however, there is a growing body of evidence that PS is an additional component integral to lipid raft biogenesis. Eloquent work done by Maekawa and Fairn (2015) showed that in PS deficient cell lines, there is a reduction in the retention of cholesterol within the inner leaflet of the plasma membrane. This finding was corroborated by observation that the pharmacological depletion of PS resulted in the loss of cholesterol from the inner leaflet of the plasma membrane. In these conditions, cholesterol was found almost exclusively within the outer leaflet. Furthermore, upon supplementation with PS cholesterol redistributed to and was retained in the inner leaflet²⁶.

In addition to a relationship between PS and cholesterol in lipid rafts, a relationship between PS and sphingolipids has also been proposed. Sphingolipids are primarily located within the outer leaflet, directly opposing the inner leaflet cholesterol within lipid rafts. It has been hypothesized that sphingolipids on the outer leaflet recognize PS species within the inner leaflet and. Specifically, lipidomic and molecular dynamic studies has estimated that PS enriched areas of the inner leaflet could theoretically span 60-80% of the area enriched by sphingolipids on the outer leaflet^{134,135}.

Lipid rafts and PS have been widely implicated in the entry and exit of several classes of viruses. The purported relationship between PS and lipid rafts may present an additional link responsible for the dependency of lipids on both PS, sphingolipids, cholesterol and lipid rafts.

2.8.1.1 Viral exploitation of lipid rafts

Lipid rafts have been implicated in viral entry and/or exit for a multitude of retroviruses, enveloped and non-enveloped DNA viruses as well as enveloped and non-enveloped RNA viruses (reviewed in^{136,137}). A nexus between lipid rafts and viral entry/exit has also been purported for several (-) sense enveloped RNA viruses, including *paramyxoviruses* (human parainfluenza virus

(PIV), Newcastle disease virus (NDV)¹³⁸, RSV¹³⁹, Sendai virus (SeV)^{140,141}, MeV^{142,143}, and NiV^{98,138}), the *orthomyxovirus* influenza virus^{144–146}, and *filoviruses* (EBOV^{85,147}, MARV¹⁴⁷).

The role of lipid rafts in viral entry and exit has been largely conveyed by two key observations, either the presence of lipid raft proteins in purified virions or by the colocalization of viral proteins with lipid raft makers following cellular fractionation and sucrose gradients. Raft associated proteins, like flotillin-2, have been isolated in NDV particles¹³⁸. Additionally, glycosphingolipids and cholesterol have been isolated from HIV-1 virions¹⁴⁸.

Lipid rafts are resistant to detergent solubilization and are therefore frequently referred to as “detergent-resistant membranes” (DRM). As a result, raft associated cellular and viral proteins can be isolated by solubilization of cellular membranes with cold non-ionic detergents, like NP-40 and Triton-X-100. Association with DRMs has been widely reported for viral glycoproteins and matrix proteins. SeV¹⁴⁰, influenza A virus¹⁴⁹, and RSV¹⁵⁰ matrix protein localization to DRMs has been reported to be dependent on glycoprotein expression. In the case of MeV-M, one study found that ~10% of MeV-M independently localized to DRMs and that co-expression of F promoted MeV-M DRM localization¹⁵¹.

Conversely, robust localization of several matrix proteins to DRMs independently of glycoprotein expression has also been observed. The punctate localization of HIV-1 gag within the plasma was preliminary evidence that matrix protein localization may be confined to distinct membrane structures¹⁵². To date, numerous reports have identified DRMs as sites of HIV-gag assembly^{153,154}. Similar punctate membrane localization is observed for GFP-MeV-M and GFP-NiV-M (unpublished data). Although eVP40^{87,91} and mVP40⁹⁰ plasma membrane localization appears to be more continuous, there is also evidence that eVP40 cellular oligomerization occurs within DRMs⁸⁵. mVP40 is speculated to associate with DRMs¹⁴⁷, however this has not yet been fully elucidated.

In Akiyama et al. (2014), the localization of GFP-HIV-1 gag was utilized to delineate the localization of various GFP-fused matrix proteins to membrane rafts. GFP-fused NiV-M, eVP40 and HeV-M were all found at the periphery of the plasma membrane and correlated with regions of the plasma membrane enriched with the glycosphingolipid lipid raft marker, GM-1. However, NiV-M, eVP40 and HeV-M were found in regions distinct from HIV-1 gag localization⁹⁸. This suggests that these matrix proteins associate with similar but microscopically distinct regions of the plasma membrane.

The biological significance of matrix protein localization to DRMs is not clear. For SeV, incorporation of the matrix protein into DRMs does not necessarily equate to the production of viral particles. Moreover, cholesterol depletion failed to inhibit SeV release¹⁴¹. However, the same study reported that although budding levels were intact upon cholesterol extraction, particles that were released were ~40% less infectious. The same finding was observed for two related *paramyxoviruses*, the *morbillivirus* canine distemper virus¹⁵⁵ and the *avulavirus* NDV¹³⁸. In the case of NDV infection, cholesterol depletion significantly altered particle morphology, which may explain the reduced infectivity¹³⁸.

Raft disruption and cholesterol extraction is routinely done through M β CD treatment. However, Hirama et al. (2017) recently investigated that indirect effects of extracting cholesterol from the plasma membrane with M β CD. Following treatment of cells with M β CD, the high affinity PS probe LactC2, was significantly redistributed from the plasma membrane to intracellular membranes. *In vitro* analysis of the affinity of LactC2 to liposomes confirmed that the presence of cholesterol did not alter the affinity of LactC2 to PS, ruling out that possibility that the displacement of LactC2 from the plasma membrane following cholesterol extraction was a result of decreased LactC2 affinity to PS. Moreover, M β CD treatment resulted in an increase in the negative charge density within the inner leaflet of red blood cells¹⁵⁶. An increase in negative surface charge density has been reported to lead to the generation of positive curvature to relieve electrostatic repulsion between anionic lipids^{45,157}. Taken together, Hirama et al. (2017) presents a model where cholesterol extraction results in an increase in the negative surface charge density of the inner leaflet which is relieved by the subsequent generation of spontaneous positive curvature. The observed positive curvature facilitates endocytic events and the concomitant loss of the abundant anionic lipid, PS, from within the plasma membrane¹⁵⁶.

Moreover, a recent investigation reported that cholesterol indirectly enhanced Rous sarcoma virus matrix protein and HIV-1 gag membrane binding by enhancing lipid packing, therefore increasing membrane surface charge density¹⁵⁸. Reducing the apparent concentration of a cognate lipid binding partner while simultaneously altering membrane curvature could drastically alter the ability of viral proteins to associate with the plasma membrane. Taken together, these findings suggest that cholesterol and lipid rafts may have a multifaced and indirect role in viral entry/exit and should be carefully examined through numerous techniques.

2.8.2 Caveolae

Caveolae are invaginations of the plasma membrane with a similar lipid composition to lipid rafts. Caveolae, “little caves”, are formed by the interaction of lipids, integral membrane proteins (Caveolins), and cytosolic proteins (Cavins)¹⁵⁹. Upon recruitment to caveolin enriched regions of the plasma membrane, cavins will oligomerize into the caveolae complex. Caveolae are important to an assortment of cellular functions, including signal transduction, apoptosis, lipid homeostasis and endocytosis^{159,160}.

The multifaceted functions of caveolae indicate that these structures potentially function in viral infection. Due to the reliable localization of caveolins and cavins to caveolae, cellular fractionation, co-immunoprecipitation assays, and fluorescence colocalization can be used to determine lipids and proteins present within caveolae and that interact with caveolae proteins.

2.8.2.1 Viruses & Caveolae

Although direct membrane fusion (*paramyxovirus* entry) or endocytosis (*filovirus* entry) are the principal mechanisms of viral entry, alternate entry mechanisms have been reported for diverse viruses. A multitude of DNA viruses (Simian virus 40¹⁶¹, human papilloma virus¹⁶²), retroviruses (HIV-1¹⁶³, amphotropic murine leukemia virus¹⁶⁴) and RNA viruses have been reported to commandeer caveolae, either for entry, exit, or both. In the context of RNA viruses, usurpation of caveolae is observed in both (+) sense (Japanese encephalitis virus (JE))¹⁶⁵, echovirus¹⁶⁶) and (-) sense RNA viruses RSV¹⁶⁷, NDV¹⁶⁸, PIV-5¹⁶⁹, human influenza virus¹⁷⁰, filoviruses¹⁷¹).

Caveolae have been implicated in entry of NDV¹⁶⁸, EBOV¹⁷¹, and MARV¹⁷¹. Immunofluorescence studies revealed a colocalization of EBOV and MARV with caveolin-1 during entry¹⁷¹. Moreover, treatment of cells with caveolae disrupting agents (phorbol myristate 13-acetate and nystatin) reduced NDV¹⁶⁸, EBOV, and MARV¹⁷¹ infectivity. However, treatment of cells with M β CD also reduced viral infectivity to a similar extent as caveolae disrupting agents^{168,171}. Caveolae are enriched in cholesterol¹⁵⁹. Therefore, it remains unclear as to whether caveolae structures, cholesterol, or both are significant contributors to NDV, EBOV, and MARV entry.

There are numerous reports which link viral exit and caveolae. Strikingly, caveolin-1 has been identified in RSV¹⁶⁷, PIV-5¹⁶⁹, and NDV^{138,172} particles. The *paramyxovirus* RSV is hypothesized to assemble at caveolae rich membranes, supported by the observation that caveolin-1 and cavin-1 are actively recruited and incorporated into the viral envelope, though an actin-dependent process. Further corroborating the model of RSV assembly within caveolae is the observation that RSV infection increased cavin protein levels¹⁶⁷.

Beyond incorporation of caveolae proteins into released virions, several viruses have been reported to colocalize with or directly interact with caveolin-1 within the cell. Through pull-downs and co-immunoprecipitation assays, the M2 matrix protein of influenza was shown to directly bind to caveolin-1 through a putative caveolin-1 binding domain¹⁷⁰. Moreover, knockdown of caveolin-1 significantly decrease influenza viral titers¹⁷⁰. Lastly, caveolin-1 was shown to colocalize with PIV-5 viral proteins and cluster at sites of viral budding¹⁶⁹.

Central to the context of viral budding, caveolins and cavins display a high affinity for membranes enriched in PS and PI(4,5)P₂^{23,159}. Through confocal microscopy competition assays in cells co-expressing GFP-LactC2 and GFP-Cavin, GFP-LactC2 outcompeted GFP-Cavin for PS binding therefore reducing GFP-Cavin plasma membrane localization. Additionally, co-expression of GFP-LactC2 and GFP-Cavin resulted in a higher mobility of cavin proteins, suggesting that blocking cavin binding to PS within the plasma membrane is imperative for proper oligomerization of cavin and caveolae formation. This was validated by complementary confocal microscopy and EM experiments where co-expression of GFP-LactC2 with GFP-Cavin reduced the number of caveolae puncta observed²³.

A different role for PI(4,5)P₂ in caveolae assembly was reported. Depletion of PI(4,5)P₂ did not significantly decrease the abundance of caveolae puncta observed through EM; however, an increase in cavin protein mobility was reported. Taken together, these findings suggest that PS may be important for cavin localization to the distinct membrane regions and PI(4,5)P₂ may help anchor cavin proteins following membrane localization for proper oligomerization²³. Strikingly, a similar mechanism has been reported for eVP40, where PS is postulated to guide initial binding and assembly while PI(4,5)P₂ stabilizes extensive eVP40 oligomerization^{91,95}.

2.9 Matrix proteins & host proteins

Viruses circumvent their limited machinery by also subverting cellular proteins. Although the primary aim of this chapter is to present the current understanding of the role of lipids in viral infection and specifically viral budding, the role of host proteins in the viral life cycle cannot be ignored. Through mimicking protein binding interfaces, viral proteins divert and hijack host proteins from their designated functions. Extensive work has underscored the importance of host proteins in each stage of the viral life cycle, and detailed reviews are available of these interactions (reviewed in^{99,173,174}). To remain in the context of viruses and lipids, the remainder of this chapter will focus on a few key host proteins involved in matrix protein-dependent viral budding that also have implications in membrane and lipid biology.

2.9.1 The ESCRT machinery

Viral budding is analogous to the numerous membrane budding events throughout the cell. Cellular membrane curvature and scission processes are mediated by a complex and diverse family of proteins, the endosomal sorting complex required for transport (ESCRT) machinery (reviewed in¹⁷⁵). The ESCRT machinery interacts with individual ESCRT proteins, ESCRT protein complexes and membrane lipids to carry out membrane scission. ESCRT-mediated membrane scission occurs naturally at the endosomal membrane (during multivesicular body biogenesis and mediated primarily through PI(3)P)¹⁷⁶ and at the nuclear envelope (during cytokinesis and mediated through PI(4,5)P₂). Importantly, ESCRT is also highly active at the plasma membrane (supported by PI(4,5)P₂)¹⁷⁷, rendering this machinery an ideal candidate for viruses to hijack during viral budding.

2.9.1.1 ESCRT in viral budding

Viral-ESCRT interactions are mediated through conserved late domains (L-domains) within matrix proteins. L-domains were initially identified in HIV-1 gag¹⁷⁸, however, L-domains have subsequently been identified in *retroviruses*, *arenaviruses*, *flaviviruses*, *rabdoviruses*, *herpesviruses*, and *filoviruses*¹⁷⁵. Two overlapping L-domains (⁷PTAP¹⁰ and ¹⁰PPEY¹³) have been identified in eVP40^{179–181}, and one (¹⁶PPPY¹⁹) in mVP40¹⁸². Although no putative L-domains have

been identified in MeV-M or NiV-M^{183,184}, two non-classical L-domains have been reported in NiV-M (⁶²YMYL⁶⁵ and ⁹²YPLGVG⁹⁷)^{185,186}.

Although L-domains mediate interactions between matrix proteins and ESCRT proteins to facilitate viral budding, ESCRT proteins must associate with other ESCRT proteins and with membrane lipids during membrane scission events. NEDD-4, a member of the ESCRT machinery shown to facilitate eVP40 and mVP40 budding^{181,182}, associates with the plasma membrane through its calcium-dependent C2 domain¹⁷⁵. Furthermore, the ESCRT component ALIX is regulated by the phospholipase PLD¹⁸⁷ and has been implicated in EBOV budding¹⁸⁸. Although the role of lipids in ESCRT mediated events is not well understood, it would be worthy of closer examination. Moreover, targeting lipids central to matrix protein assembly and ESCRT function would be an innovative approach to inhibiting viral budding.

Important to the context of viral budding, ESCRT proteins have been reported to interact with specific anionic lipids as well as alter the physical properties of membranes. Total internal reflection (TIRF) microscopy with fluorescently labelled ESCRT proteins on SLBs is a useful tool for monitoring membrane specific events as TIRF limits detection to ~100 nm from the sample surface (i.e. membrane surface). Additionally, use of phase-sensitive dyes, such as DiI, are useful tools in investigating the physical partitioning of lipids into domains. DiI associates with disordered regions of membranes and is unable to associate with ordered regions, rendering it a useful fluorescent tool for studying phase behavior in membranes.

An initial study investigating the *in vitro* affinity of ESCRT proteins to liposomes found that ESCRT-1 complexes associate with anionic lipids in a charge density dependent manner. However, the most robust binding of a fully assembled ESCRT-1 complex (which included the eVP40 binding protein Tsg101¹⁸⁹) was observed when PS or PI(4,5)P₂ were present, with a marginally higher affinity to PS¹⁹⁰. Lastly, a positively charged surface in a putative membrane binding site was identified in the crystal structure of an ESCRT-complex¹⁹⁰, functionally equivalent to the positively charged membrane binding surfaces within matrix proteins.

In a follow-up study, the impact of ESCRT-assembly on lipid phase formation was investigated¹⁹¹. Upon incubation of a GFP-ESCRT-II protein with SLBs, ESCRT-II proteins clustered with themselves and with ESCRT-III complexes when a minimum of 15% cholesterol was incorporated into the SLBs, a concentration far lower than that observed within the cell. Moreover, ESCRT-II clustering induced phase separation within the SLBs, confirmed by the

exclusion of a phase-sensitive fluorescent dye (DiI) within ESCRT-II enriched regions of the SLBs¹⁹¹.

Lastly, CHMP2 is a component of the ESCRT-III complex which has been implicated in HIV-1 budding¹⁹². To understand the membrane targeting properties of CHMP2, GFP-CHMP2 and fluorescently labelled GUVs were utilized. Using spinning disk confocal microscopy, Alqabandi et al. (2019) observed a colocalization of fluorescent PI(4,5)P₂ and GFP-CHMP2B. Moreover, a mesh-like structure of GFP-CHMP2B was observed with overlap of high intensity patches of PI(4,5)P₂¹⁹³. This observation suggests that CHMP2B recruited PI(4,5)P₂ to sites of its self-assembly of the membrane surface.

2.9.2 The actin network

The cytoskeletal network consists of proteins and lipids working in concert to help maintain cell morphology and stability with functional implications in cell signaling, trafficking and membrane scission events¹⁹⁴. Although cytoskeletal-lipid interactions are at the center stage of membrane biology, little is known regarding the molecular details of how cytoskeletal proteins and lipid interactions mutually influence one another.

Actin is a ubiquitous component of the cytoskeletal network. Monomeric actin will polymerize into a filamentous network that can then interact with a variety of cellular proteins influencing a vast range of trafficking and membrane remodeling events, such as curvature¹⁹⁴. The generation of membrane curvature is a fundamental parameter to cellular membranes and is also required for viral budding and scission. The concerted efforts of lipids, cellular proteins and actin dynamics aid in the development of membrane curvature.

The observation that actin plays a role in viral budding dates back to the 1970s, when an abundance of actin was found in purified MeV¹⁹⁵ and SeV virions¹⁹⁶. Actin has since been identified in purified MARV¹¹⁷, NDV¹³⁸, HIV-1^{197,198}, and influenza¹⁹⁹ virions. Additionally, actin depolymerization (through cytochalasin D treatment) reduced MeV²⁰⁰ and MARV²⁰¹ virion release.

Strikingly, independent expression of eVP40 in cells resulted in the packaging of actin in VLPs. Moreover, disruption of the actin network with latrunculin-A reduced eVP40 VLP production²⁰². In a separate study, single-particle tracking of eVP40 and mCherry-Actin revealed a significant overlap in their movement within cells²⁰³. Moreover, there are numerous reports of co-localization between eVP40^{202,203}/mVP40²⁰¹ and actin. Although a direct interaction between

eVP40 and mVP40 and actin has not been established, it has been documented for SeV-M and NDV-M²⁰⁴. Lastly, to the best of our knowledge, no interaction between NiV-M and actin has been reported; however, actin accessory proteins have been reported to interact with NiV-M.

Importantly, actin dynamics and regulation has been linked to membrane lipids central to viral budding (reviewed in²⁰⁵). Early evidence indicated that high levels of PS increased the phosphorylation rate of actin²⁰⁶ and also enhanced intracellular MAPK signaling cascade²⁰⁷, both of which stimulated actin polymerization²⁰⁶. Lastly, actin has been implicated in the confinement of PS into microdomains²⁰⁸, which have been observed in M1¹¹³ and eVP40 assembly (unpublished data).

PI(4,5)P₂ is another membrane critically linked to actin dynamics and viral budding. PI(4,5)P₂ has been identified as an important indirect activator of actin polymerization^{194,209}, filopodia formation^{210,211}, and membrane phase separation. Numerous actin binding proteins contain PH domains, which are activated upon interaction with PI(4,5)P₂^{209,212}. Interestingly, in uniform GUVs containing PI(4,5)P₂, actin polymerization resulted in significant formation of distinct domains within previously homogeneously distributed GUVs²¹³. This may have significant implications in viral budding as numerous (-) sense RNA viruses are hypothesized to preferentially assemble on rigidified membranes^{137,147}. Taken together, these findings suggest a dual role for lipids in coordinating actin polymerization and matrix assembly and further studies are needed to clarify the role of lipids in actin-matrix protein mediated budding.

2.10 References

1. White, S. H., Ladokhin, A. S., Jayasinghe, S. & Hristova, K. How Membranes Shape Protein Structure. *Journal of Biological Chemistry* **276**, 32395–32398 (2001).
2. Tanford, C. Amphiphile orientation: physical chemistry and biological function. *Biochem. Soc. Trans.* **15 Suppl**, 1S-7S (1987).
3. Yang, Y., Lee, M. & Fairn, G. D. Phospholipid subcellular localization and dynamics. *J. Biol. Chem.* **293**, 6230–6240 (2018).
4. Vance, J. E. Phospholipid Synthesis and Transport in Mammalian Cells. *Traffic* **16**, 1–18 (2015).
5. Dutta, A. & Sharma-Walia, N. Curbing Lipids: Impacts ON Cancer and Viral Infection. *Int. J. Mol. Sci.* **20**, (2019).
6. Altan-Bonnet, N. Lipid tales on viral replication and transmission. doi:10.1016/j.tcb.2016.09.011
7. Strating, J. R. & van Kuppeveld, F. J. Viral rewiring of cellular lipid metabolism to create membranous replication compartments. *Current Opinion in Cell Biology* **47**, 24–33 (2017).
8. Zhang, Z. *et al.* Host lipids in positive-strand RNA virus genome replication. *Frontiers in Microbiology* **10**, (2019).
9. Dumas, F. & Haanappel, E. Lipids in infectious diseases - The case of AIDS and tuberculosis. *Biochim. Biophys. acta. Biomembr.* **1859**, 1636–1647 (2017).
10. Martín-Acebes, M. A., Vázquez-Calvo, Á. & Saiz, J. C. Lipids and flaviviruses, present and future perspectives for the control of dengue, Zika, and West Nile viruses. *Progress in Lipid Research* **64**, 123–137 (2016).
11. Amarasinghe, G. K. *et al.* Taxonomy of the order Mononegavirales: update 2018. *Arch. Virol.* **163**, 2283–2294 (2018).
12. Corradi, V. *et al.* Lipid-Protein Interactions Are Unique Fingerprints for Membrane Proteins. *ACS Cent. Sci.* **4**, 709–717 (2018).
13. Bittova, L., Stahelin, R. V. & Cho, W. Roles of Ionic Residues of the C1 Domain in Protein Kinase C- α Activation and the Origin of Phosphatidylserine Specificity. *J. Biol. Chem.* **276**, 4218–4226 (2001).
14. Vance, J. E. Phosphatidylserine and phosphatidylethanolamine in mammalian cells: Two metabolically related aminophospholipids. *Journal of Lipid Research* **49**, 1377–1387 (2008).
15. Yeung, T. *et al.* Membrane phosphatidylserine regulates surface charge and protein localization. *Science (80-.)*. **319**, 210–213 (2008).
16. Bartoli, J. *et al.* The Long Hunt for pssR-Looking for a Phospholipid Synthesis Transcriptional Regulator, Finding the Ribosome. *J. Bacteriol.* **199**, (2017).
17. Carman, G. M. & Han, G.-S. Phosphatidate phosphatase regulates membrane phospholipid synthesis via phosphatidylserine synthase. *Adv. Biol. Regul.* **67**, 49–58 (2018).
18. Tasseva, G., Cole, L. & Vance, J. E. N-Myc and SP regulate phosphatidylserine synthase-1 expression in brain and glial cells. *J. Biol. Chem.* **286**, 1061–73 (2011).
19. Voelker, D. R. & Frazier, J. L. Isolation and characterization of a Chinese hamster ovary cell line requiring ethanolamine or phosphatidylserine for growth and exhibiting defective phosphatidylserine synthase activity. *J. Biol. Chem.* **261**, 1002–8 (1986).
20. Kuge, O., Akamatsu, Y. & Nishijima, M. Abortive infection with Sindbis virus of a Chinese hamster ovary cell mutant defective in phosphatidylserine and phosphatidylethanolamine biosynthesis. *Biochim. Biophys. Acta* **986**, 61–9 (1989).

21. Adu-Gyamfi, E. *et al.* Host Cell Plasma Membrane Phosphatidylserine Regulates the Assembly and Budding of Ebola Virus. *J. Virol.* **89**, 9440–53 (2015).
22. Van Meer, G., Voelker, D. R. & Feigenson, G. W. Membrane lipids: Where they are and how they behave. *Nature Reviews Molecular Cell Biology* **9**, 112–124 (2008).
23. Hirama, T. *et al.* Phosphatidylserine dictates the assembly and dynamics of caveolae in the plasma membrane. *J. Biol. Chem.* **292**, 14292–14307 (2017).
24. Cho, K.-J. *et al.* Inhibition of Acid Sphingomyelinase Depletes Cellular Phosphatidylserine and Mislocalizes K-Ras from the Plasma Membrane. *Mol. Cell. Biol.* **36**, 363–74 (2016).
25. Ayala-Sanmartin, J., Henry, J. P. & Pradel, L. A. Cholesterol regulates membrane binding and aggregation by annexin 2 at submicromolar Ca²⁺ concentration. *Biochim. Biophys. Acta - Biomembr.* **1510**, 18–28 (2001).
26. Maekawa, M. & Fairn, G. D. Complementary probes reveal that phosphatidylserine is required for the proper transbilayer distribution of cholesterol. *J. Cell Sci.* doi:10.1242/jcs.164715
27. Hirama, T. & Fairn, G. D. Induction of spontaneous curvature and endocytosis: Unwanted consequences of cholesterol extraction using methyl- β -Cyclodextrin. *Commun. Integr. Biol.* **11**, 1–4 (2018).
28. Di Paolo, G. & De Camilli, P. Phosphoinositides in cell regulation and membrane dynamics. *Nature* **443**, 651–7 (2006).
29. Balla, T. Phosphoinositides: tiny lipids with giant impact on cell regulation. *Physiol. Rev.* **93**, 1019–137 (2013).
30. Feng, Z., Xu, K., Kovalev, N. & Nagy, P. D. Recruitment of Vps34 PI3K and enrichment of PI3P phosphoinositide in the viral replication compartment is crucial for replication of a positive-strand RNA virus. *PLoS Pathog.* **15**, (2019).
31. Cohen, J. I. Herpesviruses in the activated phosphatidylinositol-3-kinase- δ syndrome. *Frontiers in Immunology* **9**, (2018).
32. Nakatsu, F. *et al.* Ptdins4P synthesis by PI4KIII α at the plasma membrane and its impact on plasma membrane identity. *J. Cell Biol.* **199**, 1003–1016 (2012).
33. Altan-Bonnet, N. & Balla, T. Phosphatidylinositol 4-kinases: Hostages harnessed to build panviral replication platforms. *Trends in Biochemical Sciences* **37**, 293–302 (2012).
34. Malek, M. *et al.* PTEN Regulates PI(3,4)P₂ Signaling Downstream of Class I PI3K. *Mol. Cell* **68**, 566–580.e10 (2017).
35. Qiu, S. *et al.* Ebola virus requires phosphatidylinositol (3,5) bisphosphate production for efficient viral entry. *Virology* **513**, 17–28 (2018).
36. Dickson, E. J. & Hille, B. Understanding phosphoinositides: Rare, dynamic, and essential membrane phospholipids. *Biochemical Journal* **476**, 1–23 (2019).
37. Hale, B. G., Jackson, D., Chen, Y. H., Lamb, R. A. & Randall, R. E. Influenza A virus NS1 protein binds p85 β and activates phosphatidylinositol-3-kinase signaling. *Proc. Natl. Acad. Sci. U. S. A.* **103**, 14194–14199 (2006).
38. Zoncu, R. *et al.* Loss of endocytic clathrin-coated pits upon acute depletion of phosphatidylinositol 4,5-bisphosphate. *Proc. Natl. Acad. Sci. U. S. A.* **104**, 3793–3798 (2007).
39. Antonescu, C. N., Aguet, F., Danuser, G. & Schmid, S. L. Phosphatidylinositol-(4,5)-bisphosphate regulates clathrin-coated pit initiation, stabilization, and size. *Mol. Biol. Cell* **22**, 2588–2600 (2011).
40. Vázquez-Calvo, Á., Sobrino, F. & Martín-Acebes, M. A. Plasma Membrane

- Phosphatidylinositol 4,5 Bisphosphate Is Required for Internalization of Foot-and-Mouth Disease Virus and Vesicular Stomatitis Virus. *PLoS One* **7**, (2012).
41. Stillwell, W. Membrane Polar Lipids. in *An Introduction to Biological Membranes* 63–87 (Elsevier, 2016). doi:10.1016/b978-0-444-63772-7.00005-1
 42. Wang, X., Devaiah, S. P., Zhang, W. & Welti, R. Signaling functions of phosphatidic acid. *Prog. Lipid Res.* **45**, 250–78 (2006).
 43. Capelluto, D. G. S. *et al.* Biophysical and Molecular-Dynamics Studies of Phosphatidic Acid Binding by the Dvl-2 DEP Domain. (2014). doi:10.1016/j.bpj.2014.01.032
 44. Exton, J. H. Phosphatidylcholine breakdown and signal transduction. *Biochimica et Biophysica Acta (BBA)/Lipids and Lipid Metabolism* **1212**, 26–42 (1994).
 45. Kooijman, E. E., Chupin, V., de Kruijff, B. & Burger, K. N. J. Modulation of membrane curvature by phosphatidic acid and lysophosphatidic acid. *Traffic* **4**, 162–174 (2003).
 46. Hyodo, K. *et al.* Phosphatidic Acid Produced by Phospholipase D Promotes RNA Replication of a Plant RNA Virus. *PLOS Pathog.* **11**, e1004909 (2015).
 47. Oguin, T. H. *et al.* Phospholipase D facilitates efficient entry of influenza virus, allowing escape from innate immune inhibition. *J. Biol. Chem.* **289**, 25405–17 (2014).
 48. Taylor, H. E. *et al.* Phospholipase D1 Couples CD4⁺ T Cell Activation to c-Myc-Dependent Deoxyribonucleotide Pool Expansion and HIV-1 Replication. *PLoS Pathog.* **11**, (2015).
 49. Bi, K., Roth, M. G. & Ktistakis, N. T. Phosphatidic acid formation by phospholipase D is required for transport from the endoplasmic reticulum to the Golgi complex. *Curr. Biol.* **7**, 301–307 (1997).
 50. O'Reilly, M. C. *et al.* Discovery of a highly selective PLD2 inhibitor (ML395): a new probe with improved physiochemical properties and broad-spectrum antiviral activity against influenza strains. *ChemMedChem* **9**, 2633–7 (2014).
 51. Chung, J. *et al.* PI4P/phosphatidylserine countertransport at ORP5- and ORP8-mediated ER - Plasma membrane contacts. *Science (80-.).* **349**, 428–432 (2015).
 52. Lees, J. A. *et al.* Lipid transport by TMEM24 at ER-plasma membrane contacts regulates pulsatile insulin secretion. *Science* **355**, (2017).
 53. van der Schaar, H. M., Dorobantu, C. M., Albulescu, L., Strating, J. R. P. M. & van Kuppeveld, F. J. M. Fat(al) attraction: Picornaviruses Usurp Lipid Transfer at Membrane Contact Sites to Create Replication Organelles. *Trends in Microbiology* **24**, 535–546 (2016).
 54. Stoeck, I. K. *et al.* Hepatitis C Virus Replication Depends on Endosomal Cholesterol Homeostasis. *J. Virol.* **92**, (2017).
 55. Kornberg, R. D. & McConnell, H. M. Lateral diffusion of phospholipids in a vesicle membrane. *Proc. Natl. Acad. Sci. U. S. A.* **68**, 2564–2568 (1971).
 56. Devaux, P. & McConnell, H. M. Lateral Diffusion in Spin-Labeled Phosphatidylcholine Multilayers. *J. Am. Chem. Soc.* **94**, 4475–4481 (1972).
 57. Kornberg, R. D. & McConnell, H. M. Inside-Outside Transitions of Phospholipids in Vesicle Membranes. *Biochemistry* **10**, 1111–1120 (1971).
 58. Bai, J. & Pagano, R. E. Measurement of spontaneous transfer and transbilayer movement of BODIPY- labeled lipids in lipid vesicles. *Biochemistry* **36**, 8840–8848 (1997).
 59. Bell, R. M., Ballas, L. M. & Coleman, R. A. Lipid topogenesis. *J. Lipid Res.* **22**, 391–403 (1981).
 60. Bevers, E. M., Tilly, R. H. J., Senden, J. M. G., Comfurius, P. & Zwaal, R. F. A. Exposure of Endogenous Phosphatidylserine at the Outer Surface of Stimulated Platelets Is Reversed by Restoration of Aminophospholipid Translocase Activity. *Biochemistry* **28**, 2382–2387

- (1989).
61. Zwaal, R. F. A., Comfurius, P. & Bevers, E. M. Lipid-protein interactions in blood coagulation. *Biochimica et Biophysica Acta - Reviews on Biomembranes* **1376**, 433–453 (1998).
 62. Fadok, V. A., De Cathelineau, A., Daleke, D. L., Henson, P. M. & Bratton, D. L. Loss of phospholipid asymmetry and surface exposure of phosphatidylserine is required for phagocytosis of apoptotic cells by macrophages and fibroblasts. *J. Biol. Chem.* **276**, 1071–1077 (2001).
 63. Fadok, V. A. *et al.* Exposure of phosphatidylserine on the surface of apoptotic lymphocytes triggers specific recognition and removal by macrophages. *J. Immunol.* **148**, 2207–16 (1992).
 64. Suzuki, J., Umeda, M., Sims, P. J. & Nagata, S. Calcium-dependent phospholipid scrambling by TMEM16F. *Nature* **468**, 834–840 (2010).
 65. Suzuki, J. *et al.* Calcium-dependent phospholipid scramblase activity of TMEM 16 protein family members. *J. Biol. Chem.* **288**, 13305–13316 (2013).
 66. Gyobu, S., Ishihara, K., Suzuki, J., Segawa, K. & Nagata, S. Characterization of the scrambling domain of the TMEM16 family. *Proc. Natl. Acad. Sci. U. S. A.* **114**, 6274–6279 (2017).
 67. Zwaal, R. F. A., Comfurius, P. & Bevers, E. M. Scott syndrome, a bleeding disorder caused by defective scrambling of membrane phospholipids. *Biochimica et Biophysica Acta - Molecular and Cell Biology of Lipids* **1636**, 119–128 (2004).
 68. Yu, A., Byers, D. M., Ridgway, N. D., McMaster, C. R. & Cook, H. W. Preferential externalization of newly synthesized phosphatidylserine in apoptotic U937 cells is dependent on caspase-mediated pathways. *Biochim. Biophys. Acta* **1487**, 296–308 (2000).
 69. Yu, A., McMaster, C. R., Byers, D. M., Ridgway, N. D. & Cook, H. W. Stimulation of phosphatidylserine biosynthesis and facilitation of UV-induced apoptosis in Chinese hamster ovary cells overexpressing phospholipid scramblase 1. *J. Biol. Chem.* **278**, 9706–14 (2003).
 70. Suzuki, J., Denning, D. P., Imanishi, E., Horvitz, H. R. & Nagata, S. Xk-related protein 8 and CED-8 promote phosphatidylserine exposure in apoptotic cells. *Science (80-.).* **341**, 403–406 (2013).
 71. Liu, L. Fields Virology, 6th Edition. *Clin. Infect. Dis.* **59**, 613–613 (2014).
 72. Nanbo, A. *et al.* Ebola virus requires a host scramblase for externalization of phosphatidylserine on the surface of viral particles. *PLOS Pathog.* **14**, e1006848 (2018).
 73. Kolesnikova, L., Ryabchikova, E., Shestopalov, A. & Becker, S. Basolateral Budding of Marburg Virus: VP40 Retargets Viral Glycoprotein GP to the Basolateral Surface. *J. Infect. Dis.* **196**, S232–S236 (2007).
 74. Kolesnikova, L., Mittler, E., Schudt, G., Shams-Eldin, H. & Becker, S. Phosphorylation of Marburg virus matrix protein VP40 triggers assembly of nucleocapsids with the viral envelope at the plasma membrane. *Cell. Microbiol.* **14**, 182–197 (2012).
 75. Nanbo, A., Watanabe, S., Halfmann, P. & Kawaoka, Y. The spatio-temporal distribution dynamics of Ebola virus proteins and RNA in infected cells. *Sci. Rep.* **3**, (2013).
 76. Baudin, F., Petit, I., Weissenhorn, W. & Ruigrok, R. W. H. In vitro dissection of the membrane and RNP binding activities of influenza virus M1 protein. *Virology* **281**, 102–108 (2001).
 77. Dessen, A. Crystal structure of the matrix protein VP40 from Ebola virus. *EMBO J.* **19**,

- 4228–4236 (2000).
78. Oda, S.-I. *et al.* Crystal Structure of Marburg Virus VP40 Reveals a Broad, Basic Patch for Matrix Assembly and a Requirement of the N-Terminal Domain for Immunosuppression. *J. Virol.* **90**, 1839–48 (2016).
 79. Shtykova, E. V. *et al.* Solution Structure, Self-Assembly, and Membrane Interactions of the Matrix Protein from Newcastle Disease Virus at Neutral and Acidic pH. *J. Virol.* **93**, (2018).
 80. Bornholdt, Z. A. *et al.* Structural rearrangement of ebola virus vp40 begets multiple functions in the virus life cycle. *Cell* **154**, 763–774 (2013).
 81. Liu, Y. C., Grusovin, J. & Adams, T. E. Electrostatic Interactions between Hendra Virus Matrix Proteins Are Required for Efficient Virus-Like-Particle Assembly. *J. Virol.* **92**, (2018).
 82. Gaudier, M., Gaudin, Y. & Knossow, M. Crystal structure of vesicular stomatitis virus matrix protein. *EMBO J.* **21**, 2886–2892 (2002).
 83. GC, J. B. *et al.* Interdomain salt-bridges in the Ebola virus protein VP40 and their role in domain association and plasma membrane localization. *Protein Sci.* 1648–1658 (2016). doi:10.1002/pro.2969
 84. Timmins, J. *et al.* Oligomerization and polymerization of the filovirus matrix protein VP40. *Virology* **312**, 359–368 (2003).
 85. Panchal, R. G. *et al.* In vivo oligomerization and raft localization of Ebola virus protein VP40 during vesicular budding. *Proc. Natl. Acad. Sci. U. S. A.* **100**, 15936–41 (2003).
 86. Hoenen, T. *et al.* Oligomerization of Ebola virus VP40 is essential for particle morphogenesis and regulation of viral transcription. *J. Virol.* **84**, 7053–63 (2010).
 87. Adu-Gyamfi, E., Digman, M. A., Gratton, E. & Stahelin, R. V. Investigation of Ebola VP40 assembly and oligomerization in live cells using number and brightness analysis. *Biophys. J.* **102**, 2517–25 (2012).
 88. Ruigrok, R. W. *et al.* Structural characterization and membrane binding properties of the matrix protein VP40 of Ebola virus. *J. Mol. Biol.* **300**, 103–12 (2000).
 89. Koehler, A., Pfeiffer, S., Kolesnikova, L. & Becker, S. Analysis of the multifunctionality of Marburg virus VP40. *J. Gen. Virol.* **99**, 1614–1620 (2018).
 90. Wijesinghe, K. J. & Stahelin, V. Investigation of the Lipid Binding Properties of the Marburg Virus. *J. Virol.* **90**, 3074–3085 (2016).
 91. Johnson, K. A., Taghon, G. J. F., Scott, J. L. & Stahelin, R. V. The Ebola Virus matrix protein, VP40, requires phosphatidylinositol 4,5-bisphosphate (PI(4,5)P₂) for extensive oligomerization at the plasma membrane and viral egress. *Sci. Rep.* **6**, 19125 (2016).
 92. Emanuel, J., Marzi, A. & Feldmann, H. Filoviruses: Ecology, Molecular Biology, and Evolution. in *Advances in Virus Research* **100**, 189–221 (Academic Press Inc., 2018).
 93. Jasenosky, L. D., Neumann, G., Lukashevich, I. & Kawaoka, Y. Ebola virus VP40-induced particle formation and association with the lipid bilayer. *J. Virol.* **75**, 5205–14 (2001).
 94. Silva, L. P., Vanzile, M., Bavari, S., Aman, J. M. J. & Schriemer, D. C. Assembly of ebola virus matrix protein VP40 is regulated by latch-like properties of N and C terminal tails. *PLoS One* **7**, (2012).
 95. Johnson, K. A. *et al.* PI(4,5)P₂ Binding Sites in the Ebola Virus Matrix Protein Modulate 2. *bioRxiv* 341248 (2018). doi:10.1101/341248
 96. Stahelin, R. V. Membrane binding and bending in Ebola VP40 assembly and egress. *Frontiers in Microbiology* **5**, 300 (2014).
 97. Thibault, P. A., Watkinson, R. E., Moreira-Soto, A., Drexler, J. F. & Lee, B. Zoonotic

- Potential of Emerging Paramyxoviruses: Knowns and Unknowns. in *Advances in Virus Research* **98**, 1–55 (Academic Press Inc., 2017).
98. Akiyama, H. *et al.* Virus particle release from glycosphingolipid-enriched microdomains is essential for dendritic cell-mediated capture and transfer of HIV-1 and henipavirus. *J. Virol.* **88**, 8813–25 (2014).
 99. Latorre, V., Mattenberger, F. & Geller, R. Chaperoning the mononegavirales: Current knowledge and future directions. *Viruses* **10**, (2018).
 100. Wang, Y. E., Pernet, O. & Lee, B. Regulation of the nucleocytoplasmic trafficking of viral and cellular proteins by ubiquitin and small ubiquitin-related modifiers. *Biology of the Cell* **104**, 121–138 (2012).
 101. Pantua, H. D., McGinnes, L. W., Peeples, M. E. & Morrison, T. G. Requirements for the Assembly and Release of Newcastle Disease Virus-Like Particles. *J. Virol.* **80**, 11062–11073 (2006).
 102. Battisti, A. J. *et al.* Structure and assembly of a paramyxovirus matrix protein. *Proc. Natl. Acad. Sci. U. S. A.* **109**, 13996–14000 (2012).
 103. Cho, W. & Stahelin, R. V. Membrane-protein interactions in cell signaling and membrane trafficking. *Annual Review of Biophysics and Biomolecular Structure* **34**, 119–151 (2005).
 104. Stahelin, R. V. Lipid binding domains: More than simple lipid effectors. *Journal of Lipid Research* **50**, S299–30 (2009).
 105. Lodish, H. *et al.* *Molecular Cell Biology - NCBI Bookshelf*. (2000).
 106. Julkowska, M. M., Rankenbreg, J. M. & Testerink, C. Liposome-Binding Assays to Assess Specificity and Affinity of Phospholipid--Protein Interactions. in *Plant Lipid Signaling Protocols* (eds. Munnik, T. & Heilmann, I.) 261–271 (Humana Press, 2013). doi:10.1007/978-1-62703-401-2_24
 107. Del Vecchio, K. & Stahelin, R. V. Using surface plasmon resonance to quantitatively assess lipid–protein interactions. in *Methods in Molecular Biology* **1376**, 141–153 (Humana Press Inc., 2016).
 108. Kahya, N. Protein-protein and protein-lipid interactions in domain-assembly: Lessons from giant unilamellar vesicles. *Biochimica et Biophysica Acta - Biomembranes* **1798**, 1392–1398 (2010).
 109. Wijesinghe, K. J. *et al.* Detection of lipid-induced structural changes of the Marburg virus matrix protein VP40 using hydrogen/deuterium exchange-mass spectrometry. *J. Biol. Chem.* **292**, 6108–6122 (2017).
 110. Santiago, C. *et al.* Structures of T Cell Immunoglobulin Mucin Protein 4 Show a Metal-Ion-Dependent Ligand Binding Site where Phosphatidylserine Binds. *Immunity* **27**, 941–951 (2007).
 111. Chan, R. *et al.* Retroviruses Hiv and Mlv Are Enriched in Phosphoinositides. *J Virol* **82**, 11228–11238 (2008).
 112. Saad, J. S. *et al.* Structural basis for targeting HIV-1 Gag proteins to the plasma membrane for virus assembly. *Proc. Natl. Acad. Sci. U. S. A.* **103**, 11364–11369 (2006).
 113. Bobone, S. *et al.* Phosphatidylserine Lateral Organization Influences the Interaction of Influenza Virus Matrix Protein 1 with Lipid Membranes. *J. Virol.* **91**, 1–15 (2017).
 114. Gerl, M. J. *et al.* Quantitative analysis of the lipidomes of the influenza virus envelope and MDCK cell apical membrane. *J. Cell Biol.* **196**, 213–221 (2012).
 115. Kerviel, A., Thomas, A., Chaloin, L., Favard, C. & Muriaux, D. Virus assembly and plasma membrane domains: which came first? *Virus research* **171**, 332–340 (2013).

116. Subhashri, R. & Shaila, M. S. Characterization of membrane association of Rinderpest virus matrix protein. *Biochem. Biophys. Res. Commun.* **355**, 1096–1101 (2007).
117. Kolesnikova, L., Bugany, H., Klenk, H.-D. & Becker, S. VP40, the Matrix Protein of Marburg Virus, Is Associated with Membranes of the Late Endosomal Compartment. *J. Virol.* **76**, 1825–1838 (2002).
118. Barros, M. *et al.* Membrane Binding of HIV-1 Matrix Protein: Dependence on Bilayer Composition and Protein Lipidation. *J. Virol.* **90**, 4544–4555 (2016).
119. Soni, S. P., Adu-Gyamfi, E., Yong, S. S., Jee, C. S. & Stahelin, R. V. The Ebola virus matrix protein deeply penetrates the plasma membrane: An important step in viral egress. *Biophys. J.* **104**, 1940–1949 (2013).
120. Adu-Gyamfi, E. *et al.* The ebola virus matrix protein penetrates into the plasma membrane: A key step in viral protein 40 (VP40) oligomerization and viral egress. *J. Biol. Chem.* **288**, 5779–5789 (2013).
121. Sha, B. & Luo, M. Structure of a bifunctional membrane-RNA binding protein, influenza virus matrix protein M1. *Nat. Struct. Biol.* **4**, 239–244 (1997).
122. Tsfasman, T. *et al.* Amphipathic alpha-helices and putative cholesterol binding domains of the influenza virus matrix M1 protein are crucial for virion structure organisation. *Virus Res.* **210**, 114–118 (2015).
123. Shishkov, A. *et al.* The In Situ Structural Characterization of the Influenza A Virus Matrix M1 Protein within a Virion. *Protein Pept. Lett.* **16**, 1407–1413 (2009).
124. Heggeness, M. H., Smith, P. R. & Choppin, P. W. In vitro assembly of the nonglycosylated membrane protein (M) of Sendai Virus. *Proc. Natl. Acad. Sci. U. S. A.* **79**, (1982).
125. Leyrat, C., Renner, M., Harlos, K., Huiskonen, J. T. & Grimes, J. M. Article Structure and Self-Assembly of the Calcium Binding Matrix Protein of Human Metapneumovirus. *Struct. Des.* **22**, 136–148 (2014).
126. Hilsch, M. *et al.* Influenza a matrix protein m1 multimerizes upon binding to lipid membranes. *Biophys. J.* **107**, 912–923 (2014).
127. Solon, J., Gareil, O., Bassereau, P. & Gaudin, Y. Membrane deformations induced by the matrix protein of vesicular stomatitis virus in a minimal system. *J. Gen. Virol.* **86**, 3357–3363 (2005).
128. Dahmani, I., Ludwig, K. & Chiantia, S. Influenza A matrix protein M1 induces lipid membrane deformation via protein multimerization. *Biosci. Rep.* **39**, (2019).
129. Saletti, D. *et al.* The Matrix protein M1 from influenza C virus induces tubular membrane invaginations in an in vitro cell membrane model. *Sci. Rep.* **7**, (2017).
130. Soni, S. P. & Stahelin, R. V. The Ebola virus matrix protein VP40 selectively induces vesiculation from phosphatidylserine-enriched membranes. *J. Biol. Chem.* **289**, 33590–7 (2014).
131. Shnyrova, A. V. *et al.* Vesicle formation by self-assembly of membrane-bound matrix proteins into a fluidlike budding domain. *J. Cell Biol.* **179**, 627–633 (2007).
132. Shimshick, E. J. & McConnell, H. M. Lateral Phase Separation in Phospholipid Membranes. *Biochemistry* **12**, 2351–2360 (1973).
133. Simons, K. & Ikonen, E. Functional rafts in cell membranes. *Nature* **387**, 569–572 (1997).
134. Llorente, A. *et al.* Molecular lipidomics of exosomes released by PC-3 prostate cancer cells. *Biochim. Biophys. Acta - Mol. Cell Biol. Lipids* **1831**, 1302–1309 (2013).
135. Skotland, T. *et al.* Molecular lipid species in urinary exosomes as potential prostate cancer biomarkers. *Eur. J. Cancer* **70**, 122–132 (2017).

136. Takahashi, T. & Suzuki, T. Function of membrane rafts in viral lifecycles and host cellular response. *Biochemistry Research International* (2011). doi:10.1155/2011/245090
137. Chazal, N. & Gerlier, D. Virus Entry, Assembly, Budding, and Membrane Rafts. *Microbiol. Mol. Biol. Rev.* **67**, 226–237 (2003).
138. Laliberte, J. P., McGinnes, L. W. & Morrison, T. G. Incorporation of functional HN-F glycoprotein-containing complexes into newcastle disease virus is dependent on cholesterol and membrane lipid raft integrity. *J. Virol.* **81**, 10636–48 (2007).
139. McCurdy, L. H. & Graham, B. S. Role of Plasma Membrane Lipid Microdomains in Respiratory Syncytial Virus Filament Formation. *J. Virol.* **77**, 1747–1756 (2003).
140. Ali, A. & Nayak, D. P. Assembly of Sendal virus: M protein interacts with F and HN proteins and with the cytoplasmic tail and transmembrane domain of F protein. *Virology* **276**, 289–303 (2000).
141. Gosselin-Grenet, A. S., Mottet-Osman, G. & Roux, L. From assembly to virus particle budding: Pertinence of the detergent resistant membranes. *Virology* **344**, 296–303 (2006).
142. Verine Vincent, S., Gerlier, D. & Manié, S. N. *Measles Virus Assembly within Membrane Rafts. JOURNAL OF VIROLOGY* **74**, (2000).
143. Manié, S. N., de Breyne, S., Debreyne, S., Vincent, S. & Gerlier, D. Measles virus structural components are enriched into lipid raft microdomains: a potential cellular location for virus assembly. *J. Virol.* **74**, 305–11 (2000).
144. Takeda, M., Leser, G. P., Russell, C. J. & Lamb, R. A. Influenza virus hemagglutinin concentrates in lipid raft microdomains for efficient viral fusion. *Proc. Natl. Acad. Sci. U. S. A.* **100**, 14610–14617 (2003).
145. Sieczkarski, S. B. & Whittaker, G. R. Influenza Virus Can Enter and Infect Cells in the Absence of Clathrin-Mediated Endocytosis. *J. Virol.* **76**, 10455–10464 (2002).
146. Verma, D. K., Gupta, D. & Lal, S. K. Host Lipid Rafts Play a Major Role in Binding and Endocytosis of Influenza A Virus. *Viruses* **10**, (2018).
147. Bavari, S. *et al.* Lipid raft microdomains: A gateway for compartmentalized trafficking of Ebola and Marburg viruses. *J. Exp. Med.* **195**, 593–602 (2002).
148. Aloia, R. C., Tian, H. & Jensen, F. C. Lipid composition and fluidity of the human immunodeficiency virus envelope and host cell plasma membranes. *Proc. Natl. Acad. Sci. U. S. A.* **90**, 5181–5185 (1993).
149. Ali, A., Avalos, R. T., Ponimaskin, E. & Nayak, D. P. Influenza Virus Assembly: Effect of Influenza Virus Glycoproteins on the Membrane Association of M1 Protein. *J. Virol.* **74**, 8709–8719 (2000).
150. Henderson, G., Murray, J. & Yeo, R. P. Sorting of the respiratory syncytial virus matrix protein into detergent-resistant structures is dependent on cell-surface expression of the glycoproteins. *Virology* **300**, 244–254 (2002).
151. Pohl, C., Duprex, W. P., Krohne, G., Rima, B. K. & Schneider-Schaulies, S. Measles virus M and F proteins associate with detergent-resistant membrane fractions and promote formation of virus-like particles. *J. Gen. Virol.* **88**, 1243–50 (2007).
152. Hermida-Matsumoto, L. & Resh, M. D. Localization of Human Immunodeficiency Virus Type 1 Gag and Env at the Plasma Membrane by Confocal Imaging. *J. Virol.* **74**, 8670–8679 (2000).
153. Ono, A. & Freed, E. O. Plasma membrane rafts play a critical role in HIV-1 assembly and release. *Proc. Natl. Acad. Sci. U. S. A.* **98**, 13925–13930 (2001).
154. Lindwasser, O. W. & Resh, M. D. Multimerization of Human Immunodeficiency Virus

- Type 1 Gag Promotes Its Localization to Barges, Raft-Like Membrane Microdomains. *J. Virol.* **75**, 7913–7924 (2001).
155. Imhoff, H., von Messling, V., Herrler, G. & Haas, L. Canine distemper virus infection requires cholesterol in the viral envelope. *J. Virol.* **81**, 4158–65 (2007).
 156. Hirama, T. *et al.* Membrane curvature induced by proximity of anionic phospholipids can initiate endocytosis. *Nat. Commun.* **8**, (2017).
 157. Fuller, N., Benatti, C. R. & Rand, R. P. Curvature and bending constants for phosphatidylserine-containing membranes. *Biophys. J.* **85**, 1667–74 (2003).
 158. Doktorova, M. *et al.* Cholesterol Promotes Protein Binding by Affecting Membrane Electrostatics and Solvation Properties. (2017). doi:10.1016/j.bpj.2017.08.055
 159. Field, S. J. Spelunking for lipids in caveolae. *Journal of Biological Chemistry* **292**, 14308–14309 (2017).
 160. Kurzchalia, T. V & Parton, R. G. Membrane microdomains and caveolae. *Curr. Opin. Cell Biol.* **11**, 424–31 (1999).
 161. Norkin, L. C. & Kuksin, D. The caveolae-mediated sv40 entry pathway bypasses the golgi complex en route to the endoplasmic reticulum. (2005). doi:10.1186/1743-422X-2-38
 162. Bousarghin, L., Touze, A., Sizaret, P.-Y. & Coursaget, P. Human Papillomavirus Types 16, 31, and 58 Use Different Endocytosis Pathways To Enter Cells. *J. Virol.* **77**, 3846–3850 (2003).
 163. Mergia, A. The role of caveolin 1 in HIV infection and pathogenesis. *Viruses* **9**, (2017).
 164. Beer, C., Andersen, D. S., Rojek, A. & Pedersen, L. Caveola-Dependent Endocytic Entry of Amphotropic Murine Leukemia Virus. *J. Virol.* **79**, 10776–10787 (2005).
 165. Xu, Q. *et al.* Caveolin-1-mediated Japanese encephalitis virus entry requires a two-step regulation of actin reorganization. *Future Microbiol.* **11**, 1227–1248 (2016).
 166. Marjomaki, V. *et al.* Internalization of Echovirus 1 in Caveolae. *J. Virol.* **76**, 1856–1865 (2002).
 167. Werling, D. *et al.* Involvement of caveolae in the uptake of respiratory syncytial virus antigen by dendritic cells. *J. Leukoc. Biol.* **66**, 50–58 (1999).
 168. Cantín, C., Holguera, J., Ferrerira, L., Villar, E. & Muñoz-Barroso, I. Newcastle disease virus may enter cells by caveolae-mediated endocytosis. *J. Gen. Virol.* **88**, 559–569 (2007).
 169. Ravid, D., Leser, G. P. & Lamb, R. A. A Role for Caveolin 1 in Assembly and Budding of the Paramyxovirus Parainfluenza Virus 5. *J. Virol.* **84**, 9749–9759 (2010).
 170. Sun, L., Hemgård, G. V., Susanto, S. A. & Wirth, M. Caveolin-1 influences human influenza A virus (H1N1) multiplication in cell culture. *Virol. J.* **7**, (2010).
 171. Empig, C. J. & Goldsmith, M. A. Association of the Caveola Vesicular System with Cellular Entry by Filoviruses. *J. Virol.* **76**, 5266–5270 (2002).
 172. Laliberte, J. P., McGinnes, L. W., Peeples, M. E. & Morrison, T. G. Integrity of Membrane Lipid Rafts Is Necessary for the Ordered Assembly and Release of Infectious Newcastle Disease Virus Particles. *J. Virol.* **80**, 10652–10662 (2006).
 173. Liu, Y. & Harty, R. N. Viral and host proteins that modulate filovirus budding. *Future Virology* **5**, 481–491 (2010).
 174. Gordon, T. B., Hayward, J. A., Marsh, G. A., Baker, M. L. & Tachedjian, G. Host and viral proteins modulating ebola and marburg virus egress. *Viruses* **11**, (2019).
 175. Wollert, T. *et al.* The ESCRT machinery at a glance. *J. Cell Sci.* **122**, 2163–6 (2009).
 176. Wollert, T. & Hurley, J. H. Molecular mechanism of multivesicular body biogenesis by ESCRT complexes. *Nature* **464**, 864–869 (2010).

177. Garnier-Lhomme, M. *et al.* Nuclear envelope remnants: Fluid membranes enriched in STEROLS and polyphosphoinositides. *PLoS One* **4**, (2009).
178. Ott, D. E., Coren, L. V., Chertova, E. N., Gagliardi, T. D. & Schubert, U. Ubiquitination of HIV-1 and MuLV Gag. *Virology* **278**, 111–121 (2000).
179. Han, Z. *et al.* ITCH E3 Ubiquitin Ligase Interacts with Ebola Virus VP40 To Regulate Budding. *J. Virol.* **90**, 9163–71 (2016).
180. Han, Z. *et al.* Ubiquitin Ligase WWP1 Interacts with Ebola Virus VP40 To Regulate Egress. *J. Virol.* **91**, (2017).
181. Harty, R. N., Brown, M. E., Wang, G., Huibregtse, J. & Hayes, F. P. A PPxY motif within the VP40 protein of Ebola virus interacts physically and functionally with a ubiquitin ligase: Implications for filovirus budding. *Proc. Natl. Acad. Sci. U. S. A.* **97**, 13871–13876 (2000).
182. Urata, S. & Yasuda, J. Regulation of Marburg virus (MARV) budding by Nedd4.1: A different WW domain of Nedd4.1 is critical for binding to MARV and Ebola virus VP40. *J. Gen. Virol.* **91**, 228–234 (2010).
183. Harrison, M. S., Sakaguchi, T. & Schmitt, A. P. Paramyxovirus assembly and budding: Building particles that transmit infections. *International Journal of Biochemistry and Cell Biology* **42**, 1416–1429 (2010).
184. Schmitt, A. P., Leser, G. P., Morita, E., Sundquist, W. I. & Lamb, R. A. Evidence for a new viral late-domain core sequence, FPIV, necessary for budding of a paramyxovirus. *J. Virol.* **79**, 2988–97 (2005).
185. Ciancanelli, M. J. & Basler, C. F. Mutation of YMYL in the Nipah Virus Matrix Protein Abrogates Budding and Alters Subcellular Localization. *J. Virol.* **80**, 12070–12078 (2006).
186. Patch, J. R. *et al.* The YPLGVG sequence of the Nipah virus matrix protein is required for budding. (2008). doi:10.1186/1743-422X-5-137
187. Ghossoub, R. *et al.* Syntenin-ALIX exosome biogenesis and budding into multivesicular bodies are controlled by ARF6 and PLD2. *Nat. Commun.* **5**, (2014).
188. Han, Z. *et al.* ALIX Rescues Budding of a Double PTAP/PPEY L-Domain Deletion Mutant of Ebola VP40: A Role for ALIX in Ebola Virus Egress. *J. Infect. Dis.* **212**, S138–S145 (2015).
189. Timmins, J. *et al.* Ebola virus matrix protein VP40 interaction with human cellular factors Tsg101 and Nedd4. *J. Mol. Biol.* **326**, 493–502 (2003).
190. Boura, E. & Hurley, J. H. Structural basis for membrane targeting by the MVB12-associated β -prism domain of the human ESCRT-I MVB12 subunit. *Proc. Natl. Acad. Sci. U. S. A.* **109**, 1901–1906 (2012).
191. Boura, E., Ivanov, V., Carlson, L. A., Mizuuchi, K. & Hurley, J. H. Endosomal sorting complex required for transport (ESCRT) complexes induce phase-separated microdomains in supported lipid bilayers. *J. Biol. Chem.* **287**, 28144–28151 (2012).
192. Morita, E. *et al.* ESCRT-III protein requirements for HIV-1 budding. *Cell Host Microbe* **9**, 235–242 (2011).
193. Alqabandi, M. *et al.* The ESCRT-III Isoforms CHMP2A And CHMP2B Display Different Effects On Membranes Upon Polymerization. *bioRxiv Biophys.* doi:10.1101/756403
194. Senju, Y. & Lappalainen, P. Regulation of actin dynamics by PI(4,5)P₂ in cell migration and endocytosis. *Current Opinion in Cell Biology* **56**, 7–13 (2019).
195. Tyrrell, D. L. & Norrby, E. Structural polypeptides of measles virus. *J. Gen. Virol.* **39**, 219–29 (1978).
196. Lamb, R. A., Mahy, B. W. & Choppin, P. W. The synthesis of sendai virus polypeptides in

- infected cells. *Virology* **69**, 116–31 (1976).
197. Ott, D. E. *et al.* Cytoskeletal proteins inside human immunodeficiency virus type 1 virions. *J. Virol.* **70**, 7734–43 (1996).
 198. Stauffer, S. *et al.* The Nucleocapsid Domain of Gag Is Dispensable for Actin Incorporation into HIV-1 and for Association of Viral Budding Sites with Cortical F-Actin. *J. Virol.* **88**, 7893–7903 (2014).
 199. Shaw, M. L., Stone, K. L., Colangelo, C. M., Gulcicek, E. E. & Palese, P. Cellular proteins in influenza virus particles. *PLoS Pathog.* **4**, (2008).
 200. Dietzel, E., Kolesnikova, L. & Maisner, A. Actin filaments disruption and stabilization affect measles virus maturation by different mechanisms. *Virol. J.* **10**, (2013).
 201. Kolesnikova, L., Bohil, A. B., Cheney, R. E. & Becker, S. Budding of Marburgvirus is associated with filopodia. *Cell. Microbiol.* **9**, 939–951 (2007).
 202. Han, Z. & Harty, R. N. Packaging of actin into Ebola virus VLPs. *Virol. J.* **2**, 1–5 (2005).
 203. Adu-Gyamfi, E., Digman, M. A., Gratton, E. & Stahelin, R. V. Single-particle tracking demonstrates that actin coordinates the movement of the Ebola virus matrix protein. *Biophys. J.* **103**, L41-3 (2012).
 204. Giuffre, R. M., Tovell, D. R., Kay, C. M. & Tyrrell, D. L. Evidence for an interaction between the membrane protein of a paramyxovirus and actin. *J. Virol.* **42**, 963–8 (1982).
 205. Bezanilla, M., Gladfelter, A. S., Kovar, D. R. & Lee, W. L. Cytoskeletal dynamics: A view from the membrane. *Journal of Cell Biology* **209**, 329–337 (2015).
 206. Reiss, N., Oplatka, A., Hermon, J. & Naor, Z. Phosphatidylserine directs differential phosphorylation of actin and glyceraldehyde-3-phosphate dehydrogenase by protein kinase C: Possible implications for regulation of actin polymerization. *IUBMB Life* **40**, 1191–1200 (1996).
 207. Nomura, W. & Inoue, Y. Contribution of phosphatidylserine to Rho1- and Pkc1-related repolarization of the actin cytoskeleton under stressed conditions in *Saccharomyces cerevisiae*. *Small GTPases* **10**, 449–455 (2019).
 208. Kay, J. G., Koivusalo, M., Ma, X., Wohland, T. & Grinstein, S. Phosphatidylserine dynamics in cellular membranes. *Mol. Biol. Cell* **23**, 2198–2212 (2012).
 209. Scott, C. C. *et al.* Phosphatidylinositol-4, 5-bisphosphate hydrolysis directs actin remodeling during phagocytosis. *J. Cell Biol.* **169**, 139–149 (2005).
 210. Li, H., Chen, G., Zhou, B. & Duan, S. Actin filament assembly by myristoylated, alanine-rich C kinase substrate-phosphatidylinositol-4,5-diphosphate signaling is critical for dendrite branching. *Mol. Biol. Cell* **19**, 4804–4813 (2008).
 211. Lee, K., Gallop, J. L., Rambani, K. & Kirschner, M. W. Self-assembly of filopodia-like structures on supported lipid bilayers. *Science (80-.).* **329**, 1341–1345 (2010).
 212. Arjonen, A., Kaukonen, R. & Ivaska, J. Cell Adhesion & Migration Filopodia and adhesion in cancer cell motility. *Cell Adhes. Migr.* **421 Cell Adhes. Migr.** **5**, 421–430
 213. Liu, A. P. & Fletcher, D. A. Actin polymerization serves as a membrane domain switch in model lipid bilayers. *Biophys. J.* **91**, 4064–4070 (2006).

CHAPTER 3. MOLECULAR DETAILS OF PARAMYXOVIRUS MATRIX PROTEIN & PLASMA MEMBRANE ASSOCIATION

3.1 Introduction

With a rise in Measles virus (MeV) infections throughout the world, the high fatality observed in Nipah virus (NiV) infections and a lack of therapeutics to treat either virus, research illuminating the mechanisms by which these viruses cause disease is paramount to the success of developing a therapeutic. Common to viruses within the paramyxovirus family, MeV and NiV coalesce with viral proteins, host proteins and membrane lipids to orchestrate budding of virions from the plasma membrane. Although each virus possesses the genetic profile to encode six proteins to fulfill the structural and functional tasks of the virus, the matrix (M) proteins of these viruses are the chief orchestrators of the viral budding process¹⁻³. In fact, MeV-M and NiV-M interact with host proteins^{4,5} as well as other viral proteins^{6,7}. While many of these interactions are conserved amongst matrix proteins from divergent paramyxoviruses, the morphology and size of particles produced is highly variable and the role that matrix proteins play in the structure of budding virions is not understood⁸. Likewise, the crystal structure of MeV-M and NiV-M has not been elucidated and the lipids these proteins interact with have yet to be identified.

The goal of this chapter is to characterize the molecular details of matrix proteins and plasma membrane interactions. Through scanning electron microscopy we elucidated the ability of MeV-M and NiV-M to generate both filamentous and spherical particles, indicating enormous plasticity in their conformation shapes and interactions with the membrane. Additionally, a combination of *in vitro* assays examining protein-lipid interactions, and confocal imaging using fluorescently tagged proteins, cell-permeable membrane modulating compounds, the co-expression of a lipid phosphatase and staining with fluorescently tagged lipids, we were able to identify PS, PI(3,5)P₂ and PI(4,5)P₂ as important lipids involved in MeV-M and NiV-M membrane interactions. These studies taken together also suggest that MeV-M traffics to and interacts with the plasma membrane through different mechanisms. MeV-M primarily relies on stereospecific interactions during association with the plasma membrane lipids, while non-specific electrostatics and weak stereospecific interactions govern NiV-M membrane association. We also broadened our study to examine the efficacy of commercially available small molecule lipid kinase inhibitors in disrupting the localization of MeV-M or NiV-M to the plasma membrane in cells and found that

a phosphatidylinositol 5-kinase inhibitor significantly reduced localization of NiV-M and MeV-M to the plasma membrane.

3.2 Materials and Methods

3.2.1 Plasmids

GFP-NiV-M and GFP-MeV-M were kind gifts from Erica Ollman Sapphire (La Jolla Institute for Immunology). EGFP-VP40 was prepared as described previously⁹. LactC2-EGFP and KRΦ-mRFP were kind gifts from Sergio Grinstein (University of Toronto). PLCδ-PH-GFP was a gift from Tamas Balla (NIH). AKT-PH-mRFP was from Tobias Meyer (Stanford University). Myc-5-phosphatase-WT (MycVPtase-WT) and Myc-5-phosphatase-Δ1 (MycVPtase-Δ1) were kind gifts from Philip Majerus (Washington University). All plasmids were transformed in DH5α competent cells and maxi-preps were prepared using a Qiagen endotoxin free maxi-prep kit.

3.2.2 Reagents

Live cell imaging solution (A14291DJ) and Pierce ECL western blotting substrate (PI32209) were purchased from ThermoFisher Scientific (Waltham, MA). Clarity Western ECL substrate (1705060) was purchased from Bio-Rad. Lipofectamine LTX + PLUS (15338100), Hoechst 33342 (PI62249), WGA Alexa Fluor™ 647 (W32466), Raffinose pentahydrate (ICN10279725), Wortmannin (AC328590010) LY294002 (44-020) and PIK93 (64-405) were all purchased from Fisher Scientific (Hampton, NH). Apilimod (HY-14644) and ISA-2011B (HY-16937) was purchased from MedChem Express (Monmouth Junction, NJ). Ultra-pure grade DMSO (97063-136) was purchased from VWR.

3.2.3 Cell Culture & Transfections

HEK293 and COS-7 cells were obtained from the American Type Culture Collection and maintained in DMEM with 10% FBS, 1% PS at 37°C and 5% CO₂. In preparation for imaging experiments, cells were washed with 1xPBS and trypsinized and seeded into the appropriate vessel 24 hours prior to transfection. For scanning electron microscopy experiments, cells were seeded onto collagen coated coverslips in 12-well plates at 30% confluency. For confocal microscopy

experiments, cells were seeded onto No 1.5 glass bottom 8 well plates (MatTek (Ashland, MA)) at 70% confluency. All transfections were performed in optiMEM (LifeTechnologies) using Lipofectamine LTX + PLUS reagent (LifeTechnologies) according to the manufacturers protocol.

3.2.4 Lipids

All lipids were purchased from Avanti Polar Lipids, Inc. (Alabaster, AL) and used without further purification. 1-palmitoyl-2-oleoyl-glycero-3-phosphocholine (POPC; #850457), 1-palmitoyl-2-oleoyl-sn-glycero-3-phosphoethanolamine (POPE; #850757), 1,2-dioleoyl-sn-glycero-3-phosphoethanolamine-N-(5-dimethylamino-1-naphthalenesulfonyl) (dansylPE; #810330), 1-palmitoyl-2-oleoyl-sn-glycero-3-phosphate (POPA; #840857), 1-palmitoyl-2-oleoyl-sn-glycero-3-phospho-L-serine (POPS; #840034), 1,2-dioleoyl-sn-glycero-3-phospho-(1'-myo-inositol-3'-phosphate) (PI(3)P; #850150), 1,2-dioleoyl-sn-glycero-3-phospho-(1'-myo-inositol-4'-phosphate) (PI(4)P; #850151), 1,2-dioleoyl-sn-glycero-3-phospho-(1'-myo-inositol-5'-phosphate) (PI(5)P; #850152), 1,2-dioleoyl-sn-glycero-3-phospho-(1'-myo-inositol-3',4'-bisphosphate) (PI(3.4)P₂; #850153), 1,2-dioleoyl-sn-glycero-3-phospho-(1'-myo-inositol-3',5'-bisphosphate) (PI(3.5)P₂; #850154), L- α -phosphatidylinositol-4,5-bisphosphate (brain PI(4.5)P₂; #840046) and 1,2-dioleoyl-sn-glycero-3-phospho-(1'-myo-inositol-3',4',5'-trisphosphate) (PI(3.4.5)P₃; #850156) were used for liposome sedimentation assays. D-erythro-sphingosine (sphingosine; #860490) and 1-oleoyl-2-(6-((4,4-difluoro-1,3-dimethyl-5-(4-methoxyphenyl)-4-bora-3a,4a-diaza-s-indacene-2-propionyl)amino)hexanoyl)-sn-glycero-3-phosphoinositol-4,5-bisphosphate (TopFluor® TMR PI(4.5)P₂; #810384) were used for cellular imaging experiments. 1,2-dioleoyl-sn-glycero-3-phosphocholine (DOPC; #850375), 1,2-dioleoyl-sn-glycero-3-phospho-L-serine (DOPS; #840035), and 1-palmitoyl-2-(dipyrrometheneboron difluoride)undecanoyl-sn-glycero-3-phosphocholine (TopFluor PC; #810281) were also used for imaging of giant unilamellar vesicle (GUVs)

All lipid stocks were prepared in CHCl₃ (with the exception of PIPs which were stored in CHCl₃:Methanol 10:1) and stored at -20°C.

3.2.5 Pharmacological Treatments

Sphingosine/Charge Neutralization Assays: Sphingosine aliquots were dried under a steady stream of N₂ and stored at -20°C until use. On each experimental day, a fresh aliquot was thawed and resuspended in ethanol to a final concentration of 75 mM. At 24 hr post transfection, cells were treated with either sphingosine (final concentration= 37.5 µM) or ethanol (1:2000 vol/vol) for 1 hour at 37°C. Cells were then prepared for live cell imaging. Since sphingosine treatment required preparation of sphingosine in ethanol, ethanol was used as the diluent and control treatment in wortmannin and apilimod experiments.

Wortmannin/PIP(3) Depletion: Wortmannin aliquots were prepared in ethanol and stored at -20°C until use. On each experimental day, a fresh aliquot of wortmannin (200 µM) was brought to RT. At 24 hr post transfection, cells were treated with either wortmannin (final concentration= 100 nM) or ethanol (1:2000 vol/vol) for 1 hour at 37°C. Cells were then prepared for live cell imaging.

Apilimod/PI(3)P Depletion: Apilimod aliquots were prepared in DMSO and stored at -20°C until use. On each experimental day, a fresh aliquot of Apilimod (200 µM) was thawed. At 24 hr post transfection, cells were treated with either Apilimod (final concentration= 200 nM) or ethanol (1:2000 vol/vol) for 1-1.5 hr at 37°C. Cells were then prepared for live cell imaging.

ISA-2011B/PIP5K α Inhibition: ISA-2011B aliquots were prepared in DMSO and stored at -20°C until use. On each experimental day, a fresh aliquot of ISA-2011B (40 mM) was thawed. At 8 hr post transfection, cells were treated with either ISA-2011B (final concentration= 40 µM) or DMSO (1:1000 vol/vol) for 24 hrs at 37°C. Cells were then fixed using 4% paraformaldehyde in PBS and stored at 4°C until imaging.

LY294002/PI3K Inhibition: LY294002 aliquots were prepared in DMSO and stored at -20°C until use. On each experimental day, a fresh aliquot of LY294002 (6 mM) was thawed. At 8 hr post transfection, cells were treated with either LY294002 (final concentration= 6 µM) or DMSO (1:1000 vol/vol) for 24 hrs at 37°C. Cells were then fixed using 4% paraformaldehyde in PBS and stored at 4°C until imaging.

PIK93/PI3K and PI4K Inhibitor: PIK93 aliquots were prepared in DMSO and stored at 4°C until use. On each experimental day, a fresh aliquot (150 µM) was thawed. At 8 hr post transfection, cells were treated with either PIK93 (final concentration= 0.15 µM) or DMSO

(1:1000 vol/vol) for 24 hrs at 37°C. Cells were then fixed using 4% paraformaldehyde in PBS and stored at 4°C until imaging.

3.2.6 Liposome (LUVs) Preparation

Large unilamellar vesicles (LUVs) were prepared by combining POPC, POPE and dansylPE with either phospholipids, phosphoinositides, or both (at the indicated concentrations) and dried under a steady stream of N₂. In each experiment, addition of negatively charged lipids was compensated with an equal mol% decrease in POPC, while POPE (9%) and dansylPE (1%) were held constant. On each experimental day, lipid films were brought to RT and hydrated in extrusion buffer (250 mM raffinose pentahydrate, 50 mM Tris, 150 mM NaCl, pH 7.4) for 45 min at 37 °C. LUVs were vigorously vortexed prior to extrusion through a 200 nm Whatman polycarbonate filter (GE Healthcare). LUVs were diluted with 3x vol. of LUV buffer (50 mM Tris, 150 mM NaCl, pH 7.4) and centrifuged at 50,000 x g for 15 min at RT. The supernatant was discarded and the pelleted LUVs were resuspended in 1x vol. of LUV buffer. For NaCl dependent liposome sedimentation assays, pelleted LUVs were resuspended in 1x vol of LUV buffer with the indicated concentration of NaCl (Tris and pH were held constant).

3.2.7 Liposome Sedimentation Assays

Liposome sedimentation assays were performed as described in detail in Julkowska et al. 2013¹³. Recombinant NiV-M and MeV-M were kind gifts from Erica Ollman Sapphire (La Jolla Institute for Immunology). In brief, NiV-M and MeV-M (0.01 mg/mL) were incubated with LUVs (400 mM) at a 1:1 volume for 30 min at RT. Following incubation, protein-bound LUVs (pellet fraction) were separated from unbound protein (supernatant fraction) through centrifugation. Samples were then subjected to SDS-PAGE and western blotting. Equal volumes of pellet and supernatant fractions were loaded into a 10% SDS-PAGE gel and separated at 150V for 45 min at RT. Samples were then transferred to a nitrocellulose membrane (100 V 45 min in ice) using ice cold transfer buffer. Membranes were blocked with 5% non-fat milk-TBST (20 mM Tris, 150 mM NaCl, 0.1% (w/v) Tween® 20, pH 7.4) and subsequently probed for their respective antibodies (**See Table 1 in Appendix**). HRP-conjugated antibodies were detected using Pierce ECL reagent or Clarity ECL substrate on an Amersham imager 600 (GE Healthcare). Percent (%) protein bound

was determined using densitometry analysis in ImageJ, according to the following equation: % protein bound= (density_{pellet} / density_{SNT+pellet}) *100. Values are reported as mean \pm standard deviation. Unless otherwise indicated, 3 replicates were performed in duplicate.

3.2.8 Scanning Electron Microscopy

Cells on cover slips were fixed in 2.5% glutaraldehyde in 0.1 M sodium cacodylate buffer, post-fixed in buffered 1% osmium tetroxide, dehydrated with a graded series of ethanol, and dried in a Tousimis 931 critical point dryer. Dried samples were coated with platinum in a Cressington 208HR sputter coater and imaged in a FEI Nova NanoSEM 200.

3.2.9 Cellular Confocal Microscopy

Prior to imaging, cells were post-stained with Hoechst 33342 (final concentration = 16 μ M) and WGA Alexa FluorTM 647 (final concentration= 5 μ g/mL). Live cell imaging was then performed in live cell imaging solution or cells were fixed with 4% paraformaldehyde (in PBS) and stored at 4°C and protected from light until imaging. Confocal imaging experiments were performed on the Zeiss LSM 880 upright microscope using a LD C-Apochromat 40x 1.1 numerical aperture water objective or Plan Apochromat 63x 1.4 numerical aperture oil objective. A 405 nm laser was used to excite Hoechst stain, and Argon lasers were used to excite GFP (488 nm), mCherry/RFP/TopFluor® (561 nm) and WGA Alexa FluorTM 647 (633 nm). Percent (%) cells with plasma membrane localization was ratiometrically determined by counting the number of cells with GFP fluorescence signal localized at the plasma membrane compared to the number of cells without GFP fluorescence signal localized at the plasma membrane. In each of the 3 replicates performed, at least 45 cells for each condition were counted. Values are reported as the mean \pm standard deviation.

3.3 Results

3.3.1 MeV-M and NiV-M generate spherical and filamentous cell surface extensions

The ability of paramyxovirus matrix proteins to bud independently of other viral proteins has been established^{14,15}; however, members of the paramyxovirus family have variable viral

particle morphologies. Similarly to other matrix proteins within the paramyxovirus family^{16,17}, upon incubation with anionic lipids both MeV-M and NiV-M self-assemble into long filaments (data now shown; done in collaboration with Mike Norris at LaJolla Institute for Immunology; manuscript in preparation). To delineate if this phenomenon is relevant in cells and indicative of viral budding, scanning electron microscopy (SEM) experiments were performed. SEM permits low nanometer resolution imaging of cell surface topography and morphology, making it a suitable technique to visualize viral budding.

To interpret MeV-M and NiV-M mediated budding, both MeV-M and NiV-M were transiently expressed in HEK293 and COS-7 cells for 24 hours. HEK293 and COS-7 cells were selected based on their high transfection efficiency, minimal cellular filopodia, and previous use in MeV, NiV, EBOV, and MARV studies^{18–22}. Mock transfections were performed to generate a baseline for typical cell surface morphology. In concordance with previous findings, a low degree of filopodia were observed in HEK293 cells (**Figure 3.1 a top panel**) albeit to a higher level than was observed in COS-7 cells (**Figure 3.1 b left column**).

Next, to positively identify matrix protein driven budding, HEK293 and COS-7 cells were transiently transfected with eVP40 for 24 hours. Analogous to MeV-M and NiV-M, eVP40 localizes to the plasma membrane and generates budding of viral like particles (VLPs) which are nearly indistinguishable from authentic EBOV virions²³. As depicted in **Figure 3.1 b (right column)**, eVP40 expression in both HEK293 and COS-7 cells led to an abundance of filaments

extending from the cell surface. These observations agree with the widely reported intrinsic ability

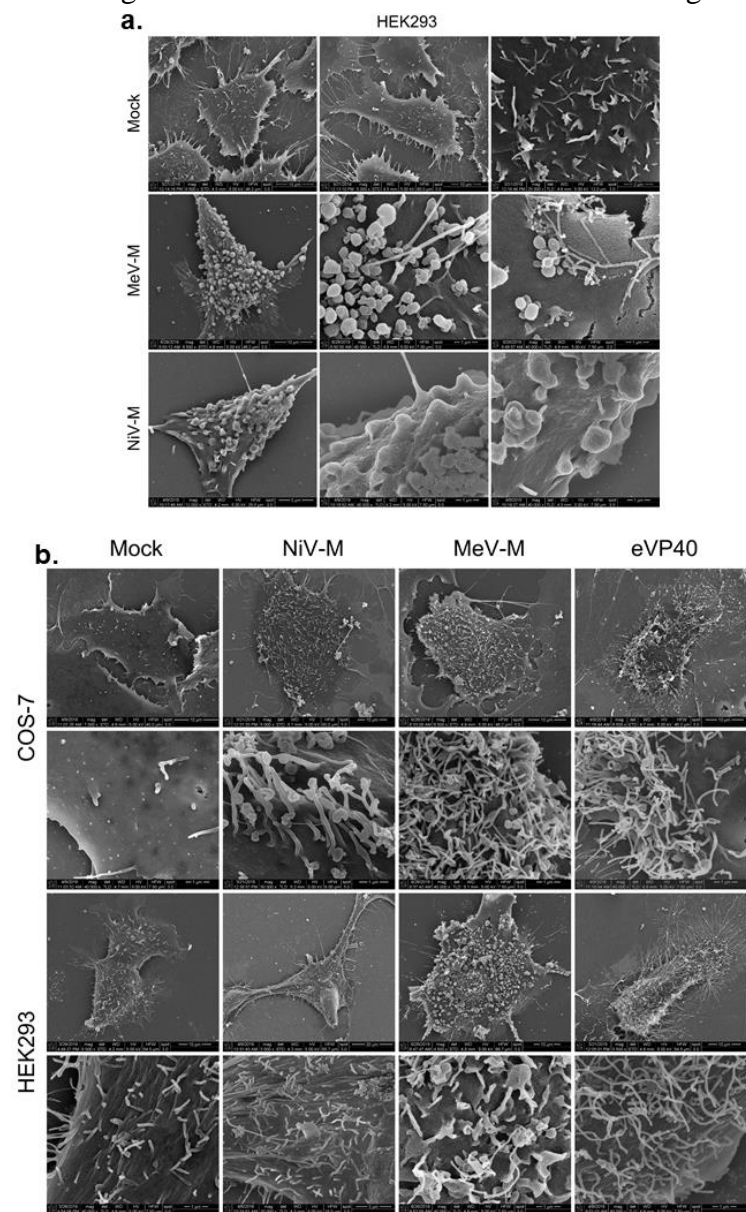


Figure 3.1. Morphology of NiV-M and MeV-M viral budding using SEM. COS-7 and HEK293 cells were transfected with either NiV-M, MeV-M or eVP40. After 24 hours of transfection, cells were fixed using 2.5% glutaraldehyde and processed for SEM imaging. (a) Representative micrographs of HEK293 cells expressing the indicated protein (or mock transfected) showing spherical budding particles emanating from the cell surface. Mock (top panel), MeV-M (middle panel), NiV-M (bottom panel) (b) Representative micrographs of COS-7 cells (top two panels) and HEK293 cells (bottom two panels) expressing the indicated protein (or mock transfected) showing filamentous budding particles emanating from the cell surface. Mock (left panel), NiV-M (middle-left panel), MeV-M (middle-right panel), eVP40 (right panel). SEM: scanning electron microscopy.

of eVP40 to produce filamentous VLPs on the cell surface.

Finally, to define the morphology of MeV-M and NiV-M driven budding, HEK293 and COS-7 cells were transfected with the respective matrix protein for 24 hours and subsequently analyzed by SEM. In agreement with the literature, expression of MeV-M and NiV-M in HEK293 and COS-7 cells resulted in an abundance of spherical protrusions emanating from the cell surface (**Figure 3.1 a middle and bottom panels**). However, a large population of filamentous protrusions were also observed in cells expressing MeV-M and NiV-M, similar to the filamentous VLPs observed upon expression of eVP40 (**Figure 3.1 b middle columns**). Although MeV-M and NiV-M formed filamentous VLPs, the extent of filamentous VLPs were markedly lower than upon eVP40 expression. This is possibly a result of MeV-M and NiV-M having the ability to form both spherical and filamentous VLPs, while eVP40 only forms filamentous VLPs. These SEM experiments indicate that filamentous

structures observed when recombinant protein is incubated with anionic lipids is not an artifact of *in vitro* M proteins and membrane interactions and occurs during the budding process; however, the mechanisms by which these M proteins assemble *in vitro* and in cells to form VLPs is not understood.

3.3.2 Determining MeV-M and NiV-M lipid affinity

There is limited information available detailing how MeV-M and NiV-M interact with lipids at the plasma membrane. To shed light on the specific molecular interactions occurring between the plasma membrane and M proteins during viral budding, liposome sedimentation assays were performed. Liposome sedimentation assays are a simple and conventional technique to quantitatively assess protein affinity and specificity to lipids²⁴. Upon incubation of a protein with LUVs, protein that associates with the LUVs can be separated from unbound protein through centrifugation, rendering a supernatant (unbound protein) and pellet fraction (protein associated with LUVs). In each assay, protein binding to control LUVs (PC:PE) was established. To determine protein affinity to specific anionic lipids, the mol% of PC was reduced to compensate the addition of each anionic lipid. To calculate protein binding, the protein band density in the supernatant and pellet fraction were calculated and % protein bound was determined by the pellet density / total density. Neither MeV-M (**Figure 3.2 a lane 1-2**) or NiV-M (**Figure 3.2 b lane 1-2**) displayed specific binding to control LUVs, with less than 15% of MeV-M and less than 10% NiV-M found within the pellet fractions (**Figure 3.2 c**).

3.3.2.1 MeV-M and NiV-M associate with phosphatidylserine enriched membranes

Our next goal was to establish if MeV-M or NiV-M interacts with any anionic phospholipids which reside within the plasma membrane, such as PA and PS, which have been implicated in numerous viral matrix protein-membrane interactions²⁵⁻²⁸. Therefore, 2.5% PA or 30% PS were added to LUVs. Although PA carries a negative charge (-1 to -2), neither MeV-M or NiV-M exhibited any binding to PA beyond the background binding to control LUVs (**Figure 3.2 a-b lanes 3-4**). Conversely, both MeV-M and NiV-M bound significantly to PS, which possesses a -1 charge at physiological pH (**Figure 3.2 a-b lanes 5-6**). Interesting, incubation of NiV-M with LUVs containing 30% PS resulted in 43% of NiV-M in the pellet fraction (**Figure 2**

c), while 72% of MeV-M was associated in the pellet following incubation with LUVs containing 30% PS (**Figure 3.2 c**). These results indicate that both MeV-M and NiV-M preferentially associate with PS and not PA, and that the two proteins may be employing alternative mechanisms for associating with the plasma membrane as indicated by the observation that MeV-M binding to PS membranes is almost 2x more abundant than NiV-M.

3.3.2.2 MeV-M and NiV-M differentially associate with phosphatidylinositol membranes

An important class of phospholipids which reside within the plasma membrane are the phosphatidylinositols. The phosphatidylinositol lipid species comprise a diverse class of lipid molecules which can be mono, di, and tri phosphorylated at the D3, D4, and D5 position of the inositol ring. Importantly, phosphatidylinositols are increasingly regarded as important lipids to both normal cell functions (e.g. cytoskeletal dynamics²⁹⁻³¹) and viral matrix protein function (e.g. eVP40³² and HIV-1-gag³³). Therefore, MeV-M and NiV-M association to each of the phosphatidylinositol species was evaluated using liposome sedimentation assays.

MeV-M and NiV-M displayed minimal binding to each of the mono-phosphorylated PI species (PI3P, PI4P, PI5P) (**Figure 3.2 d lanes 1-6, Figure 3.2 e lanes 1-6, Figure 3.2 f**). However, differing binding profiles were observed for the di-phosphorylated PI species for MeV-M and NiV-M. MeV-M displayed strong binding to PI(3,5)P₂ and PI(4,5)P₂, with 60% of MeV-M present in the pellet fraction for both lipid species (**Figure 3.2 d lanes 9-12, Figure 3.2 f**). Conversely, NiV-M only displayed strong binding to PI(4,5)P₂, with ~100% of NiV-M present in the pellet fraction (**Figure 3.2 e lanes 11-12, Figure 3.2 f**). Neither protein associated with PI(3,4)P₂. These results indicate that the phosphate group located on the D5 position is important to MeV-M association with membranes while phosphorylation at both D4 and D5 is important for NiV-M association with membranes. Furthermore, MeV-M did not exhibit strong binding to membranes containing the tri-phosphorylated PI, PI(3,4,5)P₃ (PIP₃) (**Figure 3.2 d lanes 13-14, Figure 3.2 f**), while 70% of NiV-M was present in the pellet fraction of PIP₃ containing membranes (**Figure 3.2 e lanes 3-14, Figure 3.2 f**). The ability of NiV-M to associate with PIP₃ containing membranes is in agreement with our previous liposome sedimentation assay data, as PIP₃ contains a phosphate

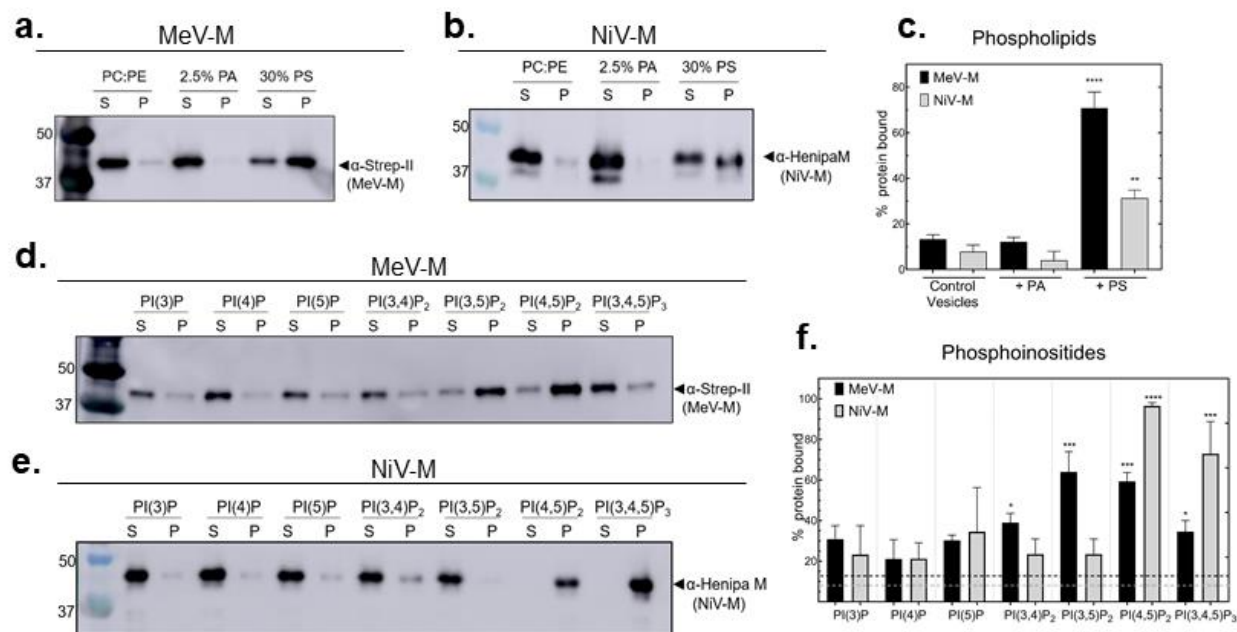


Figure 3.2. Lipid binding properties of MeV-M and NiV-M. Liposome sedimentation assays and western blotting were performed on LUVs with varying anionic lipids and MeV-M or NiV-M. Supernatant (unbound protein) and pellet (protein bound to LUVs) were separated and analyzed through western blotting using a HRP-conjugated antibodies. **(a-c)** Phospholipid binding properties of MeV-M and NiV-M. Representative western blot showing MeV-M **(a)** and NiV-M **(b)** bind to LUVs containing 30% PS but not control vesicles (PC:PE) or PA. **(c)** Densitometry analysis was performed on supernatant and pellet fraction bands to determine % MeV-M bound. % protein bound was calculated using the following equation= pellet density/total band density; where total band density=supernatant+ pellet band density. **(d-f)** Phosphatidylinositol binding properties of MeV-M and NiV-M. **(d)** Representative western blot showing MeV-M binds to LUVs containing PI(3.5)P₂ and PI(4.5)P₂. **(e)** Representative western blot showing NiV-M binds to LUVs containing PI(4.5)P₂ and PI(3.4.5)P₃. **(f)** Densitometry analysis was performed on supernatant and pellet fraction bands to determine % NiV-M bound, which was calculated the same as **(c)**. Black and gray dashed line indicates extent of MeV-M and NiV-M binding to control vesicles, respectively. Values are reported as mean \pm s.d. N=5-6 n=3. A one-way ANOVA with multiple comparisons was performed. ****p<0.0001, ***p<0.0005 **p<0.003 *p<0.05. PC: phosphatidylcholine; PE: phosphatidylethanolamine; PA: phosphatidic acid; PS: phosphatidylserine; PIP: phosphatidylinositol- phosphate; S: supernatant fraction; P: pellet fraction; LUVs: large unilamellar vesicles;

group at both D4 and D5. Taken together with the PS binding profile, our results indicate that MeV-M and NiV-M are interacting with anionic lipids within the plasma membrane through different mechanisms.

3.3.3 Additive and synergistic binding

Within the plasma membrane, peripheral proteins can interact with multiple lipid binding partners as a mechanism to increase the strength of the protein-membrane interaction. Therefore, MeV-M and NiV-M affinity to membranes containing multiple lipid binding partners identified in

Figure 3.2 was assessed through liposome sedimentation assays. As ~100% NiV-M was located in the pellet fraction of LUVs with 2.5% PI(4,5)P₂ in **Fig. 2** for this experiment the amount of PI(4,5)P₂ was reduced to 1% in order to observe an increase upon addition of PS to the LUVs. Furthermore, MeV-M binding to LUVs saturated at 65% of protein in the pellet fraction (**Figure 3.3 a-b**), therefore the PS content was reduced to 15% (from 30%) and PI content was reduced to 1% (from 2.5%) in order to detect an increase in binding with PI species were incorporated into the LUVs.

To first evaluate MeV-M affinity to membranes containing more than one anionic lipid binding partner identified from Fig. 2, baseline binding of MeV-M to LUVs containing 15% PS, 1% PI(3,5)P₂ or 1% PI(4,5)P₂ was established. Binding of MeV-M to 15% PS, 1% PI(3,5)P₂ and 1% PI(4,5)P₂ was observed (**Figure 3.3 c lanes 1-6**), with ~30% of MeV-M residing in the pellet fraction for both 15% PS and 1% PI(3,5)P₂ LUVs and ~10% of MeV-M within the pellet fraction for 1% PI(4,5)P₂ LUVs (**Figure 3.3 d**). When both 15% PS and 1% PI(3,5)P₂ were incorporated into LUVs, the bound fraction of MeV-M increased from ~30% to ~70% (**Figure 3.3 c lanes 7-8, Figure 3.3 d**), indicative of an additive effect of each lipid on MeV-M lipid binding. Conversely, an increase binding of MeV-M to membranes was observed with 15% PS and 1% PI(4,5)P₂ were incorporated into LUVs (**Figure 3.3 c lanes 9-10**) with binding increased to ~70% (**Figure 3.3 d**).

Next, to evaluate NiV-M affinity to membranes containing more than one anionic lipid, baseline binding of NiV-M to 30% PS LUVs and 1% PI(4,5)P₂ vesicles was established with ~40% of NiV-M and ~10% of NiV-M in the pellet fraction, respectively (**Figure 3.3 e lanes 1-4, Figure 3.3 f**). Strikingly, inclusion of both PS and PI(4,5)P₂ increased NiV-M binding to ~95% (**Figure 3.3 e lane 5-6, Figure 3.3 f**), a convincing indication that NiV-M association to membranes is synergistically enhanced when both PS and PI(4,5)P₂ are incorporated into membranes. Taken together, these results indicate that the presence of both PS and PI(4,5)P₂ into membranes synergistically enhanced MeV-M and NiV-M binding to membranes. PS and PI(4,5)P₂ are the predominant anionic lipids found within the plasma membrane³⁴, therefore synergistic binding of MeV-M and NiV-M to these lipids may be a mechanism for each protein to target to the plasma membrane where it facilitates their critical viral budding function.

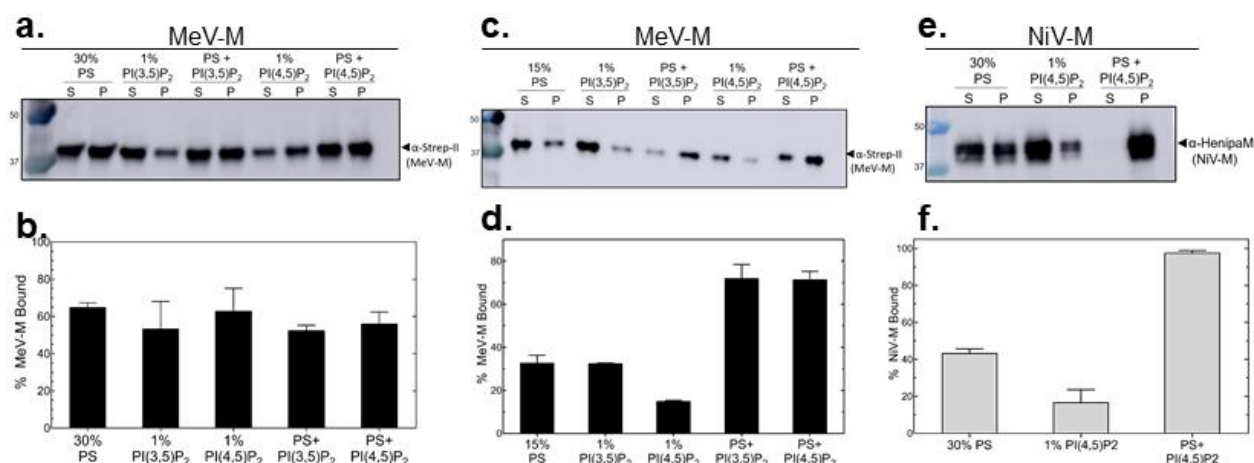


Figure 3.3. Effect of multiple lipids on MeV-M and NiV-M affinity to liposomes. Liposome sedimentation assays and western blotting were performed on LUVs with varying anionic lipids and MeV-M or NiV-M. Supernatant (unbound protein) and pellet (protein bound to LUVs) were separated and analyzed through western blotting using a HRP-conjugated antibodies. **(a-b)** MeV-M liposome sedimentation assays using LUVs with 30% PS +/- PIP shows MeV-M binding saturates ~60%. **(a)** Representative western blot showing MeV-M binds to each anionic lipid composition **(b)** Densitometry analysis was performed on supernatant and pellet fraction bands to determine % MeV-M. % protein bound was calculated using the following equation= pellet density/total band density; where total band density=supernatant+ pellet band density. **(c-d)** MeV-M liposome sedimentation assays using LUVs with 15% PS +/- PIP shows MeV-M binds in an additive fashion (PS+PI(3,5)P₂) and synergistic mechanism (PS+PI(4,5)P₂). **(d)** Densitometry analysis was performed on supernatant and pellet fraction bands to determine % MeV-M bound. **(e-f)** NiV-M liposome sedimentation assays using LUVs with 30% PS +/- PIP shows synergistic binding with LUVs containing both PS and PI(4,5)P₂ **(e)** Representative western blot showing NiV-M binding to LUVs containing 30%PS, 1% PI(4,5)P₂ and PS+PI(4,5)P₂ **(f)** Densitometry analysis was performed on supernatant and pellet fraction bands to determine % NiV-M bound, which was calculated the same as in **(b&d)**. Values are reported as mean \pm s.d. N=5-6 n=3. PC:PE were used in each LUV composition and mol% PC was modified to account for changes in anionic lipid mol%. PC: phosphatidylcholine; PE: phosphatidylethanolamine; PA: phosphatidic acid; PS: phosphatidylserine; PIP: phosphatidylinositol- phosphate; S: supernatant fraction; P: pellet fraction; LUVs: large unilamellar vesicles;

3.3.4 MeV-M and NiV-M interact with anionic lipids through electrostatic and stereospecific interactions

Lastly, the biochemical nature of MeV-M and NiV-M interactions to anionic lipids was assessed through liposome sedimentation assays. Different modes of protein-lipid interactions are present within the cell, and the molecular basis of these interactions have direct implications on the biology they carry out³⁵⁻³⁷. Specifically, electrostatics, hydrophobics, and stereospecific interactions are the predominant mechanisms by which peripheral proteins interact with lipids (reviewed in Chapter 2). Therefore, to identify which mechanism underlies MeV-M and NiV-M association with lipids, liposome sedimentation assays were performed with increasing NaCl conditions. When a protein interacts with a binding partner through charge complementary

electrostatic interactions increasing the NaCl concentration will interfere with binding, and a reduction of protein in the pellet fraction would be observed. However, when stereospecific interactions are employed between a protein and binding partner, an increase in NaCl concentration does not affect the interaction and therefore the amount of protein in the pellet fraction should not significantly change. To ensure increasing NaCl concentration from 150 mM, 300 mM and 500mM did not affect protein binding to control vesicles, background binding of both MeV-M and NiV-M to control vesicles (PC:PE) was evaluated in each NaCl condition and no significant binding was observed (**Figure 3.4 a-b top panels, Figure 3.4 c-d**).

3.3.4.1 Electrostatics govern binding to phosphatidylserine

First the effect of increasing NaCl on MeV-M and NiV-M binding to phosphatidylserine was determined. In the presence of 150 mM NaCl both MeV-M (**Figure 3.4 a**) and NiV-M (**Figure 3.4 b**) were found in the pellet fraction. When NaCl was increased to 300 mM, MeV-M and NiV-M binding to 30% PS was reduced by a factor of 2 (**Figure 3.4 c-d**). Furthermore, increasing NaCl to 500 mM resulted in a further loss of MeV-M and NiV-M binding to LUVs containing 30% PS (**Figure 3.4 a-d**). These findings support the hypothesis that both MeV-M and NiV-M associate with PS through primarily electrostatic interactions, a mechanism similar to mVP40 membrane association²⁵.

3.3.4.2 MeV-M and NiV-M interact with phosphatidylinositol lipids through stereospecific interactions

Lastly, the effect of increasing NaCl on MeV-M and NiV-M binding to PI binding partners identified in **Figure 3.2** was determined. MeV-M strongly associated with PI(3,5)P₂ and PI(4,5)P₂ LUVs (**Figure 3.4 a, c**) while NiV-M strongly associated with PI(4,5)P₂ LUVs (**Figure 3.4 b, d**) under 150 mM NaCl conditions, in agreement with our previous liposome sedimentation assay data (**Figure 3.2**). Surprisingly, following incubation of MeV-M with LUVs containing 2.5% PI(3,5)P₂ or 2.5% PI(4,5)P₂ in 300 mM NaCl conditions, binding of MeV-M to each LUV composition was not significantly different than binding of MeV-M in 150 mM NaCl conditions (**Figure 3.4 a, c**). Furthermore, when binding was assessed in 500 mM NaCl conditions, MeV-M association to each LUV composition was reduced by a factor of 2 (compared to 150 mM NaCl) (**Figure 3.4 a, c**). These findings support the hypothesis that MeV-M associates to both PI(3,5)P₂

and PI(4,5)P₂ through stereospecific interactions, indicated by the finding that in 500 mM NaCl conditions, although the extent of binding was significantly less than in 150 mM NaCl, more than 20% of protein was still associated with the lipids in 500 mM NaCl buffer. Lastly, increasing the NaCl to 300 mM significantly reduced NiV-M binding to LUVs containing 2.5% PI(4,5)P₂, and when examined under 500 mM NaCl conditions NiV-M binding to 2.5% PI(4,5)P₂ LUVs was reduced to levels near binding of NiV-M to background vesicles (**Figure 3.4 b, d**). Taken together, these results further support the hypothesis that MeV-M and NiV-M are interacting with the membrane through differing mechanism, where MeV-M may employ tighter close-range stereospecific interactions with two PI species, while NiV-M engages with PI(4,5)P₂ through selective but more non-specific electrostatic interactions.

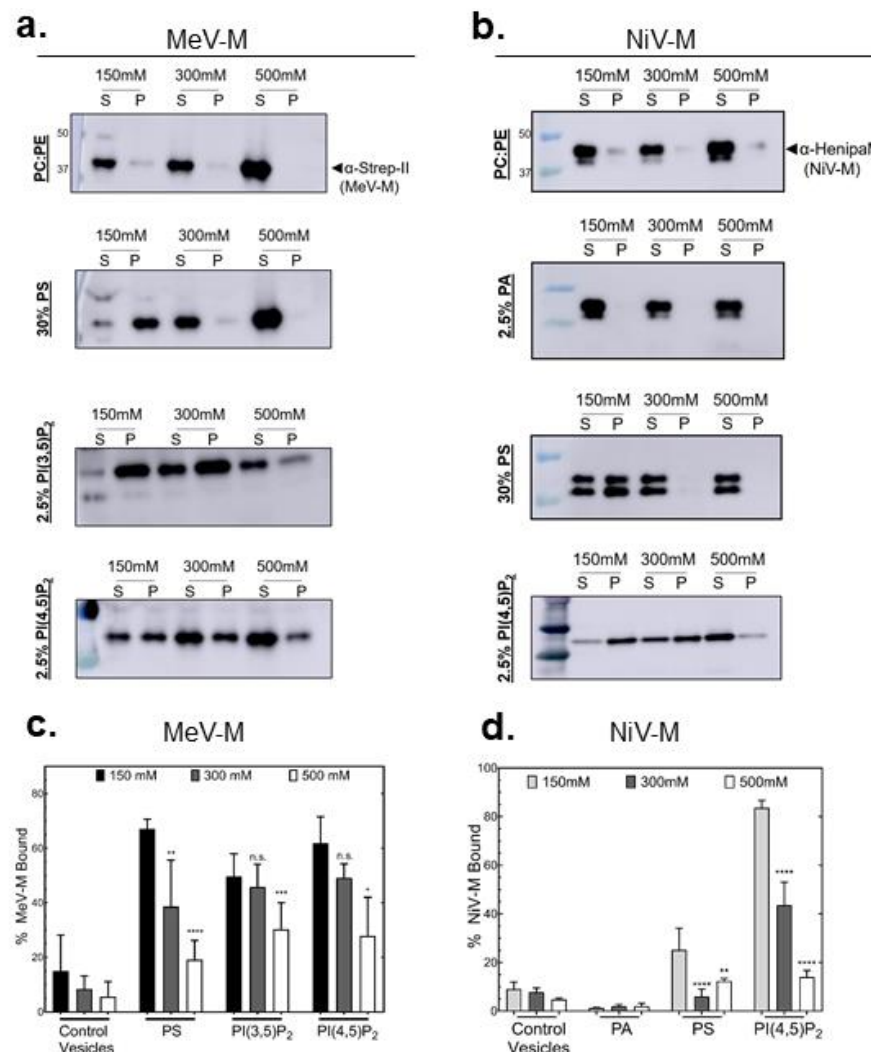


Figure 3.4. Evaluation of changing NaCl on MeV-M and NiV-M interaction with lipids.

Liposome sedimentation assays and western blotting were performed on LUVs with varying anionic lipids and MeV-M or NiV-M under different NaCl conditions (150 mM, 300 mM, 500 mM). Supernatant (unbound protein) and pellet (protein bound to LUVs) were separated and analyzed through western blotting using HRP-conjugated antibodies. **(a-b)** Representative western blots of MeV-M **(a)** and NiV-M **(b)** showing the effect of increasing NaCl on their affinity to LUVs with varying lipid compositions. **(c-d)** Densitometry analysis was performed on supernatant and pellet fraction bands to determine % MeV-M bound **(c)** and % NiV-M bound **(d)** for each lipid composition in each NaCl condition. % protein bound was calculated using the following equation = pellet density/total band density; where total band density = supernatant + pellet band density. Control vesicles are PC:PE. Additionally, PC:PE were used in each LUV composition and mol% PC was modified to account for changes in anionic lipid mol%. Values are reported as mean \pm s.d. N=5-6 n=3. A one-way ANOVA with multiple comparisons was performed. ****p<0.0001, ***p<0.0005 **p<0.003 *p<0.05.

3.3.5 Live cell imaging depicts differential mechanisms of membrane association

3.3.5.1 Investigating charge sensing mechanisms

To test the conclusions drawn from the *in vitro* liposome sedimentation assays, we examined the lipid-dependent mechanisms for MeV-M and NiV-M association with the plasma membrane in cells. We first aimed to quantify the contribution of non-specific anionic charge sensing mechanisms within the interaction of MeV-M or NiV-M to the plasma membrane by treating cells with sphingosine (**Figure 3.5**). Sphingosine is a membrane permeable base which upon addition to cells, incorporates into the inner-leaflet of the plasma membrane effectively neutralizing the negatively charged surface of the inner leaflet³⁸.

The effect of membrane charge neutralization on MeV-M or NiV-M plasma membrane localization was evaluated using confocal microscopy of COS-7 cells transiently expressing GFP-MeV-M or GFP-NiV-M treated with sphingosine for 1 hour at 24 hours post transfection. Following sphingosine treatment, cells were imaged and cells with and without plasma membrane fluorescence were counted. COS-7 cells transiently expressing KR ϕ -RFP and EGFP-eVP40 were used as controls, as KR ϕ -RFP is a polycationic fluorescent membrane charge sensor which localizes to the plasma membrane through electrostatics³⁹ and EGFP-eVP40 plasma membrane localization has been shown to be mediated through stereospecific interactions and unaffected by sphingosine treatment³². In cells expressing KR ϕ -RFP, sphingosine treatment significantly reduced the percentage of cells with KR ϕ plasma membrane localization by ~60% ($p < 0.0001$) (**Figure 3.5 a-b**). Additionally, eVP40 plasma membrane localization was not significantly affected by sphingosine treatment (**Figure 3.5 b-c**), validating the previously published finding that eVP40 associates to the plasma membrane through stereospecific interactions³².

Next we evaluated the effect of sphingosine treatment on GFP-NiV-M and GFP-MeV-M plasma membrane localization. In vehicle treated cells, GFP-NiV-M and GFP-MeV-M membrane localization profile was similar, where ~70% and ~65%, respectively, of cells exhibited high fluorescence at the plasma membrane in cells expressing GFP-NiV-M (**Figure 3.5 b, d top panel**) or GFP-MeV-M (**Figure 3.5 b, e top panel**). Following 1 hr of sphingosine treatment, a significant reduction in cells with plasma membrane fluorescence was observed in GFP-NiV-M expressing cells (**Figure 3.5 b, e bottom panel**), with only ~33% of cells displaying plasma membrane fluorescence compared to 70% in vehicle treatment ($p < 0.0001$). On the contrary, sphingosine had

no effect on the percentage of cells with high fluorescence intensity at the plasma membrane in cells expressing GFP-MeV-M (~65% in vehicle treated and ~62% in sphingosine treated cells;

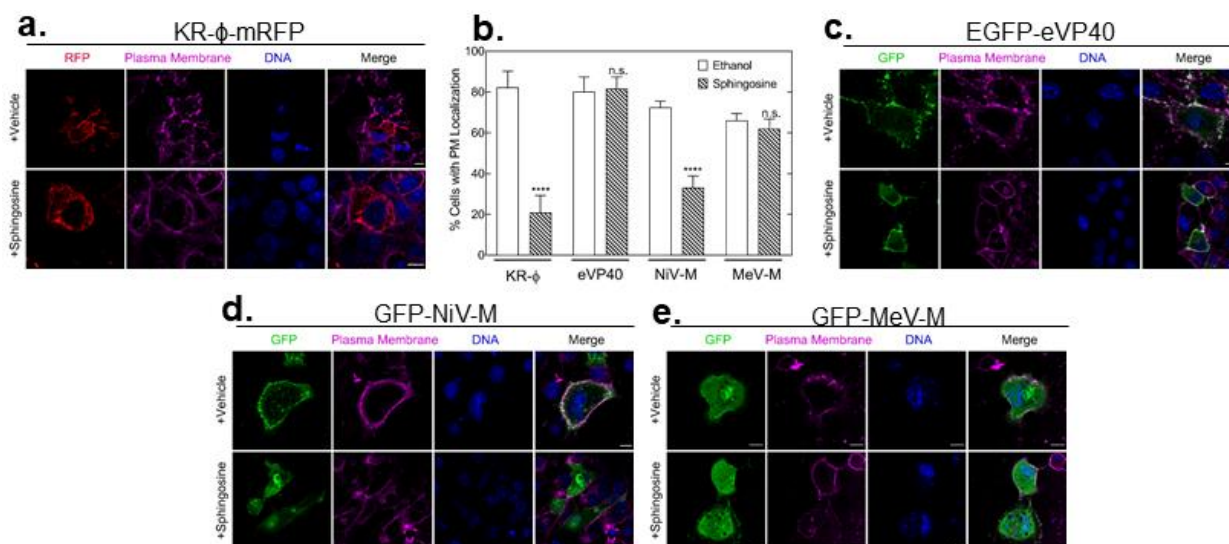


Figure 3.5. Effect of membrane charge neutralization on peripheral protein plasma membrane localization. COS-7 cells expressing the indicated GFP/mRFP-fused proteins for 24 hours were treated with the membrane permeable base, 37.5 μ M sphingosine (or ethanol vehicle; 1:2000 vol:vol), for 1 hour at 37°C prior to staining with WGA AlexaFluor™647 (plasma membrane stain) and Hoescht (DNA stain) and subsequent imaging on a fluorescence confocal microscope. Cells with or without GFP fluorescence signal localized to the PM were counted to calculate the % of cells with PM localization. **(a,c,d,e)** Representative confocal images of COS-7 cells expressing each indicated protein: **(a)** Polycationic fluorescent probe KR ϕ -mRFP +/- sphingosine treatment **(c)** filovirus matrix protein EGFP-eVP40 +/- sphingosine treatment **(d)** GFP-NiV-M +/- sphingosine treatment **(e)** GFP-MeV-M +/- sphingosine treatment. **(b)** % cells with PM localization was determined by counting the number of cells with high GFP fluorescence signal intensity at the PM and the number of cells without GFP fluorescence signal intensity at the PM. In each replicate, a minimum of 45 cells were counted. Scale bar= 5 μ m. Values are reported as mean \pm s.d. $N \geq 135$ $n=3$. A one-way ANOVA with multiple comparisons was performed (compared to the vehicle treatment group for that protein). **** $p < 0.0001$. WGA: wheat germ agglutinin; PM: plasma membrane

Figure 3.5 b, e). These observations validate our *in vitro* liposome sedimentation assays where NiV-M association to LUVs was selective for PI(4,5)P₂ but also relied on a degree on non-specific electrostatics, and this interaction was perturbed by increasing NaCl concentration while MeV-M association to LUVs was unaltered by increasing NaCl concentrations.

3.3.5.2 MycVptase and PI(4,5)P₂ depletion

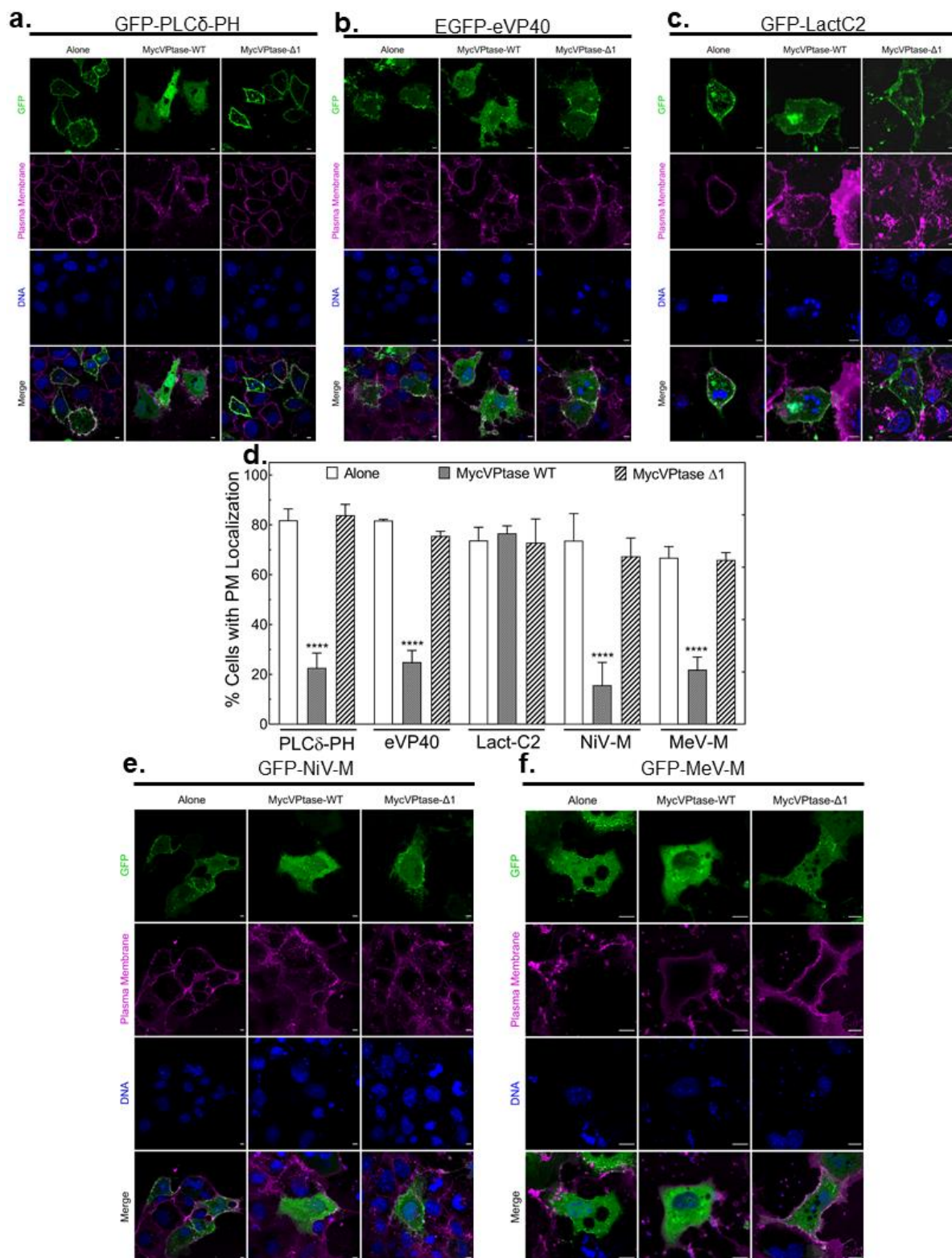
We next evaluated the hypothesis that both MeV-M and NiV-M associate with the plasma membrane by interacting with PI(4,5)P₂. To address this we co-expressed GFP-NiV-M and GFP-MeV-M with MycVptase-WT, a phosphoinositide 5-phosphatase which cleaves the phosphate

from the D5 position of PI(4,5)P₂, which reduces PI(4,5)P₂ levels at the plasma membrane (**Figure 3.6**). This expression system has been used previously to study HIV-1 gag plasma membrane localization³³. As a control, a catalytically inactive mutant was also used (MycVPtase-Δ1). Twenty-four hours post transfection, fluorescence confocal microscopy was performed and the number of cells with and without high GFP fluorescence at the plasma membrane were counted to determine the % cells with plasma membrane GFP localization. COS-7 cells co-expressing the PI(4,5)P₂ sensor GFP-PLCδ-PH (**Figure 3.6 a**), PS sensor GFP-Lact-C2 (**Figure 3.6 b**), or EGFP-eVP40 (**Figure 3.6 c**) alone or with the active or inactive MycVPtase were also used as controls. In agreement with previous findings, PLCδ-PH was localized to the plasma membrane when expressed alone (~82% of cells; **Figure 3.6 a left column, Figure 3.6 d**) and when co-expressed with MycVPtase-Δ1 (~84% of cells) (**Figure 3.6 a middle column, Figure 3.6 d**). On the other hand, PLCδ-PH was predominately cytosolically located upon co-expression with MycVPtase-WT (**Figure 3.6 a right column**) with only ~23% of cells maintaining GFP fluorescence at the plasma membrane (**Figure 3.6 d**), a ~60% reduction ($p < 0.0001$) in the percentage of cells with high GFP fluorescence at the plasma membrane. Similar results were observed for eVP40 (**Figure 3.6 b, d**), which corroborates previous reports that eVP40 plasma membrane localization is dependent on PI(4,5)P₂³². To confirm that expression of MycVPtase does not interfere with peripheral protein binding to other anionic lipids (e.g. PS) within the plasma membrane, cells expressing Lact-C2 alone (**Figure 3.6 c left column**) or co-expressed with either MycVPtase-WT (**Figure 3.6 c middle panel**) or MycVPtase-Δ1 (**Figure 3.6 c right panel**) were also imaged. **Figure 3.6 d** highlights that across each condition, Lact-C2 localized to the plasma membrane in ~75% of cells, indicating that enzymatic depletion of PI(4,5)P₂ did not affect PS within the plasma membrane or peripheral protein binding to PS (in agreement with previous report³³).

Finally, confocal microscopy was performed to determine the effects of enzymatic depletion of PI(4,5)P₂ on NiV-M and MeV-M plasma membrane localization (**Figure 3.6 d-f**). When expressed alone, ~75% of cells expressing NiV-M (**Figure 3.6 d, Figure 3.6 e left column**) and ~65% of cells expressing MeV-M (**Figure 3.6 d, Figure 3.6 f left column**) had intense GFP fluorescence at the plasma membrane. However, co-expression of NiV-M and MeV-M with MycVPtase-WT altered NiV-M and MeV-M localization (**Figure 3.6 e-f middle column**). Depletion of PI(4,5)P₂ from the plasma membrane significantly reduced NiV-M and MeV-M

plasma membrane localization by ~60% ($p < 0.0001$) and ~45% ($p < 0.0001$), respectively (Fig. 6d). This reduction is similar to the reduction of PLC δ -PH plasma membrane localization in the presence of MycVPtase-WT (compared to PLC δ -PH alone; **Figure 3.6 d**). Additionally, co-expression of NiV-M and MeV-M with MycVPtase- $\Delta 1$ had no significant effect on NiV-M and MeV-M plasma membrane localization (**Figure 3.6 d, Figure 3.6 e-f right column**). Taken together these findings support our *in vitro* conclusions that MeV-M and NiV-M strongly associate with membranes containing PI(4,5)P₂ and is a direct line of evidence that PI(4,5)P₂ at the plasma membrane is central to proper plasma membrane localization for both MeV-M and NiV-M.

Figure 3.6. Effect of enzymatic depletion of PI(4,5)P2 on peripheral protein plasma membrane localization. COS-7 cells expressing the indicated GFP-fused proteins for 24 hours were expressed alone, with MycVPTase-WT or with MycVPTase- Δ 1. Immediately prior to imaging cells were stained with WGA AlexaFluor™647 (plasma membrane stain) and Hoescht (DNA stain) and subsequently imaged on a fluorescence confocal microscope. Cells were counted and binned into whether they displayed high fluorescence signal localization at the PM. **(a-c)** Representative confocal images of COS-7 cells expressing each indicated protein alone (*left panels*) or with MycVPTase-WT (*middle panels*) or MycVPTase- Δ 1 (*right panels*): **(a)** the PI(4,5)P2 sensor, PLC δ -PH **(b)** the filoviral matrix protein **(c)** the PS sensor, GFP-LactC2. **(d)** % cells with PM localization was determined by counting the number of cells with high fluorescence signal at the M and the number of cells without high fluorescence signal at the PM. In each replicate, a minimum of 45 cells were counted. **(e-f)** Representative confocal images of COS-7 cells expressing either GFP-NiV-M **(e)** or GFP-MeV-M **(f)** alone (*left panels*) or with MycVPTase-WT (*middle panels*) or MycVPTase- Δ 1 (*right panels*). Scale bar= 5 μ m. Values are reported as mean \pm s.d. N \geq 135 n=3. A one-way ANOVA with multiple comparisons was performed (compared to the protein expressed alone group for that protein). ****p<0.0001. WGA: wheat germ agglutinin; PM: plasma membrane



3.3.5.3 Apilimod treatment to explore role of PI(3,5)P₂

An additional lipid unveiled in our *in vitro* results to be important for MeV-M membrane association (but not NiV-M), was PI(3,5)P₂, an important PIP within the endocytic and trafficking pathways⁴⁰. To investigate if this interaction is important in cells, COS-7 cells expressing GFP-MeV-M, EGFP-eVP40 and PLCδ-PH-GFP were treated with apilimod for 1 hour after 24 hours of transient expression (**Figure 3.7**). Apilimod is a cell-permeable small molecule drug which inhibits phosphatidylinositol-3-phosphate 5-kinase (PIKfyve), thereby reducing PI(3,5)P₂, increasing PI(3)P, and altering cellular phenotypes by generating large intracellular vacuole structures⁴¹. Interestingly, apilimod has been shown to be effective in inhibiting filoviral infections by blocking trafficking during viral entry⁴². However in this study, EGFP-eVP40 was used as a control as apilimod was previously shown to not impact plasma membrane localization of eVP40³², an observation supported by our results in **Figure 3.7 a-b**. Apilimod and vehicle treated cells had ~80% of cells with GFP fluorescence at the plasma membrane. PLCδ-PH was also used as a control to validate that PI(3,5)P₂ depletion with PIKfyve inhibition does not interfere with peripheral protein binding to PI(4,5)P₂. Representative images (**Figure 3.7 c**) show that treatment with apilimod had no effect on PLCδ-PH plasma membrane localization compared to vehicle treated cells, with each treatment harboring ~80% of cells exhibiting high fluorescence at the plasma membrane (**Figure 3.7 b**).

Finally, we investigated the hypothesis that MeV-M affinity to membranes is enhanced in the presence of PI(3,5)P₂. In COS-7 cells expressing GFP-MeV-M and treated with vehicle, ~60% of cells exhibited high fluorescence at the plasma membrane (**Figure 3.7 b**, **Figure 3.7 d top panel**). However, in cells treated with apilimod, only ~40% of cells had strong fluorescence localization at the plasma membrane, a significant 20% decrease from control treated cells (p=0.0041) (**Figure 3.7 b**, **Figure 3.7 d bottom panel**). Therefore PI(3,5)P₂ may be important for MeV-M plasma membrane localization. It is important to note that PI(3,5)P₂ is primarily found on intracellular membranes and not likely within the plasma membrane⁴⁰, so it is possible that apilimod treatment is disrupting trafficking of MeV-M to the plasma membrane and not inhibiting a direct interaction with the plasma membrane. Lastly, to validate that apilimod treatment was effective, COS-7 cells expressing lysosomal-associated protein-1 (LAMP-1) were also treated with apilimod (or vehicle) and the size of intracellular vesicles were measured. In agreement with

previous reports, apilimod treatment significantly increased the size of intracellular vesicles from ~1.7 μm (control treated) to ~2.2 μm (apilimod treated) ($p < 0.0001$) (**Figure 3.7 e-f**).

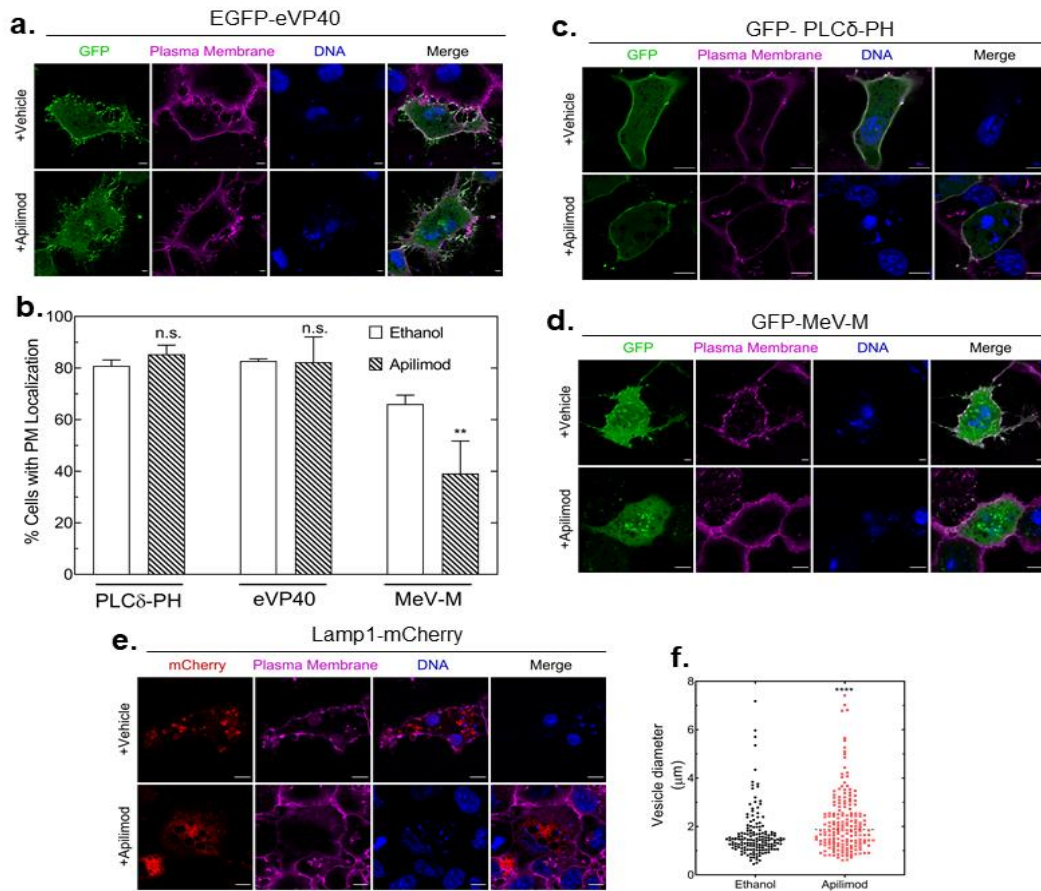


Figure 3.7. Effect on PIKfyve inhibition with Apilimod treatment on peripheral protein membrane localization and vesicle size. COS-7 cells expressing the indicated GFP/mCherry-fused proteins for 24 hours were treated with 200 nM Apilimod (or ethanol vehicle 1:2000 vol:vol) for 1 hour at 37°C. Following treatment, cells were stained with WGA AlexaFluor™647 (plasma membrane stain) and Hoescht (DNA stain) and subsequently imaged on a fluorescence confocal microscope. Cells were counted and binned into either displaying high fluorescence localization at the plasma membrane or not. **(a)** Representative confocal images of COS-7 cells expressing EGFP-eVP40 +/- Apilimod treatment **(b)** Quantification of plasma membrane localization for panels **(a,c,d)**: % cells with PM localization was determined by counting the number of cells with high fluorescence signal at the PM and the number of cells without high fluorescence signal at the PM. In each replicate, a minimum of 45 cells were counted **(c)** Representative confocal images of COS-7 cells expressing PLCδ-PH-GFP +/- Apilimod treatment. **(d)** Representative confocal images of COS-7 cells expressing GFP-MeV-M +/- Apilimod treatment. Scale bar= 5 μm . Values are reported as mean \pm s.d. $N \geq 135$ $n = 3$. A one-way ANOVA with multiple comparisons was performed (compared to the vehicle treated group for each protein). ** $p = 0.0041$. **(e-f)** Analysis of Apilimod treatment on intracellular vesicle size using COS-7 cells expressing LAMP-1. **(e)** Representative confocal images of COS-7 cells expressing LAMP-1-mCherry +/- Apilimod treatment. **(f)** Quantification of vesicle size from panel **(e)**: intracellular vesicles were measured using imageJ and plotted. $n = 1$. Scale bar= 5 μm . Individual measurements are reported. A two-tailed t-test was performed **** $p < 0.0001$. PIKfyve: phosphatidylinositol-3-phosphate 5-kinase; LAMP1: lysosomal associated membrane protein-1.

3.3.5.4 Wortmannin

Our last aim was to investigate whether the affinity of NiV-M or MeV-M to PIP₃ discovered from our liposome sedimentation assays was functionally significant in a cellular system. To test this, we used the fungal derivative wortmannin, a non-competitive irreversible inhibitor of phosphatidylinositol 3-kinase (PI3K)⁴³. PI3K phosphorylates the D3 position of the inositol head group generating PIP₃ from PI(4,5)P₂⁴⁴. Similar to apilimod treatment, wortmannin has been reported to interfere with viral entry. In CHO cells, wortmannin slowed the delivery of Semliki forest virus to lysosomes during entry⁴⁵. However, wortmannin has not been tested in a MeV or NiV model.

To address whether NiV-M or MeV-M affinity to the plasma membrane is altered in response to PIP₃ depletion, COS-7 cells expressing GFP/mRFP-fused proteins were treated after 24 hours of expression with wortmannin (or ethanol vehicle) for 1 hour and fluorescence confocal microscopy was performed (representative images in **Figure 3.8 a-d**). COS-7 cells expressing the PIP₃ biosensor AKT-PH-mRFP was used as control. In vehicle-treated cells AKT-PH was localized to the plasma membrane in ~75% of cells, (**Figure 3.8 a left panel, Figure 3.8 e**); however, wortmannin treatment significantly reduced the population of cells with AKT-PH at the plasma membrane to ~20% ($p < 0.0001$) and AKT-PH was primarily cytosolic (**Figure 3.8 a right panel, Figure 3.8 e**). Furthermore, to ensure wortmannin treatment did not affect plasma membrane localization of a peripheral protein that interacts with PI(4,5)P₂ within the plasma membrane, COS-7 cells expressing EGFP-eVP40 were also examined (**Figure 3.8 b**). In both control and wortmannin-treated cells, ~80% of cells had high EGFP-eVP40 localization at the plasma membrane (**Figure 3.8 e**), which validates a previously published report that wortmannin does not disrupt eVP40 plasma membrane localization³².

Finally, we assessed the effect of wortmannin on NiV-M and MeV-M plasma membrane localization. In control-treated cells, GFP-NiV-M was predominantly localized to the plasma membrane in ~70% of cells (**Figure 3.8 c left panel, Figure 3.8 e**) as was GFP-MeV-M, albeit to a lesser extent in ~60% of cells (**Figure 3.8 d left panel, Figure 3.8 e**). Interestingly, wortmannin treatment had no effect on the plasma membrane localization of either NiV-M or MeV-M

(Figure 3.8 c-d right panels, Figure 3.8 e). Taken together, these results indicate that in cells, MeV-M and NiV-M do not depend on PIP₃ for proper plasma membrane localization.

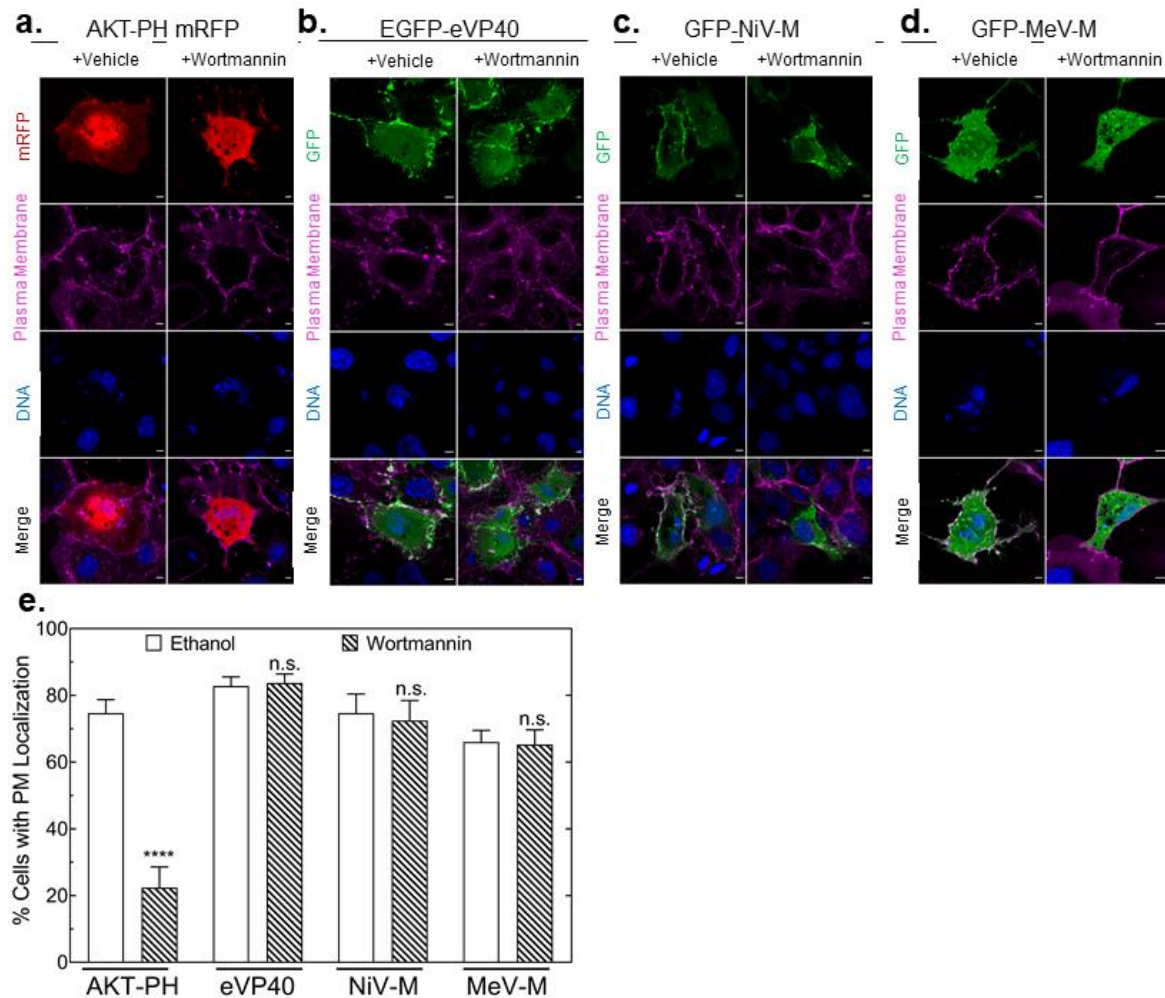


Figure 3.8. Effect of PI3K inhibition with wortmannin on peripheral protein plasma membrane localization. COS-7 cells expressing the indicated GFP/mRFP-fused proteins for 24 hours were treated with 100 nM wortmannin or ethanol vehicle (1:2000 vol:vol) for 1 hour at 37°C, stained with WGA AlexaFluor™647 (plasma membrane stain) and Hoescht (DNA stain) and subsequently imaged on a fluorescence confocal microscope. Cells were counted and binned into either displaying high fluorescence localization at the plasma membrane or not. **(a-d)** Representative confocal images of COS-7 cells expressing each indicated protein treated with vehicle (left panels) or wortmannin (right panels) **(a)** Cells expressing PI(3,4,5)P3 sensor AKT-PH-mRFP **(b)** Cells expressing filovirus matrix protein EGFP-eVP40 **(c)** Cells expressing GFP-NiV-M **(d)** Cells expressing GFP-MeV-M **(e)** % cells with PM localization was determined by counting the number of cells with high fluorescence at the PM and the number of cells without high fluorescence at the PM. In each replicate, a minimum of 45 cells were counted. Scale bar= 5 µm. Values are reported as mean ± s.d. N≥135 n=3. A one-way ANOVA with multiple comparisons was performed (compared to the vehicle treated group for that protein). ****p<0.0001. PI3K: phosphatidylinositol 3-kinase.

3.3.6 PI Kinase inhibitors: potential anti-viral strategies

Lipid kinases are important enzymes regulating a wealth of signaling cascades associated with cell division and survival^{36,46}. Furthermore, numerous lipid kinase inhibitors are available and are currently under investigation in clinical trials as anti-cancer therapeutics. Our liposome sedimentation and confocal imaging experiments have outlined strong evidence that targeting PIs involved in paramyxovirus matrix protein plasma membrane localization may be efficacious in blocking viral budding. Therefore, we extended our studies to test whether available lipid kinase inhibitors are effective in inhibiting NiV-M or MeV-M plasma membrane localization in cells (**Figure 3.9**).

To test this hypothesis, we employed three different commercially available small molecule lipid kinase inhibitors: ISA2011-B, LY294002 and PIK93. ISA2011-B is a relatively new and promising PI-5-kinase- α (PIP5K α) inhibitor which inhibits the production of PI(4,5)P₂ from PI(4)P. ISA2011-B has been identified as a potent inhibitor of cancer cell growth *in vitro* and *in vivo*^{47,48}, but has not been investigated in paramyxovirus infection. LY294002 is a selective phosphatidylinositol 5-kinase (PI3K) inhibitor, which inhibits the production of PIP₃ from PI(4,5)P₂ by inhibiting the phosphorylation of the D3 position on the inositol ring. PI3K has been shown to be central to downstream Akt phosphorylation pathways involved in cell survival and proliferation as well as microtubule formation. Although LY294002 has not advanced in clinical trials due to toxicity issues, efforts are underway to develop pro-drugs and analogs of LY294002 with decreased toxicity and increased efficacy⁴⁹. Lastly, PIK93 was used as control, as it inhibits phosphatidylinositol-4kinase-III β (PI4KIII β),⁵⁰ blocking the production of PIP₃ from PI(4,5)P₂, and at higher concentrations (>40 nM) inhibits PI3K to block the production of PIP₃ from PI(4,5)P₂⁵¹.

COS-7 cells expressing GFP-NiV-M or GFP-MeV-M were treated with the indicated compounds at 8 hours post transfection (concentrations above their respective IC₅₀ for lipid specific depletion were selected). After 24 hours of treatment, cells were fixed and imaged using a fluorescence confocal microscope. In DMSO-treated cells, GFP-MeV-M (**Figure 3.9 a left column**) and GFP-NiV-M (**Figure 3.9 b left column**) localized to regions of the plasma membrane. To clearly depict the effect of inhibitors on plasma membrane localization, the % of cells with high plasma membrane GFP fluorescence localization was calculated for DMSO-treated cells and normalized to 1 (**Figure 3.9 c**). Upon treatment with 40 μ M ISA-2011B, GFP-MeV-M

plasma membrane localization was reduced by nearly 50% ($p=0.0009$) (**Figure 3.9 a middle left column, Figure 3.9 c**) and GFP-NiV-M plasma membrane localization was reduced by ~35% ($p=0.0006$) (**Figure 3.9 b middle left column, Figure 3.9 c**). Similar to ISA2011-B, treatment with 6 μ M LY294002 had a more significant effect on MeV-M plasma membrane reduction (~30% reduction; $p=0.0101$) (**Figure 3.9 a middle right column, Figure 3.9 c**) than it did on NiV-M, which was reduced by ~25% ($p=0.0282$) (**Figure 3.9 b middle right column, Figure 3.9 c**). Lastly, treatment with 0.15 μ M PIK93 had no effect on plasma membrane localization of either MeV-M or NiV-M (**Figure 3.9 a-b right columns, Figure 3.9 c**). Taken together, these results indicate that ISA-2011B shows promise in reducing plasma membrane localization of both Me-M and NiV-M and could be used as a tool to slow down viral spread.

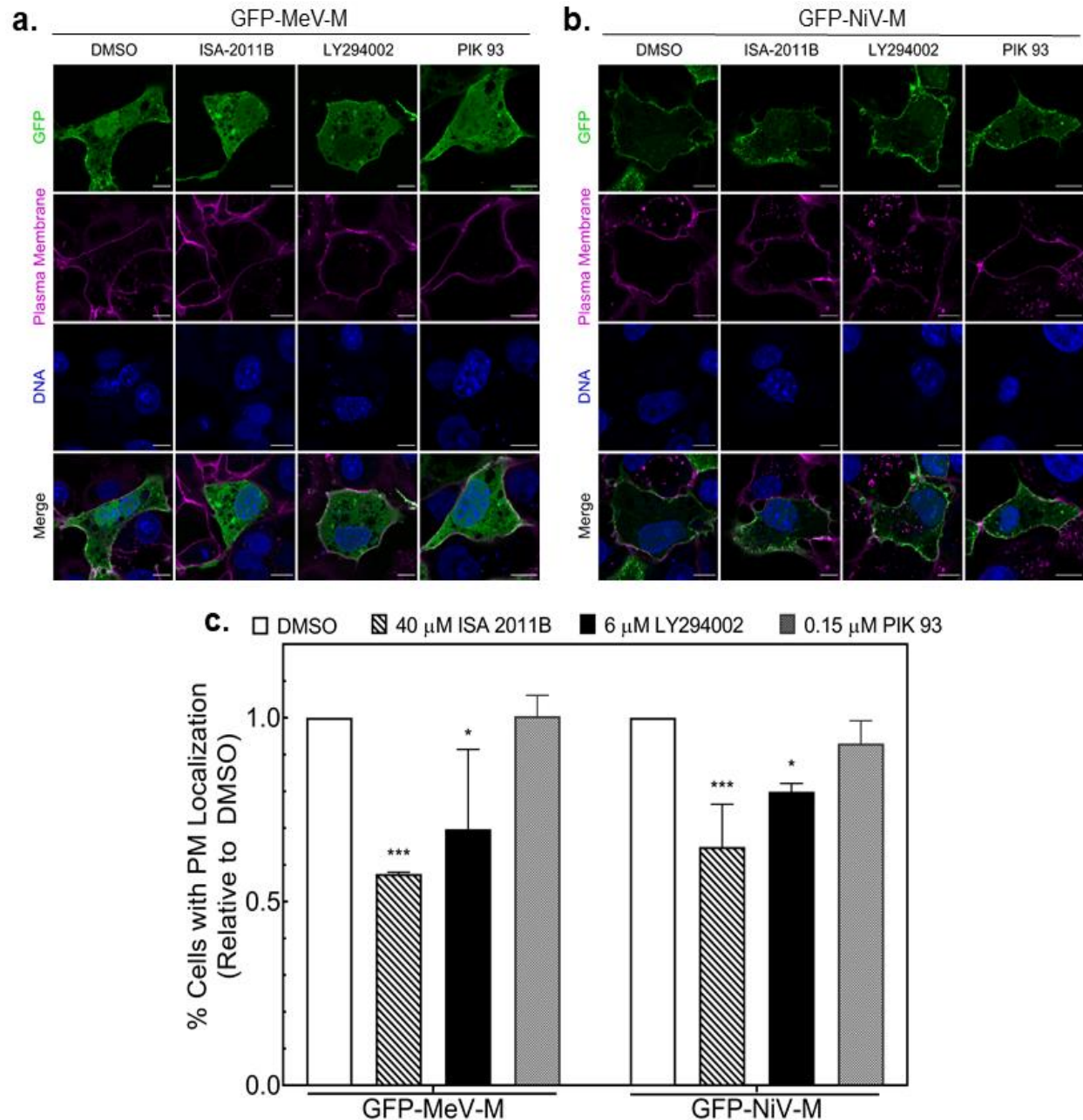


Figure 3.9. Effect of PIK inhibitors on paramyxovirus matrix protein plasma membrane localization. COS-7 cells expressing the GFP-NiV-M or GFP-MeV-M were treated with the indicated compounds after 8 hours of protein expression. Cells were treated with vehicle (DMSO, 1:1000 vol:vol) or compound for 24 hours, stained with WGA AlexaFluor™647 (plasma membrane stain) and Hoescht (DNA stain), fixed in 4% PFA and subsequently imaged on a fluorescence confocal microscope. Cells were counted and binned into either displaying high fluorescence localization at the plasma membrane or not. **(a-b)** Representative confocal images of COS-7 cells expressing GFP-MeV-M **(a)** or GFP-NiV-M **(b)** and treated with vehicle (left panel) or compound (right panels). **(c)** % cells with PM localization was determined by counting the number of cells with high fluorescence at the PM and the number of cells without high fluorescence at the PM. In each replicate, a minimum of 45 cells were counted. Scale bar= 5 μ m. Values are reported as mean \pm s.d. $N \geq 135$ $n=3$. A one-way ANOVA with multiple comparisons was performed (compared to the vehicle treated group for that protein). **** $p < 0.0001$. PIK: phosphatidylinositol kinase; PFA: paraformaldehyde;

3.3.7 MeV-M and NiV-M localize to regions of plasma membrane enriched in PI(4,5)P₂

Our report so far has demonstrated that PI(4,5)P₂ is an integral lipid component involved in the localization of both MeV-M and NiV-M to the plasma membrane. Localization of paramyxovirus matrix proteins to the plasma membrane is a key step in the viral budding and spread process, as these viruses bud from the plasma membrane of cells. Therefore, it was of interest to see if we could capture the interaction of PI(4,5)P₂ with MeV-M or NiV-M within the plasma membrane of cells. To this end, we expressed GFP-MeV-M or GFP-NiV-M in COS-7 cells for 24 hours to allow adequate localization to the plasma membrane. Prior to imaging on a confocal microscope, cells were supplemented with a fluorescent PI(4,5)P₂, TopFluor TMR-PI(4,5)P₂ (TF-TMR PI(4,5)P₂) (**Figure 3.10**). GFP-MeV-M and GFP-NiV-M were localized to the plasma membrane in cells (**Figure 3.10 a-b**). In addition to MeV-M and NiV-M plasma membrane localization, TF-TMR PI(4,5)P₂ was efficiently incorporated into the plasma membrane (**Figure 3.10 a-b**). To delineate whether regions of the plasma membrane enriched with GFP-matrix proteins contained PI(4,5)P₂, plot profile analysis was performed. Lines were drawn to intersect regions of the plasma membrane with high GFP fluorescence, irrespective of TF-TMR PI(4,5)P₂ signal. Upon plot profile analysis of the GFP (MeV-M/NiV-M) and TF-TMR PI(4,5)P₂ fluorescence signals, both GFP-MeV-M (**Figure 3.10 c**) and GFP-NiV-M (**Figure 3.10 d**) fluorescence signals correlated to regions of the plasma membrane enriched with TF-TMR PI(4,5)P₂. These findings corroborate our hypothesis and previous results that PI(4,5)P₂ plays an important role in MeV-M and NiV-M association to the plasma membrane, and warrants further exploration into whether targeting this interaction could be an effective pan-viral therapeutic strategy.

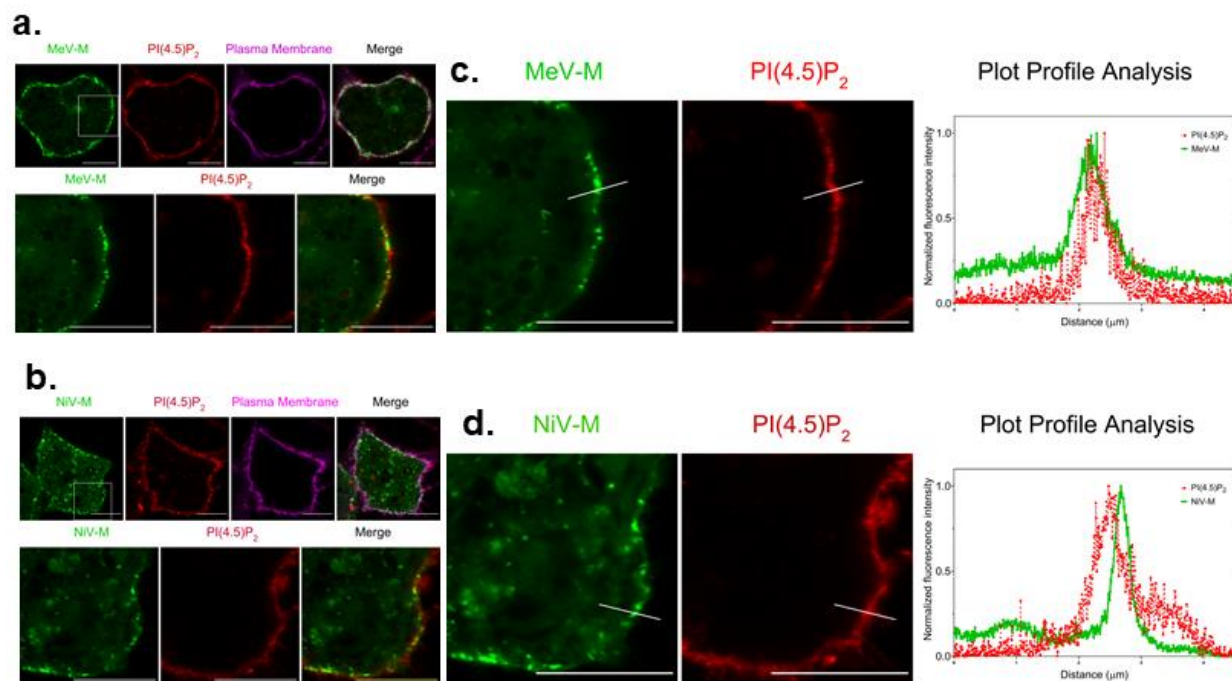


Figure 3.10. Correlation of PI(4,5)P₂ and paramyxovirus matrix proteins at the plasma membrane in cells. COS-7 cells were transfected with either GFP-MeV-M (a-b) or GFP-NiV-M (c-d). At 24 hours post transfection, cells were washed, and media supplemented with TF-TMR- PI(4,5)P₂ was added to cells for 30 min. Following incubation, cells were washed thoroughly, stained with WGA-AlexaFluor™ 647 (plasma membrane), fixed with 4% PFA and imaged on a fluorescence confocal microscope. **(a)** Representative confocal images of COS-7 cells expressing GFP-MeV-M supplemented with TF-TMR-PI(4,5)P₂. **(b)** Plot profile analysis of fluorescence signals correlation between GFP-MeV-M (solid green line) and TF-TMR-PI(4,5)P₂ (red dotted line). White line indicates where plot profile analysis was performed. **(c)** Representative confocal images of COS-7 cells expressing GFP-NiV-M supplemented with TF-TMR-PI(4,5)P₂. **(d)** Plot profile analysis of fluorescence signals correlation between GFP-NiV-M (solid green line) and TF-TMR-PI(4,5)P₂ (red dotted line). White line indicates where plot profile analysis was performed. scale bar= 5μm. TF-TMR-PI(4,5)P₂: TopFluor TMR-PI(4,5)P₂.

3.4 Discussion

Lipids within the plasma membrane are diverted by numerous matrix proteins to execute their primary function, facilitate the budding of progeny virions from the plasma membrane. While previous reports have shown that the paramyxovirus matrix proteins MeV-M and NiV-M can produce viral like particles independently of other viral proteins, little is known regarding how these matrix proteins interact with the plasma membrane to facilitate viral budding. As no therapeutics are available for either MeV or NiV, unveiling key mechanisms involved in their infectious and deadly nature are a fundamental step to pave the way for the development of pan-viral therapeutics.

Although it is widely believed that paramyxoviruses bud in spherical virions, this report shows conclusive SEM evidence that MeV-M and NiV-M can produce filamentous viral-like particles (similar to those observed with filoviruses). Filamentous viral particles are possibly advantageous to the virus by allowing a growing particle to stay connected to the infected cell and bend to infect a neighboring cell allowing efficient fusion to the neighboring cell (mediated by the F protein). This mechanism of cell-cell fusion, or “syncytia” is a mechanism of spread known for MeV^{52,53} and NiV-M^{54,55}. In addition to our SEM data, *in vitro* data collected through transmission electron microscopy (data collected by Dr. Mike Norris at The La Jolla Institute for Immunology) shows that recombinant MeV-M and NiV-M form extensive filamentous structures upon incubation with PI(4,5)P₂, indicating that the filamentous structures akin to filamentous viral particles are formed independent of host proteins. Therefore, it was of great interest to us to illuminate which lipids were important to MeV-M and NiV-M plasma membrane localization and investigate their plausibility of therapeutic targets.

In this study, we demonstrated that MeV-M and NiV-M both associate to lipid membranes through multiple lipid binding partners. Both MeV-M and NiV-M associated to membranes containing PS *in vitro*, with MeV-M displaying higher selectivity to PS compared to NiV-M. Furthermore, interfering with electrostatic interactions with increasing NaCl almost completely abrogated NiV-M binding to PS membranes, an indication that the NiV-M and PS interaction was based on electrostatics. Conversely, increasing NaCl did not abrogate MeV-M association to PS membranes, suggesting that MeV-M is interacting with PS in a stereospecific manner, which are canonically stronger interactions than electrostatics. It is interesting to note that neither protein bound to PA containing membranes; however, the head group of PA is exceptionally small and may not be complementary to the membrane binding interface of either protein. Notably, our experiments do not rule out the possibility that PA may be important in other stages of the budding process (e.g. interacting with host proteins involved).

Unique to MeV-M membrane binding was the relationship between MeV-M and PI(3,5)P₂. MeV-M associated to membranes containing PI(3,5)P₂ to a similar level as it did to membranes containing PS. Furthermore, MeV-M displayed additive binding effects to membranes containing both PS and PI(3,5)P₂. These findings suggest that MeV-M associated with either PS or PI(3,5)P₂ but that the presence of both lipids within a membrane does not enhance the affinity of MeV-M to the other lipid. Interestingly, a clear stereospecific interaction was demonstrated by the observation

that increasing NaCl failed to alter MeV-M binding to PI(3,5)P₂ membranes. PI(3,5)P₂ is not abundant within the plasma membrane but more commonly found in intracellular vesicles within the endocytic trafficking pathway. Taken together, it is possible that the relationship of MeV-M with PS and PI(3,5)P₂ could be a mode of regulation for vesicular trafficking of MeV-M throughout the cell and to the plasma membrane. Intracellularly, MeV-M engages in a stereospecific interaction with PI(3,5)P₂ for possible assembly or host protein interactions, and upon delivery to the plasma membrane interacts with PS where the MeV-M structure is postured to commence viral budding. This hypothesis is supported by the finding that apilimod treatment (reduction of PI(3,5)P₂) significantly reduced MeV-M plasma membrane localization but did not completely block it. In other words, if MeV-M was already localized to the plasma membrane prior to treatment, it was unaffected by apilimod-dependent PI(3,5)P₂ depletion; however, no new MeV-M could reach the plasma membrane.

It is well documented that many viral matrix proteins associate with the plasma membrane in a PI(4,5)P₂ dependent manner^{25,32,33,56,57}; however, this is the first study presenting direct evidence that PI(4,5)P₂ is important for MeV-M and NiV-M membrane localization *in vitro* and in cells. Both MeV-M and NiV-M associated with PI(4,5)P₂ containing membranes *in vitro* and our enzymatic depletion system and confocal imaging with TF-TMR PI(4,5)P₂ validated that this interaction is important in cells. Interestingly, the association of NiV-M with the plasma membrane appears to be more sensitive to PI(4,5)P₂ levels, as MycVPtase-WT expression had a greater effect on NiV-M plasma membrane localization than MeV-M plasma membrane localization. This may be explained by the biochemical nature of their interactions. Similar to the relationship of each protein with PS, our data suggests that MeV-M interacts with PI(4,5)P₂ in a stereospecific fashion, while the NiV-M interaction with PI(4,5)P₂ is likely mediated by electrostatics. Interestingly, when both PS and PI(4,5)P₂ were incorporated into membranes, synergistic binding was observed for MeV-M and NiV-M. This suggests that upon binding to one lipid increases the affinity of the protein for the other lipid, possibly mediated through a conformational change in the protein. If two independent binding sites were present with NiV-M, additive binding would have been observed in our lipid sedimentation assays. As both MeV-M and NiV-M oligomerize at the plasma membrane to form the budding particle, this may be a mechanism by which the protein and membrane work cooperatively to facilitate the budding process.

An additional interesting finding was that MeV-M and NiV-M associated with membranes containing PIP₃. The plasma membrane contains exceptionally low levels of PIP₃, and therefore it is likely this interaction is not physiologically relevant but an artifact of PIP₃ containing a net charge of (-6). It also must be pointed out that PIP₃ contains a phosphate group at the D4 and D5 position. MeV-M and NiV-M strongly associate with PI(4,5)P₂, therefore it is possible that the presence of the phosphate on the D4 and D5 position are responsible for the interaction between MeV-M and NiV-M with PIP₃. This hypothesis was supported by our finding that wortmannin (reduces production of PIP₃) had no effect on MeV-M or NiV-M plasma membrane localization.

The conclusions derived from our *in vitro* results that NiV-M was more dependent on anionic charge of the membrane than MeV-M for membrane association were further substantiated in cells using our membrane charge neutralization assay. NiV-M plasma membrane was significantly decreased upon treatment with sphingosine, while MeV-M plasma membrane localization was insensitive to the treatment (in line with our *in vitro* liposome sedimentation assay results). Interestingly, the effect was not as profound as the displacement of KR ϕ from the plasma membrane (an interaction solely based on electrostatics). This observation further corroborates our hypothesis that a conformational change within NiV-M occurs following its interaction with either PS or PI(4,5)P₂, which permits a new stereospecific interaction with the membrane required for proper assembly and budding.

Lastly, this study investigated whether commercially available small molecule inhibitors of lipid kinases could be used to block MeV-M or NiV-M association to the plasma membrane, a necessary step for viral spread. The PIP5K α inhibitor ISA2011-B successfully inhibited the localization of both NiV-M and MeV-M to the plasma membrane in cells. Additionally, the inhibition was slightly more profound on MeV-M membrane localization. It was interesting that inhibition of PI3K had an inhibitory effect on MeV-M and NiV-M plasma membrane localization; however, it is possible this inhibition was a result of PI3K roles in microtubule formation and not a direct result of PIP₃ depletion.

Overall this study aimed to shed light on the mechanisms by which MeV-M and NiV-M are interacting with the plasma membrane, and their credibility as therapeutic targets. Small molecule lipid kinase inhibitors have shown great promise in clinical trials in cancer studies, but have yet to be explored in paramyxovirus infections. While future investigations are needed to bridge the gap between how matrix proteins, lipids, and host proteins work in concert to form

virions, this study creates a foundation needed to elucidate how the matrix proteins of MeV and NiV direct the spread of the viruses in cells.

3.5 References

1. Wang, L. *et al.* Molecular biology of Hendra and Nipah viruses. *Microbes Infect.* **3**, 279–87 (2001).
2. Patch, J. R. *et al.* The YPLGVG sequence of the Nipah virus matrix protein is required for budding. (2008). doi:10.1186/1743-422X-5-137
3. Ciancanelli, M. J. & Basler, C. F. Mutation of YMYL in the Nipah Virus Matrix Protein Abrogates Budding and Alters Subcellular Localization. *J. Virol.* **80**, 12070–12078 (2006).
4. Johnston, G. P. *et al.* Nipah Virus-Like Particle Egress Is Modulated by Cytoskeletal and Vesicular Trafficking Pathways: a Validated Particle Proteomics Analysis. *mSystems* **4**, (2019).
5. Zhao, H., Hakala, M. & Lappalainen, P. ADF/cofilin binds phosphoinositides in a multivalent manner to act as a PIP(2)-density sensor. *Biophys. J.* **98**, 2327–2336 (2010).
6. Iwasaki, M. *et al.* The Matrix Protein of Measles Virus Regulates Viral RNA Synthesis and Assembly by Interacting with the Nucleocapsid Protein. *J. Virol.* **83**, 10374–10383 (2009).
7. Liljeroos, L., Huiskonen, J. T., Ora, A., Susi, P. & Butcher, S. J. Electron cryotomography of measles virus reveals how matrix protein coats the ribonucleocapsid within intact virions. *Proc. Natl. Acad. Sci. U. S. A.* **108**, 18085–18090 (2011).
8. Liu, L. Fields Virology, 6th Edition. *Clin. Infect. Dis.* **59**, 613–613 (2014).
9. Adu-Gyamfi, E., Digman, M. A., Gratton, E. & Stahelin, R. V. Investigation of Ebola VP40 assembly and oligomerization in live cells using number and brightness analysis. *Biophys. J.* **102**, 2517–25 (2012).
10. Reeves, J. P. & Dowben, R. M. Formation and properties of thin-walled phospholipid vesicles. *J. Cell. Physiol.* **73**, 49–60 (1969).
11. Darszon, A. *et al.* Reassembly of protein-lipid complexes into large bilayer vesicles: perspectives for membrane reconstitution. *Proc. Natl. Acad. Sci. U. S. A.* **77**, 239–243 (1980).
12. Yamashita, Y., Oka, M., Tanaka, T. & Yamazaki, M. A new method for the preparation of giant liposomes in high salt concentrations and growth of protein microcrystals in them. *Biochim. Biophys. Acta* **1561**, 129–34 (2002).
13. Julkowska, M. M., Rankenberg, J. M. & Testerink, C. Liposome-Binding Assays to Assess Specificity and Affinity of Phospholipid–Protein Interactions. in 261–271 (2013). doi:10.1007/978-1-62703-401-2_24
14. Akiyama, H. *et al.* Virus particle release from glycosphingolipid-enriched microdomains is essential for dendritic cell-mediated capture and transfer of HIV-1 and henipavirus. *J. Virol.* **88**, 8813–25 (2014).
15. Pantua, H. D., McGinnes, L. W., Peeples, M. E. & Morrison, T. G. Requirements for the Assembly and Release of Newcastle Disease Virus-Like Particles. *J. Virol.* **80**, 11062–11073 (2006).
16. Heggeness, M. H., Smith, P. R. & Choppin, P. W. In vitro assembly of the nonglycosylated membrane protein (M) of Sendai Virus. *Proc. Natl. Acad. Sci. U. S. A.* **79**, (1982).
17. Shtykova, E. V. *et al.* Solution Structure, Self-Assembly, and Membrane Interactions of the Matrix Protein from Newcastle Disease Virus at Neutral and Acidic pH. *J. Virol.* **93**, (2018).
18. Pohl, C., Duprex, W. P., Krohne, G., Rima, B. K. & Schneider-Schaulies, S. Measles virus M and F proteins associate with detergent-resistant membrane fractions and promote

- formation of virus-like particles. *J. Gen. Virol.* **88**, 1243–50 (2007).
19. Huang, M. *et al.* Determination of a phosphorylation site in Nipah virus nucleoprotein and its involvement in virus transcription. *J. Gen. Virol.* **92**, 2133–2141 (2011).
 20. Sugai, A. *et al.* Newly Identified Minor Phosphorylation Site Threonine-279 of Measles Virus Nucleoprotein Is a Prerequisite for Nucleocapsid Formation. *J. Virol.* **88**, 1140–1149 (2014).
 21. Ha, M. N. *et al.* Mutations in the fusion protein of measles virus that confer resistance to the 2 membrane fusion inhibitors carbobenzoxy-D-Phe-L-Phe-Gly and AS-48 3 4 5 Downloaded from. (2017). doi:10.1128/JVI.01026-17
 22. Yu, X., Shahriari, S., Li, H. M. & Ghildyal, R. Measles virus matrix protein inhibits host cell transcription. *PLoS One* **11**, (2016).
 23. Jasenosky, L. D., Neumann, G., Lukashevich, I. & Kawaoka, Y. Ebola virus VP40-induced particle formation and association with the lipid bilayer. *J. Virol.* **75**, 5205–14 (2001).
 24. Julkowska, M. M., Rankenbreg, J. M. & Testerink, C. Liposome-Binding Assays to Assess Specificity and Affinity of Phospholipid--Protein Interactions. in *Plant Lipid Signaling Protocols* (eds. Munnik, T. & Heilmann, I.) 261–271 (Humana Press, 2013). doi:10.1007/978-1-62703-401-2_24
 25. Wijesinghe, K. J. & Stahelin, V. Investigation of the Lipid Binding Properties of the Marburg Virus. *J. Virol.* **90**, 3074–3085 (2016).
 26. Adu-Gyamfi, E. *et al.* Host Cell Plasma Membrane Phosphatidylserine Regulates the Assembly and Budding of Ebola Virus. *J. Virol.* **89**, 9440–53 (2015).
 27. Del Vecchio, K. *et al.* A cationic, C-terminal patch and structural rearrangements in Ebola virus matrix VP40 protein control its interactions with phosphatidylserine. *J. Biol. Chem.* **293**, 3335–3349 (2018).
 28. Bobone, S. *et al.* Phosphatidylserine Lateral Organization Influences the Interaction of Influenza Virus Matrix Protein 1 with Lipid Membranes. *J. Virol.* **91**, 1–15 (2017).
 29. Liu, A. P. & Fletcher, D. A. Actin polymerization serves as a membrane domain switch in model lipid bilayers. *Biophys. J.* **91**, 4064–4070 (2006).
 30. Di Paolo, G. & De Camilli, P. Phosphoinositides in cell regulation and membrane dynamics. *Nature* **443**, 651–7 (2006).
 31. Senju, Y. & Lappalainen, P. Regulation of actin dynamics by PI(4,5)P₂ in cell migration and endocytosis. *Current Opinion in Cell Biology* **56**, 7–13 (2019).
 32. Johnson, K. A., Taghon, G. J. F., Scott, J. L. & Stahelin, R. V. The Ebola Virus matrix protein, VP40, requires phosphatidylinositol 4,5-bisphosphate (PI(4,5)P₂) for extensive oligomerization at the plasma membrane and viral egress. *Sci. Rep.* **6**, 19125 (2016).
 33. Ono, A., Ablan, S. D., Lockett, S. J., Nagashima, K. & Freed, E. O. HIV-1 Gag targeting to the plasma membrane. *October* **101**, 14889–94 (2004).
 34. Yang, Y., Lee, M. & Fairn, G. D. Phospholipid subcellular localization and dynamics. *J. Biol. Chem.* **293**, 6230–6240 (2018).
 35. Van Meer, G., Voelker, D. R. & Feigenson, G. W. Membrane lipids: Where they are and how they behave. *Nature Reviews Molecular Cell Biology* **9**, 112–124 (2008).
 36. Balla, T. Phosphoinositides: tiny lipids with giant impact on cell regulation. *Physiol. Rev.* **93**, 1019–137 (2013).
 37. Altan-Bonnet, N. & Balla, T. Phosphatidylinositol 4-kinases: Hostages harnessed to build panviral replication platforms. *Trends in Biochemical Sciences* **37**, 293–302 (2012).
 38. Yeung, T. *et al.* Membrane phosphatidylserine regulates surface charge and protein

- localization. *Science* (80-.). **319**, 210–213 (2008).
39. Yeung, T. *et al.* Receptor activation alters inner surface potential during phagocytosis. *Science* (80-.). **313**, 347–351 (2006).
 40. Hasegawa, J., Strunk, B. S. & Weisman, L. S. PI5P and PI(3,5)P₂: Minor, but essential phosphoinositides. *Cell Struct. Funct.* **42**, 49–60 (2017).
 41. Sbrissa, D., Naisan, G., Ikononov, O. C. & Shisheva, A. Apilimod, a candidate anticancer therapeutic, arrests not only PtdIns(3,5)P₂ but also PtdIns5P synthesis by PIKfyve and induces bafilomycin A1-reversible aberrant endomembrane dilation. *PLoS One* **13**, e0204532 (2018).
 42. Nelson, E. A. *et al.* The phosphatidylinositol-3-phosphate 5-kinase inhibitor apilimod blocks filoviral entry and infection. *PLoS Negl. Trop. Dis.* **11**, e0005540 (2017).
 43. Zalkow, L., Matter, W. F., Dodge, J., Grindey, G. & Vlahos, C. J. Wortmannin, a Potent and Selective Inhibitor of Phosphatidylinositol-3-kinase. *Cancer Res.* **54**, 2419–2423 (1994).
 44. Arcaro, A. & Wymann, M. P. Wortmannin is a potent phosphatidylinositol 3-kinase inhibitor: The role of phosphatidylinositol 3,4,5-trisphosphate in neutrophil responses. *Biochem. J.* **296**, 297–301 (1993).
 45. Martys, J. L. *et al.* Wortmannin-sensitive trafficking pathways in Chinese hamster ovary cells: Differential effects on endocytosis and lysosomal sorting. *J. Biol. Chem.* **271**, 10953–10962 (1996).
 46. Nanbo, A. *et al.* Ebolavirus is internalized into host cells via macropinocytosis in a viral glycoprotein-dependent manner. *PLoS Pathog.* **6**, e1001121 (2010).
 47. Semenas, J. *et al.* The role of PI3K/AKT-related PIP5K1 α and the discovery of its selective inhibitor for treatment of advanced prostate cancer. *Proc. Natl. Acad. Sci. U. S. A.* **111**, (2014).
 48. Sarwar, M. *et al.* Targeted suppression of AR-V7 using PIP5K1 α inhibitor overcomes enzalutamide resistance in prostate cancer cells. *Oncotarget* **7**, 63065–63081 (2016).
 49. Zhao, W., Qiu, Y. & Kong, D. Class I phosphatidylinositol 3-kinase inhibitors for cancer therapy. *Acta Pharmaceutica Sinica B* **7**, 27–37 (2017).
 50. Arita, M. *et al.* Phosphatidylinositol 4-Kinase III Beta Is a Target of Enviroxime-Like Compounds for Antipoliavirus Activity. *J. Virol.* **85**, 2364–2372 (2011).
 51. Monet, M., Francoeur, N. & Boulay, G. Involvement of phosphoinositide 3-kinase and PTEN protein in mechanism of activation of TRPC6 protein in vascular smooth muscle cells. *J. Biol. Chem.* **287**, 17672–17681 (2012).
 52. Herschke, F. *et al.* Cell-Cell Fusion Induced by Measles Virus Amplifies the Type I Interferon Response. *J. Virol.* **81**, 12859–12871 (2007).
 53. Lamb, R. A. & Jardetzky, T. S. Structural basis of viral invasion: lessons from paramyxovirus F. *Current Opinion in Structural Biology* **17**, 427–436 (2007).
 54. Lamp, B. *et al.* Nipah Virus Entry and Egress from Polarized Epithelial Cells. *J. Virol.* **87**, 3143–3154 (2013).
 55. Aguilar, H. C. *et al.* N-Glycans on Nipah Virus Fusion Protein Protect against Neutralization but Reduce Membrane Fusion and Viral Entry. *J. Virol.* **80**, 4878–4889 (2006).
 56. Johnson, K. A. *et al.* PI(4,5)P₂; Binding Sites in the Ebola Virus Matrix Protein Modulate Assembly and Budding. *bioRxiv* 341248 (2018). doi:10.1101/341248

57. Barros, M. *et al.* Membrane Binding of HIV-1 Matrix Protein: Dependence on Bilayer Composition and Protein Lipidation. *J. Virol.* **90**, 4544–4555 (2016).

CHAPTER 4. CHARACTERIZING MARBURG VP40 ASSEMBLY

4.1 Introduction

Marburg virus (MARV) and Ebola virus (EBOV) were both discovered in the late 1900s; however evolutionary history suggests they diverged from a common ancestor more than one thousand years ago¹. Both EBOV and MARV are lipid-enveloped negative sense RNA viruses which bud from the host cell, and in the process repurposing the plasma membrane into its own viral envelope². With limited viral machinery, the viral matrix protein of EBOV and MARV (eVP40 and mVP40, respectively) is the primary viral component responsible for directing the assembly of budding viral particles. Matrix proteins across viral families share significant structural and functional properties, even in the absence of sequence homology (e.g. the ability of eVP40 and mVP40 to produce viral like particles (VLPs) in the absence of other viral proteins). Although the discovery of MARV preceded EBOV by nearly ten years^{3,4}, mechanistic insight into the MARV life cycle is lagging behind EBOV. The first step in understanding this process is a comprehensive understanding of the matrix protein structures, lipids they interact with during budding, and assembly processes.

The crystal structure of dimeric mVP40 was solved in 2016⁵; however, to date no known higher ordered structures have been discovered aside from an octameric ring⁶. The dimeric eVP40 crystal structure and hexameric eVP40 crystal structures were resolved simultaneously in 2013⁷. Early investigations hypothesized that the paucity of distinct higher ordered oligomeric mVP40 structures is a result of the extremely high propensity of mVP40 to oligomerize, indicated by the presence of extensive stacked rings⁶. Strikingly, the same investigation successfully captured four distinct eVP40 oligomeric states, suggesting that mVP40 and eVP40 oligomerization may have fundamental differences.

Concomitant with the mVP40 dimer associating with anionic lipids at the plasma membrane is the dynamic and extensive self-oligomerization of mVP40 into the extensive matrix, which confers the virion shape and stability. Although advances in the lipid binding properties of mVP40 have been established^{8,9}, a dearth of information is available regarding the assembly process of mVP40 that ensues following lipid binding. To address this concern, our lab began work using hydrogen deuterium exchange mass spectrometry (HDXMS) of mVP40 and anionic lipids

to identify regions of the protein outside of the membrane binding interface with deuteration profiles that changed upon incubation with lipids. Based on these preliminary results, two distinct regions were identified. Within the N-terminal domain (NTD) lies W83 and N148. Although separated by sequence, upon proper folding these residues are in close proximity. Lastly, L226 and S229 within the $\alpha 4$ helix of the C-terminal domain (CTD) were also identified as a possible interface involved in mVP40 assembly (manuscript in preparation).

Using mVP40 mutants (prepared previously by Kaveesha Wijesinghe) with mutations on key residues located within the hypothesized oligomerization interfaces, we investigated the assembly of mVP40 (**Figure 4.1**). Through the combination of *in vitro* and cellular techniques, the aim of this chapter was to provide supplementary evidence to a larger piece of work investigating a model of mVP40 assembly based on two purported distinct oligomerization interfaces within mVP40. Through size exclusion chromatography (SEC) and *in vitro* liposome pelleting assays we

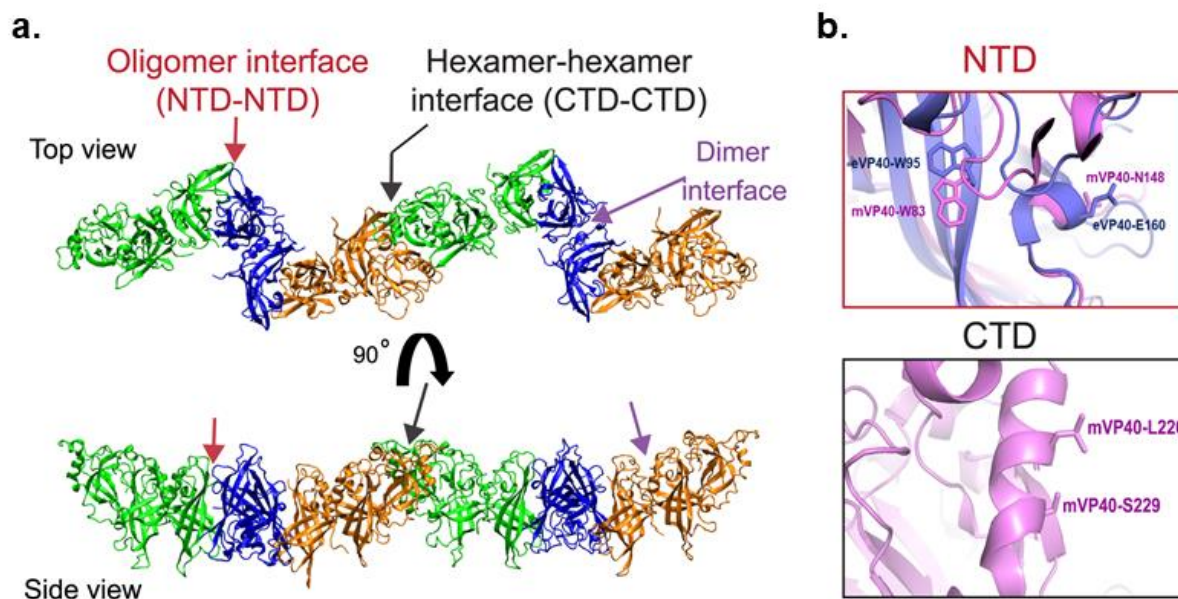


Figure 4.1. Model of mVP40 assembly based on two oligomerization interfaces within the NTD and CTD regions. (a) top and side views of filamentous mVP40 (higher order structure) composed of two hexamers assembled in an end-end fashion; each hexamer is formed through a NTD-NTD interaction while the end-end connection between two hexamers is facilitated by a CTD-CTD interaction. (b) Zoomed view of the mVP40 structure at the NTD oligomer interface (*upper panel*) highlighting W83 and N148 residues (pink) involved in the oligomerization overlaid with the Ebola virus VP40 (eVP40) structure with corresponding residues W95 and E160 (purple). The CTD interface (*bottom panel*) highlighting the proposed residues L226 and S229 involved in hexamer-hexamer interaction. Both were modeled using PyMOL based on mVP40 dimer structure (PDB ID: 5B0V) and eVP40 (PDB ID: 4LDB). (prepared for manuscript by Kaveesha Wijesinghe). mVP40: Marburg VP40; NTD: N-terminal domain; CTD: C-terminal domain.

confirmed that introducing each of the studied mutations did not alter the protein's ability to dimerize or bind to anionic lipids. However, Number & Brightness (N&B) in living cells underscored that these mutations reduce mVP40 oligomerization at the plasma membrane (compared to mVPP40-WT). Lastly, cellular functional budding assays were performed to detail the importance of these interfaces on membrane association and virion assembly. Taken together, these studies support an innovative model of mVP40 oligomerization which departs from the model of eVP40 oligomerization and assembly at the plasma membrane during virion assembly.

4.2 Materials and Methods

4.2.1 Reagents & plasmids

PBS 1x was purchased from Gibco (Life Technologies, Carlsbad, CA). DMEM was purchased from Corning (Corning, NY) and Lipofectamines LTX + Plus was purchased from Life Technologies (Carlsbad, CA). Invitrogen Live Cell Imaging Solution, Halts protease inhibitor Cocktail (100X), phenylmethylsulfonylfluoride (PMSF) and Pierce bicinchoninic acid (BCA) protein assay kit were supplied by Thermo Fisher Scientific (Waltham, MA). Ni-NTA agarose was from Qiagen (Valencia, CA). Amicon 3K and 30K MWCO concentration tubes are from Millipore Sigma (Burlington, MA). All lipids were purchased from Avanti Polar Lipids (Alabaster, AL) and used without further purification. Rabbit α -mVP40 (0303-001) was from IBT-BioServices (Rockville, MD); Mouse α -His (A5588) was from Sigma Aldrich (St. Louis, MO); Mouse α -GFP (MA1-952) and Mouse α -GAPDH were from Thermo Fisher Scientific (Waltham, MA); HRP-Goat- α -Rabbit (ab205718) and HRP-Sheep- α -Mouse (ab6808) were from Abcam (Cambridge, United Kingdom).

pcDNA3.1-EGFP-WT-mVP40 and pET46-6xHis-WT-mVP40 were a kind gift from E. Ollman Sapphire (La Jolla Institute for Immunology) and mutants for each vector were made by site directed mutagenesis previously by Kaveesha Wijesinghe mVP40 using Q5-side directed mutagenesis kit (manuscript in preparation). EGFP was prepared as described previously^{11,12}.

4.2.2 Cells & transfections

HEK293 cells were maintained in DMEM (Invitrogen) containing 10% FBS and 1% Penicillin/streptomycin at 37°C in a 5% CO₂ humidified incubator. 24 hours prior to transfection, cells were seeded into either 6 well plates with poly-D-lysine coated coverslips (Number & Brightness) or into 100 mm collagen coated cell culture dishes (VLP collections) at 70% confluency. Transfections were performed using Lipofectamine LTX + PLUS according to the manufacturer's protocol.

4.2.3 Protein Purification

Purification of mVP40 wild type, mutants (W83R/N148A, L226R, W83R/N148A/L226R) and His-tag alone proteins was adapted from a previously established protocol⁸. In brief, protein expression was performed at 18°C for 18-20 hours with 250 µM isopropyl β-d-1-thiogalactopyranoside (IPTG) and stopped once the optical density (OD_{600nm}) reached 0.7 to 0.8. The bacteria pellets then stored at -20°C until further use. During protein purification, bacterial pellets were lysed for 30 min on ice in lysis buffer (20 mM Tris pH 8.0, 500 mM NaCl, 1x halt protease inhibitors, 300 µg/ml lyzosome, 100 µg/ml RNase and 3 µM PMSF). The lysis solutions were then subjected to 5 sonication cycles at 38% (10 sec on, 59 sec off) and immediately centrifuged for 1 hour (15,000 x *g* at 4°C) to clarify the lysate from cell debris and membranes. The clarified protein solutions were incubated with Ni-NTA agarose for 30 min at 4°C with continuous rocking and subsequently washed in with 5x the column volume of wash buffer (20 mM Tris pH 8.0, 500 mM NaCl and 50 mM Imidazole). Following the wash, three 5 min stepwise elutions were performed with elution buffer (20 mM Tris pH 8.0, 500 mM NaCl and 300 mM Imidazole). The mVP40 eluted fraction was washed and dialyzed against storage buffer (20 mM Tris pH 8.0, 500 mM NaCl, 20 % glycerol) using 30K MWCO concentration tubes. The protein purity and enrichment were confirmed by SDS-PAGE and size exclusion. However, for in vitro assays with lipids, the proteins were used post dialysis.

4.2.4 Functional budding assays and western blotting

Functional budding assays were adapted from an established protocol¹⁰. HEK293 cells at $1-1.5 \times 10^6$ density, were transfected with GFP-fused mVP40 constructs with or without co-expression of Marburg GP using Lipofectamine LTX + PLUS according to the manufacturer's protocol. At 24 hours post transfection, the media containing virus like particles (VLPs) was harvested and clarified using low speed centrifugation (1000 RPM, 4°C, 10 min). Following centrifugation, the supernatants were gently added to a 20% sucrose cushion in STE buffer (10mM Tris, 1 mM EDTA, 100 mM NaCl, pH 7.4) and VLPs were pelleted through high speed centrifugation ($220,000 \times g$, 4°C, 2 hours)¹⁰. The supernatant was discarded, and the VLP pellets were air dried for 5 minutes at room temperature, resuspended in STE buffer, and stored at -80°C until western blotting analysis. For cell lysate collections, cells were scraped in 1x PBS, pelleted (900 rpm, 25°C, 7 min), and washed again with PBS before lysis in RIPA lysis buffer (150 mM NaCl, 5 mM EDTA pH 8.0, 50 mM Tris pH 8.0, 0.5% sodium deoxycholate, 0.1% SDS, supplemented with Halts protease inhibitor (ThermoFisher, Waltham, MA)). Cell lysates were incubated on ice for 1 hr with occasional and gentle vortexing. Cell lysates were then centrifuged ($25,000 \times g$, 4°C, 20 min) and the supernatants containing soluble protein were stored at -80°C until western blotting analysis. Protein concentrations were determined using Pierce BCA protein kits (ThermoFisher, Waltham, MA).

Equal total protein content (5 μ g) of soluble proteins from cell lysates and VLP proteins were resolved on a 15-well 12% SDS-PAGE gel prior to transferring onto nitrocellulose membranes. Target proteins were detected using the appropriate primary antibody (for mVP40: Rabbit α -mVP40: 1:200,000 O/N at 4°C and in one replicate Mouse α -GFP: 1:2000 for 1.5 hr at RT; for GAPDH: Mouse α -GAPDH: 1:10,000 O/N at 4°C) followed by the appropriate secondary antibodies horseradish peroxidase (HRP) conjugated (HRP-Goat α -Rabbit: 1:5000 for 1.5 hr at RT or Sheep α -Mouse: 1:5000 for 1 hr at RT). HRP signal was detected using Amersham Prime ECL reagent (GE Lifesciences, Chicago, IL) and imaged on the GE Amersham 600 imager. VLP budding index of different mVP40 proteins, was performed with densitometry analysis using ImageJ (<http://rsb.info.nih.gov/ij/>). The following equation was applied: $\text{density}_{\text{VLP}} / \text{density}_{\text{C+VLP}}$ (where $\text{density}_{\text{VLP}}$ is the eVP40 VLP band density and $\text{density}_{\text{C+VLP}}$ is the eVP40 cell lysate + VLP band density). The budding index of each mutant was normalized to the WT-mVP40 budding index.

4.2.5 Liposome Sedimentation Assays

Large unilamellar vesicles (LUV) were used for liposome sedimentation assays. Lipid mixtures were prepared at the indicated compositions, chloroform soluble lipids were dried to form lipid films under a continuous stream of N₂. In each experiment, addition of negatively charged lipids was compensated with an equal mol% decrease in POPC, while POPE (9%) and dansylPE (1%) were held constant. Lipid films were then hydrated in liposome sedimentation buffer (260 μM raffinose pentahydrate in PBS, pH 7.4), vortexed vigorously, and extruded through a 200 nm Whatman polycarbonate filter (GE Healthcare) after incubation at 37°C. Vesicle size was confirmed by dynamic light scattering using a DelsaNano S Particle Analyzer (Beckman Coulter, Brea, CA). LUV solutions were diluted 4 times in PBS (pH 7.4) to reduce the raffinose pentahydrate concentration, and LUVs were pelleted at 50,000 x g, 22°C for 15 min. The supernatant was discarded and the raffinose filled-LUVs were resuspended in PBS (pH 7.4).

Liposome sedimentation assays were performed as described previously¹³. In brief, equal volumes of protein (final concentration= 5.0 μg/mL) and LUVs (final concentration = 2 mM) were incubated for 30 min on ice. Following incubation, protein bound-LUVs were pelleted (16,000 xg, 4°C, 30 min), and the supernatants containing unbound proteins were transferred in new tubes. The protein bound-LUV pellet was washed in PBS and pelleted again (16,000 x g, 4°C, 30 min). The supernatant was discarded, and the pellet was resuspended in equal volume as the unbound protein supernatant sample.

Equal volumes of supernatant and pellet samples were resolved on a 10% SDS-PAGE gel and transferred onto a nitrocellulose membrane. The proteins were detected using the primary antibody (Mouse α-His; 1:2500 for 1 hr at RT) followed by the secondary antibody HRP conjugated (Sheep α-Mouse; 1:7000 for 1 hr at RT). The HRP signals were detected using Amersham ECL reagent (GE Lifesciences, Chicago, IL), imaged on GE Amersham 600 imager and analyzed through densitometry analysis in ImageJ. To calculate %protein bound the following equation was used: $\text{density}_{\text{pellet}} / \text{density}_{\text{total}}$ where $\text{density}_{\text{total}} = \text{density}_{\text{supernatant}} + \text{density}_{\text{pellet}}$.

4.2.6 Number & Brightness (N&B) analysis on mammalian cells

N&B experiments were performed as described previously^{11,12,14}. HEK293 cells were seeded onto 1.5 mm poly-D-lysine coated coverslips 0.17 mm thickness, in a 6-well plate at 70%

confluency. Cells were transfected with either EGFP or EGFP-tagged mVP40 constructs using Lipofectamine LTX + PLUS according to the manufacturers protocol. 24 hours post transfection, cells were washed with 1X PBS, transferred to Attotfluor chambers (Invitrogen), and imaged in Live cell imaging solution using the Zeiss LSM 880 upright microscope using a LD “C-Apochromat” 40x/1.1 W Corr M27 objective. A 488 nm argon laser was used to excite EGFP.

Each image was acquired using the same laser power (0.01), resolution (256x256), pixel dwell time (16 us), frames (50), and zoom (pixel size of 50 nm). SimFCS Globals Software (Laboratory for Fluorescence Dynamics, University of California, Irvine, CA) was used for analysis.

On each experimental day, EGFP expressing cells were imaged and SimFCS4 software (G-SOFT Inc.) was used to determine the true brightness (B) of a monomeric EGFP (0.058-0.13). To calculate the apparent brightness value of mVP40 oligomers, the B_{monomer} value was multiplied by the corresponding oligomer value (i.e. dimer = 2, hexamer = 6). Using SimFCS, bins were placed in the brightness plot to correspond with the respective oligomer size. The number of pixels of monomer-hexamer, hexamer-12mer, 12mer-24mer, and 24mer+ bins were recorded. Average % Pixels of each oligomeric state was ratiometrically determined by the total number of pixels in each bin vs. the total number of pixels in the image.

4.3 Results

4.3.1 mVP40 mutants form dimers in solution

Prior to detailed investigations into the assembly processes of mVP40 mutants, our first goal was to ensure introducing mutations into the proposed oligomerization interfaces did not disrupt the ability of mVP40 to dimerize. To this end, we performed SEC on mVP40 proteins purified from *E. coli*. The ability of WT-mVP40 to form a dimer in solution has been previously reported⁵, and under our SEC conditions WT-mVP40 eluted after ~75 mL (**Figure 4.2 a**). Therefore, each subsequent protein was expected to elute at the same fraction if it were also dimeric. Furthermore, T105R-mVP40 exists as a monomer, which was corroborated by our SEC finds where the protein eluted after 75 mL (**Figure 4.2 b**).

Next, we purified W83R/N148A-mVP40, W83R/N148A/L226R-mVP40, and L226R-mVP40 and performed SEC. Following separation using SEC, the chromatogram for each protein

indicated that none of the mutations interfered with dimerization, as each protein eluted at ~75 mL (**Figure 4.2 c-e**) proteins. The confirmation that each protein can form a dimer ensures that any

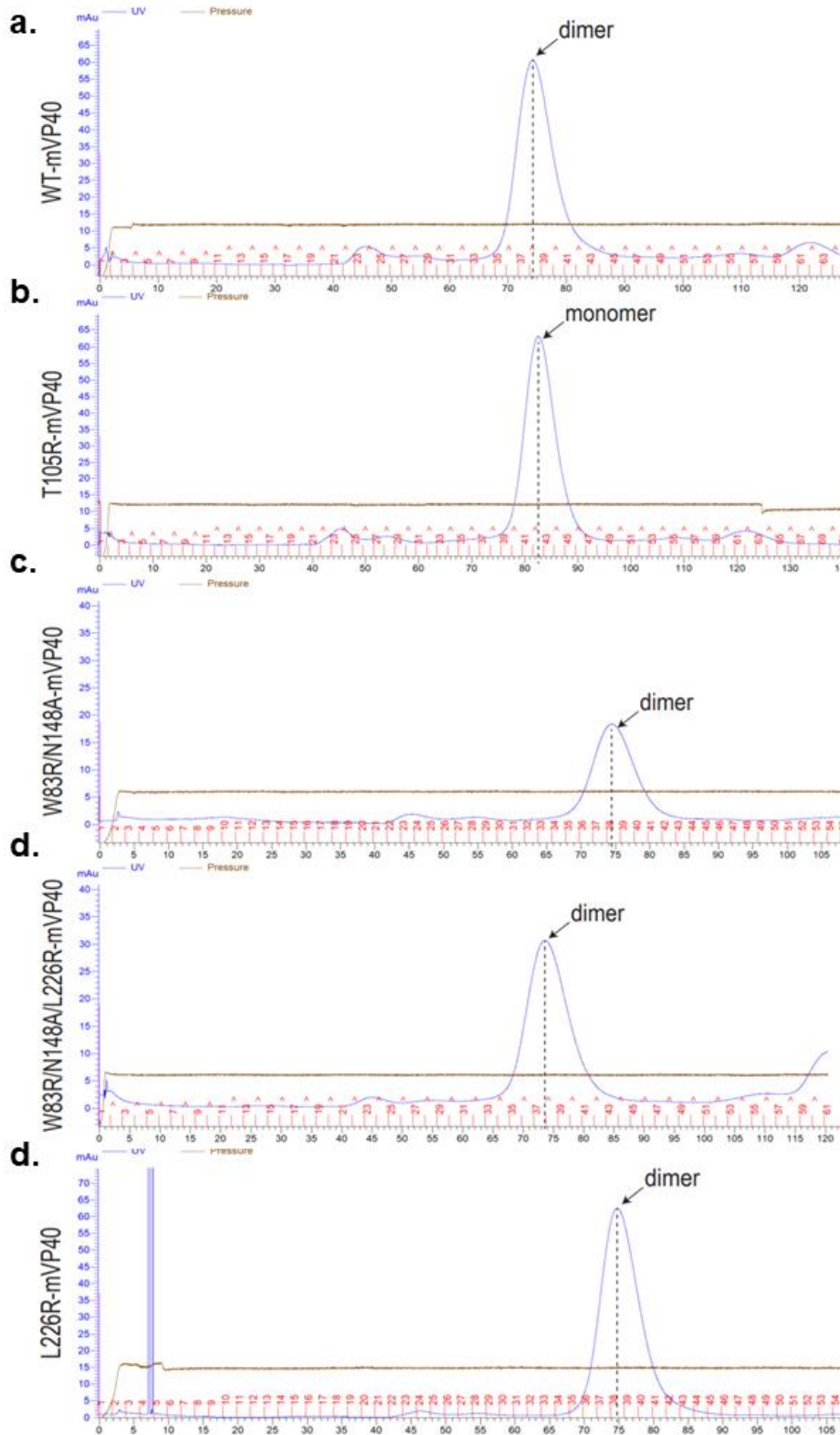


Figure 4.2. Mutation of the predicted oligomerization interfaces of mVP40 did not alter dimer formation. Size exclusion chromatography of 6xHis- mVP40 constructs purified from *Escherichia coli* was performed to assess the ability of mVP40 to dimerize. **(a)** mVP40 WT chromatogram indicated the presence of dimeric mVP40. **(b)** mVP40 T105R chromatograph indicated the T105R point mutation resulted in loss of dimeric mVP40, as previously reported¹¹. **(c)** mVP40 W83R/N148A chromatogram indicated the W83R/N148A protein is still able to form a dimer. **(d)** W83R/N148A/L226R chromatogram indicated the W83R/N148A/L226R protein did not disrupt dimer formation. **(e)** L226R chromatogram indicated the L226R point mutation did not disrupt dimer formation.

subsequent observations are not a result of the protein's inability to dimerize but possibly its ability to interact with lipids or oligomerize into higher order structures.

4.3.2 Mutation of putative oligomerization interfaces does not alter anionic lipid binding

The ability of mVP40 to associate non-specifically with anionic lipids within the plasma membrane (e.g. PS and PI(4,5)P₂) has previously been established⁸. Therefore, to evaluate if introducing any of the putative oligomerization deficient mutations affected the propensity of each mVP40 mutant to associate with lipid membranes, liposome sedimentation assays were performed. A liposome sedimentation assay is a straightforward and inexpensive technique to evaluate protein-lipid binding *in vitro*. LUVs were prepared containing either no anionic lipids (control membranes) or with 30% PS and 2.5% PI(4,5)P₂ (anionic membranes).

A representative western blot is shown in Figure 4.3A and quantified results from densitometry analysis are shown in Figure X. In agreement with previously published findings, WT-mVP40 does not associate with neutral membranes, indicated by no detectable protein in the control membrane pellet fraction (Fig. 4.3A *lane 1* & Fig. 4.3B). Conversely, when anionic membranes were incubated with WT-mVP40, nearly 100% of the protein was detected in the pellet fraction (Fig. 4.3A *lane 6* & Fig. 4.3B), validating the previously published report that WT-mVP40 strongly associates with anionic lipids⁸. Furthermore, regardless of the mutation introduced, no protein was detected in the pellet fraction of any samples incubated with neutral membranes and nearly 100% of the protein was detected in the pellet fraction of samples incubated with anionic membranes (Fig. 4.3A-B). As a control, mVP40-T105R lipid binding was also assessed. mVP40-T105R has been extensively reported to exist as a monomer which fails to dimerize and associate with the plasma membrane^{5,15}. This finding is confirmed by our liposome sedimentation assay data, where no detectable mVP40-T105R protein is observed when incubated with either the control or anionic membranes (Fig. 4.3A-B). These findings suggest that no mutations introduced altered the ability of mVP40 to associate with anionic lipids known to reside within the plasma membrane which facilitate mVP40 viral budding.

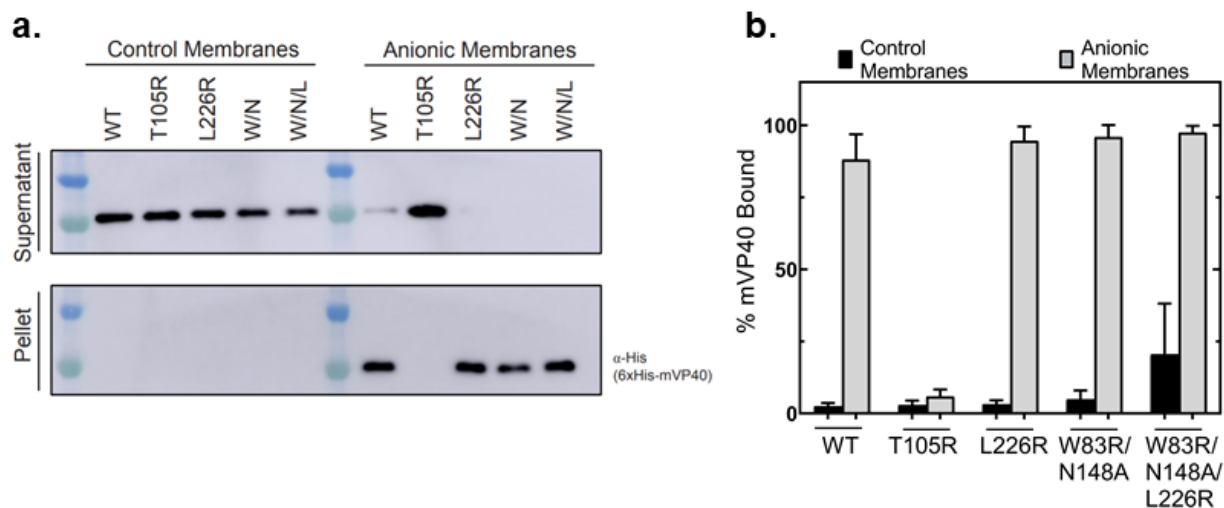


Figure 4.3. *In vitro* lipid binding profile of mVP40 mutants revealed no change in anionic lipid binding compared to mVP40-WT. Liposome sedimentation assays were performed using the indicated mVP40 construct and either control membranes (no anionic lipids) and anionic membranes (30% PS and 2.5% PI(4,5)P₂). 6xHis-mVP40 WT, 6xHis-mVP40 T105R, 6xHis-mVP40 L226R, 6xHis-mVP40 W83R/N148A, and 6xHis-mVP40 W83R/N148A/L226R purified from *Escherichia coli* Rosetta pLysS cells and further purified using SEC. **(a)** Representative western blot from liposome sedimentation assays with the supernatant fraction (top panel) and pellet fraction (bottom panel). 6xHis-mVP40 was probed with a Mouse α -His primary antibody and HRP-Sheep α -Mouse secondary antibody, and detected using ECL. BioRad Kaleidoscope protein ladder was used for a reference to protein size. **(b)** Quantification of liposome sedimentation assays. To determine % mVP40 bound, the mVP40 supernatant density and mVP40 pellet density was measured using densitometry analysis (performed in ImageJ). The ratio of mVP40 pellet density vs. total mVP40 density (pellet + supernatant) was calculated and the average was plotted (N=6, n=3). Values are reported as mean \pm standard deviation, and a two-way ANOVA was performed (* p <0.05 and *** p <0.0001)

4.3.3 Aberrant oligomerization is observed in mVP40 mutants

A critical step in the viral budding process is the assembly of the viral matrix layer, a dynamic process facilitated by the extensive oligomerization of mVP40. Initially, HDXMS experiments were performed with purified mVP40 and liposomes and identified several amino acids with differential deuterium exchange profiles following incubation of mVP40 with liposomes (manuscript in preparation). Therefore, we hypothesized that these regions were involved in the mVP40 assembly process following binding to anionic lipids.

To study the role of these amino acids in mVP40 assembly, GFP-fused mVP40 mutants were generated and mVP40 oligomerization was evaluated in living cells using N&B. N&B is a powerful tool to detect the multimerization of proteins in living cells in real time with pixel resolution. Moreover, this technique has been used to evaluate viral matrix protein oligomerization^{11,12,14}.

To determine the brightness value for a monomer, GFP was expressed in HEK293 cells. To determine the brightness value of higher ordered oligomeric states of GFP-mVP40 constructs expressed in HEK293 cells, multiples of the EGFP monomer brightness value was extrapolated to the corresponding oligomeric states. Pixel intensities correlating to monomer-hexamer (red), hexamer-12mer (green), 12mer-24mer (blue), and >24mer (pink) oligomeric states of mVP40 were analyzed in SimFCS Globals Software (Laboratory for Fluorescence Dynamics, University of California, Irvine, CA), mapped onto the original composite image of the cell and plotted as a percent of total pixels in the image.

Prior to examining the effects mutations had on mVP40 oligomerization, we first established the oligomerization profile of WT-mVP40. N&B analysis revealed the largest population of GFP-WT-mVP40 was in the monomer-hexamer assembly state (~52% total pixels). Additionally, each higher ordered oligomeric state was roughly equally represented (~13%-19% total pixels), which is visually represented by the green, blue and pink pixels within the brightness selection plot (**Figure 4.4 a top panel, Figure 4.4 b**). To evaluate the degree of oligomerization changes in each mutant, a two-way ANOVA was performed comparing the number of pixels in each oligomerization state of the mutant to the number of pixels in each oligomerization state for WT.

We also validated our experimental settings through N&B analysis on cells expressing GFP-mVP40-T105R. mVP40-T105R has been experimentally evaluated through numerous techniques reported to exist as a monomer and fails to form dimers or higher ordered oligomers⁵. As we hypothesized, ~98% of total pixels in GFP-mVP40-T105R expressing cells resided in the monomeric-hexameric population (**Figure 4.4 b**), which is significantly more than WT-mVP40 ($p < 0.0001$) and represented by the large proportion of red pixels in the T105R brightness selection plot (**Figure 4.4 c**). Oligomerization of GFP-mVP40-T105R was effectively lost, as no measurable amount of pixels were detected in any higher ordered oligomeric state, depicted by the lack of any green, blue, or pink pixels in the T105R brightness selection plot (**Figure 4.4 c**).

4.3.3.1 Mutating residues with the NTD-oligomerization interface significantly interferes with mVP40 oligomerization

A single point mutation was made at W83R to investigate the role of W83 in mVP40 oligomerization, an amino acid conserved in eVP40 and postulated to be important for eVP40

oligomerization⁷. The GFP-mVP40-W83R mutant had a ~10% reduction in protein within the >24mer oligomeric state compared to GFP-WT-mVP40. This increase was compensated for by a slight increase in the monomer-hexamer population (~8% increase compared to WT) and hexamer-12mer population (~3% increase from WT) (**Figure 4.4 a-b**). This indicates that W83R point mutation is stalling at an early stage of mVP40 assembly, however is still capable of efficiently forming oligomers up to the hexamer.

An additional amino acid conserved within dimeric mVP40 and eVP40 was also evaluated for its implications on mVP40 assembly. Two point mutations were introduced within mVP40, GFP-mVP40-W83R/N148A (mVP40-W/N). The oligomerization of GFP-mVP40-W/N was significantly altered from the oligomerization profile of GFP-WT-mVP40. A significant reduction in the >24mer population was observed for GFP-mVP40-W/N compared to WT-mVP40 ($p=0.0223$)(**Figure 4.4 a-b**). GFP-WT-mVP40 had ~19% of total pixels in the >24mer population, while GFP-mVP40-W/N had only ~3% of total pixels in the >24mer population, a ~16% reduction (**Figure 4.4 a-b**). Furthermore, a robust albeit not statistically significant reduction in the 12-24mer population was also observed in the GFP-mVP40-W/N oligomerization profile (a 9% reduction from WT-mVP40). These reductions were compensated by a significant increase in the monomer-hexamer population (a 29% increase from ~52% in GFP-WT-mVP40 to ~81% in GFP-mVP40-W/N) ($p<0.0001$)(**Figure 4.4 b**), which is indicated by the increase in red pixels in the brightness selection plot (**Figure 4.4 a**).

HDX-MS data also revealed a third amino acid within the $\alpha 4$ helix of mVP40 with potential implications on mVP40 oligomerization, therefore a third point mutation was introduced to generate GFP-mVP40-W38R/N148A/L226R (mVP40-W/N/L) and N&B analysis was performed. Contrary to GFP-WT-mVP40, GFP-mVP40-W83R and GFP-mVP40-W/N, oligomerization of GFP-mVP40-W/N/L was effectively abolished. The largest population of oligomeric GFP-mVP40-W/N/L was the hexamer-12mer population at ~3% of total pixels; however, this was a 10% reduction from the GFP-WT-mVP40 hexamer-12mer population (~13% in WT-mVP40). Additionally, a 13% reduction of the 12mer-24mer population was detected, from ~14% in GFP-WT-mVP40 to ~1% in GFP-mVP40-W/N/L (**Figure 4.4 a-b**). Furthermore, a significant reduction of 19% was observed for the >24mer population, from ~19% in GFP-WT-mVP40 to ~0.2% in GFP-mVP40-W/N/L ($p<0.0001$)(**Figure 4.4 a-b**). Lastly, ~95% of GFP-mVP40-W/N/L was detected in the monomeric-hexameric population, a significant 43% increase from GFP-WT-

mVP40 (~52% in WT-mVP40)($p < 0.0001$)(**Figure 4.4 a-b**). Each of these changes to the oligomerization profile of GFP-mVP40-W/N/L is readily observable in the brightness selection plot (**Figure 4.4 a**) with a large increase in the red pixels (monomer-hexamer) and reduction in each of the higher order oligomeric states (green, blue and pink pixels).

4.3.3.2 Mutating residues in the CTD-oligomerization interface alters high ordered mVP40 oligomerization

As oligomerization was largely abrogated in GFP-mVP40-W/N/L, we next generated a single point mutation within the $\alpha 4$ helix (GFP-mVP40-L226R) to evaluate the role of this amino acid in oligomerization, independently of the other hypothesized oligomerization interface. Surprisingly, the oligomerization profile of GFP-mVP40-L226R was generally quantitatively similar to the oligomerization profile of GFP-WT-mVP40. However, a notable difference was observed in the >24 mer oligomeric population, where only ~7% of total pixels resided in the >24 mer population of GFP-mVP40-L226R (a 12% reduction from the ~19% of total pixels in the >24 mer population of GFP-WT-mVP40)(**Figure 4.4 b**). Although this reduction was not statistically significant, an observable difference is seen in the brightness selection plots (**Figure 4.4 a, c**) of GFP-WT-mVP40 and GFP-mVP40-L226R with the GFP-mVP40-L226R cells having drastically less blue (12-24mer) and pink (>24 mer) pixels and more regions of the cell with red pixels (monomer-hexamer).

An additional mutation was introduced to the $\alpha 4$ helix of mVP40 to further evaluate the role of the $\alpha 4$ helix in mVP40 oligomerization, GFP-mVP40-L226R/S229R. Based on the HDX-MS data we hypothesized a double mutation in this helix would further diminish mVP40 oligomerization (compared to WT-mVP40 and the single mutant mVP40-L226R). Surprisingly, the oligomerization profile of GFP-mVP40-L226R/S229R was not distinguishably different from the oligomerization profile of GFP-mVP40-L226R. Only ~9% of the GFP-mVP40-L226R/S229R protein population resided in the >24 mer oligomeric state, a 10% reduction compared to GFP-WT-mVP40, and nearly equivalent to the ~7% observed for the single mutant GFP-mVP40-L226R (**Figure 4.4 a-c**).

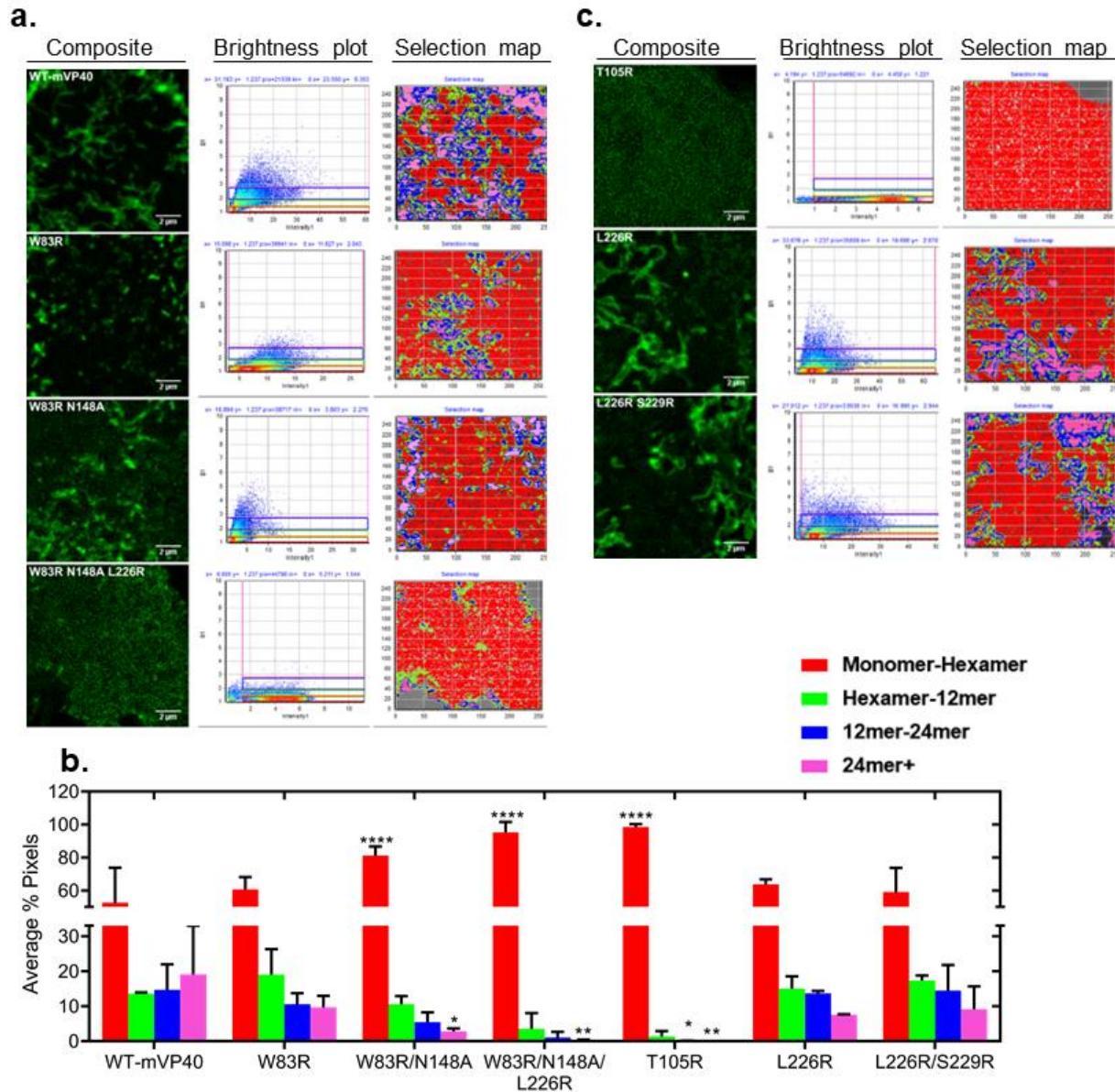


Figure 4.4. Cellular oligomerization profile of mVP40 mutants analyzed through Number & Brightness. HEK293 cells transiently expressing GFP-fused mVP40 constructs were imaged at 24 hours post transfection and Number & Brightness analysis was performed using SimFCS software. **(a)** Representative images of the workflow in SimFCS for Number & Brightness analysis of GFP-mVP40 WT, GFP-mVP40 W83R, GFP-mVP40 W83R/N148A, GFP-mVP40 W83R/N148A/L226R. The original composite of the time-lapse images (left panel), the number of pixels vs. intensity plot (middle panel) and brightness selection plot of the cell (right panel) are shown for each construct. **(b)** The percent pixels with a brightness value of xx-xx (monomer) are shown in red, xx-xx (hexamer-12mer) are shown in green, xx-xx (12mer-24mer) are shown in blue and xx-xx (>24mer) are shown in pink. The percent pixels with each corresponding brightness value were calculated per cell and the average value for each construct was plotted. Values are reported as mean \pm standard deviation. A two-way ANOVA with multiple comparisons was performed, where * $p < 0.05$, ** $p < 0.005$ and **** $p < 0.0001$. N=15, n=3 **(c)** Representative images of the workflow in SimFCS for Number & Brightness analysis of GFP-mVP40 T105R, GFP-mVP40 L226R, GFP-mVP40 L226R/S229R. The original composite of the time-lapse images (left panel), the number of pixels vs. intensity plot (middle panel) and brightness selection plot of the cell (right panel) are shown for each construct.

4.3.4 Oligomerization deficient mutants fail to produce VLPs

To understand the functional significance of GFP-mVP40 oligomerization deficient mutants, functional budding assays of HEK293 cells expressing GFP-mVP40 were performed. We hypothesized that mVP40 mutants with aberrant oligomerization would fail to produce VLPs. Additionally, an interaction between mGP and mVP40 has been previously reported¹⁶, therefore co-expression of mGP and mVP40 was performed for some of the functional budding assays. Western blotting was performed using GFP-mVP40 specific antibodies (**Figure 4.5 a**) and the relative budding efficiency was calculated (**Figure 4.5 b**)

Robust VLP production was observed for cells expressing WT-mVP40, with a slight but not significant increase in VLP production when WT-mVP40 was co-expressed with mGP (**Figure 4.5 a lanes 2-3**). No VLPs were detectable in cells expressing GFP-mVP40-W83R (**Figure 4.5 a lane 4**). This was slightly surprising as oligomerization was not totally abrogated from N&B experiments. Furthermore, functional budding assays revealed no detectable VLPs for the double (GFP-mVP40-W/N) and triple (GFP-mVP40-W/N/L) mutant (**Figure 4.5 a lane 5-8, Figure 4.5 b**). This finding corroborates N&B experiments revealed oligomerization of these mutants was further impaired compared to the single mutant (GFP-mVP40-W83R). In line with the WT-mVP40 functional budding assay results, co-expression of these two mutants (mVP40-W/N and mVP40-W/N/L) with mGP resulted in a small but not significant increase in VLP production (**Figure 4.5 a lanes 3,6,8, Figure 4.5 b**).

Mutating the second hypothesized oligomerization interface (the $\alpha 4$ helix) did not alter VLP production as drastically as the W83, N148 interface. As is seen in **Figure 4.5 b**, GFP-mVP40-L226R had ~50% reduction in VLP production compared to HEK293 cells expressing GFP-WT-mVP40 (**Figure 4.5 a lanes 10-11**). GFP-mVP40-L226R/S229R produced ~25% fewer VLPs compared to WT-mVP40 (**Figure 4.5 a lane 12, Figure 4.5 b**). Surprisingly, co-expression of mVP40-L226R/S229R with mGP led to a reduction of VLP production compared to mVP40-L226R/S229R alone (**Figure 45 a lane 13, Figure 4.5 b**). It could be possible that the L226R/S229R fails to properly interact with GP within the plasma membrane, leading to the reduced VLP production.

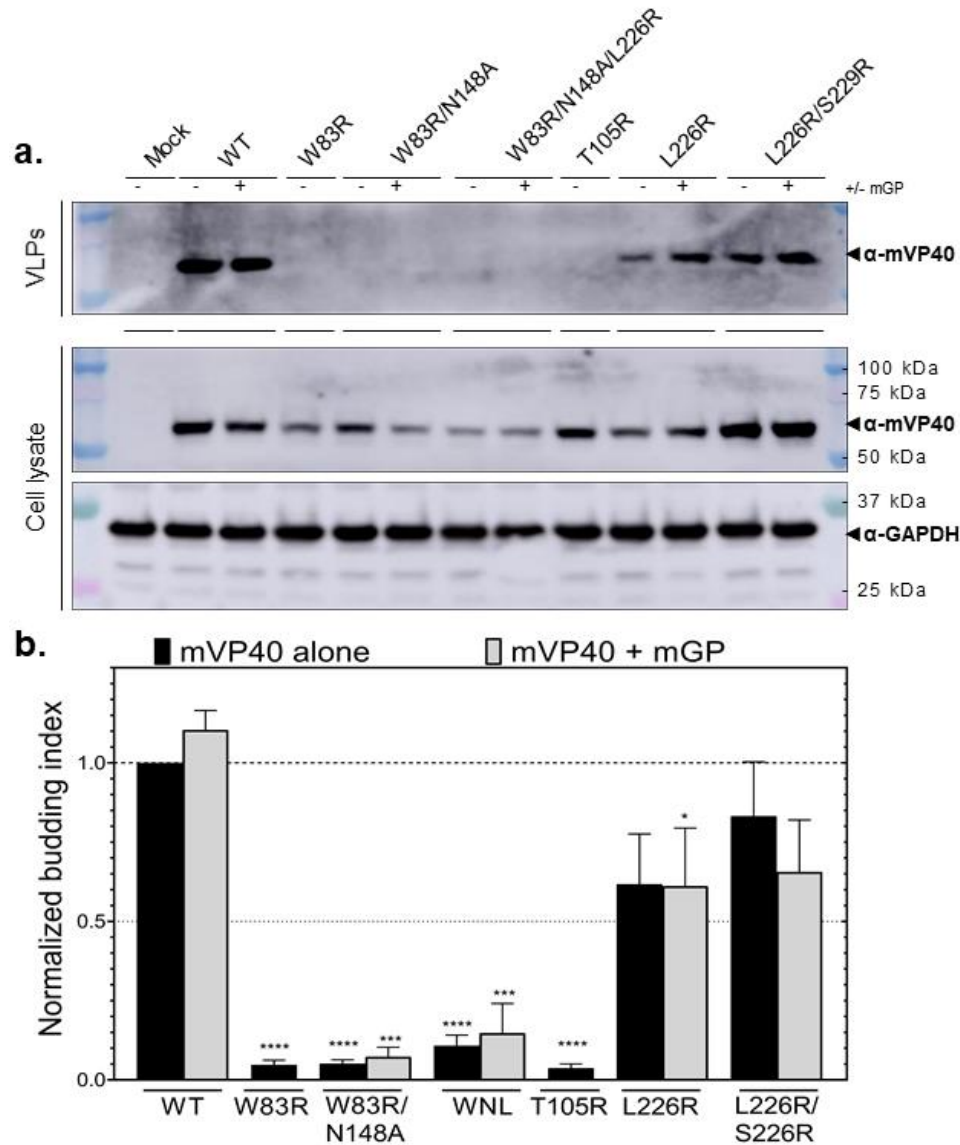


Figure 4.5. Perturbation of mVP40 oligomerization reduces VLP production. Functional budding assays were performed to assess the capacity of mVP40 WT and mutants to produce VLPs. Cell lysate and VLP samples were collected from HEK293 cells after 24 hours of transient expression of the indicated GFP-mVP40 protein in the presence and absence of mGP. (A) Representative western blot of functional budding assays. Cell lysate samples were probed for mVP40 using either the antibody information (top panel) and for the loading control GAPDH using antibody information (bottom panel). (B) Representative western blot of VLP samples from functional budding assays. VLP samples were probed for mVP40 using either the antibody information. In both (A) and (B) protein bands were detected using ECL reagent and the BioRad Kaleidoscope protein ladder was used as a reference for protein size. (C) Quantification of the budding index for each mVP40 protein was determined by densitometry analysis (performed in ImageJ). The budding index (normalized to mVP40 WT) was quantified by measuring the ratio of mVP40 band density in the VLP fraction compared to total mVP40 band density (cell lysate density + VLP density). In each western, mVP40 cell lysate density was normalized to the GAPDH loading control band density. Values are reported as the mean \pm standard deviation. $n=3-4$ and a one-way ANOVA with multiple comparisons was performed (**** $p<0.0001$).

4.4 Discussion

The innate ability of viral matrix proteins is fundamental to the physiological roles that they execute. While no clear higher order oligomeric states of mVP40 have been identified beyond the octameric ring⁶, inferences can be made from eVP40, a closely related matrix protein. Although the available crystal structures of eVP40 are helpful in directing investigations in mVP40 assembly, the two proteins embark on variable trafficking routes within the cell and interact with the plasma membrane through different mechanisms. In fact, it is well documented that mVP40 is highly associated with and traffics on intracellular membranes^{15,17–19}. Work preceding this chapter identified two novel oligomerization interfaces within dimeric mVP40, one involving W83 and N148 within the NTD and the $\alpha 4$ helix within the CTD (including residues L226 and S229). The goal of this chapter was to provide supplementary investigations into how these residues may be important for lipid association, oligomerization, and VLP production.

mVP40 exists as a dimer in solution, and through SEC we were able to show that each NTD- and CTD-mutant dimerized (with the exception of the monomeric control T105R-mVP40^{5,15}). While W/N-mVP40 has been investigated by others and shown to dimerize -each mutant forms a dimer in solution-, therefore mutating these regions does not interfere with dimer formation. Furthermore, each of the NTD and CTD mutants associated with anionic membranes, while T105R did not, which was not surprising as none of the mutations were made within the membrane binding interface. This supports the finding that dimer formation is needed for membrane association. However, it is still unclear if mVP40 oligomerizes into a pre-assembly complex on internal membranes prior to reaching the plasma membrane, and insight into this may help understand the mVP40 budding process.

In this study, our N&B results indicate clear differences between WT-mVP40 oligomerization and the ability of NTD mutants oligomerization. The single mutant W83R oligomerized to an extent similar to WT-mVP40; however, a slight decrease in structures beyond a 12mer and an increase in hexameric-12mer mVP40 was observed for W83R-mVP40. Therefore, it is possible that W83 is important for transitioning past the hexameric state. W83R-mVP40 failed to produce any VLPs, which may indicate that a stable transition beyond hexameric mVP40 is vital to efficient VLP production. Likewise, when an additional mutation was introduced to the NTD (W83R/N148A-mVP40), oligomerization was significantly affected. Each oligomeric state beyond the monomer-hexamer was reduced within W83R/N148A-mVP40 expressing cells and

the mutant failed to produce any VLPs. Furthermore the introduction of a third mutation (W83R/N148A/L226R-mVP40) completely abolished any oligomerization or VLP production. It was interesting that when examined independently, the LS226R-mVP40 did not appear to have any deficiencies in oligomerization. However, L226R-mVP40 VLP production was reduced compared to WT-mVP40. Lastly, mutating two residues within the α 4-helix of the CTD (L226R/S229R-mVP40) also did not significantly alter mVP40 oligomerization or VLP production. Taken together, our N&B analysis and budding assays suggest that the NTD and CTD oligomerization interfaces serve distinct and separate roles in mVP40 assembly where the NTD aids in early oligomerization transformations and the CTD is involved in large filament stability.

4.5 References

1. Suzuki, Y. & Gojobori, T. The origin and evolution of Ebola and Marburg viruses. *Mol. Biol. Evol.* **14**, 800–806 (1997).
2. Liu, L. Fields Virology, 6th Edition. *Clin. Infect. Dis.* **59**, 613–613 (2014).
3. Slenczka, W. & Klenk, H. D. Forty Years of Marburg Virus. *J. Infect. Dis.* **196**, S131–S135 (2007).
4. Breman, J. G. *et al.* Discovery and Description of Ebola Zaire Virus in 1976 and Relevance to the West African Epidemic during 2013–2016. *J. Infect. Dis.* **214**, S93–S101 (2016).
5. Oda, S.-I. *et al.* Crystal Structure of Marburg Virus VP40 Reveals a Broad, Basic Patch for Matrix Assembly and a Requirement of the N-Terminal Domain for Immunosuppression. *J. Virol.* **90**, 1839–48 (2016).
6. Timmins, J. *et al.* Oligomerization and polymerization of the filovirus matrix protein VP40. *Virology* **312**, 359–368 (2003).
7. Bornholdt, Z. A. *et al.* Structural rearrangement of ebola virus vp40 begets multiple functions in the virus life cycle. *Cell* **154**, 763–774 (2013).
8. Wijesinghe, K. J. & Stahelin, V. Investigation of the Lipid Binding Properties of the Marburg Virus. *J. Virol.* **90**, 3074–3085 (2016).
9. Wijesinghe, K. J. *et al.* Detection of lipid-induced structural changes of the Marburg virus matrix protein VP40 using hydrogen/deuterium exchange-mass spectrometry. *J. Biol. Chem.* **292**, 6108–6122 (2017).
10. Harty, R. N. Hemorrhagic Fever Virus Budding Studies. in *Hemorrhagic Fever Viruses: Methods and Protocols* (ed. Salvato, M. S.) **1604**, 209–215 (Springer New York, 2018).
11. Johnson, K. A., Taghon, G. J. F., Scott, J. L. & Stahelin, R. V. The Ebola Virus matrix protein, VP40, requires phosphatidylinositol 4,5-bisphosphate (PI(4,5)P₂) for extensive oligomerization at the plasma membrane and viral egress. *Sci. Rep.* **6**, 19125 (2016).
12. Adu-Gyamfi, E., Digman, M. A., Gratton, E. & Stahelin, R. V. Investigation of Ebola VP40 assembly and oligomerization in live cells using number and brightness analysis. *Biophys. J.* **102**, 2517–25 (2012).
13. Julkowska, M. M., Rankenberg, J. M. & Testerink, C. Liposome-Binding Assays to Assess Specificity and Affinity of Phospholipid--Protein Interactions. in *Plant Lipid Signaling Protocols* (eds. Munnik, T. & Heilmann, I.) 261–271 (Humana Press, 2013). doi:10.1007/978-1-62703-401-2_24
14. Bobone, S. *et al.* Phosphatidylserine Lateral Organization Influences the Interaction of Influenza Virus Matrix Protein 1 with Lipid Membranes. *J. Virol.* **91**, 1–15 (2017).
15. Koehler, A., Pfeiffer, S., Kolesnikova, L. & Becker, S. Analysis of the multifunctionality of Marburg virus VP40. *J. Gen. Virol.* **99**, 1614–1620 (2018).
16. Kolesnikova, L., Ryabchikova, E., Shestopalov, A. & Becker, S. Basolateral Budding of Marburg Virus: VP40 Retargets Viral Glycoprotein GP to the Basolateral Surface. *J. Infect. Dis.* **196**, S232–S236 (2007).
17. Kolesnikova, L., Bugany, H., Klenk, H.-D. & Becker, S. VP40, the Matrix Protein of Marburg Virus, Is Associated with Membranes of the Late Endosomal Compartment. *J. Virol.* **76**, 1825–1838 (2002).
18. Kolesnikova, L., Bamberg, S., Berghofer, B. & Becker, S. The Matrix Protein of Marburg Virus Is Transported to the Plasma Membrane along Cellular Membranes: Exploiting the

- Retrograde Late Endosomal Pathway. *J. Virol.* **78**, 2382–2393 (2004).
19. Makino, A., Yamayoshi, S., Shinya, K., Noda, T. & Kawaoka, Y. Identification of Amino Acids in Marburg Virus VP40 That Are Important for Virus-Like Particle Budding. *J. Infect. Dis.* **204**, S871–S877 (2011).

CHAPTER 5. THE EBOLA VIRUS MATRIX PROTEIN CLUSTERS PHOSPHATIDYLSERINE, A CRITICAL STEP IN VIRAL BUDDING WHICH CAN BE REDUCED WITH AN FDA APPROVED DRUG TO INHIBIT VIRAL SPREAD

5.1 Introduction

Ebola virus (EBOV), which was first discovered in 1976^{1,2} has been of much concern recently due to an ongoing outbreak in the Democratic Republic of Congo as well as the unprecedented 2014-16 outbreak in Western Africa. The FDA recently approved an EBOV vaccine that shows efficacy when administered prior to virus exposure³; however, the duration and breadth of these recent outbreaks underscore that with an increasingly interconnected world, the dangers of reoccurring outbreaks are increasingly high and there is an imminent need to develop small molecule counter measures to treat patients who test positive for EBOV and exhibit symptoms. Further, there is still a large gap in knowledge in how EBOV hijacks host cell components to replicate and spread from cell-to-cell, elucidation of which may identify new drug targets.

In the Filoviridae family, EBOV and Marburg virus (MARV) are two of the most pathogenic viruses. EBOV and MARV are lipid enveloped negative-sense single stranded RNA viruses^{4,5}. One commonly overlooked characteristic of many pathogenic viruses, including EBOV and MARV, is their lipid envelope, which is acquired from the host cell they infect. Furthermore, lipid enveloped negative-strand RNA viruses possess limited viral machinery, often encoding for just a handful of viral proteins. Amongst these viral proteins is the multi-functional matrix protein. These matrix proteins, including the VP40 protein of Ebola (eVP40) and Marburg (mVP40) viruses, are essential to efficient viral assembly and egress. In fact, independent expression of eVP40 or mVP40 leads to the production of virus-like particles (VLPs), nearly indistinguishable from infectious virions⁶⁻⁸. Although these matrix proteins travel through different trafficking pathways within cells, they coalesce at the plasma membrane to form the viral matrix, which directs viral assembly, budding and the acquisition of their characteristic lipid envelope⁹⁻¹³. Importantly, phosphatidylserine (PS) has been implicated in recruiting matrix proteins to the plasma membrane and coordinating the assembly of progeny virions¹⁴⁻¹⁶.

While lipids play a critical role in assembly of progeny viral particles, lipids are also actively involved in viral entry in a phenomenon known as “apoptotic mimicry”. Apoptotic mimicry is central to the efficient entry of numerous lipid-enveloped viruses^{17–19}. During apoptotic mimicry, PS is transferred from the inner to the outer leaflet of the plasma membrane; this causes PS to become a component of the outer viral envelope during infection^{14,20,21}. Subsequently, the exposed PS in the viral envelope is recognized by target cell receptors for viral uptake, continuing the viral lifecycle^{18,22,23}.

The two bilayers of the plasma membrane have varying compositions of four main phospholipid classes asymmetrically distributed across the two bilayers^{24,25}. The most abundant anionic lipid within the inner leaflet of the plasma membrane is PS, a frequent participant in peripheral protein recruitment²⁶. Extensive work has looked at the dynamic nature of lipids within the plasma membrane, including PS, and their tendency to cluster into domains several hundred nanometers in size^{15,27,28}. Clustering of anionic lipids into domains enriches regions of the plasma membrane with anionic charge, creating a platform for electrostatic interactions at the plasma membrane and cytosolic interface for peripheral protein recruitment. This phenomenon has been reported between PS and the matrix protein of influenza A virus¹⁵. Although significant work has underscored the importance of PS in filovirus budding and entry^{14,18,22,29–32}, the molecular details of the interaction has not been explored in the context of the lateral organization of PS, matrix assembly or implications on viral spread.

Recently, an FDA approved drug, fendiline, was reported to reduce PS levels within the plasma membrane inner leaflet^{33,34}, which was sufficient to inhibit the oncogenic protein K-Ras plasma membrane localization and signaling^{34,35}. Fendiline was initially approved by the FDA in the 1970s as a non-selective calcium channel blocker to treat coronary heart disease³⁶; however, these recently identified off target properties were found to be calcium independent and associated with the indirect inhibition of acid sphingomyelinase (ASM)^{33,34}. eVP40 and mVP40 have been shown to utilize PS for their plasma membrane localization, assembly, and production of progeny virions; however, detailed molecular insight into this relationship is lacking. To delineate the molecular architecture and requirements of PS concentration on VP40 assembly, oligomerization and budding, we employed biochemical and biophysical assays in vitro and in cells. We also tested the ability and mechanism by which VP40 clusters PS in vitro and in cells. We hypothesized that reduction of PS from the plasma membrane with fendiline treatment would perturb filovirus

assembly and inhibit viral budding. Lastly, fendiline treatment was tested as a potential therapy for inhibition of EBOV budding and spread in biosafety level (BSL)-2 and BSL-4 models of infection. Our results demonstrate that VP40 clusters PS, a critical requirement for viral budding, spread and subsequent entry that can be inhibited with the FDA-approved drug fendiline.

5.2 Materials and Methods

5.2.1 Reagents & solutions

Phosphate buffered saline (PBS), Dulbecco's modified eagle medium (DMEM), ionomycin and Lipofectamine LTX + Plus were purchased from Fisher Scientific, heat-inactivated fetal bovine serum (FBS) was purchased from Hyclone, and Minimum Essential Medium (MEM) was purchased from Corning. Invitrogen Live Cell Imaging Solution, DiI Stain, Halt Protease inhibitor cocktail, Pierce BCA Assay kit, and BS³ were purchased from ThermoFisher Scientific. Non-essential amino acids (NEAA) were purchased from Sigma Aldrich and L-glutamine was purchased from Gibco. Fendiline was purchased from Cayman Chemical, prepared in DMSO and stored at -20 °C. Ultra-Pure Grade DMSO was purchased from VWR and the Ni-NTA slurry was purchased from Qiagen. L1 chips for SPR experiments were purchased from GE Healthcare. For cell viability assays, CellTiter-Glo® was purchased from Promega. Antibody information for immunoblotting and immunofluorescence can be found in **Table 1 in Appendix 1**. Ten percent neutral buffered formalin was purchased from Val Tech Diagnostics (Brackenridge, PA). Cell staining buffer was purchased from BioLegend. Invitrogen™ Molecular Probes™ Hoechst 3342 stain was purchased from Fisher Scientific.

5.2.2 Plasmids

EGFP, EGFP-eVP40 and EGFP-WE/A-eVP40 were prepared as described previously^{37,38}. GFP-K224A-eVP40 was prepared by site directed mutagenesis³⁹. GFP-mVP40 was used as described previously^{10,16}. The GFP-LactC2 plasmid was a kind gift from Sergio Grinstein (University of Toronto). GFP-PLCδPH was a kind gift from Tamas Balla (NIH). pCAG-GPI-GFP was a gift from Anna Katerina Hadjantonakis (Addgene #32601). pEGFP-N3-Annexin A2 was a gift from Volker Gerke & Ursula Rescher (Addgene #10796). pCAGGS-FLAG-eVP40 (NR49337)

and pcDNA3.1-eGP (NR-19814) were obtained from BEI Services. pCAGGS-TIM-1 was from Heinz Feldmann⁴⁰.

5.2.3 Lipids and LUV preparation

All lipids were purchased from Avanti Polar Lipids, Inc. (Alabaster, AL) and stored in chloroform and/or methanol at -20°C until use. POPC (#850457), POPE (#850757), POPS (#840034), Brain PI(4,5)P₂ (#840046) and TopFluor® TMR-PS (#810242). For large unilamellar vesicle (LUV) preparation used in SPR and chemical crosslinking experiments, lipid mixtures were prepared at the indicated compositions, dried down to lipid films under a continuous stream of N₂, and stored at -20°C until further use. On each day of experiments, LUVs were brought to room temperature, hydrated in either SPR buffer (10 mM HEPES, 150 mM NaCl, pH 7.4) or chemical crosslinking buffer (260 µM Raffinose pentahydrate in PBS, pH 7.4), vortexed vigorously, and extruded through a 100 nm (SPR experiments) or 200 nm (chemical crosslinking experiments) filter. Vesicle size was confirmed by dynamic light scattering using a DelsaNano S Particle Analyzer (Beckman Coulter, Brea, CA).

5.2.4 Cell culture, transfections, pharmacological treatments

All BSL-2 studies were performed using HEK293 cells obtained from the American Type Culture Collection and cultured in DMEM supplemented with 10% FBS and 1% P/S. Transient transfections were performed using Lipofectamine LTX + PLUS, according to the manufacturer's protocol. All transfections were performed in DMEM supplemented with 10% FBS. Treatment with fendiline (in DMSO) occurred at 5-hours post-transfection in DMEM supplemented with 10% FBS. BSL-4 assays were also performed using Vero E6 cells cultured in MEM, 5% heat-inactivated FBS, 1% L-glutamine, and 1% NEAA. Both HEK293 and Vero E6 cells were cultured and incubated at 37°C, 5% CO₂, 80% humidity.

5.2.5 Immunoblotting

Samples prepared for western blotting analysis were first separated using SDS-PAGE (8% for chemical crosslinking and 12% for cell lysates and VLPs). Following transfer onto a nitrocellulose membrane, membranes were blocked with 5% MILK-TBST and analyzed with their

respective antibodies (See Supplement Table 1). Antibodies were detecting using an ECL detection reagent and imaged on the ImageQuant LAS 4000 or Amersham Imager 600 (GE Healthcare Life Sciences). All quantitative analysis derived from western blotting was performed using densitometry analysis in ImageJ.

5.2.6 Protein purification

The His6-eVP40-pET46 expression vector was a kind gift from Erica Ollmann Saphire (La Jolla Institute for Immunology) and was expressed and grown in Rosetta2 BL21DE3 cells (Merck Millipore, Billerica MA). The pet28a-His6-Lact C2 bacterial expression plasmid was a kind gift from Dr. Sergio Grinstein. His6-eVP40 and His6-LactC2 were grown and purified as described previously³⁷. Following elution from a Ni-NTA slurry (Qiagen), the protein samples were then further purified using size exclusion chromatography on a HiLoad 16/600 Superdex 200 pg column (ÄKTA pure, GE Healthcare). The desired fractions containing dimeric eVP40 or monomeric LactC2 were collected, concentrated and stored in 10 mM Tris, 300 mM NaCl, pH 8.0. Protein concentration was calculated using the Pierce BCA assay and the protein was stored at 4°C for no longer than 14 days.

5.2.7 Plasma membrane localization confocal microscopy

Live cell imaging experiments were performed at 24 hours and 48 hours post treatment. Experiments to quantify fluorescent protein plasma membrane localization were performed on a Zeiss LSM 710 inverted microscope using a Plan Apochromat 63x 1.4 numerical aperture oil objective. A 488 nm argon laser was used to excite GFP/EGFP. GFP-LactC2 plasma membrane localization was quantified ratiometrically by comparing the plasma membrane signal vs. the cytosolic signal. GFP-EBOV-VP40 and GFP-MARV-VP40 plasma membrane localization was quantified ratiometrically by comparing the plasma membrane signal vs. the total fluorescence signal within the cell.

5.2.8 Cellular Top Fluor TMR-PS clustering confocal microscopy

Each experimental day, a 100 μ M working stock of TopFluor® TMR-PS (TMR-PS) in methanol was prepared. Immediately prior to imaging, cells were placed in 4°C for 5 min. The

working stock was diluted to a final 500 nM TMR-PS solution in 3 mg/mL BSA/PBS. The 500 nM TMR-PS/BSA/PBS solution was incubated with cells at 4°C for 10 min, rinsed three times with cold PBS, and immediately imaged in fresh cold PBS. TMR-PS was excited at 560 nm and GFP was excited at 488 nm. For PS clustering analysis, a custom macro in ImageJ was used. Prior to the macro analysis background was subtracted, and the contrast was enhanced. To isolate the plasma membrane area, a default threshold was applied. To isolate PS clusters the Moments analysis thresholding⁴¹ was applied. Following the moments analysis thresholding, the custom ImageJ macro was applied: despeckle, close-, fill holes, and remove outliers (radius=5, threshold=50). The sum of the remaining particles area was calculated, as well as the plasma membrane area. %PS clustering was calculated according to the ratio ($\text{Area}_{\text{clusters}}/\text{Area}_{\text{plasma membrane}}$).

5.2.9 Number & Brightness

Number & Brightness experiments were performed as described previously^{15,37,38} on a Zeiss LSM 880 upright microscope using a LD “C-Apochromat” 40x/1.1 W Corr M27 objective. HEK293 cells expressing either GFP, GFP-LactC2 or GFP-eVP40 were treated with fendiline (1 or 5 μM) for 48-hours prior to N&B analysis. Cells were imaged in phenol-free live cell imaging solution. For each experimental day, the brightness value of a monomer was determined in cells expressing monomeric GFP. Each image was acquired using the same laser power (0.01), resolution (256x256), pixel dwell time (16 us), frames (50), and zoom (pixel size of 50 nm). SimFCS Globals Software (Laboratory for Fluorescence Dynamics, University of California, Irvine, CA) was used for analysis.

5.2.10 Chemical crosslinking

His6-eVP40 and His6-LactC2 were purified as previously described in Protein Purification. LUVs containing POPC and Brain PI(4,5)P₂ (2.5%) with varying PS mol% composition (0, 15, 30, 60%) were prepared as previously described in Lipids & Vesicle Preparation. Experimental protocol was adapted from Johnson K.A. et al 2016, and the manufacturers protocol for BS³ (ThermoFisher) with each step performed at RT. In brief, protein (final concentration of 0.3 μM in PBS pH 7.4) was mixed with LUVs (final concentration = 660 μM) at a 1:1 volumetric ratio for 30 min. Protein bound LUVs were separated from unbound protein through centrifugation (75,000

x g, 30 min, 22°C), and resuspended in PBS (pH 7.4) buffer containing BS3 (final concentration-200 μ M). Samples were incubated for 45 min, quenched with glycine for 15 min and then analyzed through western blotting. Following immunoblotting, oligomerization of VP40 was quantified ratiometrically by comparing VP40_o vs. VP40_{m+d} (where VP40_o is the oligomeric VP40 band density (>75 kDa) and VP40_{m+d} is the sum of monomeric and dimeric eVP40 (~37 and 74 kDa) band density).

5.2.11 Surface plasmon resonance

To determine the affinity of 6xHis-eVP40 to LUVs with increasing PS concentrations, SPR was performed. SPR experiments were performed at 25°C using a Biacore X100 as described previously.[14] In brief, an L1 chip was coated at 5 μ L/min with LUVs containing 0% PS on flow cell 1 and either 1%, 11% or 22 mol% POPS on flow cell 2 (LUV preparation described in previous section, Lipids and Vesicle Preparation). The LUV conjugated chip was stabilized by washing with 50 mM NaOH and blocked with 0.1 mg/mL BSA (in SPR buffer) at a flow rate of 10 μ L/min until the response on each flow cell was <100 response units (RU). For quantitative affinity analysis, each concentration of eVP40 was injected for 540 s at a flow rate of 10 μ L/min with a 180 s delay, and the difference in response between flow cell 1 and flow cell 2 was recorded (Δ RU). The apparent K_d of vesicle binding was determined using the non-linear least squares analysis: $Req = R_{max} / (1 + K_d / C)$ where Req (measured in RU) is plotted against protein concentration (C). R_{max} is the theoretical maximum RU response and K_d is the apparent membrane affinity. Data were fit using the Kaleidagraph fit parameter of $(m_0 * m_1) / (m_0 + m_2)$; $m_1 = 1100$; $m_2 = 1$. Δ RU data was normalized in GraphPad Prism 8 for windows (La Jolla, CA) and plotted in Kaleidagraph (Reading, PA).

5.2.12 Lipidomics

HEK293 cells were treated with the indicated concentration of fendiline for 48 hours, collected through centrifugation, rinsed with PBS and protein concentration was determined. Cells were pelleted, flash frozen in liquid N₂ and stored at -80°C until subsequent LC/MS/MS processing by Avanti Polar Lipids, Inc.. Prior to LC-MS/MS analysis, lipids were extracted using the Folch method.[71] The bottom chloroform layer taken after centrifugation was diluted with internal

standards for lysophosphatidic acid, lysophosphatidylserine, PA and PS for quantization by injection on LC-MS/MS. Samples were injected on a LC-MS/MS method using a Waters Acquity UPLC / AB Sciex 5500 MS system performing reversed phase separation of LPA and LPS and PA and PS components with MS/MS detection. Each molecular species identified by the [M-H] m/z of its acyl carbon:double bond (CC:DB i.e. 34:2 PA) was quantified against the response of the internal standards of known concentration. Content of individual and total LPA/PA and LPS/PS was reported. Values were corrected to 1×10^6 cells for all samples.

5.2.13 BSL-4 immunofluorescence assay

This work was performed by Laura Prugar and Kathleen Huie at United States Army Medical Research Institute of Infectious Diseases. Vero E6 cells were seeded at 2×10^4 cells/well in black 96-well poly-D-lysine treated plates (Greiner Bio-One Cellcoat®). Twenty-four hours prior to infection, fendiline was diluted in 0.5% DMSO and Vero E6 cell culture media at indicated concentrations and added to cells. An equivalent percentage of DMSO in culture media served as the vehicle control. Following pretreatment, compound was removed, and cells were incubated with Ebola virus (Kikwit) or Marburg virus (Ci67) at a multiplicity of infection (MOI) of 0.1 or 1.0 in a BSL-4 located at USAMRIID. Following absorption for 1 hour, virus inoculum was removed and cells were washed. Plates were divided into three post-infection treatment groups (day 0, every day- e.d., every other day-e.o.d.), and received either culture media or freshly prepared fendiline or vehicle control. Cells were then treated daily with freshly prepared compound or left to incubate based on their designated treatment group. At 48 hours (MOI=1.0), 72 or 96 hours (MOI=0.1) post infection, cells were washed with PBS and submerged in 10% neutral buffered formalin for 24 hours prior to removal from the BSL-4 laboratory. Formalin was removed and cells were washed with PBS. Cells were blocked with 3% BSA/PBS cell staining buffer (BioLegend) and incubated at 37°C for 2 hours. Ebola virus GP-specific mAb KZ52 or Marburg virus GP-specific mAb 9G4, diluted in 3% BSA/PBS, were added to appropriate wells containing infected cells and incubated at room temperature for 2 hours. Cells were washed three times with PBS prior to addition of goat anti-human or goat anti-mouse IgG-Alexa-488 secondary antibody. Following 1-hour incubation with secondary antibody, cells were washed 3 times prior to counterstaining with Hoechst's stain diluted in PBS. Cells were imaged and percent of virus

infected cells calculated using the Operetta High Content Imaging System and Harmony® High Content Imaging and Analysis Software (PerkinElmer).

5.2.14 VLP collections & functional budding assays

HEK293 cells were transfected and treated with fendiline as described in the previous section, Cell Culture, Transfection & Pharmacological Treatments. Budding assays were performed as described previously^{37,42}. In brief, VLP containing supernatants were harvested from cells and clarified through low speed centrifugation. Clarified VLPs were loaded onto a 20% sucrose cushion in STE buffer (10 mM TRIS, 100 mM NaCl, 1 mM EDTA, pH 7.6), isolated through ultracentrifugation, and resuspended in either 150 mM ammonium bicarbonate (functional budding assays), 2.5% glutaraldehyde in 0.1 M cacodylate buffer (TEM experiments), STE buffer (entry assays) or 0.1 M phosphate buffer for CD and thermal melting (PB; 0.02 M sodium phosphate monobasic, 0.08 M sodium phosphate dibasic, pH 7.4). VLP samples were stored at -80°C for functional budding assays, -20°C for entry assays or 4°C for TEM and CD analysis.

For functional budding assays, cell lysate samples were harvested and lysed on ice with RIPA buffer (150mM NaCl, 5mM EDTA pH=8, 50mM Tris pH 7.4, 1% Triton-X, 0.1% SDS, 0.5% deoxycholic acid) supplemented with Halts protease inhibitors. Prior to separation on a 12% SDS-PAGE gel, cell lysate and VLP sample volume loading were normalized to sample protein content, determined by a BCA assay. Gels were transferred to a nitrocellulose membrane and immunoblotted was performed as described previously in the section, Immunoblotting. Following ECL detection, VP40 cell lysate (VP40_{CL}) expression was normalized to the respective GAPDH band density. The relative budding index was calculated according to the ratio of $\text{density}_{\text{VLP}}/\text{density}_{\text{C+VLP}}$ (where $\text{density}_{\text{VLP}}$ is the eVP40 VLP band density and $\text{density}_{\text{C+VLP}}$ is the eVP40 cell lysate + VLP band density).

5.2.15 Scanning electron microscopy

HEK293 cells were transfected with FLAG-eVP40 and treated as described in the previous section, Cell Culture, Transfections & Pharmacological Treatments. Cells were scraped and collected through low-speed centrifugation at 48 hours post transfection, and stored in primary fixative (2% glutaraldehyde, 2% paraformaldehyde in 0.1 M cacodylate buffer, pH 7.35) at 4°C

until processing. During processing, samples were fixed to coverslips and post-stained with 1% osmium tetroxide in 0.1 M cacodylate buffer. Samples were extensively rinsed with water and dehydrated with a graded series of ethanol followed by drying in a Tousimis 931 Supercritical Autosamdri® device. Prior to imaging, samples were coated with 3 nm Iridium. A Field Emission Scanning Electron Microscope Magellan 400 (FEI) (Hillsboro, OR) was used to collect images, with assistance from Tatyana Orlova at the Notre Dame Integrated Imaging Facility.

5.2.16 Transmission electron microscopy imaging

VLPs were purified as previous described in VLP Collections & Functional Budding Assays. Following ultracentrifugation, VLPs were resuspended in fixative (2.5% glutaraldehyde in 0.1 M cacodylate buffer). Purified VLPs were applied onto glow discharged carbon formvar grids and negatively stained using 4% uranyl acetate. Samples were imaged with a FEI Tecnai T12 electron microscope equipped with a tungsten source and operating at 80 kV. VLP length and diameter measurements were quantified using ImageJ software. For diameter analysis, eight different diameters were measured across random areas on each VLP, and the mean diameter was reported.

5.2.17 DiI entry assay

VLP labeling: VLPs produced from HEK293 cells expressing FLAG-eVP40 and eGP were purified as previously described in the Functional Budding Assays section. DiI entry assays were performed as described previously^{43,44}. In brief, following ultra-centrifugation VLPs were resuspended in STE buffer and further purified by filtering through a 0.22 μ m filter. Protein content of VLP samples were normalized to 0.1 μ g/mL using STE buffer. VLPs were labeled with DiI for 1 hr at RT with gentle agitation (final DiI = 0.06 μ M). Following incubation, labeled VLP samples were concentrated down to equal volumes, and brought up to volume in phenol-free MEM with 2% FBS and 4% BSA.

TIM-1 dependent entry: HEK293 cells were transfected with TIM-1 for 24 hours prior to incubation with DiI-labeled VLPs and briefly rinsed with phenol-free MEM with 2% FBS and 4% BSA. DiI-VLPs were added to TIM-1 expressing HEK293 cells, spinoculated for 45 min at 4°C, and allowed to incubate for 1 hr at 37°C. Plates were then rinsed with PBS, fixed with 4%

paraformaldehyde in PBS, their nuclei stained with Hoechst 3342, and stored at 4°C until imaging. During image acquisition, z-stacks were acquired of 10-15 frames (1 µm steps) and 3 frames were analyzed for positive DiI infection, at the beginning, middle and end of the z-stack.

5.2.18 Toxicity analysis

HEK293 and Vero E6 cell toxicity following fendiline treatment was tested at the indicated time points using the Cell Titer Glo Viability Assay (Promega, Madison WI) according to the manufacturer's protocol. In brief, HEK293 cells were treated with the indicated concentration of fendiline or control for 24 or 48 hours. Vero E6 cells were treated for 24 hours, the drug was removed and the cells were replenished with Vero E6 culture media, to mirror the corresponding ebolavirus and Marburgvirus infections at BSL-4. Following the one-hour mock infection, cells were washed with PBS and plates were divided into three treatment groups (day 0, e.d., e.o.d.), and cells received either culture media or freshly prepared fendiline or vehicle control and were then treated daily with freshly prepared compound or left to incubate based on their designated treatment group. At 48, 72, and 96 hours following mock infection, and mirroring the post infection fixation time points, CellTiter-Glo® reagent was added to each well in accordance with the manufacturer's instructions. Both HEK293 and Vero E6 toxicity assays luminescence readings were recorded using a SpectraMax® M5 (Molecular Devices®) plate reader.

5.2.19 Mathematical model of in vitro experiments

Mathematical modeling was performed by Dr. Elsje Pienaar from the Weldon School of Engineering at Purdue University. We implemented a system of ordinary differential equations (ODEs) to describe the dynamics of host target cells, infected cells and free virus in different combinations reflecting the in vitro experimental systems used here. These equations are similar to those used to simulate Ebola virus dynamics in earlier work^{45,46}.

$$dT/dt = -\beta TV \quad (1)$$

$$dI/dt = \beta TV - \delta I \quad (2)$$

$$dV/dt = pI - cV \quad (3)$$

Where T, I and V represent numbers of susceptible target host cells, infected cells and free virions respectively and parameters are described in Supplementary Information, Table 2.

We modified appropriate parameters in equations 1-3 to represent the following experimental systems during calibration of the mathematical model:

- Viral budding assay (set $\beta=0$, $T(0) = 0$, $I(0) = 2.625 \times 10^6$, $V(0) = 0$, vary δ , c , p)
- Viral entry assay (set $p=0$, $T(0) = 6.3 \times 10^5$, $I(0) = 0$, $V(0) = 6.3 \times 10^3$, vary β , δ , c)
- BSL-4 Cellular infection assay (BSL4) ($T(0) = 5 \times 10^4$, $I(0) = 0$, $V(0) = 5 \times 10^4$ (MOI 1) or $V(0) = 5 \times 10^3$ (MOI 0.1) , vary β , δ , c , p)

Fendiline treatment effects are simulated using Emax dose response curves:

$$f_X = E_{max} \frac{C^H}{C_{50}^H + C^H}$$

Where C: concentration of fendiline, Emax: maximum effect of fendiline, H: hill constant for the dose response curve, and C50 concentration with 50% of Emax efficacy. Emax, C50 and H are fitted separately for fendiline effects on budding (fbudding) or entry (fentry). Fendiline efficacy (fX) is defined as a fraction where fX=0 implies no effect and fX=1 implies 100% inhibition of X (X = budding or entry). Fendiline effects are integrated into equations (1-3) by multiplying \square by (1-fentry) and multiplying p by (1-fbudding). Fendiline concentrations are assumed to be constant over the observation periods based on low in vitro degradation rates of the drug. Daily treatment in the BSL-4 assays (e.d.) are simulated by removing all free virus particles from the equations at each dosing time.

We calibrated the model in two stages. First, we calibrated to the budding and entry assays. The uncoupling of budding and entry in this data allows us to define biologically feasible ranges for the effects of fendiline on budding and entry separately. Using these feasible ranges, we proceed to calibrate the full model to the BSL-4 data (day-1/0 and e.d.). Therefore, we allow the budding and entry assays to inform the BSL-4 simulations without imposing strict assumptions about the equivalency between the two systems. In this way we progressively build complexity into the model accounting for fendiline effects on viral budding, entry, and infection progression.

Calibrating to budding and entry assays we restrict the value of p to be larger than 1 and c to be between 0 and 5. These assumptions are in line with previous estimates, and are necessary to qualitatively reproduce viral production observed, but not quantified, in the budding assays. Parameters are estimated using Matlab's non-linear least squares optimization algorithm. Parameter bounds and final values are defined in **Table 2 in Appendix 1**.

5.2.20 Statistical testing

All experiments were done in triplicate (unless otherwise noted). For analysis of eVLP diameter and length from TEM experiments, as well as total PA levels between control and 5 μ M fendiline treated cells, a two-tailed t-test was performed. For all experiments which contained >2 experimental groups, a one-way ANOVA with Dunnett's multiple comparisons was performed on raw data. Lastly, for N&B analysis, a two-way ANOVA with Dunnett's multiple comparisons was performed.

5.3 Results

5.3.1 EBOV VP40 localizes to PS enriched regions in membranes

Previous work investigating the relationship between PS and eVP40 has been limited to the transient expression of the PS probe, GFP-LactC2, and PS-deficient cell lines^{14,29}. The drawback to these techniques is the inability to capture PS and eVP40 localization simultaneously, as GFP-LactC2 and GFP-eVP40 compete for PS binding within the plasma membrane. To overcome this limitation, we utilized a synthetic fluorescent analogue of PS, TopFluor® TMR-PS (tetramethylrhodmaine-PS (TMR-PS)) which permits visualization of PS and eVP40 localization and dynamics in real time in synthetic membranes and in cells.

It was previously reported that eVP40 has selectivity and high affinity for PS and PI(4,5)P₂, both *in vitro* and in cells^{14,31,37,39,47,48}. Work done in our lab to supplement this project showed that eVP40 colocalized with PS using confocal microscopy of giant unilamellar vesicles labelled with TMR-PS and Alexa488 conjugated eVP40 dimer (data not shown; performed by Souad Amiar). To expand upon these *in vitro* findings, we investigated if eVP40 localizes to PS enriched regions within living cells.

PS can be exogenously added to media of cells and within minutes it will be incorporated into the inner leaflet of the plasma membrane as a result of PS flippases, which are widely expressed in mammalian cells and rapidly translocate PS from the outer to the inner leaflet of the plasma membrane⁴⁹. To visualize PS and protein localization simultaneously, we transiently expressed EGFP-fused proteins in HEK293 cells and supplemented the cells with TMR-PS immediately prior to imaging (**Figure 5.1**). Plot profile analysis of the fluorescence intensities for

both EGFP and TMR-PS was performed (**Figure 5.1 b-f**). To first verify our experimental setup, monomeric EGFP or EGFP-LactC2 were expressed in HEK293 cells. Plot profile analysis comparing the EGFP vs. TMR-PS signals revealed almost no overlap of the fluorophores, as EGFP was primarily cytosolic (**Figure 5.1 a, b**). Additionally, the plot profile analysis of the EGFP-LactC2 vs. TMR-PS signals showed strong overlap of these two fluorophores (**Figure 5.1 a, c**). These results confirmed that TMR-PS was specifically localized to the plasma membrane and was detectable by a peripheral protein with PS specificity.

To test the hypothesis that eVP40 localizes to PS enriched regions of the plasma membrane, we next examined the plot profile analysis of TMR-PS and eVP40 by expressing functionally unique EGFP fused eVP40 proteins: WT-eVP40, K224A-eVP40 (a PS-binding residue mutant³¹), and WE/A-eVP40 (oligomerization deficient mutant³⁸). The fluorescence profile of EGFP-WT-eVP40 vs. TMR-PS revealed a strong overlap between the two fluorophores (**Figure 5.1 a, d**). This cellular data corroborates our in vitro data, demonstrating that EGFP-eVP40 localizes to PS enriched regions of both model membranes and in the plasma membrane of cells. Additionally, there was no significant fluorescence signal overlap between the EGFP-K224A-eVP40 mutant and TMR-PS (**Figure 5.1 a, e**) which supports the requirement for PS binding for plasma membrane localization of eVP40³¹. Importantly, plot profile analysis revealed a moderate overlap in the fluorescence signals of the oligomerization deficient mutant WE/A-eVP40 and TMR-PS (**Figure 5.1 a, f**). This is important to note as this protein is still able to interact with PS at the plasma membrane, however, is unable to properly oligomerize^{38,50}. These results suggest that VP40 interacts with PS at the plasma membrane inner leaflet as a dimer without significant oligomerization, in line with VP40 in vitro lipid-binding³¹.

5.3.2 EBOV-VP40 enhances clustering of PS in living cells

The proper localization and function of numerous peripheral proteins are dependent on the presence of PS in the inner leaflet⁵¹⁻⁵³. Biophysical and molecular studies into PS dynamics in both model membranes and in living cells revealed that PS basally distributes into clustered domains enriched with PS^{15,27,28}. Interestingly, cellular proteins such as Annexins are known to significantly enhance the clustering of PS⁵⁴ and viral proteins such as M1 of Influenza A virus have a selectivity for these PS clusters¹⁵. However, detailed examination of PS clustering and whether filovirus matrix proteins such as eVP40 alter the organization of PS has not yet been

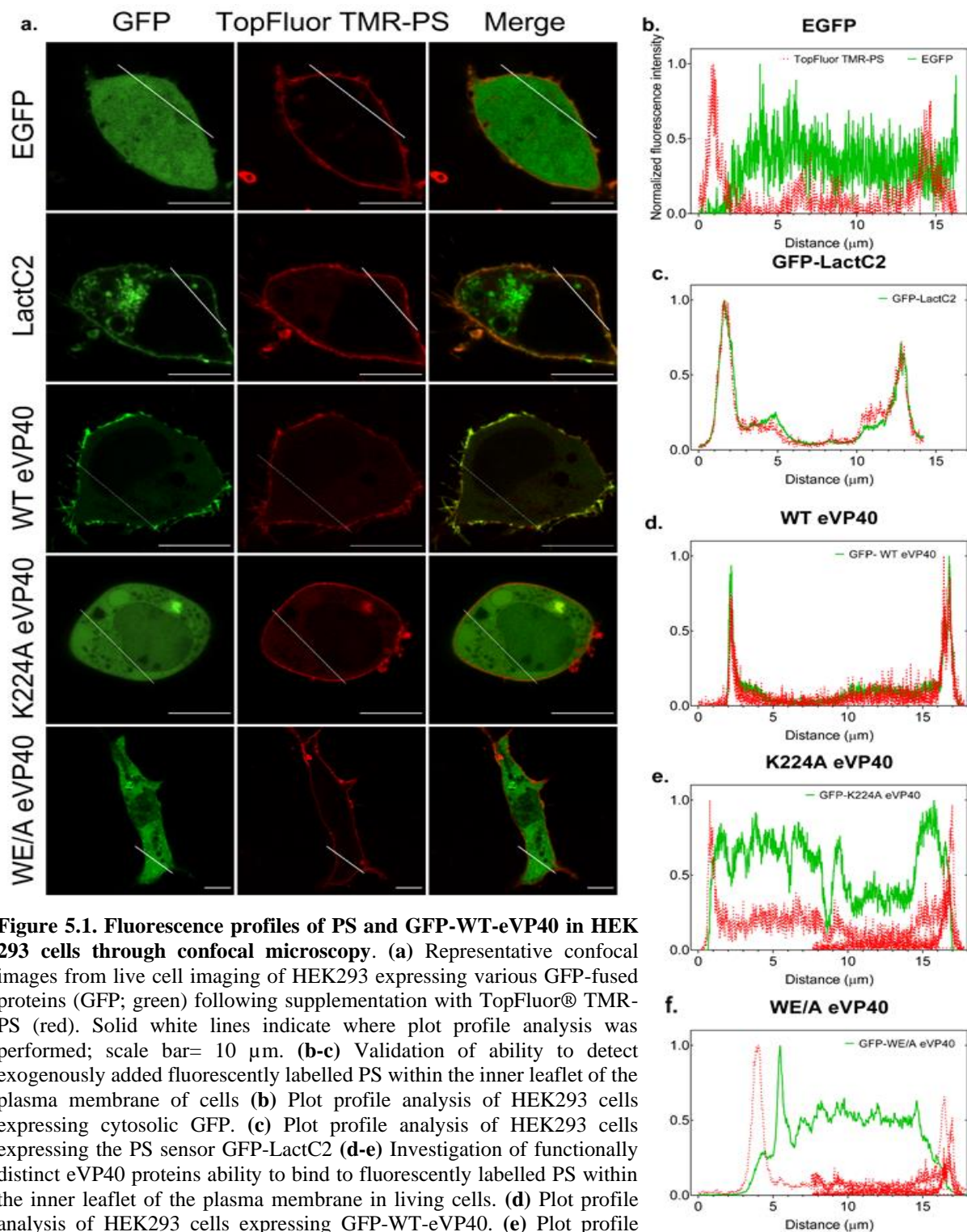


Figure 5.1. Fluorescence profiles of PS and GFP-WT-eVP40 in HEK 293 cells through confocal microscopy. (a) Representative confocal images from live cell imaging of HEK293 expressing various GFP-fused proteins (GFP; green) following supplementation with TopFluor® TMR-PS (red). Solid white lines indicate where plot profile analysis was performed; scale bar= 10 μm . (b-c) Validation of ability to detect exogenously added fluorescently labelled PS within the inner leaflet of the plasma membrane of cells (b) Plot profile analysis of HEK293 cells expressing cytosolic GFP. (c) Plot profile analysis of HEK293 cells expressing the PS sensor GFP-LactC2 (d-e) Investigation of functionally distinct eVP40 proteins ability to bind to fluorescently labelled PS within the inner leaflet of the plasma membrane in living cells. (d) Plot profile analysis of HEK293 cells expressing GFP-WT-eVP40. (e) Plot profile analysis of HEK293 cells expressing GFP-K224A-eVP40 (PS-binding residue mutant). (f) Plot profile analysis of HEK293 cells expressing GFP-WE/A-eVP40 (oligomerization deficient mutant). TopFluor TMR-PS fluorescence signal intensity (red dotted line) and GFP fluorescence signal intensity (green solid line).

explored. Preliminary *in vitro* work performed in our lab highlighted that eVP40 induced clustering of PS in GUVs in the presence of PI(4,5)P₂ (data not shown; performed by Souad Amiar).

Therefore, we were interested to determine if eVP40 was able to induce PS clustering in cells. We first expressed monomeric EGFP in HEK293 cells supplemented with TMR-PS and examined the ability of confocal microscopy to detect PS clusters (**Figure 5.2 a top panel, Figure 5.2 b**). As previously mentioned, PS selectively localizes into clustered regions^{15,27,28}; therefore, a basal degree of PS clustering should be observed. We developed a custom ImageJ macro to perform a moments-based thresholding analysis to identify regions of the plasma membrane with enriched PS content (**Figure 5.2 c**). From there, we quantified the total area of these identified clusters as a percentage of the entire plasma membrane area. Through this analysis we were able to detect a basal level of PS enriched clusters in our control GFP expressing cells, with PS clusters accounting for approximately ~8% of the plasma membrane (**Figure 5.2 b**). Our method was further validated by expressing an additional control protein with a glycosylphosphatidylinositol membrane anchor conjugated to GFP (GFP-GPI) in HEK293 cells supplemented with TMR-PS, which revealed PS clusters in ~8% of the plasma membrane area (**Figure 5.2 b-c**).

We next sought to determine if our technique accurately captured enhanced PS clustering, therefore, we expressed EGFP-Annexin A2 in HEK293 cells. Annexin A2 has been shown to enhance the clustering of PS in a calcium dependent manner⁵⁴. Therefore, in EGFP-Annexin A2 expressing cells, supplementation with TMR-PS was preceded with supplementing the cellular media with 10 mM calcium and 5 μ M of the calcium ionophore ionomycin. As shown in **Figure 5.2 d-e**, expression of EGFP-Annexin A2 in cells significantly enhanced PS clustering roughly 2-fold, compared to EGFP expressing cells (***p=0.0001). Taken together, these findings corroborate the previously reported effect of Annexin A2 on PS organization, as well as validate the method developed for our assay.

To further examine the selectivity of PS clustering for lipid-binding proteins that localize to the plasma membrane inner leaflet, we expressed EGFP-PLC δ -PH and EGFP-LactC2 in HEK293 cells supplemented with TMR-PS (Representative images **Figure 5.2 d middle & bottom panel**). EGFP-PLC δ -PH binds specifically to PI(4,5)P₂, another critical component of many virus assembly processes, including filoviral assembly³⁷. Again, EGFP-LactC2 specifically and reversibly binds to PS. As expected, expression of neither EGFP-PLC δ -PH or EGFP-LactC2 significantly altered the extent of PS clustering (**Figure 5.2 b**). This confirms that transient

expression of fluorescently conjugated lipid-binding proteins is insufficient to enhance PS clustering at the plasma membrane.

Finally, we evaluated the effect of eVP40 expression on PS organization across the plasma membrane. We independently expressed three functionally distinct EGFP fused eVP40 constructs: WT-eVP40, K224A-eVP40, and WE/A-eVP40 and supplemented the cells with TMR-PS prior to imaging. Strikingly, expression of EGFP-WT-eVP40 increased PS clustering by ~2 fold (* $p=0.004$), similar to the PS clustering observed with Annexin A2 expression (**Figure 5.2 a-b**). However, expression of the PS-binding deficient mutant EGFP-K224A-eVP40 showed no significant change in PS clustering (**Figure 5.2 a-b**), supporting the hypothesis that eVP40 must interact with PS to promote its clustering at the plasma membrane. Additionally, to investigate if eVP40 matrix oligomerization was important for PS clustering, we expressed EGFP-WE/A-eVP40 in HEK293 cells. It is important to note that this mutant still colocalizes with PS at the plasma membrane (**Figure 5.2 a-b**) albeit to a lesser extent than WT³⁸. Although the WE/A-eVP40 and PS interaction is maintained in cells, no significant increase in PS clustering was observed (**Figure 5.2 a-b**). To the best of our knowledge, this is the first account of a filovirus matrix protein modulating the organization of PS within the plasma membrane. Moreover, these results demonstrate that both membrane binding and oligomerization of eVP40 is central to eVP40-mediated PS clustering.

5.3.3 eVP40 membrane binding and oligomerization are dependent on phosphatidylserine content in lipid membranes

As eVP40 binds to PS through electrostatic and stereospecific interactions^{14,31,47}, we hypothesized eVP40 may require PS clustering for productive interactions at the plasma membrane during assembly. Enrichment of PS within regions of the plasma membrane would provide additional PS molecules available to recruit eVP40 to platforms of viral budding. To investigate how increasing the amount of PS within membranes dictates eVP40 membrane affinity, surface plasmon resonance (SPR) was performed with His6-eVP40 and large unilamellar vesicles (LUVs) with increasing concentrations of PS (from 1% to 22 mol% PS; **Figure 5.3 a-c**). eVP40 displayed moderate binding to LUVs with 1% PS, with an apparent affinity of 2.3 μM (**Figure 5.3 a**). However, increasing the concentration of PS to 11% increased the apparent affinity of eVP40 to

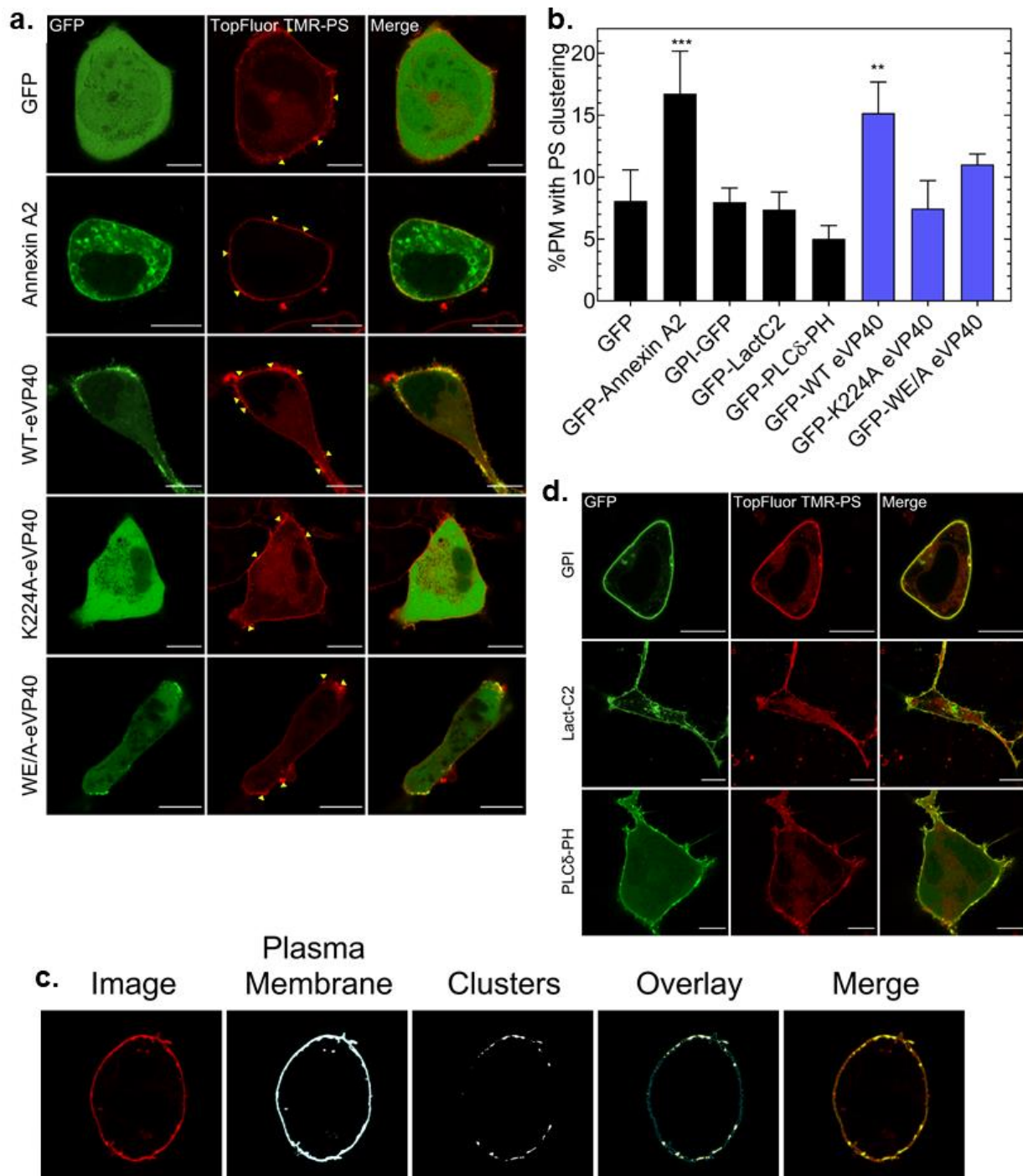


Figure 5.2. Clustering of PS by eVP40 in HEK293 cells. (a) Representative confocal images of HEK293 cells expressing various GFP-fused proteins (green) and supplemented with TopFluor® TMR-PS (red); Yellow arrows: high intensity PS fluorescence regions (b) %PM with PS clusters = area of high intensity fluorescent PS clusters / total plasma membrane area. Black bars: control proteins and blue bars: eVP40 proteins. Values are reported as mean \pm s.d.; N>18, n=3; A one-way ANOVA was performed with multiple comparisons compared to the control GFP %PS clustering (***p=0.0007, **p=0.004). PS: phosphatidylserine; PM: plasma membrane. (c) Representative images of the step-wise image analysis workflow of quantifying PS clustering in living HEK293 cells expressing GFP-fused proteins using a custom ImageJ macro. (d) Representative images from live cell imaging experiments of HEK293 cells expressing control GFP-fused proteins specific for the plasma membrane (GPI), and specific lipids, PS (LactC2) and PI(4,5)P₂ (PLCδ-PH). scale bar= 10μm.

0.65 μM (**Figure 5.3 b**). eVP40 displayed even stronger affinity to vesicles with 22% PS, with an apparent affinity of $\sim 0.18 \mu\text{M}$ (**Figure 5.3 c**). These results indicate that by increasing the amount of PS in membranes, the affinity of eVP40 to lipid membranes can be modulated. This finding supports the hypothesis that PS clustering may be a mechanism for the virus to provide the necessary electrostatic contacts needed for matrix assembly during viral production.

Once at the plasma membrane, VP40 oligomerizes into the extensive matrix that gives rise to the stability and structure of the virion. Previously, Adu-Gyamfi et al. (2015) highlighted the importance of PS in this process, where a cell line deficient in PS synthesis showed a significant reduction in eVP40 oligomerization at the plasma membrane. Moreover, our confocal clustering data (**Figure 5.2 a-b**) revealed that eVP40 oligomerization is crucial for modulating PS organization into clustered domains. To investigate how increasing PS concentration alters eVP40 oligomerization, we utilized chemical crosslinking of His6-eVP40 which had been incubated with LUVs of increasing PS concentration (**Figure 5.3 d-e**). We found that when eVP40 is incubated with LUVs that contain 0% PS, no detectable higher order structures of eVP40 are found (**Figure 5.3 d lane 1, Figure 5.3 e**). However, by introducing 15% PS into LUVs, the extent of eVP40 oligomerization beyond dimeric eVP40 is significantly higher than when 0% PS LUVs are used (**Figure 5.3 d lane 2, Figure 5.3 e**). We next tested LUVs containing 30% and 60% PS and found that eVP40 oligomerization was even more significantly detected than when just 15% PS was used (**Figure 5.3 d lanes 3-4, Figure 5.3 e**). Compared to LUVs with 0% PS, both 30% PS and 60% led to a significant increase in eVP40 oligomerization (* $p=0.021$ and * $p=0.017$, respectively). Further, eVP40 oligomerization appeared to saturate when 30% PS was included, as increasing PS content to 60% did not increase eVP40 oligomerization (compared to 30% PS). Taken together, these studies suggest a dynamic relationship between PS clustering and eVP40 affinity and oligomerization as a critical step in eVP40 viral assembly.

5.3.4 Total cellular and plasma membrane levels of phosphatidylserine are reduced by fendiline treatment

A recent study reported an FDA-approved drug, fendiline, inhibited K-Ras plasma membrane localization and signaling³⁵ and reduced plasma membrane PS content in MDCK cells³³. Therefore, it was our goal to determine if fendiline could also reduce PS levels in the human cell line HEK293, a cell line commonly used in BSL-2 filovirus studies, and subsequently inhibit

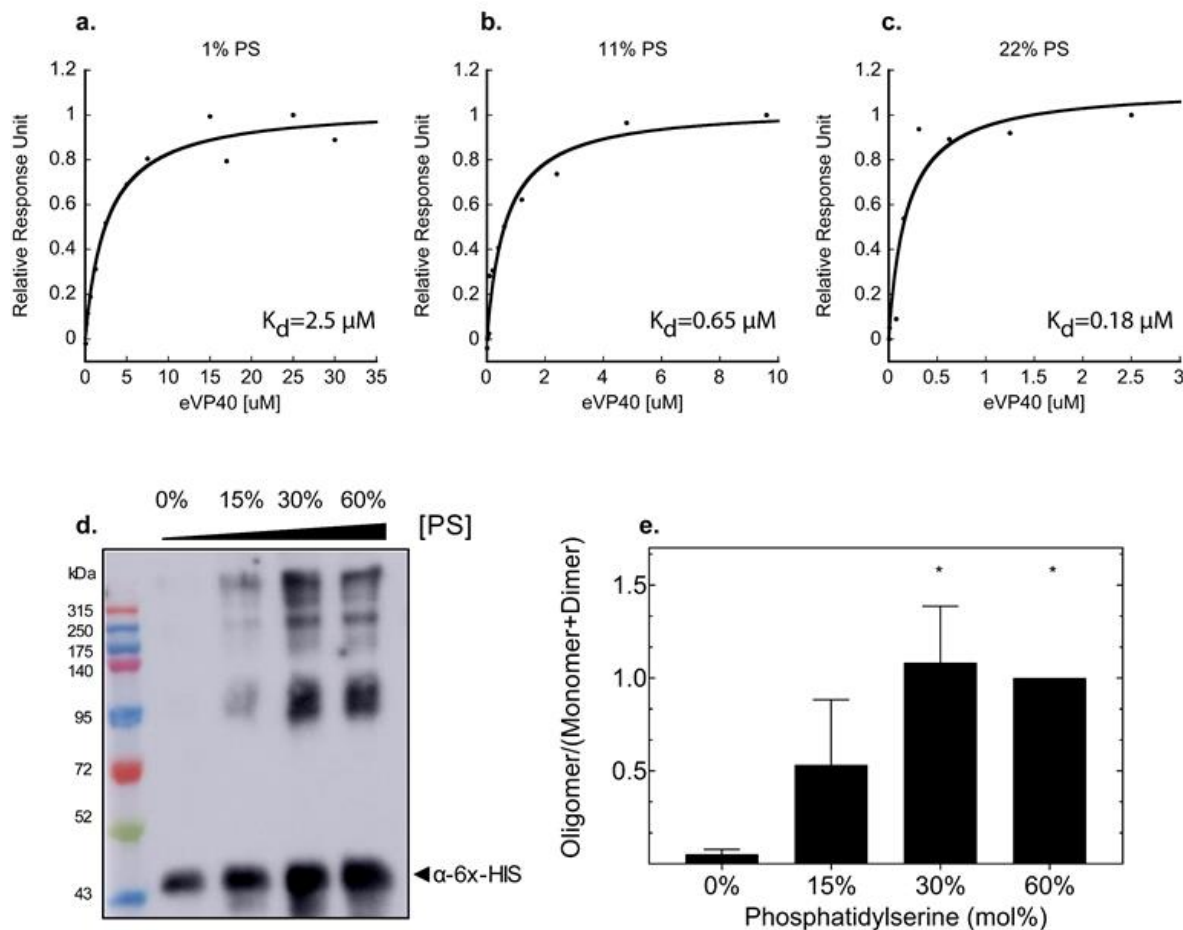


Figure 5.3 Effect of PS concentration on eVP40 binding affinity to and oligomerization on membranes. (a-c) SPR demonstrates that eVP40 affinity to LUVs increases in relation to PS concentration. (a) Representative normalized sensorgram of His6-eVP40 binding to LUVs containing 1% PS indicating an apparent affinity of 2.5 μM . (b) Representative normalized sensorgram of His6-eVP40 binding to LUVs containing 11% PS indicating an apparent affinity of 0.65 μM . (c) Representative normalized sensorgram of His6-eVP40 binding to LUVs containing 22% PS indicating an apparent affinity of 0.18 μM . (d-e) PS concentration in LUVs enhances the ability of His6-eVP40 to oligomerize on membranes. (d) Representative western blot of chemical crosslinking performed on His6-WT-eVP40 following incubation with LUVs of varying PS content (detected by Mouse α -His antibody & HRP-Sheep α -Mouse). (e) Oligomerization capacity was determined from the western blot band density ratio of oligomers/(monomer + dimer) from chemical crosslinking experiments. A one-way ANOVA was performed with multiple comparisons compared to the control 0% PS LUVs control (30% PS $*p=0.021$; 60% PS $*p=0.017$). $n=3$. Values are reported as mean \pm s.d.; SPR: surface plasmon resonance; LUVs: large unilamellar vesicles; PS: phosphatidylserine; HRP: horseradish peroxidase.

virus spread. The initial finding that fendiline reduced PS levels within the plasma membrane (40% reduction, $\text{IC}_{50} \sim 3\mu\text{M}$) was conducted in MDCK cells using thin-layer chromatography³³, therefore it had not been established if this effect was cell-type specific. To address this, we first established fendiline's toxicity in HEK293 cells. After 24 and 48 hours of treatment, no significant

toxicity was observed in treatments up to 5 μ M fendiline (**Figure 5.4 a**). Next, to evaluate the effect of fendiline on PS in HEK293 cells, cells were treated with fendiline for 48 hours, harvested, and lipids were extracted and quantified by liquid chromatography-tandem mass spectrometry (LC-MS/MS) (**Figure 5.4 b-d**). We observed a significant reduction in cellular PS levels compared to DMSO treated cells, after 48 hour treatment with 1 μ M fendiline (~18% reduction; * $p=0.012$) and 5 μ M fendiline (~30% reduction; *** $p=0.0003$) (**Figure 5.4 b**). Fendiline exhibited no selectivity in reducing different PS species, as 5 μ M fendiline reduced long chain ($C>38$) and saturated PS species nearly equally (**Figure 5.4 c**). It is important to note that the effect of fendiline on PS was specific in that fendiline treatment had no significant effect on another anionic phospholipid, phosphatidic acid (**Figure 5.4 d**). Therefore, our data supports the reported finding that fendiline reduced total cellular levels of PS, and that the effect is not cell dependent.

As PS is an integral anionic component of the plasma membrane inner leaflet, we sought to confirm that fendiline treatment also reduced PS levels within the plasma membrane in HEK293 cells. PS localization within the plasma membrane has been readily studied by expressing EGFP-LactC2 in mammalian cells^{49,55}. Therefore, HEK293 cells expressing EGFP-LactC2 were imaged at 24 hours (**Figure 5.5 a-b**) and 48 hours (**Figure 5.5 c-d**) post-treatment with increasing concentrations of fendiline. Single doses of 500 nM fendiline had no effect on EGFP-LactC2 plasma membrane localization at 24 or 48 hours post treatment. However, we found a ~30% reduction in plasma membrane EGFP-LactC2 localization after 24 hours of treatment for both 1 μ M (** $p=0.0003$) and 5 μ M fendiline (** $p=0.0045$) (**Figure 5.5 a-b**). However, a single dose of 1 μ M fendiline treatment did not significantly affect Lact-C2 plasma membrane localization after 48 hours of treatment (**Figure 5.5 c-d**). Conversely, a single dose of 5 μ M fendiline significantly reduced Lact-C2 plasma membrane localization even at 48 hours post treatment (~30% reduction; ** $p=0.0031$; **Figure 5.5 c-d**), a reduction similar to that observed at 24 hours post treatment. These finding corroborate Cho et al. (2015) where reduction of PS levels by fendiline at the plasma membrane were slow acting but could be sustained with 5 μ M treatment after 48 hours³³ and were also consistent with our LC-MS/MS analysis (**Figure 5.4**).

5.3.5 Fendiline reduces PS clustering

Next, we hypothesized that reduced levels of PS within the plasma membrane would therefore reduce the degree of PS clustering. To determine if fendiline treatment reduced the

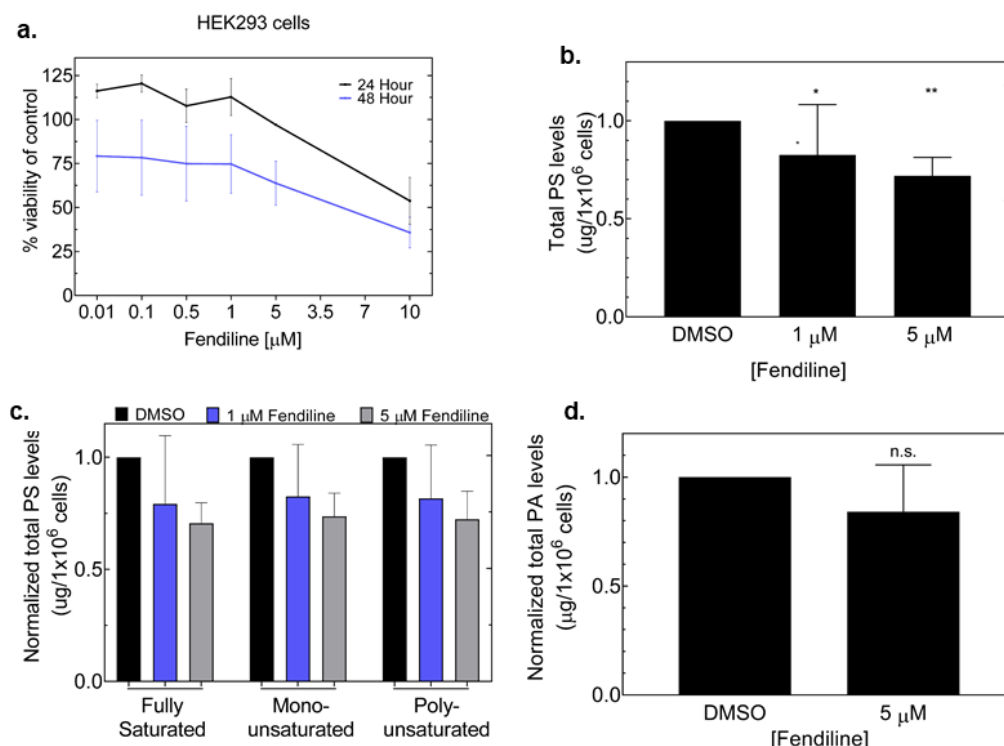


Figure 5.4. Toxicity and Lipidomic analysis of Fendiline treated cells. (a). CellTiter-Glo® viability results of HEK293 cells. HEK293 cells were treated with fendiline for 24 hours (black line) and 48 hours (blue line) and viability was assessed as a % viability of control. (b-d) Lipidomic analysis (LC/MS/MS) of total lipids extracted from HEK293 cells treated with the indicated concentration of fendiline (48 hours). (b) PS level analysis from lipidomic analysis (LC/MS/MS) of total lipids extracted from HEK293 cells treated with indicated concentration of fendiline. (c) PS saturation analysis from lipidomic analysis (LC/MS/MS) of total lipids extracted from HEK293 cells treated with the indicated concentration of fendiline. (d) PA level analysis from lipidomic analysis (LC/MS/MS) of total lipids extracted from HEK293 cells treated with 5 μ M. Values are normalized to DMSO control and are reported as mean \pm s.d.; n=3; A one-way ANOVA was performed with multiple comparisons compared to the control DMSO. (*p=0.0120, ***p=0.0003).

degree of PS clustering, we utilized the Number & Brightness technique (N&B). N&B is a quantitative fluorescence microscopy technique that allows one to detect the aggregation state of proteins with pixel resolution in real time within living cells⁵⁶. Previously, N&B was used to quantify PS clustering by analyzing the N&B profile of EGFP-LactC2¹⁵. To accurately capture PS clustering at the plasma membrane, imaging was performed at a focal plane near the cell surface. Importantly, HEK293 cells expressing monomeric EGFP were imaged and quantified to establish the experimental brightness value for a monomeric aggregation state (**Figure 5.6 a**).

To evaluate PS clustering, HEK293 cells expressing EGFP-LactC2 were treated with the control or fendiline for 48 hours and the EGFP-LactC2 N&B profile was examined (**Figure 5.6 b-c**). Three different cluster bin sizes were examined, 1—5, 5-10 and >10. The average percentage

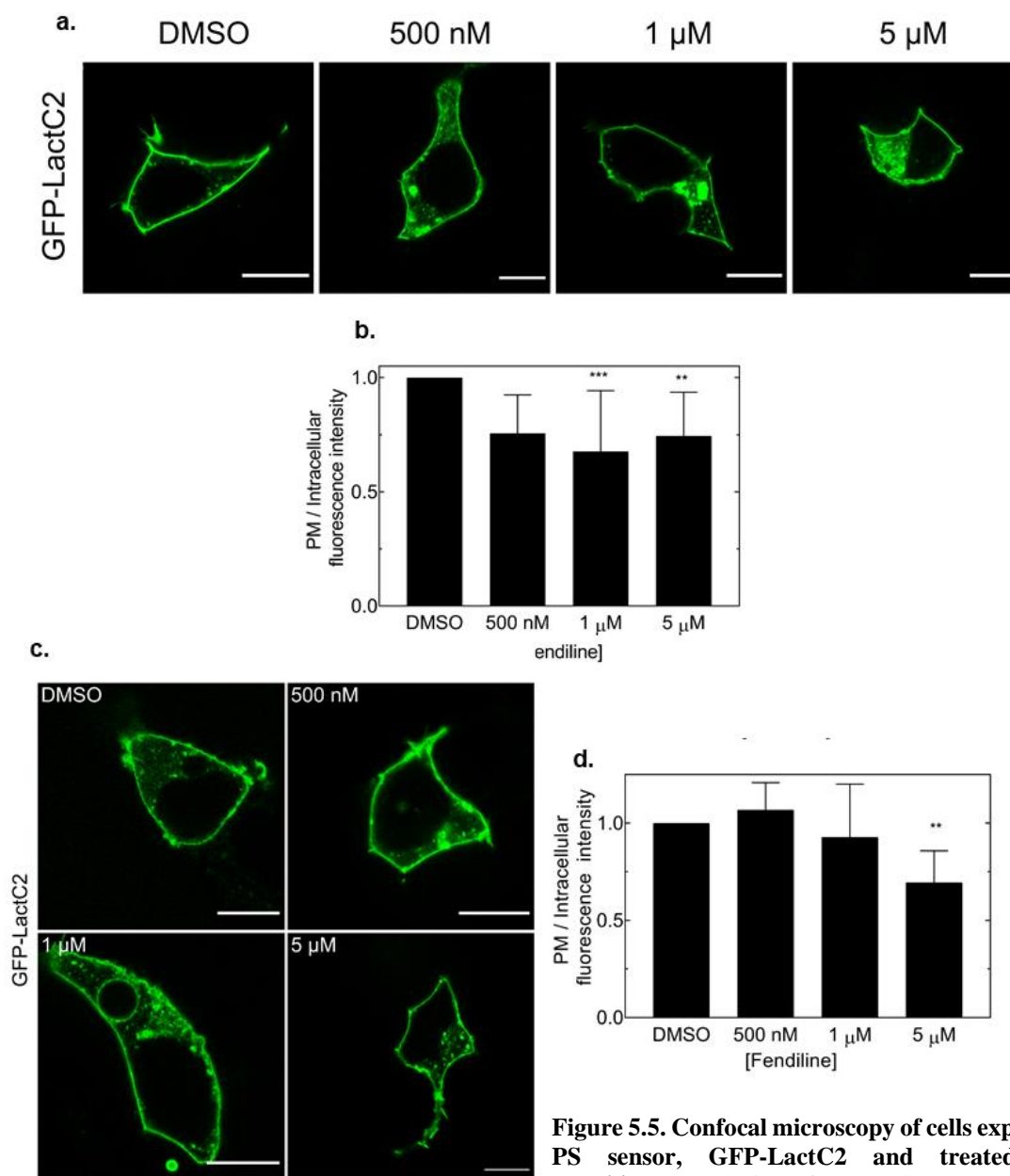


Figure 5.5. Confocal microscopy of cells expressing PS sensor, GFP-LactC2 and treated with Fendiline. Analysis of PS plasma membrane localization in response to 24 hour fendiline treatment (**a-b**) and 48 hour fendiline treatment (**c-d**). Representative confocal images from live cell imaging of HEK293 cells expressing GFP-LactC2 and treated with fendiline for 24 hours (**a**) and 48 hours (**c**). Effect of fendiline on PS plasma membrane localization at 24 hours (**b**) and 48 hours (**d**) was calculated by the ratio of GFP fluorescence at the (plasma membrane intensity/intracellular intensity). Values are normalized to DMSO control and are reported as mean \pm s.d.; N>15, n=3; A one-way ANOVA was performed with multiple comparisons compared to the DMSO control. (**b**): **p=0.0045; ***p=0.0003 (**d**) (**p=0.0031). scale bars= 10 μ m.

of pixels in each bin was calculated and plotted (**Figure 5.6 c**). Within control-treated cells, significant aggregation of EGFP-LactC2 was observed, with 25% present in complexes of 5-10 LactC2 molecules and ~10% in complexes of >10 LactC2 molecules (**Figure 5.6 b top panel, Figure 5.6 c**). This corroborates previous work investigating PS clustering, which found EGFP-

LactC2 clusters up to 15 molecules in size¹⁵. Treatment of cells with 1 μ M fendiline led to no significant change in PS clustering (**Figure 5.6 b middle panel, Figure 5.6 c**). which was expected as 1 μ M fendiline had no significant effect on EGFP-LactC2 plasma membrane localization at 48

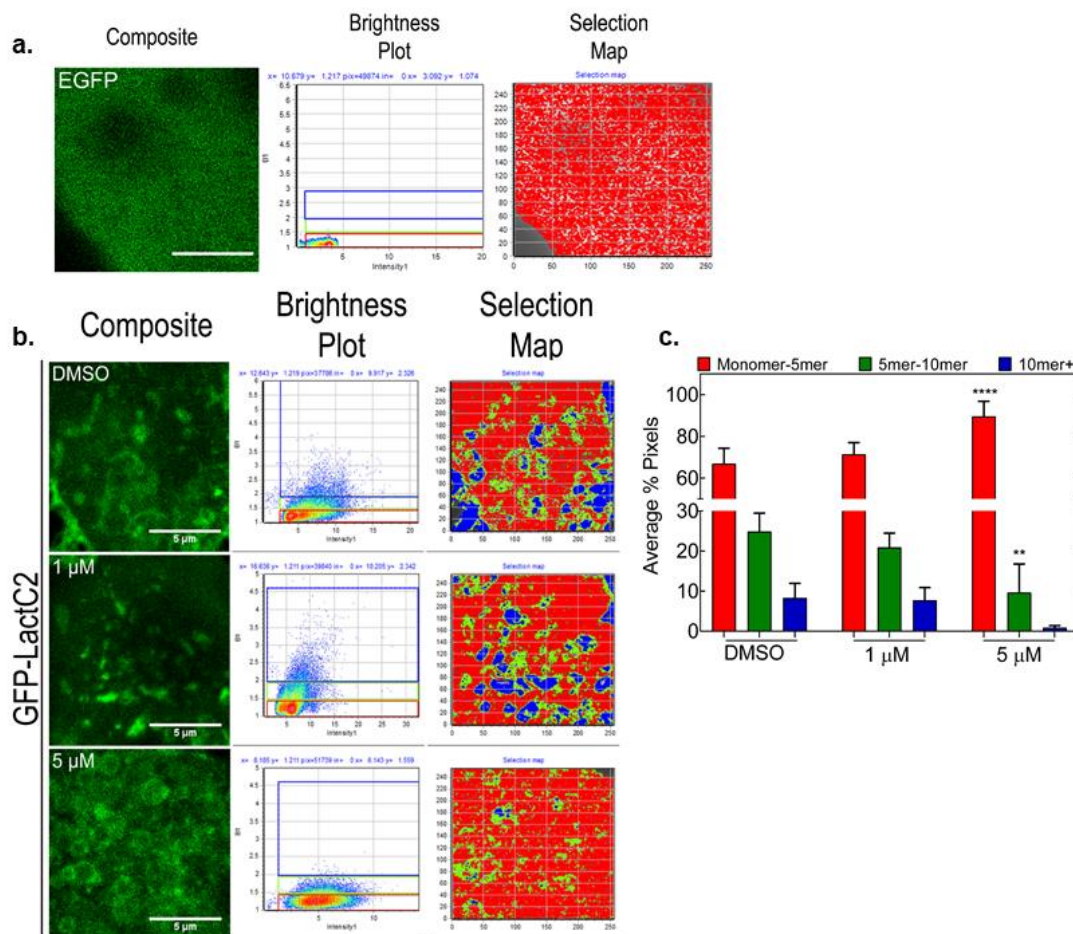


Figure 5.6. Number & Brightness analysis of LactC2 to identify PS clustering in HEK293 cells. (a) N&B analysis of HEK293 cells expressing the control GFP. Analysis was performed at 48 hours post treatment (DMSO) to align with N&B analysis performed on experiments with HEK293 cells expressing GFP-LactC2 or GFP-eVP40 and treated with the control or fendiline. *Left panel:* Representative images from time-lapse (30 frames) of HEK293 expressing EGFP and treated with fendiline for 48 hours. *Middle panel:* Brightness and Intensity plots for representative image. *Right panel:* Selection map correlating each pixel in the representative image to an oligomerization state (b value) (red: monomer). (b-c) Analysis of PS clustering in HEK293 cells in response to fendiline treatment through N&B analysis. (b) *Left panel:* Representative images from time-lapse (30 frames) imaging of HEK293 expressing GFP-LactC2 and treated with fendiline for 48 hours. *Middle panel:* Brightness and Intensity plots for each representative image. *Right panel:* Selection map correlating each pixel in the representative image to an oligomerization state (b value) (red: monomer-5mer, green: 5mer-10mer, blue: >10mer). (c) Average % pixels quantification from panel (b)= Percentage of GFP-LactC2 with brightness values corresponding to monomer-5mer (~1.-1.5), 5mer-10mer (~1.5-1.9) and >10mer (>1.9) over the total pixels within each image. Values are reported as mean \pm s.d.; N \geq 9, n=3; A two-way ANOVA was performed with Dunnett's multiple comparisons compared to the control DMSO % average pixels (****p<0.0001, **p=0.0043). GFP-LactC2: phosphatidylserine sensor; N&B: Number & Brightness analysis. scale bar= 5 μ m.

hours. Strikingly, 5 μM fendiline treatment abolished the presence of EGFP-LactC2 complexes >10 molecules and significantly reduced the number of complexes of 5-10 LactC2 molecules large (from $\sim 8\%$ in DMSO to $\sim 0\%$ in 5 μM fendiline; $**p=0.0043$) (**Figure 5.6 b bottom panel, Figure 5.6 c**). Moreover, there was a significant ($\sim 23\%$) increase in EGFP-LactC2 complexes of $\sim 1-5$ molecules in size in cells treated with 5 μM fendiline compared to control treated cells ($****p<0.0001$) (**Figure 5.6 b bottom panel, Figure 5.6 c**). Taken together, this data suggests that fendiline treatment disrupted large PS-dependent LactC2 complexes which was compensated by an increase in smaller PS-dependent complexes. Therefore, fendiline may possess antiviral properties by disassembling PS enriched regions that would otherwise have been used as platforms for viral assembly.

5.3.6 Fendiline significantly inhibits authentic EBOV and MARV replication

Recent studies have implicated PS as an essential component of the budding^{14,38} and entry^{22,23} of filovirus VLPs and authentic virions. To determine if the FDA-approved drug fendiline was able to inhibit authentic filovirus replication and spread, our collaborators at USAMRIID first established the toxicity of fendiline in Vero E6 cells (**Figure 5.7**) and then monitored the efficacy of fendiline at inhibiting EBOV and MARV replication in a BSL-4 setting (**Figure 5.8**). Vero E6 cells, an established model for BSL-4 filovirus studies⁵⁷, were used to

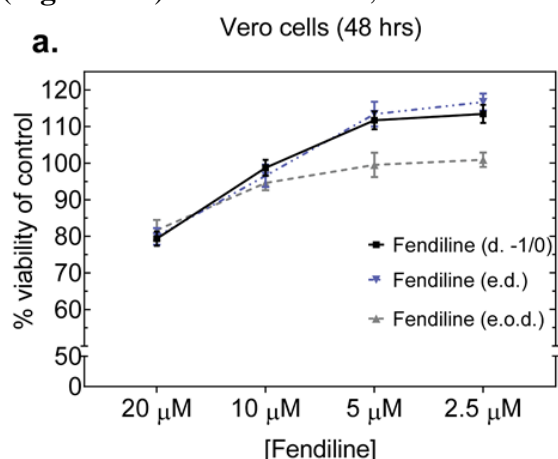


Figure 5.7. Viability assay of Vero cells following Fendiline treatment. (a) CellTiter-Glo® viability results of Vero cells. Cells were treated with control or fendiline for 48 hours according to the BSL-4 infection model; d-1/0 (black line), e.d. (blue line) and e.o.d (gray line) and viability was assessed as a % viability of control.

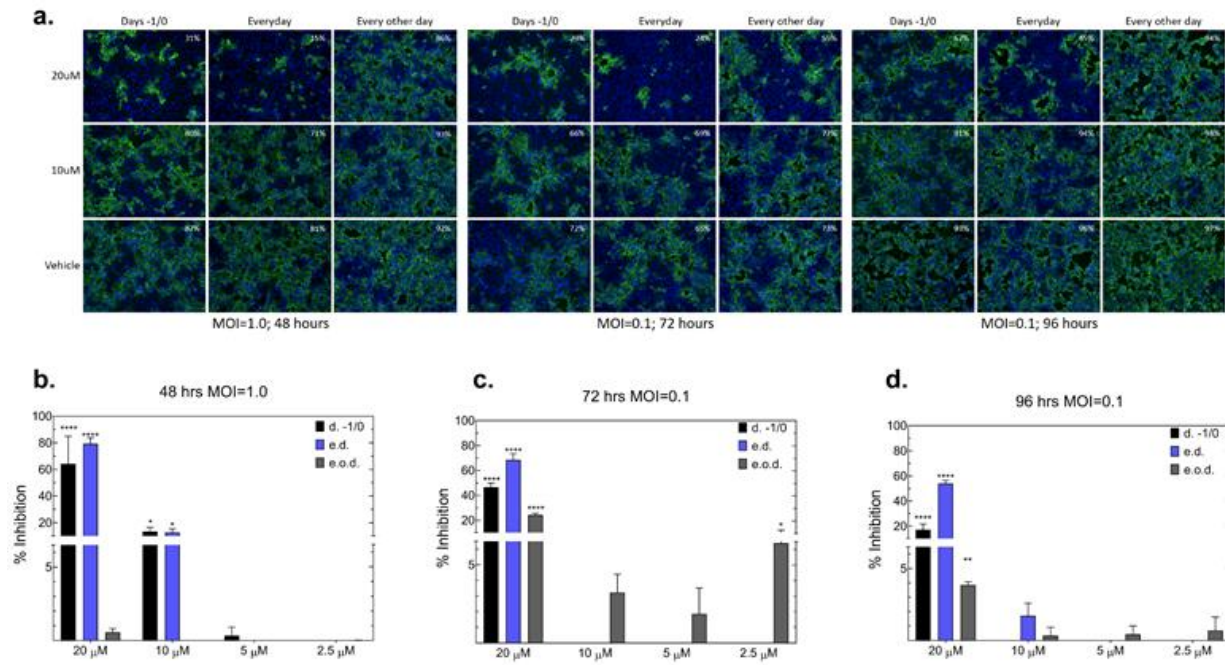
examine filovirus replication 48, 72 and 96-hours post-infection at different multiplicity of infection (MOI). Several different dosing regimens were designed to account for the slow response of fendiline in lowering cellular PS levels. The toxicity of fendiline in Vero E6 cells was first established using treatment schedules that would directly mirror treatment schedules in the filovirus infection model. As can be seen in Supplementary Fig. 5a, minimal toxicity was observed compared to the vehicle (even at the highest treatment group of 20 μM). Therefore, we proceeded with the filovirus infection model using treatments of fendiline up to

20 μ M. Cell treatment groups included increasing concentrations of fendiline (2.5 μ M, 5 μ M, 10 μ M, and 20 μ M) that were added to cell culture 24-hours prior to infection. An equivalent percent concentration of DMSO in culture media served as the vehicle control. Following removal of pretreatment compound, cells were then inoculated with either EBOV (Kikwit) or MARV (Ci67) at a multiplicity of infection MOI of 0.1 or 1.0, and incubated for 1 hour at 37C in 5% CO₂, in a BSL-4 laboratory located at USAMRIID. Following infection, plates were separated into three post-infection treatment groups (day 0, every day dosing, or every other day dosing). In order to quantify viral replication, at 48 hours (MOI=1.0), 72 or 96 hours (MOI=0.1) post-infection, cells were washed and submerged in 10% neutral buffered formalin 24 hours prior to removal from the BSL-4 laboratory. Using virus specific antibodies to the glycoprotein (GP), cells were then imaged (**Figure 5.8 a, e**) and the percent of virus infected cells calculated using a high content imaging system (**Figure 5.8 b-d, f-h**).

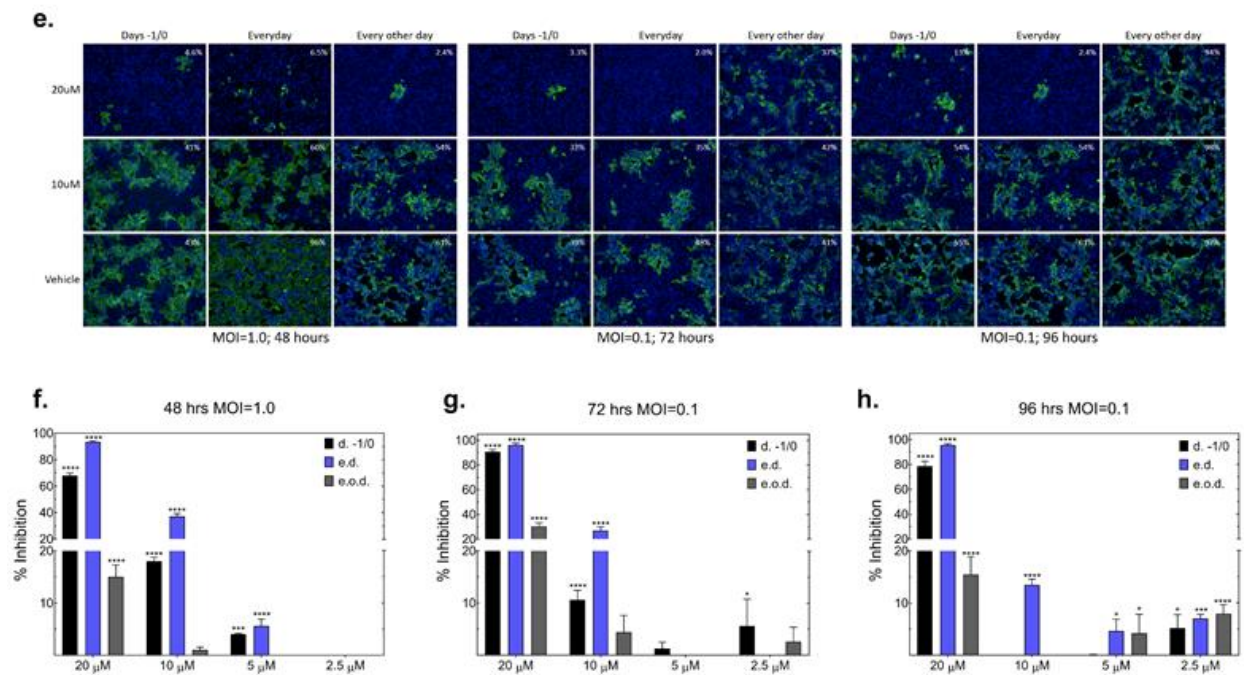
Fendiline was most effective at reducing EBOV and MARV infection in vitro at the highest 20 μ M concentrations in each treatment group with statistically significant inhibition observed for both EBOV and MARV at each time point and each treatment group (excluding EBOV 48 hours, e.d.)(**** $p < 0.0001$, ** $p < 0.0066$). Percent inhibition was directly affected by timing of treatments following infection. Furthermore, both EBOV and MARV treatment with fendiline e.d. had the highest inhibition on viral spread at each time point for 20 μ M fendiline treatments. Cells of the e.o.d. treatments group, which did not receive treatment immediately following infection with virus, had a dramatically reduced degree of inhibition as compared to the day 0 and e.d. treatment groups, both of which received fendiline immediately following viral infection of one hour.

Figure 5.8. Evaluation of fendiline efficacy in the inhibition of authentic EBOV and MARV spread. a-d Effect of fendiline on EBOV infection. **(a)** Representative confocal images of Vero E6 cells infected with EBOV (Kikwit) at the indicated MOI and treated with the indicated concentration of fendiline. Cells were pretreated 24 hours prior to infection with the indicated concentration of fendiline. Post infection, cells were treated 1 hour later (d -1/0), treated every day (e.d), or treated every other day (e.o.d) and fixed at either 48 hours, 72 hours or 96 hours post infection. (green=EBOV; blue= nuclei). White numbering in top right corner indicates %infection **(b-d)** Quantification of % inhibition of EBOV by fendiline. **(b)** 48 hours (MOI 1.0) **(c)** 72 hours (MOI 0.1) **(d)** 96 hours (MOI 0.1). Values are reported as mean \pm s.d. A one-way ANOVA was performed with multiple comparisons was performed. n=3. **(e-h)** Effect of fendiline on MARV infection. **(e)** Representative confocal images of Vero E6 cells infected with MARV (Ci67) at the indicated MOI and treated with the indicated concentration of fendiline. Cells were pretreated 24 hours prior to infection with the indicated concentration of fendiline. Post infection, cells were treated 1 hour later (d -1/0), treated every day (e.d), or treated every other day (e.o.d) and fixed at either 48 hours, 72 hours or 96 hours post infection. (green=MARV; blue= nuclei). White numbering in top right corner indicates %infection. **(f-h)** Quantification of % inhibition of MARV by fendiline. **(f)** 48 hours (MOI 1.0) **(g)** 72 hours (MOI 0.1) **(h)** 96 hours (MOI 0.1). Values are reported as mean \pm s.d. A one-way ANOVA was performed with multiple comparisons was performed. n=3. EBOV: Ebola virus; MOI: multiplicity of infection; MARV: Marburg virus; d. -1/0: treatment 1 hour after infection; e.d.: treatment every day; e.o.d.: treatment every other day.

EBOV - Fendiline Treated



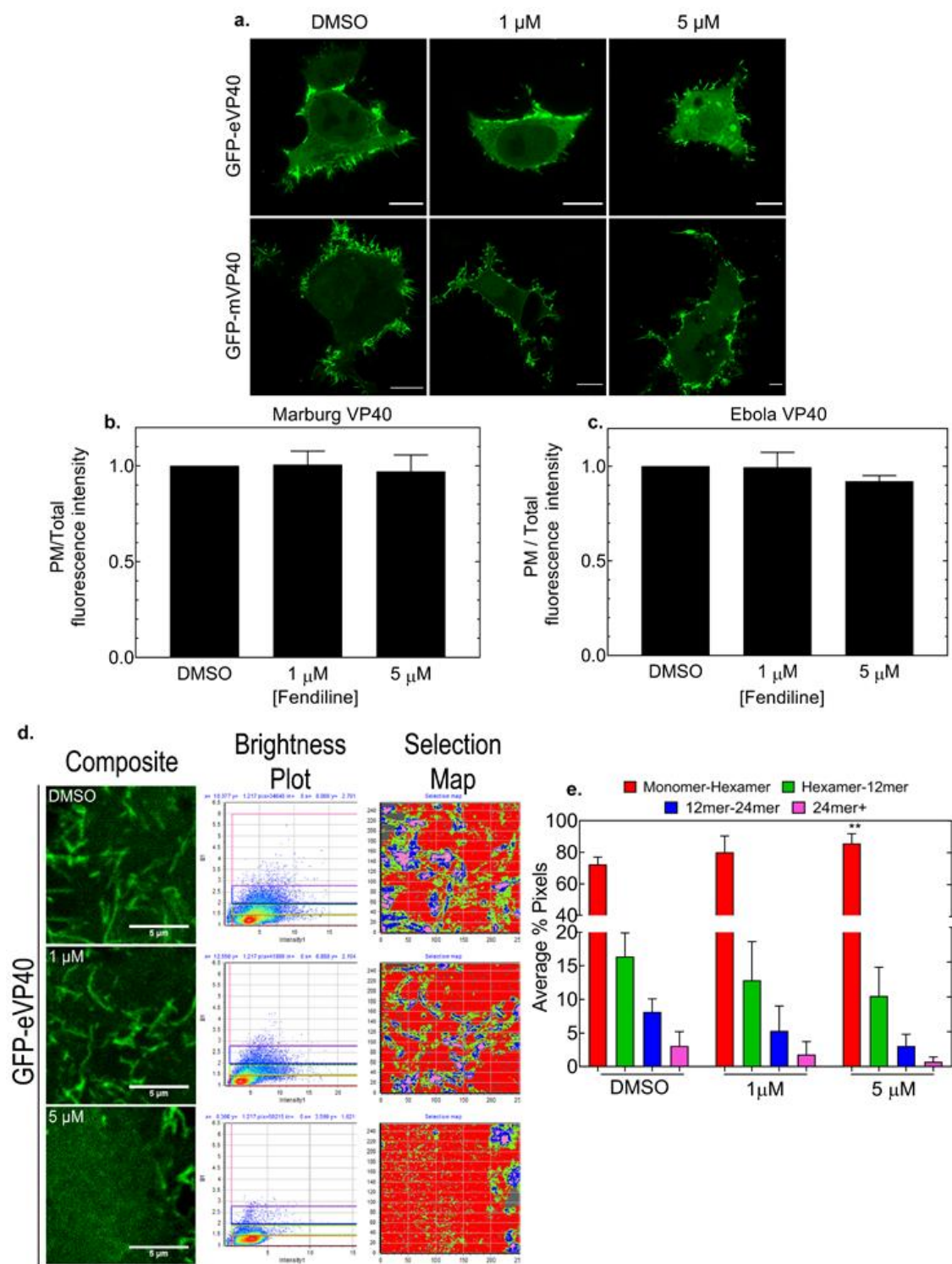
MARV - Fendiline Treated



5.3.7 Fendiline reduced EBOV-VP40 but not MARV-VP40 localization to the plasma membrane*

As both EBOV and MARV-VP40 assembly at the plasma membrane is in part governed by PS, we first analyzed both EGFP-eVP40 and EGFP-mVP40 plasma membrane localization in cells treated with fendiline for 24 or 48 hours. Treatment with 1 μ M and 5 μ M fendiline had no significant effect on eVP40 plasma membrane at 24 hours post treatment (data not shown); therefore, EGFP-mVP40 plasma membrane localization was not assessed at 24 hours. Surprisingly, no significant change in EGFP-mVP40 plasma membrane localization was observed after 48 hours with either 1 μ M or 5 μ M fendiline treatment (**Figure 5.9 a-b**); therefore, mVP40 was excluded from further experiments. In agreement with our results thus far, 1 μ M fendiline did not significantly inhibit EGFP-eVP40 plasma membrane localization after 48 hours of treatment (**Figure 5.9 a top panel, Figure 5.9 c**). However, treatment with 5 μ M fendiline for 48 hours led to a modest reduction in EGFP-eVP40 plasma membrane localization (~6% reduction compared to control treated cells; $p=0.08$) (**Figure 5.9 top panel, Figure 5.9 c**). However, the reduction of eVP40 plasma membrane localization was not robust enough to lead to the observed inhibition of EBOV by fendiline treatment in our BSL-4 studies (**Figure 5.8**). One possible explanation is that a limitation of this technique is the inability to differentiate the extent of VP40 oligomerization occurring using basic confocal microscopy. Therefore, it is possible that fendiline reduced PS levels within the plasma membrane, but not significantly enough to block VP40's ability to bind to the plasma membrane.

Figure 5.9. Analysis of eVP40/mVP40 cellular localization and oligomerization following fendiline treatment. (a-c) Effect of fendiline on eVP40 and mVP40 PM localization in HEK293 cells after 48 hours of treatment. (a) Representative confocal images from live cell imaging experiments of HEK293 cells expressing EGFP-WT-eVP40 (top panel) and EGFP-WT-mVP40 (bottom panel) after 48 hours of fendiline treatment. scale bars= 10 μ m. Effect of fendiline on eVP40 (b) and mVP40 (c) PM localization was quantified by the ratio of EGFP fluorescence intensity at the PM / total EGFP fluorescence intensity (and normalized to DMSO control). N>15, n=3. Values are reported as mean \pm s.d. A one-way ANOVA with multiple comparisons was performed compared to the DMSO control. (d-e) Analysis of eVP40 oligomerization in HEK293 cells in response to 48 hour fendiline treatment using N&B analysis. (d) *Left panel:* Representative images from time-lapse (30 frames) of HEK293 expressing EGFP-WT-eVP40 and treated with fendiline for 48 hours. scale bar = 5 μ m. *Middle panel:* Brightness and Intensity plots for each representative image. *Right panel:* Selection map correlating each pixel in the representative image to an oligomerization state (b value) (red: monomer-hexamer, green: hexamer-12mer, blue: 12mer-24mer, pink: >24mer). (e) Average % pixel quantification from panel (d)= % of GFP-WT-eVP40 with brightness values corresponding to monomer-hexamer (~1.-1.6), hexamer-12mer (~1.6-2.0), 12mer-24mer (2.0-3.2) and >24mer (>3.2) over the total pixels within each image. Values are reported as mean \pm s.d.; N \geq 9, n=3; A two-way ANOVA was performed with Dunnett's multiple comparisons compared to the control DMSO % average pixels (**p=0.0035).



5.3.8 VP40 oligomerization is significantly reduced by fendiline treatment

PS is also a key factor promoting the self-assembly of VP40 into the matrix layer of the budding virion^{14,38}. This self-assembly process has been highlighted in our in vitro crosslinking data (**Figure 5.3 d-e**) as well as previously reported in live cells utilizing the N&B technique³⁸. To assess how fendiline impacted eVP40 oligomerization in cells, we examined the oligomerization profile of EGFP-eVP40 using the previously described N&B^{37,38} (**Figure 5.9 d-e**). To accurately capture oligomerization at the plasma membrane, imaging was performed at a focal plane at the top of the cell. HEK293 cells expressing monomeric EGFP were imaged and quantified to calculate the experimental brightness value for a monomer (**Figure 5.6 a**). The crystal structure and biochemical analysis of eVP40 suggests eVP40 binds to the plasma membrane as a dimer, subsequently oligomerizes into larger oligomers such as a hexamer, and these hexamers are building blocks for extensive filamentous formation¹¹. Therefore, for our data to coincide with the current models of eVP40 oligomerization, EGFP-eVP40 oligomers were grouped into bins based on multiples of the hexamer (i.e. monomer-hexamer, hexamer-12mer, 12mer-18mer, and >18mer). The average percentage of pixels in each bin was calculated and plotted for HEK293 cells expressing EGFP-eVP40 and treated with either the control or indicated concentration of fendiline for 48 hrs (**Figure 5.9 e**).

Large eVP40 oligomeric structures corresponding to each bin size were readily detectable at the plasma membrane in control treated cells (**Figure 5.9 d top panel, Figure 5.9 e**), with ~72% of eVP40 found as a monomer-hexamer, ~16% as a hexamer-12mer, ~8% as a 12mer-18mer, and 3% in complexes >18mer. Treatment with 1 μ M fendiline led to a ~8% increase in monomeric-hexameric eVP40, and small decreases in the larger oligomeric structures, although no changes were statistically significant (**Figure 5.9 d middle panel, Figure 5.9 e**). However, the oligomeric profile of eVP40 was statistically different when cells were treated with 5 μ M fendiline. Following 5 μ M fendiline treatment, there was a significant increase in eVP40 found in the monomeric-hexameric state (~13% increase; **p=0.0035) which was counterbalanced by an equal reduction in the larger oligomeric states (~6% reduction for hexamer-12mer, 5% reduction for 12mer-18mer, and ~3% reduction for eVP40 structures >18mer) (**Figure 5.9 d bottom panel, Figure 5.9 e**). These results support our hypothesis that by reducing PS concentration and therefore the pool of PS available for clustering, eVP40 is unable to properly oligomerize once it traffics and binds to the

plasma membrane. This, in combination with the modest reduction in eVP40 plasma membrane binding following fendiline treatment, may therefore impact the production of viral particles as suggested from our BSL-4 studies.

5.3.9 Fendiline reduced VLP production at the plasma membrane

As fendiline reduced VP40 oligomerization, we sought to determine the effect of fendiline treatment on VLP production using functional budding assays. VLPs were harvested at 24 (**Figure 5.10 a-b**) and 48 hours (**Figure 5.10 c-d**) post-treatment and the relative budding index was determined with western blotting and densitometry analysis. No significant effect on VLP production was observed for cells treated with 0.5 μ M or 1 μ M fendiline at either 24 (**Figure 5.10 a lane 3-4, Figure 5.10 b**) or 48 hours post-treatment (**Figure 5.10 c lane 3-4, Figure 5.10 d**). However, treatment with one dose of 5 μ M fendiline for 24 hours led to a ~25% reduction in VLP production (**Figure 5.10 a lane 5, Figure 5.10 b**) compared to DMSO treated cells (**Figure 5.10 a lane 2, Figure 5.10 b**). More importantly, this reduction in VLP production was even more robust when monitored at 48 hours post-treatment, with a statistically significant ~60% reduction in the relative budding efficiency of 5 μ M fendiline treated cells (*p=0.0260) (**Figure 5.10 c lane 5, Figure 5.10 d**) compared to DMSO treated cells (**Figure 5.10 c lane 2, Figure 5.10 d**). The reduction in VLPs is supported by our previous findings that a single dose of 5 μ M fendiline reduced PS levels, PS clustering and the extent of eVP40 oligomerization at the plasma membrane. Therefore, we hypothesize that reduced virus budding is at least partially responsible for fendiline efficacy in authentic EBOV studies (**Figure 5.8**).

To further investigate the reduction of VLP production in fendiline treated cells, and to determine if there were any observable morphological changes in VLPs, scanning electron microscopy (SEM) experiments were performed on mock transfected cells (**Figure 5.10 e**) and cells expressing FLAG-eVP40 (**Figure 5.10 f**). Cells were treated with either the control, 1 μ M or 5 μ M fendiline for 48 hours. SEM revealed the presence of filamentous protrusions from the plasma membrane of mock transfected cells in untreated and control treated cells (**Figure 5.10 e**). In both control and fendiline treated cells expressing FLAG-eVP40, a dense filamentous protrusion population was observed at the surface of cells, indicating abundant VLP production (**Figure 5.10 f**). This extensive budding of VLPs was present in untreated, DMSO treated, and 1 μ M fendiline treated cells expressing FLAG-eVP40 (**Figure 5.10 f**). Importantly, micrographs of cells

expressing FLAG-eVP40 and treated with 5 μ M fendiline revealed minimal VLP production at the plasma membrane compared to control treated cells (**Figure 5.10 f**). These findings support the hypothesis that fendiline treatment considerably reduces the production of VLPs in eVP40 expressing cells.

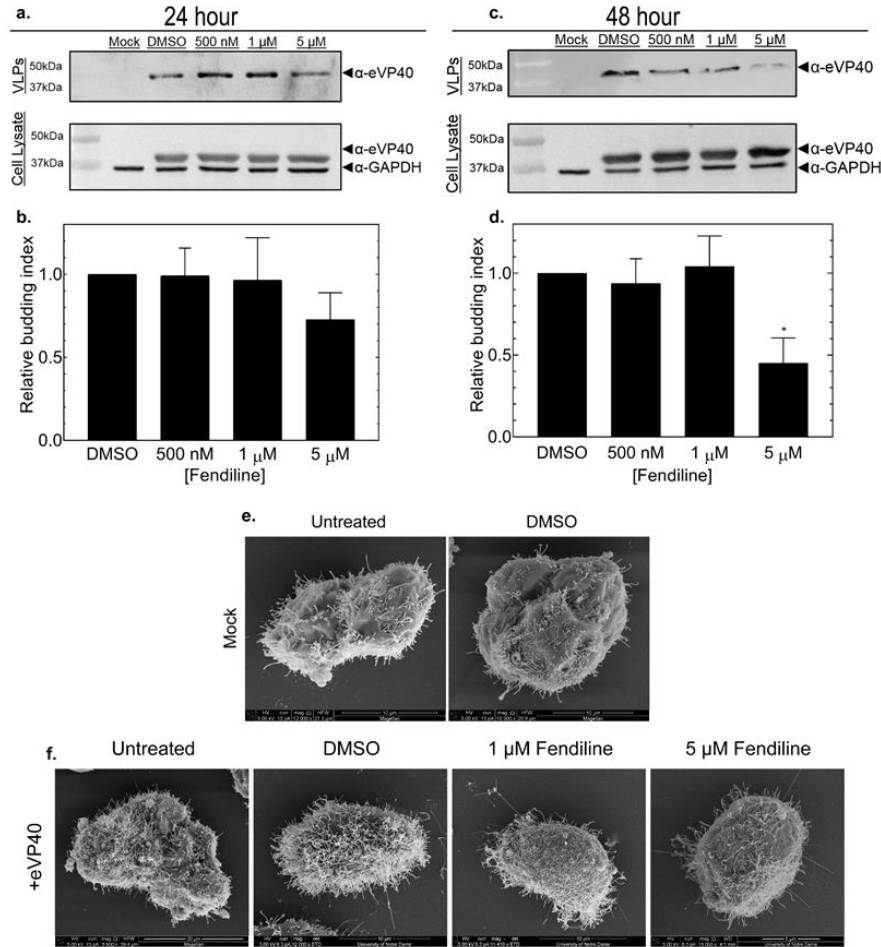


Figure 5.10. VLP production and morphology in HEK293 cells in the presence of fendiline. (a-d) Functional budding assays assessed at 24 hours (a-b) and 48 hours (c-d) post treatment. (a) Representative western blot of budding assays performed at 24 hours. VLP samples (top panel) and cell lysate samples (bottom panel) collected from HEK293 cells and immunoblotted for eVP40 expression; GAPDH served as a loading control. eVP40 detected by (Rabbit α -eVP40 and HRP-Goat α -Rabbit); GAPDH detected by mouse α -GAPDH and HRP-Sheep α -Mouse) (b) Quantification of relative budding index at 24 hours post fendiline treatment. Relative budding index was determined by the western blot band density of eVP40 in the VLP fraction/(total eVP40 cell lysate + eVP40 VLP band density) and was normalized to the DMSO control. Cell lysate eVP40 band density was normalized to GAPDH band density prior to use in budding index quantification. n=3. Values are reported as mean \pm s.d. A one-way ANOVA was performed with multiple comparisons compared to the DMSO control. (c) Representative western blot of budding assays performed at 48 hours. VLP samples (top panel) and cell lysate samples (bottom panel) collected from HEK293 cells and immunoblotted for eVP40 expression; GAPDH served as a loading control. eVP40 detected by (Rabbit α -eVP40 and HRP-Goat α -Rabbit); GAPDH detected by (Mouse α -GAPDH and HRP-Sheep α -Mouse) (d) Quantification of relative budding index at 48 hours post fendiline treatment. Relative budding index was determined by the western blot band density of eVP40 in the VLP fraction/(total eVP40 cell lysate + eVP40 VLP band density) and was normalized to the DMSO control. Cell lysate eVP40 band density was normalized to GAPDH band density prior to use in budding index quantification. n=3. Values are reported as mean \pm s.d. A one-way ANOVA was performed with multiple comparisons compared to the DMSO control. (*p=0.0260) (e-f) SEM micrographs of HEK293 cells. (e) Representative micrographs of mock transfected HEK293 cells harvested after 48 hours of no treatment or DMSO treatment. (f) Representative micrographs of HEK293 cells expressing FLAG-eVP40 and harvested after 48 hours of no treatment, DMSO treatment, or the indicated concentration of fendiline. VLPs: virus like particles; SEM: scanning electron microscopy; GAPDH: glyceraldehyde 3-phosphate dehydrogenase; HRP: horseradish peroxidase.

5.3.10 VLP morphology is altered by fendiline treatment

The structure and stability of filoviruses is derived from the VP40 matrix underlying the lipid envelope of virions². Therefore, we utilized transmission electron microscopy (TEM) of purified VLPs to determine if disturbing matrix assembly and altering the lipid components of the plasma membrane with fendiline treatment changed VLP morphology and possibly infectivity (**Figure 5.11 a-c**). During filoviral entry, surface exposed GP and viral envelope PS interact with the receptor T-cell immunoglobulin receptor-1 (TIM-1)^{18,22}. To recapitulate entry-competent VLPs (eVLPs), we co-expressed eVP40 with the Ebola virus glycoprotein (eGP). We performed TEM of eVLPs purified from control and 5 μ M fendiline treated cells (48-hour treatment) and used ImageJ software to analyze VLP length and diameter (**Figure 5.11 a-cc**). Control eVLPs were heterogenous in length with a mean length of $4.1 \mu\text{m} \pm 2.9$ (**Figure 5.11 a left panel, Figure 5.11 b**). Control eVLPs diameter also exhibited a level of heterogeneity but had a fairly consistent diameter of $75 \text{ nm} \pm 12.9$, which is similar to previous studies of both virions and VLPs^{2,7} (**Figure 5.11 a left panel, Figure 5.11 c**). The length and diameter of eVLPs derived from 5 μ M fendiline treated cells were significantly less than control eVLPs. Strikingly, fendiline treatment reduced eVLP length by ~35%, from $4.1 \mu\text{m}$ to $2.7 \mu\text{m}$ (* $p=0.0139$) (**Figure 5.11 a right panel, Figure 5.11 b**) and modestly but statistically significantly reduced eVLP diameter (* $p=0.043$) (**Figure 5.11 a right panel, Figure 5.11 c**). To ensure that eVLPs derived from fendiline treated cells were not more susceptible to damage during the purification, circular dichroism thermal melting was performed and no difference in eVLP stability was observed (CD data not shown; performed by Caroline Plescia). Reduced eVLP length and diameter could translate into reduced infectivity (e.g., less PS and less surface area and membrane available to bind TIM-1), therefore we next sought to determine the effect of fendiline on eVLP entry.

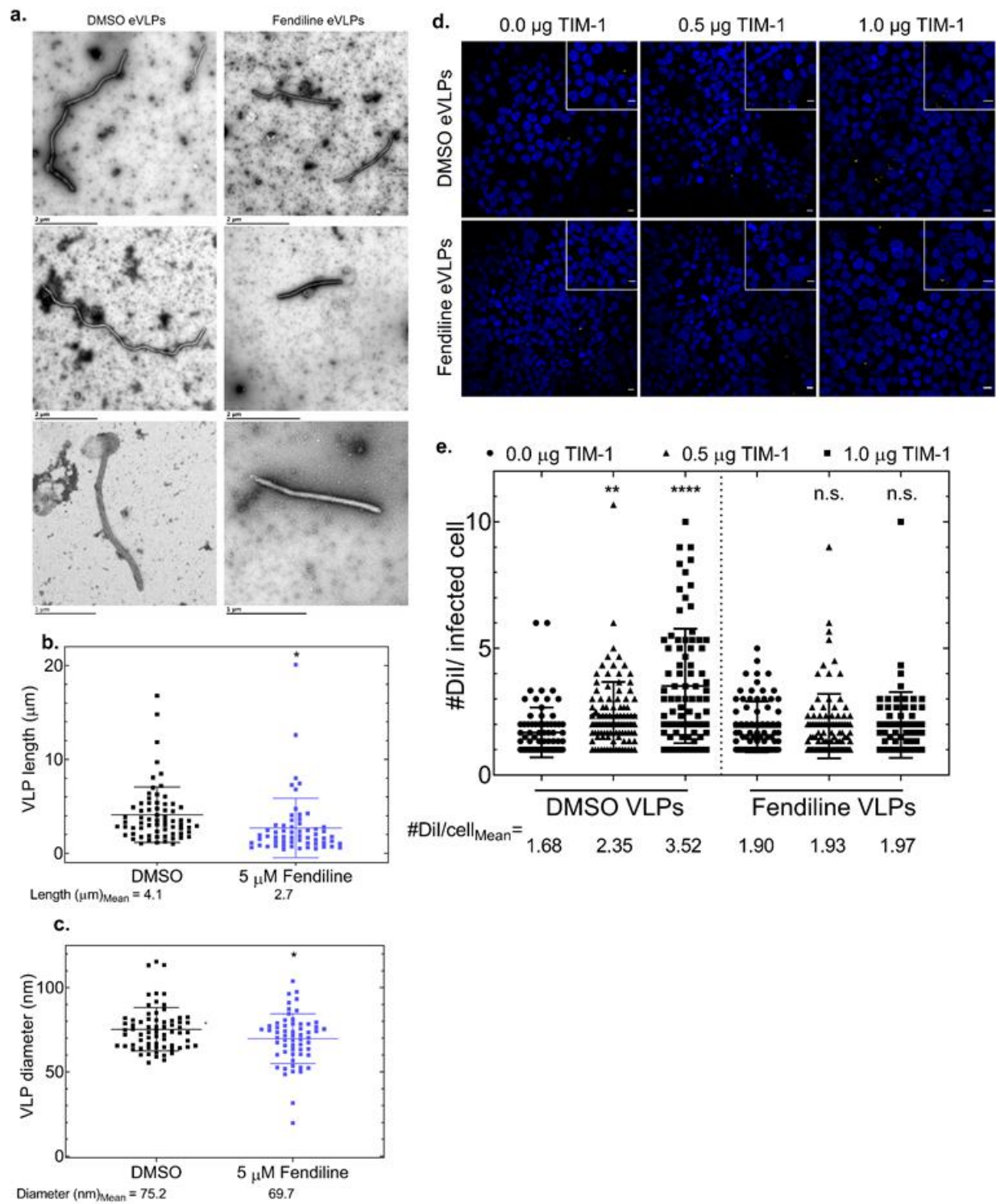
5.3.11 Fendiline blocks EBOV eVLP entry

A common characteristic of viral infectivity is the relationship between virion associated PS and the TIM-1 receptor on target cells^{18,22,23,58,59}. Moreover, it has been previously reported that other ASM inhibitors blocked EBOV infectivity⁶⁰. To determine if fendiline treatment reduced the entry of eVLPs, we performed a fluorescent based entry assay using 1,1'-dioctadecyl-3,3,3',3'-

tetramethylindocarbocyanine perchlorate (DiI) labelled eVLPs^{20,44,61}. DiI labelled eVLPs were derived from cells treated with either control or 5 μ M fendiline. By testing entry of eVLPs derived from fendiline treated cells rather than the entry of eVLPs on fendiline treated cells, we were able to determine how fendiline treatment affected eVLP entry rather than how inhibition of ASM in target cells affected eVLP entry (as previously described⁶⁰). In brief, eVLPs derived from both control and fendiline treated cells were purified and labelled with DiI, incubated with target cells overexpressing increasing amounts of TIM-1, and the DiI signal was imaged using confocal microscopy (Representative images in **Figure 5.11 d**). If entry of the eVLPs was not altered by fendiline treatment, one would expect a dose-dependent increase in infectivity with increasing TIM-1 expression. Conversely, if eVLP entry was inhibited by fendiline treatment, a dose-dependent increase in eVLP entry would not be observed with increasing TIM-1 expression.

For all VLPs, non-specific entry was observed for target cells lacking TIM-1 overexpression (\sim 1.7-1.9 DiI/infected cell, **Figure 5.11 d left panel**, **Figure 5.11 e**). This was not unexpected, as normal endocytic processes were not inhibited in these experimental conditions. However, as TIM-1 overexpression increased in target cells, a detectable and significant dose-dependent increase in control eVLP entry was observed, by more than 200% in the highest TIM-1 overexpressing cells (compared to no TIM-1 overexpression; **Figure 5.11 d top panel**, **Figure 5.11 e**). Remarkably, no measurable increase in eVLP entry was observed for fendiline derived-VLPs across any of the TIM-1 overexpressing target cell conditions (**Figure 5.11 d bottom panel**, **Figure 5.11 e**). From this comparison, these results suggest that the impaired entry of fendiline eVLPs is a result of reduced PS in the viral envelope, either from smaller VLPs or a lower % of PS content. These findings in combination with the observed reduction in VLP formation further substantiate the significant reduction of EBOV infection observed in our live virus studies following fendiline treatment.

Figure 5.11. Effect of fendiline on eVLP morphology and TIM-1 dependent eVLP entry. (a-c) TEM analysis of eVLP morphology. **(a)** Representative transmission electron micrographs of eVLPs purified from HEK293 cells expressing FLAG-eVP40 and eGP following 48 hours of DMSO (left panel) or 5 μ M fendiline treatment (right panel). **(b)** Quantification of eVLP length (μ m) of DMSO-derived eVLPs (black) and fendiline-derived eVLPs (blue). $N > 50$, $n = 3$. A two-tailed t-test was performed ($**p = 0.0139$). **(c)** Quantification of eVLP diameter (nm) of DMSO-derived eVLPs (black) and fendiline-derived eVLPs (blue). $N > 50$, $n = 3$. A two-tailed t-test was performed ($*p = 0.0430$). **(d-e)** Fluorescence based DiI TIM-1 dependent entry assay. **(d)** Representative confocal images from the DiI-entry assay comparing entry of eVLPs produced from DMSO (top panel) and fendiline-treated HEK293 cells (bottom panel) into target cells (HEK293 cells transiently expressing increasing amounts of TIM-1; 0.0 μ g, 0.5 μ g, 1.0 μ g). A stack of 10 frames was acquired for each image. DiI (initially red) was recolored to yellow for easier observation in print; blue (Hoechst 3342 stain); scale bar = 10 μ m. **(e)** Quantification of eVLP entry was performed by calculating the total number of DiI punctate / the total number of DiI-positive cells. Three images from each z-stack was quantified. $N = 9$, $n = 3$. A one-way ANOVA was performed with multiple comparisons against the 0.0 μ g TIM-1 condition for both DMSO- and fendiline derived eVLPs. ($****p < 0.0001$; $**p = 0.0093$). Values are reported as mean \pm s.d. eVLP: entry-competent viral like particles; TEM: transmission electron microscopy; TIM-1: t-cell immunoglobulin receptor-1; eVLPs: entry-competent VLPs; eGP: Ebola glycoprotein; DiI: 1,1'-Diiododecyl-3,3',3'-Tetramethylindocarbocyanine Perchlorate.



5.3.12 Mathematical model of in vitro experiments*

We next used a mathematical model to predict how the effects of fendiline on both viral budding and entry combine to produce the observed effects in the BSL-4 assays. We calibrate our mathematical model (equations 1-3) to experimental data from the budding, entry and cellular infection assays using approaches and parameter settings outlined in the methods and **Table 2 in Appendix 1**. Results from our two-phase calibration procedure are shown in **Figure 5.12 a-f** and **Figure 5.13**. The model captures key features of the data including a progressive increase in percentage of infected cells over time, differences between MOI as well as limited cell death in the first 48 hours of the experiment (**Figure 5.13**). The dynamics behind these calibrated figures suggested that fendiline treatment significantly delayed the infection process (**Figure 5.12 g-h**), resulting in the observed decrease in percent infected cells with treatment over 4 days. The effects of fendiline on budding and entry are estimated to have similar pharmacodynamics (PD), with entry effects estimated to have a slightly stronger response (lower C50 and higher Emax) compared to budding (**Table 2 in Appendix 1**). Based on PD parameters, the response to fendiline was estimated to be weaker in the BSL-4 assays, as is evident by higher C50 values and lower Emax values compared to the budding and entry assays (**Table 2 in Appendix 1, Figure 5.12 i**). These PD parameter differences between budding and entry assays vs BSL-4 results could suggest that other parts of the viral life cycle not affected by fendiline (not quantified explicitly in these experiments) become rate limiting in the BSL-4 assays, thereby reducing the overall effect of fendiline on infection progression. In summary, a mathematical model consistent with three independent experimental systems, predicts a combination of budding and entry effects resulting in the observed BSL-4 effects, and estimates PD parameters for each mechanism.

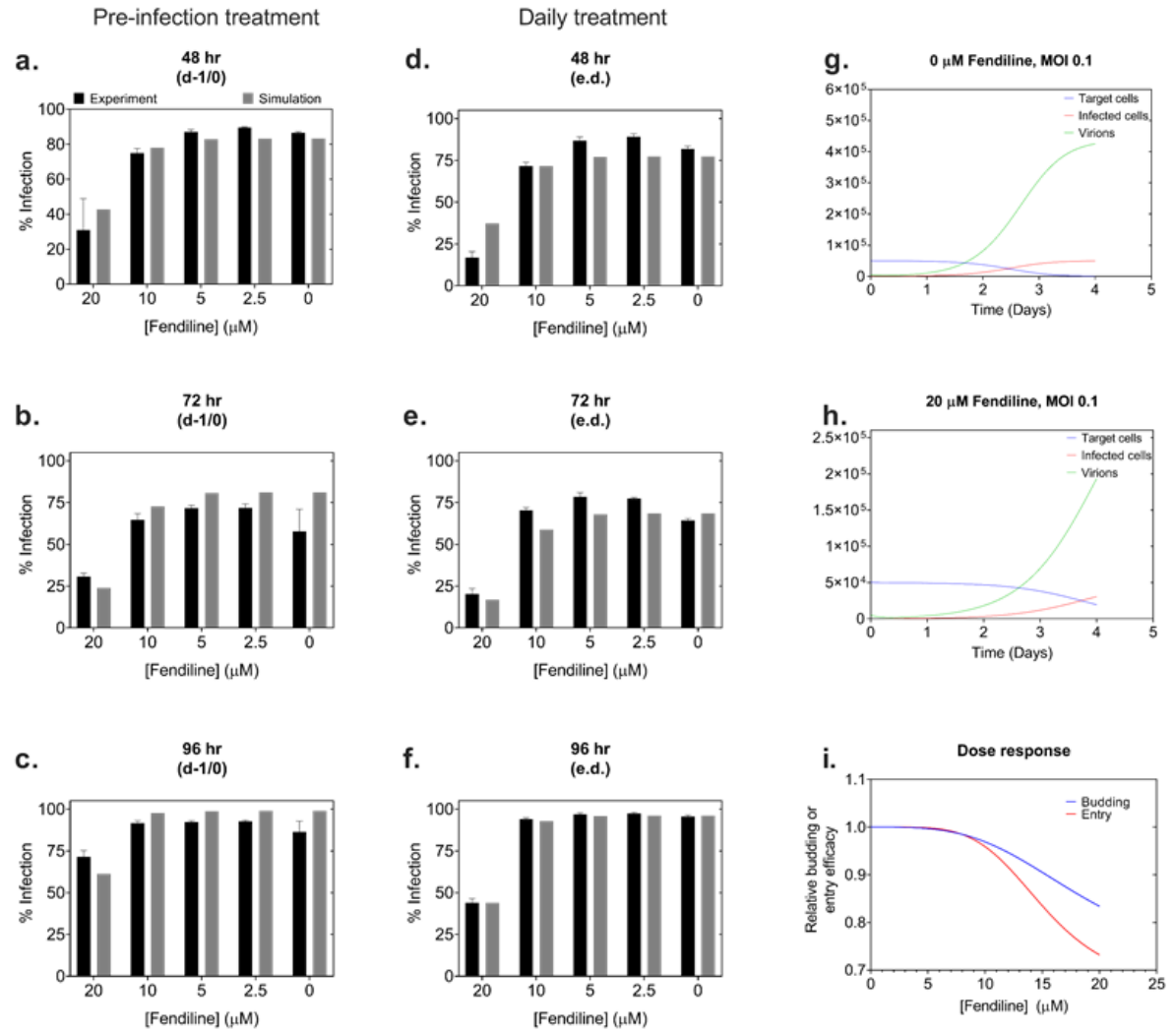


Figure 5.12. Calibrated mathematical model reproduces key observations in multiple experimental datasets. Percentage infected cells is shown for various fendiline concentrations given prior to infection (d-1/0, **a-c**) or daily (e.d., **d-f**). (**a,d**) MOI 1; (**b,c,e,f**) MOI 0.1. (**g-h**) Model predicted cell and viral dynamics for MOI 0.1. (**i**) Model predicted dose response curves for fendiline effects on viral budding and entry in the BSL4 experiments.

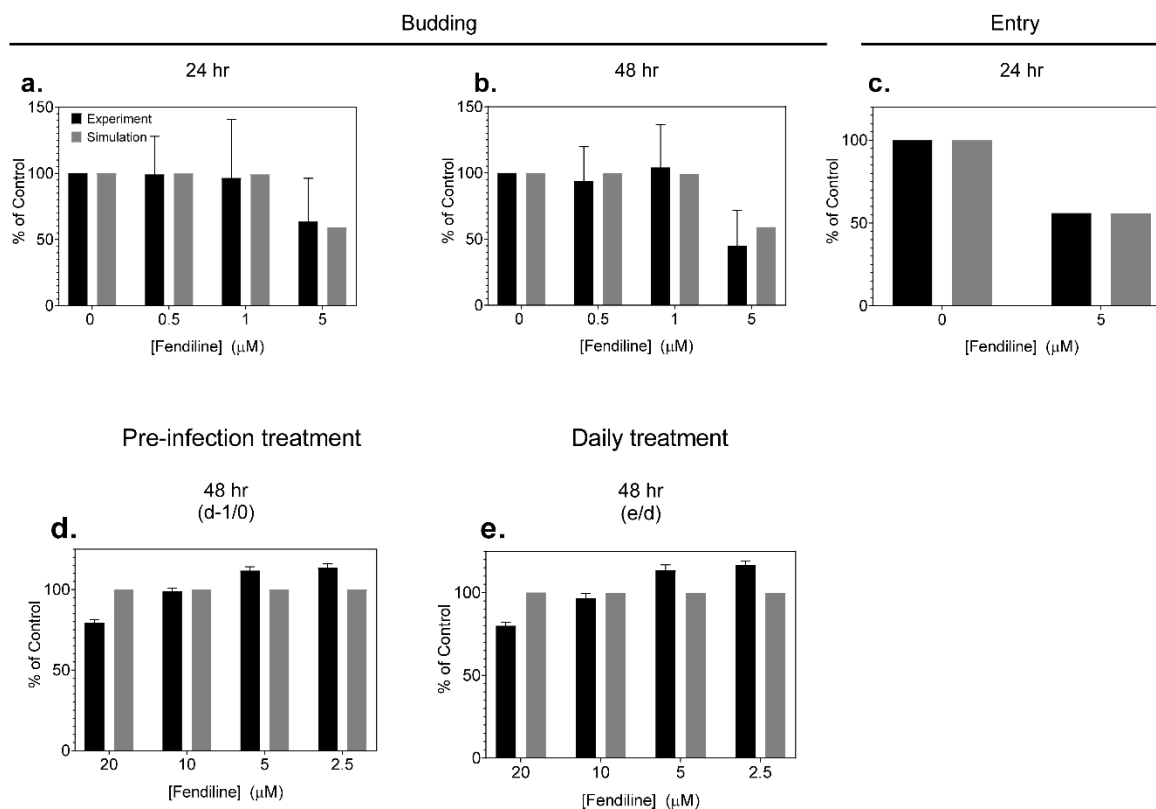


Figure 5.13. Calibration results from the first and second phase of model development. (a-c) First phase calibration results between experimental (black bars) and simulation (gray) data from budding (a-b) and entry (c) assays. (d-e) Second phase calibration results showing comparison between experimental and simulation data from cell viability assays. The mathematical model was calibrated to this data and the data in Figure 5.12 simultaneously.

5.4 Discussion

Lipids and the plasma membrane act as a platform for not just the assembly and budding of filoviruses, but also in the entry of filoviruses. The matrix protein VP40 is the principal orchestrator of the viral budding process, and independent expression of VP40 will produce VLPs that nicely recapitulate the budding process and progeny virions⁶⁻⁸. PS, the most abundant anionic lipid within the inner leaflet of the plasma membrane is also central to the budding and exit process. As eVP40 is the driving force behind viral budding, it is not surprising that the localization of eVP40 to the plasma membrane is driven by a high affinity for PS^{14,31,47,48}. Several fundamental aspects of eVP40 membrane interactions and their implications in viral budding^{14,37,38,62-64} have been explored, yet mechanistic details underlying the dynamic interaction of eVP40 and PS or the therapeutic potential of targeting this interaction had not been explored.

The ability of other viral matrix proteins ability to cluster lipids^{15,65,66} as well as the propensity of PS to form clusters within the plasma membrane^{28,54}, however had not been explored for eVP40 and PS. To address this, we investigated the ability of eVP40 to cluster PS within the plasma membrane of cells and the subsequently the implications of PS concentration on eVP40 processes. In this report, we utilized a fluorescently labelled PS supplemented into cells expressing various GFP-fused proteins to show that GFP-eVP40 enhanced PS clustering within the plasma membrane (to an extent similar to the well-documented PS clustering induced by annexins), and that the clustering of PS was dependent on the membrane localization and oligomerization of eVP40. As the plasma membrane consists of 20-30 mol% PS, the clustering of PS may be a mechanism by which the oligomerization of eVP40 recruits an abundance of PS molecule to platforms of viral assembly to support the extensive assembly of the new virion. Our *in vitro* SPR and chemical crosslinking highlighted that robust eVP40 membrane association and oligomerization did not occur at PS concentrations of 15% (below that of the plasma membrane). Furthermore, the clustering of PS may occur early on in assembly prior to binding to PI(4,5)P₂, so that once eVP40 associates with PI(4,5)P₂ there is a sufficient population of PS present to be externalized to the outer leaflet for incorporation into the viral envelope and the clustering of PS could be a cue to activate scramblases for this process^{61,67}.

A recent report highlighted that reducing PS synthesis by silencing the PSS1 gene (reviewed in 2.2.1) was effective in inhibiting EBOV⁶⁷. However, to the best of our knowledge,

small molecules aimed at targeting host cell lipid distribution have not previously been tested against EBOV. Fendiline was a logical choice to form an initial hypothesis of an FDA-approved drug that could inhibit EBOV budding as it was recently shown to lower plasma membrane PS³³ and inhibit K-Ras signaling^{34,35} suggesting this FDA-approved drug may be sufficient to inhibit EBOV budding. We showed through lipidomic analysis that in our filoviral model cell line, HEK 293 cells, fendiline reduced total PS content by ~30% and also PS content within the plasma membrane. In this report, we showed using a BSL-4 model of infectious EBOV and MARV, that fendiline was able to inhibit EBOV replication >75% at 20 μ M and MARV replication >90% when given every day post-infection.

Furthermore, follow-up studies provided compelling evidence as to the mechanistic aspect of the efficacy of fendiline against filoviral infections. Using N&B analysis we were able to show that fendiline reduced the ability of PS to form clusters within the plasma membrane of living cells, and also reduced the ability of eVP40 to oligomerize at the plasma membrane and efficiently produce VLPs. The VLPs that did form from fendiline-treated cells had an overall reduced length and surface area, which likely combined with the reduced PS-content of the virus or VLPs to limit subsequent viral entry. Thus, disruption of PM PS content by one small molecule was sufficient to effect at least three important steps in the filovirus life cycle.

Overall, this study lends credence to the hypothesis that host processes are a promising target to inhibit viral replication and spread. While the potency of fendiline was low, the combination of fendiline with other FDA-approved drugs that have shown efficacy against EBOV⁶⁸⁻⁷² or drugs within clinical trials (such as staurosporines, which disrupt PS trafficking to the plasma membrane⁷³) hold further promise. A critical balance between VP40 and PS has been resolved demonstrating a critical need for VP40 clustering in the assembly and budding process. VP40 oligomers are needed for enhanced PS clustering where PS clustering seems to ensure optimal VP40 oligomerization. These studies also lay a framework to improved pharmacological targeting strategies against either VP40 matrix assembly or PS clustering that would not only reduce viral budding and spread, but lower subsequent viral entry, which partially relies on PS in the viral envelope^{18,19,22,32}.

5.5 References

1. Breman, J. G. *et al.* Discovery and Description of Ebola Zaire Virus in 1976 and Relevance to the West African Epidemic during 2013-2016. *J. Infect. Dis.* **214**, S93–S101 (2016).
2. Liu, L. Fields Virology, 6th Edition. *Clin. Infect. Dis.* **59**, 613–613 (2014).
3. FDA. First FDA-approved vaccine for the prevention of Ebola virus disease, marking a critical milestone in public health preparedness and response | FDA. (2019). Available at: <https://www.fda.gov/news-events/press-announcements/first-fda-approved-vaccine-prevention-ebola-virus-disease-marking-critical-milestone-public-health>. (Accessed: 9th January 2020)
4. Banadyga, L., Dolan, M. A. & Ebihara, H. *Rodent-Adapted Filoviruses and the Molecular Basis of Pathogenesis*. *Journal of Molecular Biology* **428**, 3449–3466 (Academic Press, 2016).
5. Mühlberger, E. Filovirus replication and transcription. *Future Virol.* **2**, 205–215 (2007).
6. Jasenosky, L. D., Neumann, G., Lukashevich, I. & Kawaoka, Y. Ebola virus VP40-induced particle formation and association with the lipid bilayer. *J. Virol.* **75**, 5205–14 (2001).
7. Noda, T. *et al.* Ebola Virus VP40 Drives the Formation of Virus-Like Filamentous Particles Along with GP. *J. Virol.* **76**, 4855–4865 (2002).
8. Licata, J. M. *et al.* Overlapping Motifs (PTAP and PPEY) within the Ebola Virus VP40 Protein Function Independently as Late Budding Domains: Involvement of Host Proteins TSG101 and VPS-4. *J. Virol.* **77**, 1812–1819 (2003).
9. Wang, Y. E. *et al.* Ubiquitin-regulated nuclear-cytoplasmic trafficking of the Nipah virus matrix protein is important for viral budding. *PLoS Pathog.* **6**, e1001186 (2010).
10. Oda, S.-I. *et al.* Crystal Structure of Marburg Virus VP40 Reveals a Broad, Basic Patch for Matrix Assembly and a Requirement of the N-Terminal Domain for Immunosuppression. *J. Virol.* **90**, 1839–48 (2016).
11. Bornholdt, Z. A. *et al.* Structural rearrangement of ebola virus vp40 begets multiple functions in the virus life cycle. *Cell* **154**, 763–774 (2013).
12. Panchal, R. G. *et al.* In vivo oligomerization and raft localization of Ebola virus protein VP40 during vesicular budding. *Proc. Natl. Acad. Sci. U. S. A.* **100**, 15936–41 (2003).
13. Jasenosky, L. D. & Kawaoka, Y. Filovirus budding. *Virus Res.* **106**, 181–8 (2004).
14. Adu-Gyamfi, E. *et al.* Host Cell Plasma Membrane Phosphatidylserine Regulates the Assembly and Budding of Ebola Virus. *J. Virol.* **89**, 9440–53 (2015).
15. Bobone, S. *et al.* Phosphatidylserine Lateral Organization Influences the Interaction of Influenza Virus Matrix Protein 1 with Lipid Membranes. *J. Virol.* **91**, 1–15 (2017).
16. Wijesinghe, K. J. & Stahelin, V. Investigation of the Lipid Binding Properties of the Marburg Virus. *J. Virol.* **90**, 3074–3085 (2016).
17. Carnec, X. *et al.* The Phosphatidylserine and Phosphatidylethanolamine Receptor CD300a Binds Dengue Virus and Enhances Infection. *J. Virol.* **90**, 92–102 (2016).
18. Moller-Tank, S., Kondratowicz, A. S., Davey, R. A., Rennert, P. D. & Maury, W. Role of the phosphatidylserine receptor TIM-1 in enveloped-virus entry. *J. Virol.* **87**, 8327–41 (2013).
19. Jemielity, S. *et al.* TIM-family Proteins Promote Infection of Multiple Enveloped Viruses through Virion-associated Phosphatidylserine. *PLoS Pathog.* **9**, e1003232 (2013).
20. Nanbo, A. & Kawaoka, Y. Molecular Mechanism of Externalization of Phosphatidylserine

- on the Surface of Ebola Virus Particles. *DNA Cell Biol.* **38**, 115–120 (2019).
21. Amara, A. & Mercer, J. Viral apoptotic mimicry. *Nat. Rev. Microbiol.* **13**, 461–9 (2015).
 22. Brunton, B. *et al.* TIM-1 serves as a receptor for Ebola virus in vivo, enhancing viremia and pathogenesis. *PLoS Negl. Trop. Dis.* **13**, e0006983 (2019).
 23. Kondratowicz, A. S. *et al.* T-cell immunoglobulin and mucin domain 1 (TIM-1) is a receptor for Zaire Ebolavirus and Lake Victoria Marburgvirus. *Proc. Natl. Acad. Sci. U. S. A.* **108**, 8426–31 (2011).
 24. Van Meer, G., Voelker, D. R. & Feigenson, G. W. Membrane lipids: Where they are and how they behave. *Nature Reviews Molecular Cell Biology* **9**, 112–124 (2008).
 25. Bell, R. M., Ballas, L. M. & Coleman, R. A. Lipid topogenesis. *J. Lipid Res.* **22**, 391–403 (1981).
 26. Jeckel, D., Karrenbauer, A., Burger, K. N. J., Van Meer, G. & Wieland, F. Glucosylceramide is synthesized at the cytosolic surface of various Golgi subfractions. *J. Cell Biol.* **117**, 259–267 (1992).
 27. Hirama, T. *et al.* Phosphatidylserine dictates the assembly and dynamics of caveolae in the plasma membrane. *J. Biol. Chem.* **292**, 14292–14307 (2017).
 28. Fairn, G. D. *et al.* High-resolution mapping reveals topologically distinct cellular pools of phosphatidylserine. *J. Cell Biol.* **194**, 257–275 (2011).
 29. Soni, S. P. & Stahelin, R. V. The Ebola virus matrix protein VP40 selectively induces vesiculation from phosphatidylserine-enriched membranes. *J. Biol. Chem.* **289**, 33590–7 (2014).
 30. Stahelin, R. V. Membrane binding and bending in Ebola VP40 assembly and egress. *Frontiers in Microbiology* **5**, 300 (2014).
 31. Del Vecchio, K. *et al.* A cationic, C-terminal patch and structural rearrangements in Ebola virus matrix VP40 protein control its interactions with phosphatidylserine. *J. Biol. Chem.* **293**, 3335–3349 (2018).
 32. Moller-Tank, S. & Maury, W. Phosphatidylserine receptors: Enhancers of enveloped virus entry and infection. *Virology* **468**, 565–580 (2014).
 33. Cho, K.-J. *et al.* Inhibition of Acid Sphingomyelinase Depletes Cellular Phosphatidylserine and Mislocalizes K-Ras from the Plasma Membrane. *Mol. Cell. Biol.* **36**, 363–74 (2016).
 34. van der Hoeven, D. *et al.* Sphingomyelin Metabolism Is a Regulator of K-Ras Function. *Mol. Cell. Biol.* **38**, e00373-17 (2017).
 35. van der Hoeven, D. *et al.* Fendiline inhibits K-Ras plasma membrane localization and blocks K-Ras signal transmission. *Mol. Cell. Biol.* **33**, 237–51 (2013).
 36. Bayer, R. & Mannhold, R. Fendiline: a review of its basic pharmacological and clinical properties. *Pharmatherapeutica* **5**, 103–36 (1987).
 37. Johnson, K. A., Taghon, G. J. F., Scott, J. L. & Stahelin, R. V. The Ebola Virus matrix protein, VP40, requires phosphatidylinositol 4,5-bisphosphate (PI(4,5)P₂) for extensive oligomerization at the plasma membrane and viral egress. *Sci. Rep.* **6**, 19125 (2016).
 38. Adu-Gyamfi, E., Digman, M. A., Gratton, E. & Stahelin, R. V. Investigation of Ebola VP40 assembly and oligomerization in live cells using number and brightness analysis. *Biophys. J.* **102**, 2517–25 (2012).
 39. Johnson, K. A. *et al.* PI(4,5)P₂ Binding Sites in the Ebola Virus Matrix Protein Modulate 2. *bioRxiv* 341248 (2018). doi:10.1101/341248
 40. Watt, A. *et al.* A Novel Life Cycle Modeling System for Ebola Virus Shows a Genome Length-Dependent Role of VP24 in Virus Infectivity. *J. Virol.* **88**, 10511–10524 (2014).

41. Tsai, W.-H. Moment-preserving thresholding: A new approach. *Comput. Vision, Graph. Image Process.* **29**, 377–393 (1985).
42. Harty, R. N. Hemorrhagic Fever Virus Budding Studies. in *Hemorrhagic Fever Viruses: Methods and Protocols* (ed. Salvato, M. S.) **1604**, 209–215 (Springer New York, 2018).
43. Nanbo, A. *et al.* Ebola virus requires a host scramblase for externalization of phosphatidylserine on the surface of viral particles. *PLOS Pathog.* **14**, e1006848 (2018).
44. Kuroda, M. *et al.* Interaction Between TIM-1 and NPC1 Is Important for Cellular Entry of Ebola Virus. *J. Virol.* **89**, 6481–93 (2015).
45. Nguyen, V. K., Binder, S. C., Boianelli, A., Meyer-Hermann, M. & Hernandez-Vargas, E. A. *Ebola virus infection modeling and identifiability problems*. *Frontiers in Microbiology* **6**, 257 (Frontiers Media S.A., 2015).
46. Martyushev, A., Nakaoka, S., Sato, K., Noda, T. & Iwami, S. Modelling Ebola virus dynamics: Implications for therapy. *Antiviral Res.* **135**, 62–73 (2016).
47. Ruigrok, R. W. *et al.* Structural characterization and membrane binding properties of the matrix protein VP40 of Ebola virus. *J. Mol. Biol.* **300**, 103–12 (2000).
48. Scianimanico, S. *et al.* Membrane association induces a conformational change in the Ebola virus matrix protein. *EMBO J.* **19**, 6732–41 (2000).
49. Kay, J. G., Koivusalo, M., Ma, X., Wohland, T. & Grinstein, S. Phosphatidylserine dynamics in cellular membranes. *Mol. Biol. Cell* **23**, 2198–2212 (2012).
50. Hoenen, T. *et al.* Oligomerization of Ebola virus VP40 is essential for particle morphogenesis and regulation of viral transcription. *J. Virol.* **84**, 7053–63 (2010).
51. Kerr, D. *et al.* Sensitivity of peripheral membrane proteins to the membrane context: A case study of phosphatidylserine and the TIM proteins. *Biochim. Biophys. acta. Biomembr.* **1860**, 2126–2133 (2018).
52. Stahelin, R. V. Lipid binding domains: More than simple lipid effectors. *Journal of Lipid Research* **50**, S299–30 (2009).
53. Stahelin, R. V., Scott, J. L. & Frick, C. T. Cellular and molecular interactions of phosphoinositides and peripheral proteins. *Chem. Phys. Lipids* **182**, 3–18 (2014).
54. Menke, M., Gerke, V. & Steinem, C. Phosphatidylserine membrane domain clustering induced by annexin A2/S100A10 heterotetramer. *Biochemistry* **44**, 15296–15303 (2005).
55. Yeung, T. *et al.* Membrane phosphatidylserine regulates surface charge and protein localization. *Science (80-.)*. **319**, 210–213 (2008).
56. Digman, M. A., Dalal, R., Horwitz, A. F. & Gratton, E. Mapping the number of molecules and brightness in the laser scanning microscope. *Biophys. J.* **94**, 2320–2332 (2008).
57. Moe, J. B., Lambert, R. D. & Lupton, H. W. Plaque assay for Ebola virus. *J. Clin. Microbiol.* **13**, 791–3 (1981).
58. Wang, J., Qiao, L., Hou, Z. & Luo, G. TIM-1 Promotes Hepatitis C Virus Cell Attachment and Infection. *J. Virol.* **91**, (2017).
59. Dejarnac, O. *et al.* TIM-1 Ubiquitination Mediates Dengue Virus Entry. *Cell Rep.* **23**, 1779–1793 (2018).
60. Miller, M. E., Adhikary, S., Kolokoltsov, A. A. & Davey, R. A. Ebolavirus Requires Acid Sphingomyelinase Activity and Plasma Membrane Sphingomyelin for Infection. *J. Virol.* **86**, 7473–7483 (2012).
61. Nanbo, A. *et al.* Ebolavirus is internalized into host cells via macropinocytosis in a viral glycoprotein-dependent manner. *PLoS Pathog.* **6**, e1001121 (2010).
62. Adu-Gyamfi, E., Digman, M. A., Gratton, E. & Stahelin, R. V. Single-particle tracking

- demonstrates that actin coordinates the movement of the Ebola virus matrix protein. *Biophys. J.* **103**, L41-3 (2012).
63. Soni, S. P., Adu-Gyamfi, E., Yong, S. S., Jee, C. S. & Stahelin, R. V. The Ebola virus matrix protein deeply penetrates the plasma membrane: An important step in viral egress. *Biophys. J.* **104**, 1940–1949 (2013).
 64. GC, J. B. *et al.* Interdomain salt-bridges in the Ebola virus protein VP40 and their role in domain association and plasma membrane localization. *Protein Sci.* 1648–1658 (2016). doi:10.1002/pro.2969
 65. Favard, C. *et al.* HIV-1 Gag specifically restricts PI(4,5)P2 and cholesterol mobility in living cells creating a nanodomain platform for virus assembly. *Sci. Adv.* **5**, (2019).
 66. Gc, J. B., Gerstman, B. S., Stahelin, R. V. & Chapagain, P. P. The Ebola virus protein VP40 hexamer enhances the clustering of PI(4,5)P2 lipids in the plasma membrane. *Phys. Chem. Chem. Phys.* **18**, 28409–28417 (2016).
 67. Younan, P. *et al.* Disruption of Phosphatidylserine Synthesis or Trafficking Reduces Infectivity of Ebola Virus. *J. Infect. Dis.* **218**, S475–S485 (2018).
 68. Jasenosky, L. D. *et al.* The FDA-Approved Oral Drug Nitazoxanide Amplifies Host Antiviral Responses and Inhibits Ebola Virus. *iScience* **19**, 1279–1290 (2019).
 69. Dyall, J. *et al.* Identification of Combinations of Approved Drugs With Synergistic Activity Against Ebola Virus in Cell Cultures. *J. Infect. Dis.* **218**, S672–S678 (2018).
 70. Nelson, E. A. *et al.* Clomiphene and Its Isomers Block Ebola Virus Particle Entry and Infection with Similar Potency: Potential Therapeutic Implications. *Viruses* **8**, E206 (2016).
 71. Johansen, L. M. *et al.* FDA-approved selective estrogen receptor modulators inhibit Ebola virus infection. *Sci. Transl. Med.* **5**, 190ra79 (2013).
 72. Johansen, L. M. *et al.* A screen of approved drugs and molecular probes identifies therapeutics with anti-Ebola virus activity. *Sci. Transl. Med.* **7**, 290ra89 (2015).
 73. Cho, K. J. *et al.* Staurosporines disrupt phosphatidylserine trafficking and mislocalize ras proteins. *J. Biol. Chem.* **287**, 43573–43584 (2012).

APPENDIX

Target	Species	Tag	Dilution	Cat. #	Company
NiV-M	Rabbit		1/1,000	n/a	From Collaborator
MeV-M	Rabbit		1/10,000	ab76949	Abcam
eVP40	Rabbit		1/40,000	0301-010	IBT Bioservices
Rabbit	Goat	HRP	1/5,000	205718	Abcam
GAPDH	Mouse		1/5,000	8245	Abcam
Mouse	Sheep	HRP	1/10,000	6808	Abcam
EBOV-GP (KZ52)	Human		1.0 µg/ml	0260-001	IBT Bioservices
Human	Goat	Alexa-488	0.7 µg/ml	A11013	Invitrogen
MARV-GP (9G4)	Mouse		4.0 µg/ml	N/A	USARMIID Hybridoma Division
Mouse	Goat	Alexa-488	1.0 µg/ml	A11029	Invitrogen
6xHis	Mouse		1/1,000	A5588	Sigma

Table 1 Antibodies used for immunoblotting experiments.

Symbol	Description	Unit	Value from calibration to budding and entry assays	Ranges based on fits to budding and entry assays	Value from calibration to BSL4 data – using ranges defined by budding and entry assays
β	Infection rate constant of target cells by free virions	(Virion.day) ⁻¹	N/A	0 - inf	6.6x10 ⁻⁶
δ	Death rate constant of infected cells	Day ⁻¹	N/A	0 - inf	4.6x10 ⁻⁶
c	Decay rate constant of free virions	Day ⁻¹	N/A	0 - 5	5
p	Viral production rate constant by infected cells	Virions.(Infected cell.day) ⁻¹	N/A	1 - inf	49
H_b	Hill constant for Fendiline effects on VLP budding		2.7	0.5 - 7	3.4
H_e	Hill constant for Fendiline effects on VLP entry		11	0.5 - 20	4.7
C_{50}^b	Concentration with 50% of maximum Fendiline effect on VLP budding	μ M	5.7	2 - 20	18
C_{50}^e	Concentration with 50% of maximum Fendiline effect on VLP entry	μ M	4.8	0.5 - 20	15
E_{max}^b	Maximum Fendiline effect on VLP budding		0.98	0.3 - 1	0.3
E_{max}^e	Maximum Fendiline effect on VLP entry		0.76	0.3 - 1	0.33

Table 2 Mathematical model parameter descriptions and values